Flavour Independent Search for Hadronically Decaying Higgs Bosons

Dissertation

zur Erlangung des Doktorgrades
des Fachbereichs Physik
der Universität Hamburg

vorgelegt von

Götz Gaycken

aus Hamburg

Hamburg
März 2003

Gutachter der Dissertation	:	Prof. Dr. R.-D. Heuer, Prof. Dr. P. Schleper
Gutachter der Disputation	:	Prof. Dr. R.-D. Heuer, Prof. Dr. B. Naroska
Datum der Disputation	:	8. April 2003, 17 Uhr
Vorsitzender des Prüfungsausschusses	:	Dr. E. Fretwurst
Vorsitzender des Promotionsausschusses	:	Prof. Dr. G. Huber
Dekan des Fachbereichs Physik	:	Prof. Dr. F.-W. Büser

Abstract

A search for the Higgs-strahlung process was performed using events with four-jet topology selected from 425 pb^{-1} of e^+e^- collision data, which were collected at $\sqrt{s} \simeq 192 - 209$ GeV by the OPAL detector at LEP. The search only makes use of the kinematic signature of Higgs-strahlung events, and thus, is sensitive to all events in which the Higgs boson h^0 decays into quark pairs of arbitrary flavour or into gluon pairs. In contrast to searches for the Standard Model Higgs boson, which are sensitive only to $h^0 \to b\bar{b}$ (and $h^0 \to \tau^+\tau^-$), this search remains sensitive in models, such as Two-Higgs-Doublet-models, in which the branching ratio into b quarks is suppressed for certain model parameters.

The result is combined with analyses of other event topologies and previous results using data collected at $\sqrt{s} = 189$ GeV and 91 GeV. No significant excess is observed over the background predicted by the Standard Model. A limit on the cross-section of Higgs-strahlung, $e^+e^- \to Z^0h^0$, times the branching ratio $h^0 \to$ hadrons is derived. Assuming the cross-section predicted by the Standard Model and a branching ratio $\text{Br}(h^0 \to \text{hadrons}) = 100\%$, Higgs-strahlung is excluded for $m_h < 105$ GeV at the 95% confidence level. The results are interpreted in context of the general Two-Higgs-Doublet model, the large-μ scenario of the Minimal Supersymmetric extension of the Standard Model and the Randall-Sundrum model.

Zusammenfassung

Es wurde ein Suche nach dem Higgsstrahlungsprozess in Ereignissen mit Vier-Jet Topologie durchgeführt. Ausgewertet wurden Daten einer integrierten Luminosität von 425 pb^{-1}, die in e^+e^- Kollisionen bei Schwerpunktsenergien von $\sqrt{s} = 192 - 209$ GeV mit dem OPAL Detektor am LEP Speicherring aufgezeichnet wurden. Die Suche macht sich ausschließlich die kinematische Signatur von Higgsstrahlungsereignissen zu Nutze. Daher ist die Suche sensitiv auf alle Ereignisse in denen Higgsbosonen in Quarkpaare beliebiger Sorte oder Gluonpaare zerfallen. Im Gegensatz zu Suchen nach dem Standard Modell Higgsboson, die nur auf $h^0 \to b\bar{b}$ (und $h^0 \to \tau^+\tau^-$) sensitiv sind, bleibt diese Suche sensitiv in Modellen, wie z.B. Zwei-Higgs-Dublett Modellen, in denen das Verzweigungsverhältnis in bottom-Quarks für spezielle Parameter unterdrückt ist.

Die Ergebnisse dieser Analyse und Analysen anderer Topologien, sowie vorherigen Analysen bei Schwerpunktsenergien von 189 GeV und 91 GeV, weisen keine signifikante Abweichung von dem erwarteten Standard Modell Untergrund auf. Die selektierten Kandidaten wurden verwandt, um ein Obergrenze auf den Wirkungsquerschnitt des Higgsstrahlungsprozesses, $\sigma(e^+e^- \to Z^0h^0)$, mal dem Verzweigungsverhältnis, $h^0 \to$ Hadronen zu bestimmen. Unter Annahme eines Verzweigungsverhältnisses $\text{Br}(h^0 \to \text{Hadronen}) = 100\%$ und einer Kopplung des Higgsbosons an das Z Boson äquivalent zu den Vorhersagen des Standard Modells, können Higgsbosonen bis zu einer Masse von 105 GeV mit einem Konfidenzniveau von 95% ausgeschlossen werden. Das Ergebnis wird innerhalb des allgemeinen Zwei-Higgs-Dublett Modells, dem “large-μ” Szenario der Minimalen Supersymmetrischen Erweiterung des Standard Modells und dem Randall-Sundrum Modell interpretiert.

Contents

Chapter 1

Introduction

During the last century, a model has been developed, which describes in great detail the fundamental structure of matter and its interactions, known as *the Standard Model* (SM). In the SM, matter is composed of point-like fermions. Between them, there are four different interactions: electromagnetic interactions, responsible for the force between charged particles, *weak* interactions leading to e.g. radioactive decays, and *strong* interactions, which stabilise protons and neutrons, the constituents of atomic nuclei. The interactions are mediated by gauge *bosons*, where the electromagnetic, weak, and strong interactions are mediated by the photon, W and Z bosons, and gluons, respectively. So far, all attempts failed to incorporate gravity into the SM.

The fundamental fermions are classified into *quarks* and *leptons*, where leptons, in contrast to quarks, do not interact strongly. Quarks exist with two different charges, and leptons either charged or neutral. The neutral leptons, called neutrinos, interact only weakly. In total quarks exist in 6 *flavours* (down, up, strange, charm, bottom and top) and there are 6 different leptons (the electron, muon, tau and their corresponding neutrinos) each having a different mass. Moreover, for each fermion, there is a corresponding anti-fermion, whose properties are identical, but whose charge like quantum numbers are oppositely signed.

Until now all observations agree well with the SM predictions and there are no indications that the fundamental particles have any internal structure. However, many questions are not addressed. Among them are: Why are there exactly 6 quarks and leptons? Why do the particles carry their particular charge? Why do they carry their particular mass? Why are there four different interactions? Why is gravity so much weaker than the other three forces? During the development of the SM, the number of free parameters could be greatly reduced by introducing a superordinated structure. Therefore it is believed that the SM is only an effective theory; the fundamental core, a unified *Theory Of Everything*, is still to be discovered.

Nevertheless, even if these shortcomings of the SM are accepted, there are still problems not yet solved. One of them is the origin of mass. The principles on which the SM is built are symmetries. However, some of these symmetries cease to exist if particles are allowed to be massive. The most attractive solution to save this very successful model is the *Higgs mechanism*. Initially all particles are assumed to be massless. However, the vacuum is filled with an additional field. The existence of this additional field, i.e. its non vanishing vacuum expectation value, breaks the inherent symmetry of the SM. The SM particles interact with this background field, thereby appearing massive. As a further consequence, an additional massive particle is predicted, the *Higgs* boson.

The Higgs boson has not yet been found [1], but, as alternatives to the Higgs mechanism are rare, its existence is generally believed. The hunt for the Higgs boson is a major topic in experimental particle physics and will continue to be. Unfortunately, beyond the simplest possibility there are various ways of realising the Higgs mechanism. Some more fundamental models even demand an extension. Since the properties of the extended Higgs sector may differ significantly, searches are and have been performed in a broader scope [2]. In most extensions, the Higgs boson decays into pairs of quarks or gluons whereas in the minimal model the Higgs boson decays mostly into bottom quarks in the mass reach of current experiments. Searches for the Higgs boson within the minimal model extensively use the properties of this particular decay mode. But, in order to be sensitive to a larger set of possible models, searches which do not depend on the flavour of the decay products are an important supplement.

This work ties in with the flavour independent Higgs boson searches described in [3]. The analysis is based on an earlier analysis of data recorded in 1998 by the OPAL detector [4], however, the analysis is applied to data recorded in 1999 and 2000. An extension and optimisation became necessary in order to deal with the higher centre-of-mass energies and the broader energy spectrum delivered by LEP in these two years.

This thesis is organised in the following way: Since there are numerous excellent books about the SM, for example [5], their content is not repeated here. Nevertheless, a brief overview of the Higgs mechanism and the properties of its minimal realisation are given in the following chapter before a selection of possible extensions is presented in Chapter 3. Thereafter the OPAL detector is described. At the startup in 1999, the central jet chamber of the detector suffered an irreparable short in one sector. A solution to operate the detector was found, although, the data reconstruction had to be adapted. This is described in Chapter 5. An overview of the data set and simulations on which the analysis relies is given in Chapter 6. The analysis and systematic studies are detailed in Chapter 7. In Chapter 8, the results are interpreted within selected models.

Chapter 2

The Higgs Boson in the SM

The SM in its current form describes all observations precisely. However, the bosons and fermions appear to be massive which is in conflict with the underlying quantum gauge field theory since the presence of explicit mass terms for gauge bosons and fermions destroys the gauge invariance of the Lagrangian. This is shown for the electroweak interaction in the subsequent section. Such a theory would not be renormalisable since gauge invariance is essential.

In order to accomplish gauge invariance of the electroweak Lagrangian, a mechanism is needed which generates the masses dynamically. The Higgs mechanism is the only known mechanism for achieving this goal while guaranteeing renormalisability. It is recapitulated briefly after the following section. The mechanism was investigated first by F. Englert, R. Brout and P. Higgs [6] in the case of Abelian gauge theories. Later the idea was extended towards non Abelian gauge theories, see for example [7]. As a direct consequence of the proposed mechanism, additional massive spinless bosons appear, the *Higgs* bosons. Their properties are specified in Section 2.4.

Many questions remain unresolved within the SM, therefore the SM is believed to be only a low-energy approximation of the *Theory Of Everything*. Nevertheless, more fundamental theories are likely to induce a Higgs mechanism at this limit. A few possible extensions are discussed in Chapter 3.

2.1 Gauge Invariance in the Presence of Massive Weak Gauge Bosons

The SM Lagrangian describing the weak interaction of a fermion is given by (see for example [8]):

$$\bar{\psi}(i\gamma^{\mu}\mathrm{D}_{\mu}+m)\psi-\frac{1}{4}F^{k}_{\mu\nu}F^{k\mu\nu}+\frac{1}{2}M^{2}_{\mathrm{W}}\mathrm{W}^{k\mu}\mathrm{W}^{k}_{\mu}, \tag{2.1}$$

where $\psi := \mathrm{u}\otimes\chi$ comprises the Dirac spinor u and the weak isospin doublet χ, F^j are the field-strength-tensors of the weak interaction, W^j are the weak vector fields, M_{W} their masses and the covariant derivative is given by $\mathrm{D}_{\mu} = \partial_{\mu} + ig/2\ \tau^k\mathrm{W}^k_{\mu}$. The SU(2) generators are represented by τ^k. Since weak processes like β decays do not depend on the weak isospin, the Lagrangian (2.1) should be invariant under local transformations of the weak isospin $\Omega(x) := \exp(-ig/2\ \tau^j\sigma_j(x))$ as long as the transformation is applied simultaneously to the particles and gauge fields. Applying the transformation on the fermion $\psi \rightarrow \Omega\psi$ ($\bar{\psi} \rightarrow \bar{\psi}\Omega^{-1}$) and moving the transformation to the left yields:

$$\bar{\psi}(i\gamma^{\mu}(\partial_{\mu}+\Omega^{-1}(\partial_{\mu}\Omega)+ig\Omega^{-1}\tau^{k}\mathrm{W}^{k}_{\mu}\Omega)+m)\psi$$

Since the gauge fields have to be transformed at the same time, see for example [9]:

$$\begin{aligned}
\tau^{k}\mathrm{W}^{k}_{\mu}\rightarrow\quad & \tau^{k}\mathrm{W}'^{k}_{\mu} && (2.2)\\
= \quad & \Omega^{-1}\tau^{k}\mathrm{W}^{k}_{\mu}\Omega+(ig)^{-1}\Omega^{-1}(\partial_{\mu}\Omega) && (2.3)\\
= \quad & \tau^{k}\mathrm{W}^{k}_{\mu}-\tau^{l}(\partial\sigma_{l}(x))-[\tau^{k},\tau^{j}]\sigma_{j}\mathrm{W}^{k}_{\mu}+\mathcal{O}(g^{2})\mathcal{O}(\sigma^{2}) && (2.4)\\
= \quad & \tau^{k}\mathrm{W}^{k}_{\mu}-\tau^{l}(\partial\sigma_{l}(x))-\epsilon^{njk}\tau^{k}\sigma_{j}\mathrm{W}^{n}_{\mu}+\mathcal{O}(g^{2})\mathcal{O}(\sigma^{2}), && (2.5)
\end{aligned}$$

the first term of (2.1) is restored. The second term is invariant under (2.2) by construction. Apparently, the mass terms of the electroweak bosons change and thus destroy the gauge invariance of (2.1). Either the principle of gauge invariance has to be abandoned or a mechanism which generates masses dynamically in a gauge invariant way is needed. The latter is achieved by the Higgs mechanism discussed in the following section.

2.2 The Higgs Mechanism

The initially massless particles acquire a mass through the interaction with a background field. This background field is usually denoted the Higgs field. Since the mass appears to be a unique and immutable property of each particle the Higgs field must be omnipresent in order to guarantee that the interaction happens. Thus, the vacuum expectation value (VEV) of this field must not vanish.

In the SM, there are three gauge bosons acquiring masses. All of them are spin 1 vector bosons. Since massive vector bosons may also be longitudinally polarised in contrast to massless bosons, they have one additional degree of freedom each, which can only be provided by the Higgs field. Thus, the Higgs field H must have at least three degrees of freedom. In order to establish invariance under weak gauge transformations, the Higgs field must have an weak isospin component: $\mathrm{H}\in\mathbb{R}^{4}\times\mathrm{SU}(2)$ which transforms accordingly. The simplest choice is either to organise the field as a weak isospin triplet of real fields or as a doublet of complex fields likewise used for fermions. In the first case, the generators of the weak gauge transformation are represented by real 3×3 matrices, in the latter case they are those also used to transform fermions. More complex choices are possible.

Since the photon is massless, only the neutral components of the Higgs field should have a non-vanishing vacuum expectation value. This together with the choice of the weak isospin component defines its quantum numbers. For example the hypercharge and the weak isospin will be $Y=1$ and $I_{3}=\pm1/2$ if the Higgs field is organised as a weak isospin doublet of complex fields: $(\mathrm{H}^{+},\,\mathrm{H}^{0})$.

In order to accomplish a non-zero vacuum expectation value the field must exhibit self interaction. This is realised by the following potential:

$$\mathrm{U}_{\mathrm{Higgs}}:=\lambda^{2}\left(\mathrm{H}^{\dagger}(x)\mathrm{H}(x)\right)^{2}-\mu^{2}\mathrm{H}^{\dagger}(x)\mathrm{H}(x). \qquad (2.6)$$

Higher order polynomials in $|\mathrm{H}|$ are not renormalisable. For this choice the minimal value is adopted at $|\mathrm{H}(x)|=\mu/\lambda\sqrt{2}$ presuming that λ and μ are real numbers. If H is a doublet of complex fields, the vacuum state can be transformed into $(\mathrm{H}^+, \mathrm{H}^0) = (0, \mu/\lambda\sqrt{2})$ applying electroweak gauge transformations.

Investigating perturbations around the vacuum state shows that boson masses can be generated by such a mechanism. This is shown for the case of one complex doublet with the perturbed state parametrised in the following form:

$$\mathrm{H}'(x) \simeq \begin{pmatrix} \zeta_1(x) + i\zeta_2(x) \\ v + \mathrm{h}(x) + i\zeta_3(x) \end{pmatrix}, \tag{2.7}$$

where the vacuum expectation value $v := \mu/\lambda\sqrt{2}$ was introduced. The perturbed state (2.7) is an approximation of

$$\mathrm{H}'(x) = \exp\left\{\frac{i}{v}\tau^j\zeta_j(x)\right\} \begin{pmatrix} 0 \\ v + \mathrm{h}(x) \end{pmatrix} \simeq \begin{pmatrix} \zeta_1(x) + i\zeta_2(x) + \mathcal{O}(\zeta_j \mathrm{h}) \\ v + \mathrm{h}(x) + i\zeta_3(x) + \mathcal{O}(\zeta_3 \mathrm{h}) \end{pmatrix} \tag{2.8}$$

neglecting all terms with products of two or more fields ζ_j and h. The exponential factor has the form of a gauge transformation and is removed by performing the inverse transformation:

$$\mathrm{H}'(x) \to \mathrm{H}(x) = \begin{pmatrix} 0 \\ v + \mathrm{h}(x) \end{pmatrix}. \tag{2.9}$$

The fields ζ_j are the so called Goldstone bosons [10]. Since the gauge fields transform simultaneously according to (2.2) the Goldstone bosons give rise to their longitudinal degrees of freedom.

The complete Lagrangian of the Higgs field is composed of the kinetic term and the potential $\mathrm{U}_{\mathrm{Higgs}}$:

$$\mathcal{L}_{\mathrm{Higgs}} = \frac{1}{2}(\mathrm{D}^\mu \mathrm{H})^\dagger(x)\mathrm{D}_\mu \mathrm{H}(x) - \lambda^2 \left(\mathrm{H}^\dagger(x)\mathrm{H}(x)\right)^2 + \mu^2 \mathrm{H}^\dagger(x)\mathrm{H}(x). \tag{2.10}$$

The covariant derivative D^μ of the electroweak gauge theory is given by $\mathrm{D}^\mu := \partial^\mu + ig/2\ \delta_{kl}\tau^k \mathrm{V}^{l\mu}$, where $\mathrm{V}^{\mathrm{j}\mu} := \mathrm{W}^{\mathrm{j}\mu}$, $\mathrm{j} = 1, 2, 3$ are the weak gauge fields (associated to the SU(2) gauge group), $\mathrm{V}^{4\mu} := \frac{\mathrm{g}'}{\mathrm{g}}\mathrm{B}^\mu$ the gauge field associated to the U(1) gauge group, and $\tau^4 := \mathbb{1}$ the unit matrix. The approximate Lagrangian, inserting the ansatz (2.8) for H, becomes[1]:

$$\begin{aligned} \mathcal{L} = \frac{1}{2}\partial^\mu \mathrm{h}\partial_\mu \mathrm{h} - \mu^2\mathrm{h}^2 \quad &+ \quad \frac{1}{2}\left(\frac{gv}{2}\right)^2 (\tau^{\dagger k}\tau^n)_{11}\mathrm{V}^{k\mu}\mathrm{V}^n_\mu + \frac{1}{2}\left(\frac{gv}{2}\right)^2 \frac{2}{v}\mathrm{h}\mathrm{V}^{k\mu}\mathrm{V}^k_\mu \\ &+ \quad \mathcal{O}(h^2\mathrm{V}^{k\mu}\mathrm{V}^k_\mu). \end{aligned} \tag{2.11}$$

The first two terms form the equation of motion of the scalar field $\mathrm{h}(x)$ which gained the effective mass $m_{\mathrm{h}} := \sqrt{2}\mu$. This field is generally referred to as the Higgs boson. The third term generates an effective mass $m_{\mathrm{W}} := gv/2$ for the electroweak bosons:

$$\frac{1}{2}m_W^2 \left(\mathrm{W}_{1\mu}\mathrm{W}_1^\mu + \mathrm{W}_{2\mu}\mathrm{W}_2^\mu + \left(\mathrm{W}_{3\mu} - \frac{g'}{g}\mathrm{B}_\mu\right)\left(\mathrm{W}_3^\mu - \frac{g'}{g}\mathrm{B}^\mu\right)\right).$$

The mass terms of the bosons $\mathrm{W}_{1\mu}$ and $\mathrm{W}_{2\mu}$ give rise to the W boson masses, $\mathrm{W}^\pm_\mu := (\mathrm{W}_{1\mu} \pm i\mathrm{W}_{2\mu})/\sqrt{2}$, since $\mathrm{W}^{+\dagger}_\mu \mathrm{W}^{+\mu} + \mathrm{W}^{-\dagger}_\mu \mathrm{W}^{-\mu} = \mathrm{W}_{1\mu}\mathrm{W}_1^\mu + \mathrm{W}_{2\mu}\mathrm{W}_2^\mu$. The last term gives rise to the Z boson mass, $m_{\mathrm{W}}/\cos\theta_{\mathrm{W}}$, since $\mathrm{Z}^\mu \equiv (\cos\theta_{\mathrm{W}}\mathrm{W}_3^\mu - \sin\theta_{\mathrm{W}}\mathrm{B}^\mu)$, where $\tan\theta_{\mathrm{W}} := \frac{g'}{g}$ [11]. The photon

---

[1] The field operators are hermitian $\mathrm{V}^l_\mu = \mathrm{V}^{l\,\dagger}_\mu$.

$\sin\theta_{\mathrm{W}} \mathrm{W}_{3\mu} + \cos\theta_{\mathrm{W}} \mathrm{B}_{\mu}$ remains massless. Finally, the fourth term leads to an interaction of the weak bosons with the Higgs boson $\mathrm{h}(x)$. The couplings are:

$$g_{\mathrm{hVV}} := 2m_{\mathrm{W}}^2/v. \tag{2.12}$$

So far only the weak bosons have been considered, however, SU(2) gauge invariance is also destroyed by explicit mass terms for the fermions since mass terms relate left and right handed fermions which transform differently under gauge transformations. The Yukawa coupling seems to be the only gauge invariant solution to give left and right handed fermions a mass:

$$\mathcal{L}_{\mathrm{Yukawa}} := -g_{\mathrm{f}} \left(\overline{\mathrm{R}}_{\mathrm{f}} \mathrm{H}^{\dagger} \mathrm{L}_{\mathrm{f}} + \overline{\mathrm{L}}_{\mathrm{f}} \mathrm{H} \mathrm{R}_{\mathrm{f}} \right), \tag{2.13}$$

where R_{f} denotes the right handed singlet of a fermion f, L_{f} the corresponding doublet of the left handed fermions and g_{f} the Yukawa coupling. The fermions acquire their correct masses m_{f} if:

$$m_{\mathrm{f}} = g_{\mathrm{f}} \frac{v}{\sqrt{2}} \tag{2.14}$$

Thus, an individual parameter is needed for each fermion mass. The Yukawa coupling does not explain the mass hierarchies of the fermions.

2.3 The Mass of the Higgs Boson

In the previous section, the mechanism was presented, how the weak bosons acquire mass without destroying the gauge invariance of the SM Lagrangian. The mechanism predicts an additional massive boson, whose mass is a free parameter. Nevertheless, upper bounds on the mass can be derived requiring the theory to be valid up to an energy scale Λ [12]. Lower bounds follow from the requirement of vacuum stability [13]. These bounds are briefly discussed in the following.

General upper bounds are obtained by investigating scattering processes of longitudinally polarised vector bosons, $\mathrm{V_L V_L} \rightarrow \mathrm{V_L V_L}$ [14]. Without considering the exchange of Higgs bosons, the scattering amplitude would violate unitarity at a centre-of-mass energy $\sqrt{\mathrm{s}}$, indicating the limit up to which perturbation theory is applicable at most. Beyond this scale, new physics has to appear (e.g. the gauge bosons could become strongly interacting). The most restrictive upper bounds on the perturbative regime are $\sqrt{\mathrm{s}} \lesssim 1.2\,\mathrm{TeV}$, investigating other scattering processes of longitudinal polarised vector bosons. Taking processes with Higgs boson exchange into account, the scattering amplitude meets the unitarity constraint to first order at all centre-of-mass energies, if the Higgs bosons are sufficiently light, $m_{\mathrm{h}} \lesssim 700\,\mathrm{GeV}$. However, it seems to be impossible to maintain a bound independent of $\sqrt{\mathrm{s}}$, when higher orders are taken into account [15].

Further upper mass bounds are obtained by investigating the high energy behaviour of the couplings [12]. The measured coupling constants of the electroweak theory do not coincide with the bare quantities which appear in the Lagrangian. However a prescription exists which relates the bare to the observable quantities known as *renormalisation* [16]. The renormalised quantities generally depend on the energy scale μ relevant for the specific process of interest. This scale dependence of the couplings leads to the term *running* coupling constant. The asymptotic behaviour can be described by a coupled set of differential equations, the renormalisation group equations (RGE) [17]. A summary of the RGE of SM couplings can be found in [18]. The quartic Higgs coupling λ of (2.6) for example rises with the energy scale μ. Furthermore, it turns out that $\lambda(\mu)$ contains a singularity at a certain scale Λ_c referred to as the *Landau pole* [19]. Since calculations are performed in perturbation theory, the calculations will become invalid at a certain scale $\Lambda < \Lambda_c$ at which the quartic coupling $\lambda(\Lambda)$ becomes too large. Requiring the SM to remain in the perturbative regime, the Landau pole must be located beyond the scale Λ up to which the SM is considered to deliver a valid description i.e. the scale at which new physics appears. Assuming that no new physics exist, the SM should be valid up to the Planck scale $\Lambda_\mathrm{Planck} \simeq \mathcal{O}(10^{15}\,\mathrm{TeV})$, at which gravity becomes important.

The quartic coupling λ and also the position of the Landau pole depend mainly on the Higgs boson and top quark mass. Thus, an upper bound $m_{\mathrm{H_{SM}}}(\Lambda)$ on the Higgs bosons mass can be derived requiring the SM to be valid at least up to a scale Λ.

A lower bound can be derived requiring the existence of a stable solution of the vacuum [13]. This is guaranteed by the Higgs potential (2.6) at lowest order, but if the Higgs boson mass is too small, the negative contributions from top quark loops may dominate and the renormalised quartic coupling $\lambda(\mathrm{Q})$ becomes negative at large scales Q. As a consequence the potential will not be bound at large field values and a stable vacuum solution will not exist. Thus, in order to guarantee a stable vacuum up to the scale Λ, at which new phenomena appear and modify the Higgs potential, the Higgs boson mass must be large enough such that $\lambda(\mathrm{Q}) \geq 0$ for all $\mathrm{Q} < \Lambda$.

The lower and upper bounds on the Higgs boson mass as a function of the scale Λ are shown in Figure 2.1a. If the SM is valid up to the Planck scale $\Lambda \simeq 10^{15}\,\mathrm{TeV}$ the Higgs boson mass must be in the range $m_{\mathrm{H_{SM}}} \simeq 130 - 190\,\mathrm{GeV}$, however, if new phenomena enter at 1 TeV valid Higgs boson masses are in the wide range from 50 GeV to 800 GeV.

Meanwhile, direct searches for the SM Higgs boson have been performed; the most stringent limit results from the 4 LEP experiments. They excluded a SM Higgs boson up to a mass of 114.4 GeV at the 95% confidence level [1]. Further limits have been determined indirectly within the framework of the SM [20]. Many observables, e.g. masses of bosons and fermions, the coupling constants, the Weinberg angle, etc., have been measured with high precision at LEP, SLD, the TEVATRON and NUTEV. Relations exist between the observables, which are subject to higher order corrections. Some of these corrections are due to Higgs boson exchange, and therefore, they are sensitive to the Higgs boson mass. The most sensitive observables are the measurement of the top quark mass, the mass of the W and Z bosons and the Weinberg angle. In order to determine the Higgs boson mass, all parameters of the SM are fitted simultaneously to the observables. The mass of the Higgs boson is left as a free parameter. Figure 2.1b shows the deviation from the minimal χ^2 depending on the Higgs boson mass. The fit favours a light Higgs boson with $m_{\mathrm{H_{SM}}} = 81^{+52}_{-33}\,\mathrm{GeV}$, however, the χ^2-probability amounts only to 1.3% if the measurements of the NUTEV collaboration are taken into account [21]. The χ^2-probably increases to 11%, if the NUTEV results are excluded. The Higgs boson mass at minimal χ^2 does not change significantly. At the 95% confidence level, an upper bound on the Higgs boson mass of 193 GeV is obtained. The direct and the indirect bounds still permit the SM to be valid up to the Planck scale.

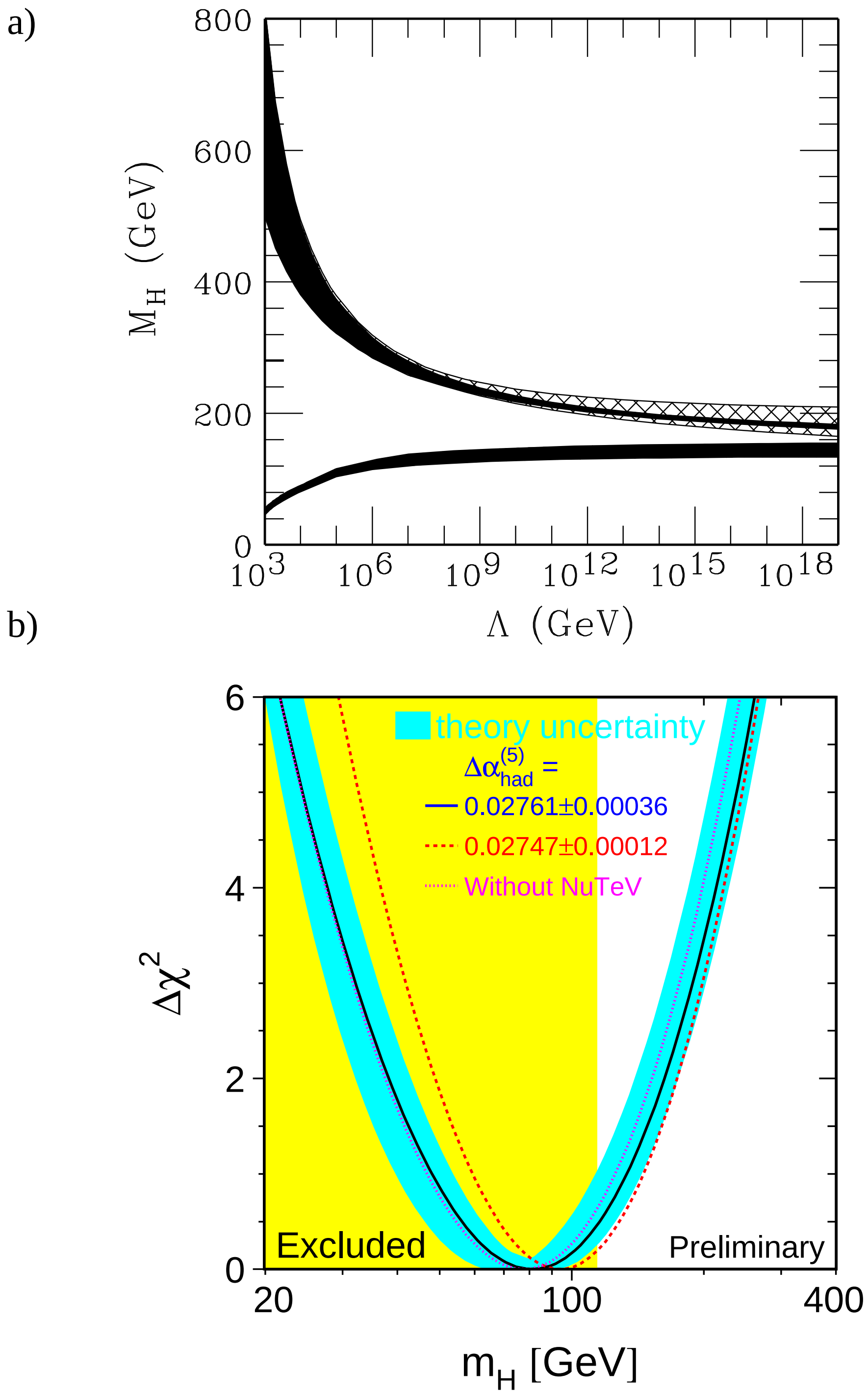

Figure 2.1: Bounds on the Higgs boson mass. Figure a) shows the upper and lower bounds on the Higgs boson mass depending on the energy scale at which new physics appears. The bands indicate the uncertainties of the bounds including the experimental error of 5 GeV on the top quark mass $m_t = 175$ GeV. The hatched area shows the change of the upper bound when the top quark mass is changed by ±25 GeV. Figure b) shows the deviation from the minimal χ^2 of the fit to electroweak precision observables depending on the Higgs boson mass. The light shaded area indicates the mass range excluded by direct searches at LEP.

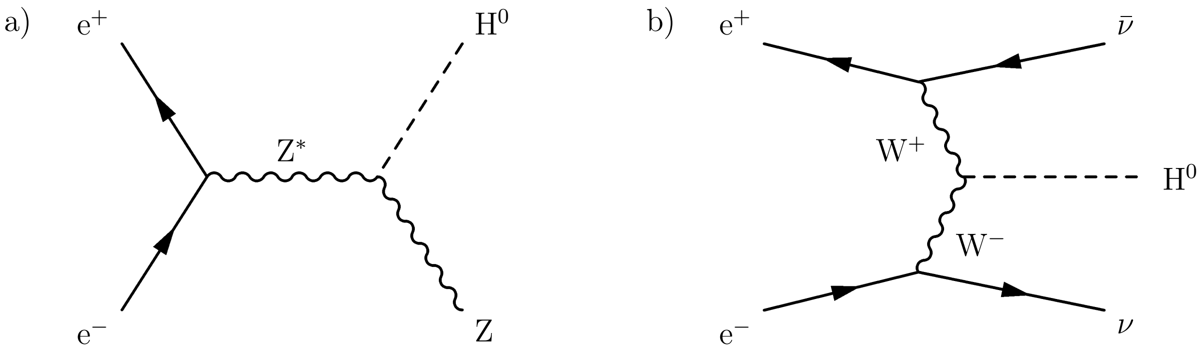

Figure 2.2: Dominant Higgs boson production processes in e^+e^- collisions. a) The dominant production process is Higgs-strahlung at centre-of-mass energies achieved by LEP and for Higgs boson masses below the kinematic limit. The cross-section decreases with the centre-of-mass energy like $\sigma \propto 1/\mathrm{s}$. b) W (or Z) boson fusion dominates beyond the kinematic limit (compare with Figure 2.4) and at larger centre-of-mass energies. The cross-section increases like $\sigma \propto \log \mathrm{s}$.

2.4 Production and Decay of Higgs bosons

The Higgs boson coupling to fermions (2.14) and bosons (2.11) is proportional to the fermion mass or boson mass. Thus, the resonant production of Higgs bosons in e^+e^--collisions is strongly suppressed, due to the small electron mass. The dominant production processes are Higgs-strahlung and W-fusion. The corresponding Feynman diagrams are depicted in Figures 2.2a and b. Nevertheless, the cross-section of W-fusion is small compared to Higgs-strahlung at the centre-of-mass energies achieved at LEP. Close to the kinematic limit the relative contribution increases; however, the total cross-section is small. The cross-sections of both processes [22] are shown in Figure 2.4, including the contribution and interference of the process $e^+e^- \rightarrow Z^0 \rightarrow H^0\nu\bar{\nu}$ with the fusion process [23].

Since the coupling of the Higgs boson to W bosons (2.12) is largest, the decay into two W bosons will predominate if the Higgs boson is heavy $m_{\mathrm{H}} \gtrsim 2m_{\mathrm{W}}$. However, if the Higgs boson is too light this decay mode is kinematically suppressed and the Higgs boson decays dominantly into the heaviest fermion pair which is kinematically accessible. The branching ratios calculated with [24] are depicted in Figure 2.4b. At centre-of-mass energies achieved at LEP only Higgs bosons with masses $m_{\mathrm{H}} \lesssim 120\,\mathrm{GeV}$ can be produced. Higgs bosons in this mass range decay predominantly into pairs of bottom quarks. The branching ratio amounts to approximately 85%. Due to the large mass of the top quark, the higher order decay via top quark loops into gluons is not negligible [25]. The process is depicted in Figure 2.3. This decay mode accounts for $4-6\%$ in the mass region $100-120\,\mathrm{GeV}$.

The total decay width is smaller than $10\,\mathrm{MeV}$ [26] since decays into heavy particles are kinematically suppressed for Higgs bosons with $m_{\mathrm{H}} < 120\,\mathrm{GeV}$, and the coupling to light particles is small.

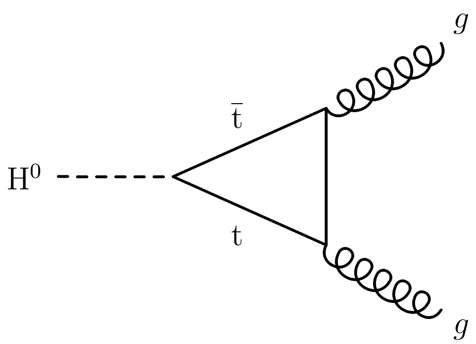

Figure 2.3: A Higgs boson decaying into gluons via a top loop. This loop-induced process is not negligible due to the large mass of the top quark.

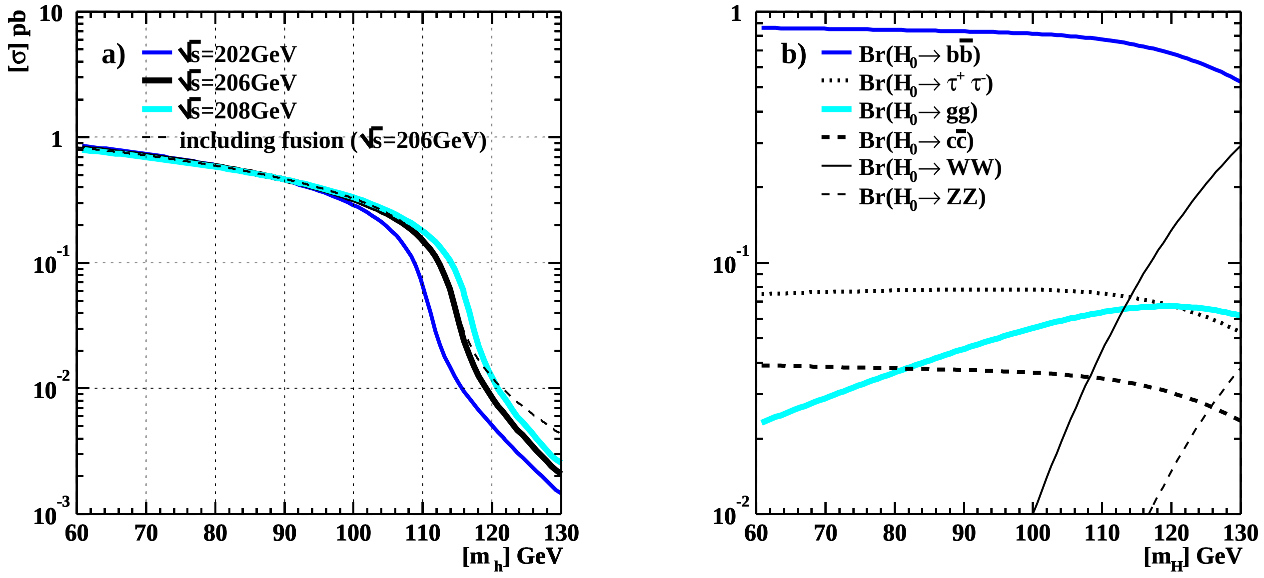

Figure 2.4: Cross-section and branching ratios of the SM Higgs boson. Figure a) shows the cross-section of Higgs-strahlung at different centre-of-mass energies. At $\sqrt{s} = 206\,\mathrm{GeV}$, also the total production cross-section is shown i.e. the cross-section of Higgs-strahlung and the W and Z boson fusion processes. Figure b) shows the dominant branching ratios depending on the Higgs boson mass.

Chapter 3

Extensions of the Minimal Higgs Sector

In the previous chapter, the minimal Higgs mechanism and its phenomenology were discussed. The Higgs sector need not necessarily be the minimal one and can be composed of an arbitrary number of Higgs singlets and multiplets. These extensions may lead to a rather different phenomenology. Frequently, the parameters in extended models have to be finely tuned in order to yield a consistent theory and to be compatible with observations. This is briefly discussed in the following section. The constraints are fulfilled automatically by Higgs sectors composed exclusively from complex doublets or singlets. More light is shed on these models, since models which require fine tuning are generally disfavoured[1]. The next simplest models after the minimal Higgs model are Two-Higgs-Doublet models. They show already features which can influence the observability of Higgs bosons. Furthermore, at least two Higgs doublets are required in supersymmetric theories. A brief overview is given in Section 3.2 followed by a short discussion of the Minimal Supersymmetric extension of the Standard Model (MSSM). In Chapter 3.4, the Randall-Sundrum model is presented. This extension of the SM tackles the problem of the hierarchy between the masses of electroweak bosons and the Planck mass. The Higgs sector is not modified directly, however, this model induces an additional massive scalar which interferes with the Higgs boson. As a consequence, the properties of the physical scalar states are different from those of the SM Higgs boson.

3.1 Constraints on the Higgs Sector

Models with an arbitrary number of Higgs multiplets and singlets are possible, but they are subject to several restrictions. It was shown in [27] that photons generally would acquire a mass. And it was pointed out that triplets or higher multiplet representations can not be used to generate fermion masses. Thus, at least one doublet seems to be necessary.

Furthermore, it turns out to be difficult to arrange the multiplets such that the W and Z boson masses, m_{W} and m_{Z}, result correctly. Precise measurements of the masses of the W and Z bosons, m_{W} and m_{Z}, and the weak mixing angle θ_{W} yield [28]:

$$\rho := \frac{m_{\mathrm{W}}^2}{m_{\mathrm{Z}}^2 \cos^2 \theta_{\mathrm{W}}} \simeq 1.0012^{+0.0023}_{-0.0014} \tag{3.1}$$

---

[1] It is questionable whether an effective theory can yield a stable universe if its parameters require to be finely tuned. "But nobody knows whether the universe is stable." (Klaus Desch)

In Section 2.2 the result, $\rho = 1$, was obtained at tree level for the simplest case of one complex doublet. The general case is treated in [29]. They prove that $\rho = 1$ is obtained to first order in all Higgs models exclusively composed of doublets and singlets. If higher representations are involved the requirement is met only for properly tuned vacuum expectation values [30], unless the following relation is fulfilled between the weak isospin T and the hypercharge Y of each Higgs multiplet:

$$(2T+1)^2 - 3Y^2 = 1. \tag{3.2}$$

Beyond the doublet representation, $T = 1/2$ and $Y = \pm 1$, the next simplest representation would be $T = 3$ and $Y = \pm 4$.

Moreover, arbitrarily complex Higgs sectors may cause sizable f*lavour changing neutral currents* (FCNC). However, the observed strong suppression [28] indicates that FCNCs can only happen due to higher order processes. In the unbroken theory, FCNCs are suppressed naturally to first order due to SU(2) gauge invariance. This was discovered first in [31] and led to the prediction of the charm quark. However, this natural suppression is generally abolished if the symmetry is broken. In [32] it was found that natural suppression is realised if the matrix of the fermion masses and the matrix of the charges can be diagonalised simultaneously. This can be established in models exclusively composed of complex doublets if all fermions with equal charge couple to the same Higgs doublet.

As mentioned in Section 2.3, without considering the coupling of Higgs bosons to vector bosons the scattering amplitude of longitudinal polarised vector bosons, $\mathrm{V_L V_L} \to \mathrm{V_L V_L}$, grows with increasing centre-of-mass energy, and finally exceeds the unitarity bound. This growth is compensated by terms involving Higgs boson exchange order by order due to the relation between the weak coupling g and the coupling of the Higgs boson to vector bosons: $g_{\mathrm{hVV}} = g m_{\mathrm{W}}$. In extended models, all Higgs bosons $\mathrm{h_i}$ contribute to this scattering process. Thus, in order to guarantee the cancelation order by order, the couplings $g_{\mathrm{h}_i\mathrm{VV}}$ have to be related to the coupling of the SM Higgs boson [33]: $f(\ldots, g_{\mathrm{h_iVV}}, \ldots) = g_{\mathrm{H_{SM}VV}}$. In models with two complex Higgs doublets the relation is:

$$\sum_{i=1}^{2} g^2_{\mathrm{h_iVV}} = g^2_{\mathrm{H_{SM}VV}}. \tag{3.3}$$

Similar rules follow for the couplings to fermion pairs in order to guarantee unitarity of the scattering amplitude of $\mathrm{f_+\bar{f}_+} \to \mathrm{V_L V_L}$, where f_+ denotes fermions with positive helicity.

None of the above constraints rules out models with Higgs triplets or higher multiplets, but these models appear unnatural due to the strong restrictions of their parameters. On the other hand, models only composed of doublets are as natural as the minimal Higgs model and are therefore more in the focus of the general interest.

3.2 Two-Higgs-Doublet Models

The simplest extension of the minimal Higgs sector of Section 2.2 is provided by one additional complex doublet. Such models are called Two-Higgs-Doublet models (THDM). Compared to the minimal Higgs model new features appear which are summarised below. More detail can be found in [34].

In a similar way to the minimal case, 3 of the 8 degrees of freedom lead to the longitudinally polarised components of the W and Z bosons. The remaining 5 degrees of freedom manifest themselves in massive scalar bosons: two neutral, CP-even bosons, h^0 and H^0, two charged bosons $\mathrm{H}^{\pm}$ and a neutral CP-odd boson A^0. The additional freedom allows the construction of Higgs potentials giving rise to CP violation. A specific CP violating scenario is discussed in [35]. In the following, only the CP conserving case is considered. The remaining free parameters are conveniently chosen to be:

- the 4 masses of the five bosons: $m_{\mathrm{h}^0} < m_{\mathrm{H}^0}$, $m_{\mathrm{H}^\pm}$ $(m_{\mathrm{H}^+} = m_{\mathrm{H}^-})$ and m_{A^0}.
- the ratio of the vacuum expectation values of the two doublets: $\tan\beta := v_2/v_1$,
- the angle α which diagonalises the mass matrix of the CP-even neutral Higgs bosons and leads to the mass eigenstates h^0 and H^0.

The correct masses of the W and Z bosons are obtained if the vacuum expectation values are chosen according to $g^2(v_1^2 + v_2^2)/2 = m_{\mathrm{W}}^2$. Relation (3.1) is fulfilled automatically to first order.

In comparison to the minimal Higgs model, additional couplings appear. However, Bose symmetry prevents the coupling of the Z to two identical Higgs bosons, and in CP conserving scenarios, two Higgs bosons are permitted to couple to Z bosons only if they carry opposite CP quantum numbers. In these scenarios, the possible couplings are:

$$\frac{g_{\mathrm{Z}^0\mathrm{Z}^0\mathrm{h}^0}}{g_{\mathrm{Z}^0\mathrm{Z}^0\mathrm{H}_{\mathrm{SM}}}} = \sin(\beta - \alpha) \quad \text{and} \quad \frac{g_{\mathrm{Z}^0\mathrm{Z}^0\mathrm{H}^0}}{g_{\mathrm{Z}^0\mathrm{Z}^0\mathrm{H}_{\mathrm{SM}}}} = \cos(\beta - \alpha) \tag{3.4}$$

$$g_{\mathrm{Z}^0\mathrm{A}^0\mathrm{h}^0} = \frac{g}{2\cos\theta_{\mathrm{W}}}\cos(\beta - \alpha) \quad \text{and} \quad g_{\mathrm{Z}^0\mathrm{A}^0\mathrm{H}^0} = \frac{g}{2\cos\theta_{\mathrm{W}}}\sin(\beta - \alpha) \tag{3.5}$$

Additionally, there are couplings involving charged Higgs bosons, which are not considered here, and triple Higgs boson couplings. Most notably, in case of a light A^0 boson, $2m_{\mathrm{A}^0} < m_{\mathrm{h}^0/\mathrm{H}^0}$, the decay $\mathrm{h}^0/\mathrm{H}^0 \to \mathrm{A}^0\mathrm{A}^0$ is allowed. The couplings of the two neutral CP-even Higgs bosons, $g_{\mathrm{Z}^0\mathrm{Z}^0\mathrm{h}^0}$ and $g_{\mathrm{Z}^0\mathrm{Z}^0\mathrm{H}^0}$, are smaller than the coupling of the single Higgs boson in the minimal model, $g_{\mathrm{Z}^0\mathrm{Z}^0\mathrm{H}_{\mathrm{SM}}}$ due to the requirement (3.3).

The coupling of the fermions to the doublets can be established in several ways. In order to avoid FCNC to first order, fermions of one charge may couple only to one doublet [32]. Generally, two possibilities are distinguished[2]:

- *type I*: down-type (d) and up-type (u) fermions couple to the same doublet. The couplings of the light Higgs boson h^0 to down-type and up-type fermions are equally reduced (enhanced) compared to the minimal Higgs model if α is large (small). The opposite is true for the heavy Higgs boson H^0:

$$\frac{g_{\mathrm{u\bar{u}h^0}}}{g_{\mathrm{u\bar{u}H_{SM}}}} = \frac{g_{\mathrm{d\bar{d}h^0}}}{g_{\mathrm{d\bar{d}H_{SM}}}} = \frac{\cos\alpha}{\sin\beta} \quad \text{and} \quad \frac{g_{\mathrm{u\bar{u}H^0}}}{g_{\mathrm{u\bar{u}H_{SM}}}} = \frac{g_{\mathrm{d\bar{d}H^0}}}{g_{\mathrm{d\bar{d}H_{SM}}}} = \frac{\sin\alpha}{\sin\beta} \tag{3.6}$$

- *type II*: down-type (d) fermions couple to one and up-type (u) fermions to the other doublet. The couplings of the lightest Higgs boson h^0 to down-type and up-type quarks behave complementary. If the couplings to up-type quarks are enhanced, the couplings to down type quarks are reduced and vice versa:

$$\frac{g_{\mathrm{u\bar{u}h^0}}}{g_{\mathrm{u\bar{u}H_{SM}}}} = \frac{\cos\alpha}{\sin\beta}, \quad \frac{g_{\mathrm{d\bar{d}h^0}}}{g_{\mathrm{d\bar{d}H_{SM}}}} = -\frac{\sin\alpha}{\cos\beta} \quad \text{and} \quad \frac{g_{\mathrm{u\bar{u}H^0}}}{g_{\mathrm{u\bar{u}H_{SM}}}} = \frac{\sin\alpha}{\sin\beta}, \quad \frac{g_{\mathrm{d\bar{d}H^0}}}{g_{\mathrm{d\bar{d}H_{SM}}}} = \frac{\cos\alpha}{\cos\beta}. \tag{3.7}$$

---

[2] One could also couple leptons to one and quarks to the other doublet, since there is no mixing between quark and lepton mass eigenstates.

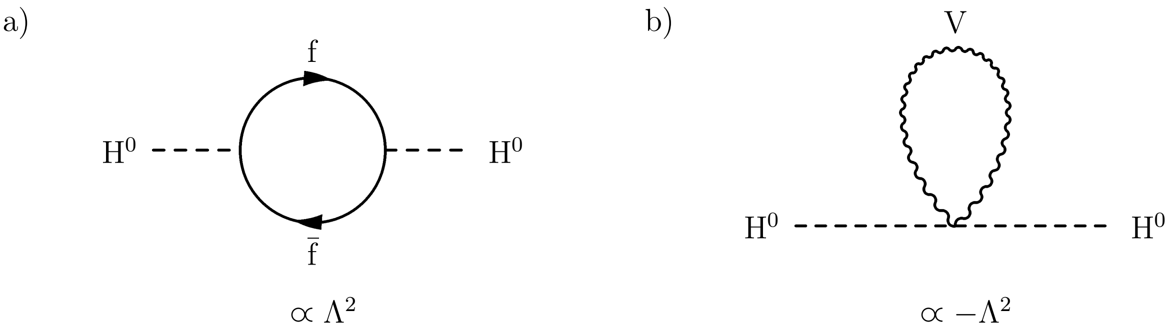

Figure 3.1: First order corrections to the Higgs boson mass. Fermion and boson loop corrections, Figures a) and b), lead to quadratic divergences of the Higgs boson mass with the opposite sign.

In type I models, the decay of the lightest Higgs boson into fermions might be generally suppressed (for $\cos\alpha \simeq 0$), thus the cross-section $\mathrm{e^+e^-} \rightarrow \mathrm{Z^0h^0} \rightarrow \mathrm{Xf\bar{f}}$ may become small. In type II models, decays into down-type fermions may be strongly suppressed, while, the decay into up-type fermions is enhanced at the same time. The lightest Higgs boson will still decay dominantly into hadrons if $m_{\mathrm{h}^0} \ll 2m_{\mathrm{W}}$, however, in regions of small α the decay into gluons will be the most frequent one due to the large mass of the top quark compared to the small mass of the charm and the up quark (see Section 2.4).

Since SM Higgs boson searches make extensive use of the signature of bottom decays in order to suppress the background, their sensitivity is strongly limited in type II models for small α. These areas can still be explored by flavour independent Higgs boson searches.

3.3 The Minimal Supersymmetric Extension of the Standard Model

The SM, including the minimal Higgs sector, achieves a good description of fundamental processes, however, many questions are not answered. Excepting these shortcomings, one problem still remains in the Higgs sector. Next-to-leading order corrections to the Higgs boson mass show quadratic divergences due to loop graphs containing SM particles [36], illustrated in Figure 3.1. However, corrections to the masses of fermions and electroweak bosons are only logarithmically divergent. Assuming the SM to be valid up to a certain scale, for example $\Lambda_{\mathrm{Pl}} \simeq 10^{15}$ TeV, the Higgs boson mass would suffer a correction of several orders of magnitude while the corrections to the fermion and boson masses are moderate. Thus, it appears very unnatural to have the electroweak scale and Higgs boson mass at the same order as required by unitarity (see Section 2.3).

This problem can be solved in a similar way to the suppression of FCNCs by the GIM mechanism [31]. For each particle a partner is introduced which is connected by a symmetry transformation under which the model is invariant. In order to get additional oppositely signed contributions which cancel the quadratic divergences exactly, the partners of the fermions must be bosons and vice versa (see for example the introduction of [36]). The associated symmetry is called *supersymmetry*.

Another important motivation to introduce supersymmetry is the possibility to unify the SM forces with gravity [37]. The construction of such a model has not yet been successful.

But, in order to construct a unified algebra describing spin 2 bosons (gravitons) and spin 1 bosons (electroweak bosons) within the framework of a relativistic quantum gauge field theory the only possibility would be the introduction of the supersymmetry operation which connects the representations associated to half and integer spins [38]. The aspects of unified theories are not pursued further and the following paragraphs concentrate on the Higgs sector only.

The additional symmetry and related interactions lead to further requirements on the Higgs sector, since invariance under this symmetry and renormalisability has to be guaranteed. In order to construct a Lagrangian invariant under supersymmetry, the terms which generate the fermion masses may not depend on the complex conjugate of the Higgs field (see for example Section 3.2 of [36]). However, if both up-type and down-type fermions couple to the same doublet, SU(2) gauge invariance requires the appearance of the complex conjugate of the Higgs field (see for example Section 11.6 of [39]). Thus, at least two Higgs doublets are needed which separately generate masses for up- and down-type fermions (THDM type II). Secondly, anomalies appear and destroy renormalisability if the total charge summed over all fermions is not zero [40]. Since the supersymmetric partners of the SM Higgs doublet would be one neutral and one charged fermion the total sum would not vanish if the Higgs sector comprised only the complex doublet of the SM. The anomalies are avoided if a second, oppositely charged doublet is added.

Since gauge bosons in contrast to fermions transform as the adjoint representation of the gauge group [9], the Lagrangian could not be invariant under both the gauge and the supersymmetry transformations if the gauge bosons were the supersymmetric partners of SM fermions. Therefore, an additional superpartner has to be introduced for each fermion and boson of the SM.

Supersymmetric particles have not been observed. Thus, their masses must be significantly larger than those of their partners. Consequently, supersymmetry must be a broken symmetry. There are various ways of establishing supersymmetry breaking. An overview of prominent mechanisms is given in Section 6 of [36]. The breaking mechanism of supersymmetry and electroweak gauge symmetry gives rise to a *superpotential.*

In the Minimal Supersymmetric extension of the Standard Model (MSSM), the superpotential can be related to the Higgs potential of general Two-Higgs-Doublet models. In a similar way to the general case, the resulting particle spectrum contains 2 CP-even and 1 CP-odd neutral and 2 charged Higgs bosons. However, relations imposed by supersymmetry reduce the free parameters, which control their masses and the mixing angle α, to only two at lowest order. The Higgs boson masses are conveniently expressed in terms of $\tan\beta$ and m_{A^0}. The relations are:

$$m^2_{\mathrm{H}^\pm} = m^2_{\mathrm{A}^0} + m^2_{\mathrm{W}} \tag{3.8}$$

$$m^2_{\mathrm{H}^0/\mathrm{h}^0} = \frac{1}{2}\left[m^2_{\mathrm{A}^0} + m^2_{\mathrm{Z}} \pm \sqrt{\left(m^2_{\mathrm{A}^0} + m^2_{\mathrm{Z}}\right)^2 - 4m^2_{\mathrm{Z}}m^2_{\mathrm{A}^0}\cos^2 2\beta}\right] \tag{3.9}$$

The mixing angle α of the neutral CP-even Higgs bosons, h^0 and H^0, becomes:

$$\cos 2\alpha = \frac{m^2_{\mathrm{Z}} - m^2_{\mathrm{A}^0}}{m^2_{\mathrm{H}^0} - m^2_{\mathrm{h}^0}} \cos 2\beta \tag{3.10}$$

Several mass bounds are easily obtained from (3.8) and (3.9): $m_{\mathrm{H}^\pm} \geq m_{\mathrm{W}}$, $m_{\mathrm{H}^0} \geq m_{\mathrm{Z}}$ and $m_{\mathrm{h}^0} \leq m_Z, m_{\mathrm{A}^0}$. In the limit $m_{\mathrm{A}^0} \to \infty$, the minimal Higgs model of the SM is obtained.

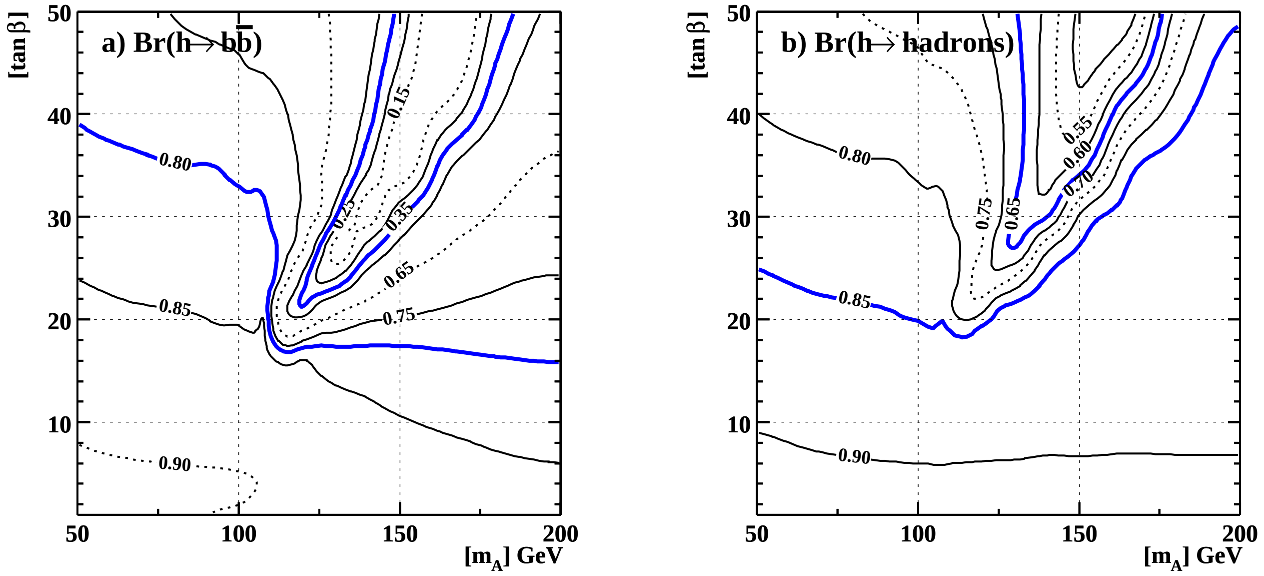

Figure 3.2: Branching ratio of the lightest Higgs boson into bottom quarks a) and hadrons b) in the large-μ scenario of the MSSM. At large $\tan\beta$ and large m_{A}, the branching ratio into b quarks is suppressed. At the same time the branching ratio into up-type quarks is enhanced. In this area, the lightest Higgs boson decays dominantly into gluons.

However, the requirement $m_{\mathrm{h}^0} \leq m_{\mathrm{Z}}$ remains. The expressions (3.8)-(3.10) are computed to first order. The picture alters significantly if higher order corrections are considered. However, the lightest Higgs boson is still bound from above: $m_{\mathrm{h}^0} \lesssim 130 \pm 5\,\mathrm{GeV}$ [41]. The corrections vary significantly with the location in the full parameter space of the MSSM, and influence all mass terms including the mixing terms, i.e. the mixing angle α. The Higgs boson masses, including m_{h^0} and m_{A^0}, and the angle α are especially influenced by the mixing of the Higgs doublets, which is controlled by the parameter μ, furthermore, by the mixing in the *stop* and *sbottom* sector, and by $\tan\beta$. The stop and sbottom sector comprises the left and right stop and sbottom, respectively, which are the partners of the left and right handed top and bottom quarks.

In order to tackle the huge parameter space efficiently, benchmark scenarios have been developed [42] which only comprise a tiny region of the whole parameter space but maximise certain effects influencing the observability in orthogonal ways. For the analysis presented in Section 7.1, the so called large-μ scenario is of particular interest. In this scenario "large" means large with respect to the supersymmetry breaking scale M_{SUSY}. The choice of this particular scenario is:

$$\begin{aligned} \mu &= 1\,\mathrm{TeV} \\ M_{\mathrm{SUSY}} &= 400\,\mathrm{GeV}. \end{aligned}$$

This scenario has been chosen such that h^0 becomes relatively light and could be produced at LEP2 for all possible values of $\tan\beta$ and m_{A^0}. A specific choice of the mixing of the left and right stop and sbottom squarks, leads to regions in which the coupling of the lightest Higgs boson to bottom quarks vanishes (see Figure 3.2a). In these regions, searches for the SM Higgs boson, which generally make use of the signature of bottom decays, lose their sensitivity.

However, the hadronic branching ratio is still larger than 45% in the region $\tan\beta < 50$ (see Figure 3.2b). Thus, a flavour independent search for hadronic final states remains sensitive.

3.4 The Randall-Sundrum Model

At present, investigations concentrate on higher dimensional models in order to describe gravity in addition to electroweak and strong interactions. The higher dimensional approach might not be the only way to a finite quantum gravity[3], but may also be the key to solving the hierarchy puzzle, i.e. the difference of the mass scale v of the electroweak bosons and fermions, which is of $\mathcal{O}(1\,\mathrm{TeV})$, and the mass scale M_{Pl}, where gravity becomes dominant, which is of $\mathcal{O}(10^{15}\,\mathrm{TeV})$. In higher dimensional theories, the Planck mass M_{Pl} appears larger in the effective four dimensional theory due to the hidden volume of the extra dimensional space [43]. The effective Planck mass M_{Pl} becomes $M_{\mathrm{Pl}}^2 = \widetilde{M}_{\mathrm{Pl}}^{2+n} V_n$ after integration over the n dimensional compact extra volume V_n. In order to reach the observed effective Planck mass $M_{\mathrm{Pl}} = 10^{15}\,\mathrm{TeV}$, many additional dimensions are necessary or each additional dimension must be extraordinarily large. Since there is no experimental sign of extra dimensional space, the extension cannot be larger than the experimental resolution. Until now experiments can probe the region down to $10^{-15}\,\mathrm{m}$ [44]. Alternatively, there could be a mechanism which prevents experiments to detect the extra dimensions. As an example, particles and forces of the SM could be constrained to a four dimensional subspace, i.e. brane, and only gravitational excitation would be permitted to propagate through the whole space [45].

This inspired the approach of L. Randall and R. Sundrum [46]. They introduce one compact extra dimension. The space is limited by two infinitely extended four dimensional branes separated by a distance r_0. The SM particles and forces are contained in one of the branes. Gravitational excitations are localised at the second brane, but they leak exponentially damped into the extra dimension in contrast to the SM forces and particles. The small overlap of the exponentially damped gravitational excitations and the SM brane explains the suppressed coupling of gravitation to SM particles. The damping between the Planck and the SM brane has to be $\sim \exp(-35)$ in order to generate the 15 orders of magnitude between the Planck mass and the mass scale $\Lambda_{\mathrm{W}} = \mathcal{O}(\,\mathrm{TeV})$ on the SM brane. The model is considered to be a low-energy approximation of a more fundamental theory and does not explain the mechanism that traps the SM fields on the brane and the mechanism that leads to the localisation of gravitational excitations on the opposite brane. But it seems to be possible to derive such a model from M-theory [47].

The additional particle spectrum has been investigated in [48] and [49] which supersedes [50]. There are massless and massive spin two excitations. The massless excitations couple with gravitational strength and can be identified with gravitons. The masses and couplings of the massive spin two excitations are set by the weak scale. These states have not yet been observed. They should become visible with next generation colliders, if they exist.

Moreover, there are spinless excitations, called *radions*. The radion corresponds to fluctuations of the branes against each other. It was pointed out in [50] that the branes would drift apart with a speed too fast to be compatible with cosmological models and observations, unless the brane distance is stabilised. In [49] it was found that the radion acquires a mass due to

---

[3] Since nobody has yet succeeded in finding a higher dimensional model achieving this goal, the approach might turn out to be only a mind boggling exercise.

the stabilisation mechanism. However, the exact form of the stabilisation potential has little influence on the actual mass. The mass is expected to be well below 1 TeV. Most likely radions are lighter than massive spin two excitations, therefore, their observation is probably the first sign of the Randall-Sundrum model if it is realised.

The radion and the Higgs boson carry the same quantum numbers, thus they can mix. This possibility was investigated first in [48]. The phenomenology of the coupled system composed of the radion and the Higgs boson is summarised in Sections 3.4.1 and 3.4.2. The physical states, the radion-like state r and the Higgs-like state h are derived and their couplings to matter are computed.

3.4.1 Physical Scalars in the RS-Model

The effective 4D Lagrangian of the radion and the couplings to SM particles have been investigated first in [48]. It was pointed out, that a further term can be added to the effective Lagrangian which leads to kinetic mixing between the radion and the Higgs boson. This idea was picked up in [49], where calculations are carried out to higher order compared to [48]. They arrive at the following effective Lagrangian, describing the kinetic and mass terms of the radion $\tilde{r}$ and the Higgs boson $\tilde{h}$:

$$\mathcal{L}_{\text{scalar}} \simeq \begin{pmatrix} \tilde{h} \\ \tilde{r} \end{pmatrix}^{\mathrm{T}} \begin{pmatrix} -\frac{1}{2}\Box - \frac{1}{2}\widetilde{m}_{\mathrm{h}}^2 & 3\xi\gamma\Box \\ 3\xi\gamma\Box & -\frac{1}{2}\left(1 + 6\xi\gamma^2\right)\Box - \frac{1}{2}\widetilde{m}_{\mathrm{r}}^2 \end{pmatrix} \begin{pmatrix} \tilde{h} \\ \tilde{r} \end{pmatrix}, \tag{3.11}$$

where ξ is a free parameter of $\mathcal{O}(1)$, leading to the kinetic mixing, and $\gamma := v/\sqrt{6}\Lambda_{\mathrm{W}}$ with the vacuum expectation value of the Higgs field v.

In order to find the physical states, the kinetic mixing has to be resolved, i.e the matrix in Equation (3.11) has to be diagonalised. The diagonalisation is performed in two steps. In the first step, the mass terms are neglected. The remaining matrix is diagonalised and the fields are canonically normalised by the choice $\tilde{h} = h' + 6\xi\gamma r'/Z$ and $\tilde{r} = r'/Z$, with:

$$Z := \sqrt{1 + 6\xi\gamma^2(1 - 6\xi)}. \tag{3.12}$$

The mixing parameter ξ is limited requiring the fields h' and r' to be real:

$$\frac{1}{12}\left(1 - \sqrt{1 + \frac{4}{\gamma^2}}\right) \leq \xi \leq \frac{1}{12}\left(1 + \sqrt{1 + \frac{4}{\gamma^2}}\right). \tag{3.13}$$

The choice of h' and r' removes the kinetic mixing but introduces mixing of the mass terms. In the second step, the states are rotated around the angle θ:

$$\tan 2\theta := 12\xi\gamma Z \frac{\widetilde{m}_{\mathrm{h}}^2}{\widetilde{m}_{\mathrm{r}}^2 - \widetilde{m}_{\mathrm{h}}^2(Z^2 - 36\xi^2\gamma^2)}. \tag{3.14}$$

This transformation diagonalises the mass terms. The canonically normalised kinetic terms are invariant under rotations. The full transformation yields the following relations between the fundamental states, $\tilde{h}$ and $\tilde{r}$, and the mass eigenstates, $\hat{\mathrm{r}}$ and $\hat{\mathrm{h}}$:

$$\begin{aligned} \tilde{h} &= (\cos\theta - \frac{6\xi\gamma}{Z}\sin\theta)\hat{\mathrm{r}} + (\sin\theta + \frac{6\xi\gamma}{Z}\cos\theta)\hat{\mathrm{r}} \\ \tilde{r} &= -\sin\theta\frac{\hat{\mathrm{r}}}{Z} + \cos\theta\frac{\hat{\mathrm{r}}}{Z}. \end{aligned} \tag{3.15}$$

The corresponding masses are given by $m_\pm$, where $m_- < m_+$:

$$m_\pm^2 := \frac{1}{2Z^2}\left(\widetilde{m}_\mathrm{r}^2 + (1+6\xi\gamma^2)\widetilde{m}_\mathrm{h}^2 \pm \sqrt{\left(\widetilde{m}_\mathrm{r}^2 - \widetilde{m}_\mathrm{h}^2(1+6\xi\gamma^2)\right)^2 + 144\gamma^2\xi^2\widetilde{m}_\mathrm{r}^2\widetilde{m}_\mathrm{h}^2}\right). \tag{3.16}$$

The masses m_+ and m_- are separated for all values of $\widetilde{m}_\mathrm{r}$ and $\widetilde{m}_\mathrm{h}$ if $\xi \neq 0$.

The assignment of m_+ and m_- to the mass eigenstates depends on the fundamental masses $\widetilde{m}_\mathrm{r}$ and $\widetilde{m}_\mathrm{h}$, and the mixing angle ξ. The rotation angle defined by (3.14) is not a continuous function of ξ. At the location where the denominator crosses zero, $\widetilde{m}_\mathrm{r} = \widetilde{m}_\mathrm{h}(Z^2 - 36\xi^2\gamma^2)$, the rotation angle flips by $\pi/2$. Simultaneously, $\hat{\mathrm{r}}$ and $\hat{\mathrm{h}}$ swap their role, i.e. they become eigenstates of the opposite mass. Here, the radion-like and Higgs-like state, r and h, are defined such that for $\xi = 0$ the fundamental radion $\tilde{r}$ and the eigenstate r coincide, and furthermore, the mass m_r and the coupling (see Section 3.4.2) are continuous functions of ξ. The definition of r is:

$$\mathrm{r} = \begin{cases} \hat{\mathrm{r}} & ; \quad \begin{array}{c} \widetilde{m}_\mathrm{r} > \widetilde{m}_\mathrm{h} \text{ and } \widetilde{m}_\mathrm{r} > \widetilde{m}_\mathrm{h}(Z^2 - 36\xi\gamma^2) \\ \text{or } \widetilde{m}_\mathrm{r} \leq \widetilde{m}_\mathrm{h} \text{ and } \widetilde{m}_\mathrm{r} \leq \widetilde{m}_\mathrm{h}(Z^2 - 36\xi\gamma^2) \end{array} \\ \hat{\mathrm{h}} & \qquad\qquad \text{otherwise} \end{cases} . \tag{3.17}$$

The corresponding mass is $m_\mathrm{r} = m_-$ if $\widetilde{m}_\mathrm{r} < \widetilde{m}_\mathrm{h}$ and $m_\mathrm{r} = m_+$ if $\widetilde{m}_\mathrm{r} \geq \widetilde{m}_\mathrm{h}$. The Higgs-like state and its mass are defined accordingly. The masses are shown in Figure 3.3 for fundamental radion and Higgs boson mass parameters $\widetilde{m}_\mathrm{r}$ and $\widetilde{m}_\mathrm{h}$ of 90 GeV and 120 GeV.

Equations (3.16) form a system of quadratic equations of m_+^2 and m_-^2 which can be solved for $\widetilde{m}_\mathrm{r}$ and $\widetilde{m}_\mathrm{h}$:

$$\begin{aligned} \widetilde{m}_\mathrm{r}^2 &= \frac{Z^2}{2}\left((m_+^2 + m_-^2) \pm \sqrt{(m_+^2 - m_-^2)^2 - \frac{144\xi^2\gamma^2}{Z^2}m_+^2 m_-^2}\right) \\ \widetilde{m}_\mathrm{h}^2 &= \frac{Z^2}{2\,(1+6\xi\gamma^2)}\left((m_+^2 + m_-^2) \pm \sqrt{(m_+^2 - m_-^2)^2 - \frac{144\xi^2\gamma^2}{Z^2}m_+^2 m_-^2}\right). \end{aligned}$$

The computed masses $\widetilde{m}_\mathrm{r}$ and $\widetilde{m}_\mathrm{h}$ are real only if:

$$\frac{m_+^2}{m_-^2} \geq \frac{1}{Z^2}\left(1 + 6\xi\gamma^2(1+6\xi) + 12\gamma\sqrt{\xi^2(6\xi\gamma^2+1)}\right). \tag{3.18}$$

This condition together with (3.13) limits the possible physical parameters, as illustrated in Figure 3.3b.

To summarise, the location in the Randall-Sundrum parameter space is specified by the physical radion and Higgs boson mass m_r and m_h, the mixing parameter ξ and the coupling suppression factor γ (see Section 3.4.2), where the radion and the Higgs boson are defined according to (3.17).

3.4.2 The Coupling of the Higgs boson and the radion to SM particles

The radion couples to the trace of the energy-momentum-tensor T_μ^μ [48], therefore, the couplings to matter are similar to those of the SM Higgs boson at lowest order since:

$$T_\mu^\mu = -(m_{ij}\bar{\psi}_i\psi_j - m_\mathrm{V}\mathrm{V}_\mu\mathrm{V}^\mu) + \ldots .$$

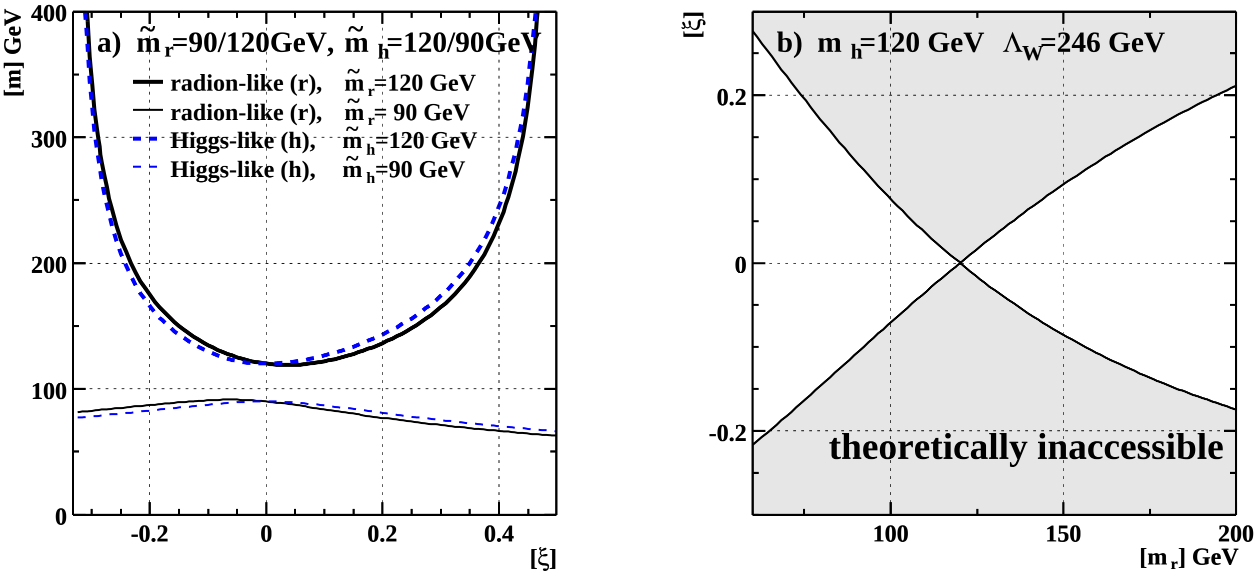

Figure 3.3: a) Masses $m_{\mathrm{r/h}}$ of the heavy and light mass eigenstate for fundamental Higgs boson and radion mass parameters $\widetilde{m}_{\mathrm{h}}$ and $\widetilde{m}_{\mathrm{r}}$ of 90 GeV and 120 GeV. b) Allowed parameter space in the m_{r} and ξ plane for a Higgs boson mass $m_{\mathrm{h}} = 120\,\mathrm{GeV}$. Outside the permitted region the Higgs and radion-like states are unphysical (ghost-like). In both figures, the weak scale was chosen to be $\Lambda_{\mathrm{W}} = 246\,\mathrm{GeV}$.

The contribution of terms with derivatives of fields or more than two fields is negligible here. The combined interaction term of the radion and the Higgs boson is:

$$\mathcal{L}_{\text{radion/Higgs inter.}} \simeq -\frac{1}{v}(m_{ij}\bar{\psi}_i\psi_j - m_{\mathrm{V}}\mathrm{V}_\mu\mathrm{V}^\mu)\left[\tilde{h} - \gamma\tilde{r}\right], \tag{3.19}$$

where v denotes the vacuum expectation value of the Higgs field. The couplings of the radion to the fermions and bosons are generally reduced by the factor $\gamma = v/\sqrt{6}\Lambda_{\mathrm{W}}$ compared to the corresponding coupling of the Higgs boson.

The couplings of the radion-like and the Higgs-like state r and h are obtained by inserting (3.15) according to (3.17) in (3.19) and comparing the resulting terms with the Higgs interaction terms of the SM Lagrangian. This yields, expressed in terms of the partial decay width relative to the SM[4]:

$$\frac{\Gamma(\mathrm{r\ or\ h} \to \bar{\mathrm{f}}\mathrm{f},\ \mathrm{VV})}{\Gamma(\mathrm{H}_{SM} \to \bar{\mathrm{f}}\mathrm{f},\ \mathrm{VV})} = (a_{1,\mathrm{r/h}} + a_{2,\mathrm{r/h}})^2, \tag{3.20}$$

where

$$a_{i,\mathrm{r}} = \begin{cases} a_{i,\hat{\mathrm{r}}} & ; \quad \begin{array}{c} \widetilde{m}_{\mathrm{r}} > \widetilde{m}_{\mathrm{h}} \text{ and } \widetilde{m}_{\mathrm{r}} > \widetilde{m}_{\mathrm{h}}(Z^2 - 36\xi\gamma^2) \\ \text{or } \widetilde{m}_{\mathrm{r}} \leq \widetilde{m}_{\mathrm{h}} \text{ and } \widetilde{m}_{\mathrm{r}} \leq \widetilde{m}_{\mathrm{h}}(Z^2 - 36\xi\gamma^2) \end{array} \\ a_{i,\hat{\mathrm{h}}} & \qquad\qquad \text{otherwise} \end{cases} \tag{3.21}$$

---

[4] The expressions have to be evaluated assuming the same masses for the SM Higgs boson and the radion r or Higgs boson h, respectively.

and $a_{i,\mathrm{h}}$ is set to $a_{i,\hat{\mathrm{h}}}$ or $a_{i,\hat{\mathrm{r}}}$, respectively. The quantities $a_{i,\hat{\mathrm{r}}}$ and $a_{i,\hat{\mathrm{h}}}$ are defined by:

$$\begin{array}{lllllll} a_{1,\hat{\mathrm{r}}} & := & \sin\theta + \frac{6\xi\gamma}{Z}\cos\theta & \quad & a_{2,\hat{\mathrm{r}}} & := & \gamma\frac{\cos\theta}{Z} \\ a_{1,\hat{\mathrm{h}}} & := & \cos\theta - \frac{6\xi\gamma}{Z}\sin\theta & \quad & a_{2,\hat{\mathrm{h}}} & := & \gamma\frac{\sin\theta}{Z}. \end{array} \tag{3.22}$$

Expression 3.20 is valid for all fermions f and massive vector bosons V at lowest order. In case the Higgs boson or radion is lighter than $2\,m_{\mathrm{t}}$, direct decays into top quarks are kinematically forbidden, but due to the large mass of the top quark, decays into gluons via top loops are generally not negligible. The matrix element of a SM Higgs boson decay into gluons is:

$$\mathrm{ME}(\mathrm{H}_{\mathrm{SM}} \to gg) := \frac{1}{2} \cdot \frac{\alpha_s}{8\pi} \cdot \frac{1}{v} H(x) F_{\frac{1}{2}}(4m_t^2/m_{\mathrm{h}}^2) \mathrm{G}_{\alpha\mu\nu}(x) \mathrm{G}_{\alpha}^{\mu\nu}(x). \tag{3.23}$$

The fields $\mathrm{G}_{\alpha\mu\nu}$ denote the gluon fields, $F_{\frac{1}{2}}(\tau)$ the form factor of the top loop, α_s the strong coupling constant and m_{h} the Higgs boson mass. A similar matrix element is obtained for the radion however it has the opposite sign and the coupling is reduced by γ. Since the radion couples to the trace of the energy momentum tensor, the anomaly of the trace contributes to the decay width into gluons and photons in addition to the loop contribution. The anomalous terms appear in the trace of the renormalised energy momentum tensor in addition to the unrenormalised trace $\tilde{T}_{\mu}^{\mu}$. This has been shown for example in [51]. The complete trace T_{μ}^{μ} reads:

$$T_{\mu}^{\mu} = \tilde{T}_{\mu}^{\mu} + \frac{\beta}{2g_{\mathrm{R}}} N[F_{\alpha\lambda\rho} F_{\alpha}^{\lambda\rho}], \tag{3.24}$$

where g_{R} denotes the renormalised coupling constant, β the renormalisation group coefficient, $F_{\alpha}^{\mu\nu}$ the field strength tensor of strong, electromagnetic and weak interaction and $N[\ldots]$ normal ordering. Thus, the radion couples directly to gluon and photon pairs due to the trace anomaly. The additional coupling to the massive vector bosons is negligible. The trace anomaly adds a term to the matrix element (3.23):

$$\mathrm{ME}_{\mathrm{anomaly}}(\mathrm{r} \to gg) := \beta \cdot (\alpha_s/8\pi) \gamma \mathrm{r}(x) \mathrm{G}_{\alpha\mu\nu}(x) \mathrm{G}_{\alpha}^{\mu\nu}(x). \tag{3.25}$$

The coefficient of the renormalisation group equation is denoted by β, 7 for QCD. In total, the partial decay width of the mass eigenstates becomes [48]:

$$\frac{\Gamma(\mathrm{r\ or\ h} \to gg)}{\Gamma(\mathrm{H}_{SM} \to gg)} = \frac{\left| 2 \cdot 7 \cdot a_{2,\mathrm{r/h}} - (a_{1,\mathrm{r/h}} + a_{2,r/h}) F_{\frac{1}{2}}(4m_t^2/m_{r/h}^2) \right|^2}{\left| F_{\frac{1}{2}}(4m_t^2/m_{r/h}^2) \right|^2}. \tag{3.26}$$

The factors $a_{i,\mathrm{r/h}}$ are those of (3.21).

Since the properties of the radion and the Higgs-boson are similar to the SM Higgs boson, the dominant production channel of the mass eigenstates r and h will be Higgs-strahlung in $\mathrm{e^+e^-}$ collisions at centre-of-mass energies achieved at LEP. The total decay width of the mass eigenstates is smaller than 100 MeV for masses of interest (m_h or $m_r \lesssim 115\,\mathrm{GeV}$). Thus only decays, $\mathrm{Z}^* \to$ Zh or Zr, into on-shell Higgs bosons or radions have to be considered. The cross-section relative to Higgs-strahlung in the SM is derived from 3.20 and given by:

$$\frac{\sigma(\mathrm{e^+e^-} \to \mathrm{Zr\ or\ Zh})}{\sigma(\mathrm{e^+e^-} \to \mathrm{ZH_{SM}};\ m_{\mathrm{H}} = m_{\mathrm{r}},\ m_{\mathrm{h}})} = \frac{\Gamma(\mathrm{r\ or\ h} \to \bar{\mathrm{f}}\mathrm{f},\ \mathrm{VV})}{\Gamma(\mathrm{H}_{SM} \to \bar{\mathrm{f}}\mathrm{f},\ \mathrm{VV})}. \tag{3.27}$$

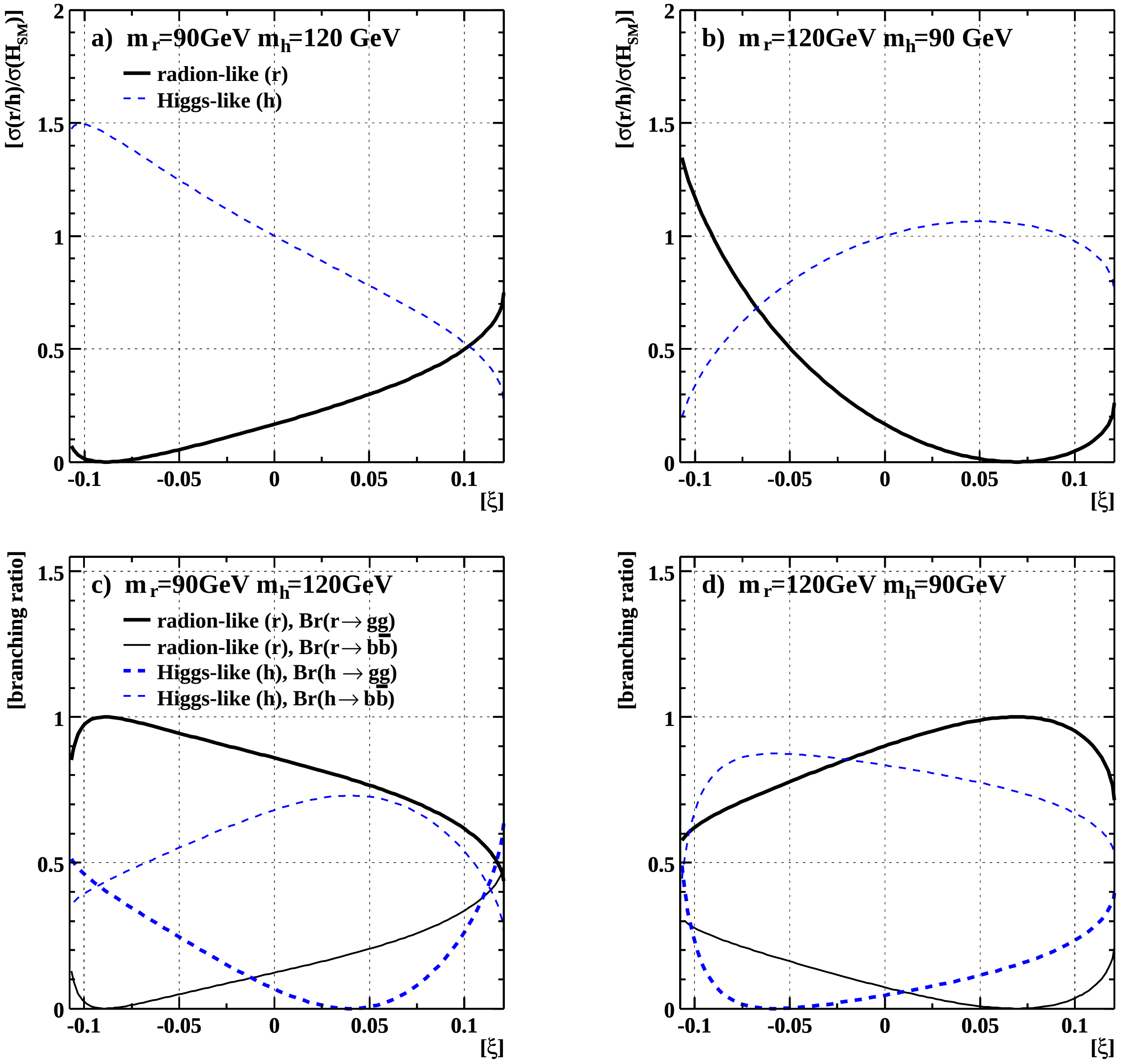

Figure 3.4: a) and b) show the cross-sections for the processes $e^+e^- \rightarrow Z^0r$ or Z^0h of the radion-like and the Higgs-like state, r and h, relative to the corresponding cross-section of a SM Higgs boson. Figures c) and d) show the branching ratios of r and h into gluon pairs and $b\bar{b}$. The parameter Λ_W was chosen to be 246 GeV. The cross-sections and branching ratios of the Higgs-like state h are identical to those of a SM Higgs boson for $\xi = 0$.

In Figure 3.4, the cross-section and branching ratios of the two mass eigenstates are displayed depending on the mixing parameter ξ. Due to the contribution from the trace anomaly the radion decays dominantly into gluon pairs. Since the cross-section and branching ratios of the Higgs-like state h are significantly altered, the current limits on the Higgs boson mass have to be revised within the Randall-Sundrum model. This is discussed in Section 8.6.

3.5 Summary

The SM cannot be the fundamental theory since many questions are unanswered and problems remain. In a similar way to supersymmetric models, other extended or more fundamental models may require an extended Higgs sector. Arbitrarily complex extensions of the Higgs sector are possible. Nevertheless, models composed of one or two complex doublets seem to be the most natural choice.

A few extensions of the SM have been presented which solve problems of the SM or give answers to some of the remaining questions. All these extensions modify or require extensions of the Higgs sector which cause particularities not present in the minimal model. Most notably the coupling of the lightest Higgs boson (or scalar) to bottom quarks may be suppressed while the coupling to up-type quarks or gluons (e.g. coupling of the radion) is enhanced. Further models, which predict suppressed couplings to bottom quarks but substantial branching ratios into hadrons can be found in [52] and [53]. Thus, in order to be sensitive to a larger class of models, a search which does not depend on the flavour of the Higgs decay products is an important supplement to searches for the SM Higgs boson, which rely on the signature of bottom decays. Fermiophobic models, in which decays into fermions are entirely suppressed, are discussed in [54].

Chapter 4

The OPAL Detector

The OPAL detector was a general purpose detector located at the LEP storage ring. It was operational between 1989 and 2000. The detector showed approximately cylindrical symmetry with respect to the beam axis, and mirror symmetry with respect to the plane perpendicular to the beam axis, reflecting the symmetry of the e^+e^- collisions. The detector is sketched in Figure 4.1. It was composed of components to measure charged particle tracks, their time-of-flight to reject cosmic particles, calorimeters for energy measurement and muon detectors. The forward and backward region were covered by *endcaps* consisting of a separate set of time-of-flight counters and calorimeters. Additionally, *forward detectors* were installed close to the beam pipe to improve the hermeticity and to measure the luminosity. The instrumented parts covered 98% of the angular space. The tracking devices were placed inside the solenoid of a magnet providing a field of 0.435 T. The track detectors were composed of high resolution tracking devices, the silicon micro vertex detector and the vertex chamber, to measure the impact parameter of charged particles, and the large jet chamber supplemented by z chambers allowing a precise measurement of their momenta from the curvature in the magnetic field. The vertex, jet and z-chambers are placed inside a pressure vessel. The calorimeters were composed of the presampler, the electromagnetic and the hadronic calorimeter. The presampler was used to determine the dimensions of showers which had already developed in the material in front of the calorimeters. The forward detectors are: the silicon tungsten sandwich calorimeter installed in 1993, the original forward detector, the far forward detector, the gamma catcher and, since 1997, the MIP plug. A thorough description of the OPAL detector is given in [55]. The final upgrade of the silicon micro vertex detector is detailed in [56]. The MIP plug is described in [57] and the gamma catcher in [58]. In the following sections, an overview of the individual components is given. The OPAL coordinate system uses cylindrical coordinates (r, ϕ, z) and if more appropriate polar coordinates $(\mathrm{r}, \phi, \theta)$ to describe the geometry. The z-axis points in the direction of the electron beam and θ denotes the polar angle with respect to the beam axis.

4.1 The Central Track Detectors

4.1.1 The Silicon Micro Vertex Detector

In the first years of data taking the synchrotron radiation at the interaction point turned out to be much smaller than expected. The beam pipe was narrowed and the additional space was used to install the silicon micro vertex detector [59]. The detector was upgraded in 1993 [60]

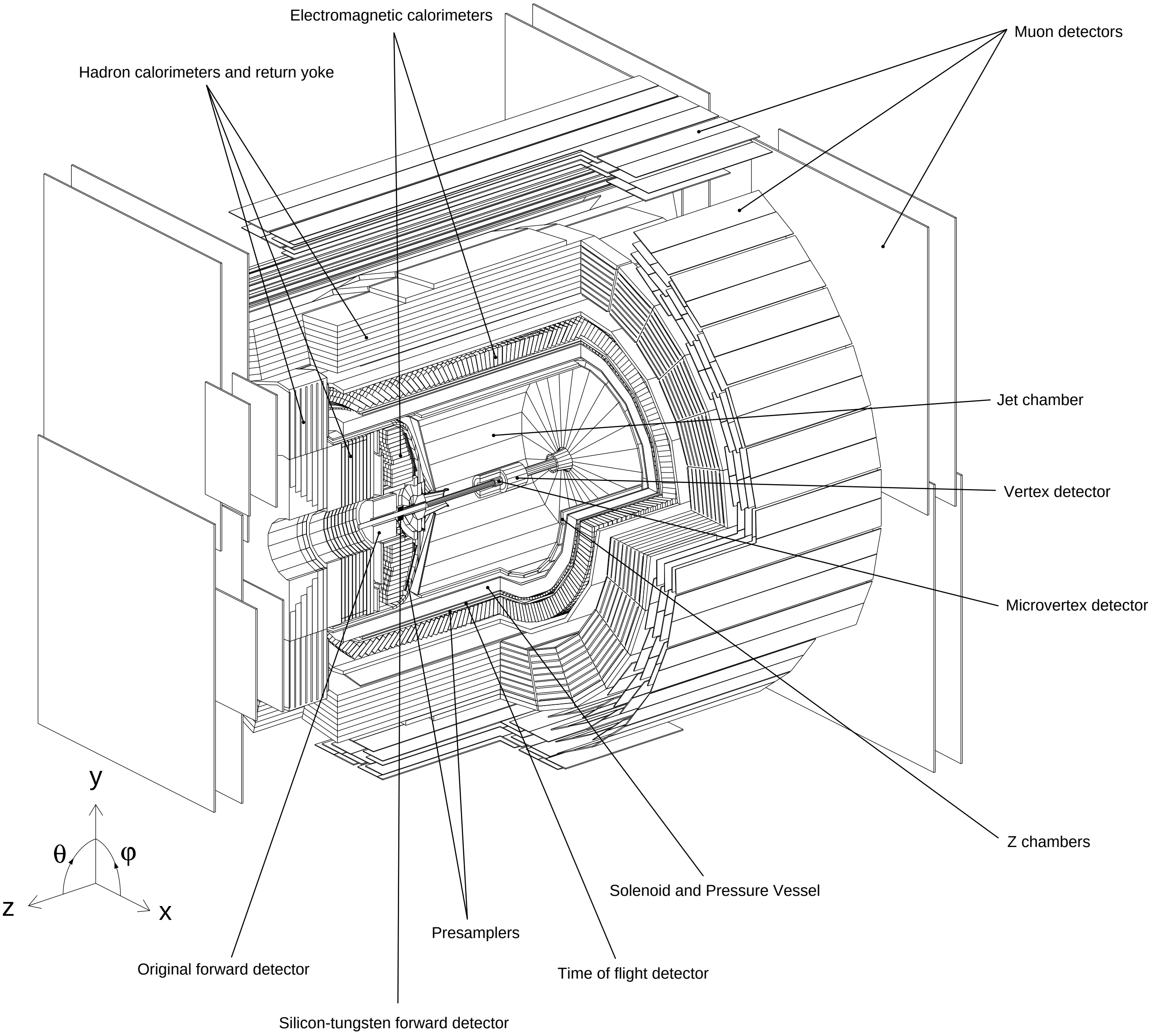

Figure 4.1: The OPAL Detector. The detector has a total length of 12 m. The central jet chamber has a diameter of 3.7 m and a length of 4 m.

and 1995 [56].

The latest silicon micro vertex detector consisted of two layers at radii of 6.1 cm and 7.4 cm composed of 12 and 15 ladders, respectively. The covered range of the polar angle with respect to the beam axis was $|\cos\theta| < 0.98$. The ladders were tilted by 5.5° and 7.5° at the inner and outer layer with respect to the tangents and were mounted with a small overlap in order to achieve hermeticity for particles coming from the interaction region. Each ladder was built by two perpendicular aligned strip detectors with a thickness of $300\,\mu$m glued together. Each second and fourth strip, respectively, was read out yielding a spatial resolution for traversing particles of $5\,\mu$m in a direction perpendicular to the beam axis and $13\,\mu$m parallel to beam axis. This translates to an impact parameter resolution of $18\,\mu$m and $24\,\mu$m, respectively.

4.1.2 The Vertex Chamber

Before the installation of the micro vertex detector, the vertex chamber had been the only instrument to measure the impact parameter of tracks. The vertex chamber was a cylindrical drift chamber of 1 m length and an inner and outer radius of 8.8 cm and 23.5 cm, respectively. The chamber was subdivided into 36 sectors by cathode and anode wire planes. The inner part of each plane was built by wires parallel to the beam axis and the outer part was built by wire pairs tilted against each other by 4°. The anode plane was built alternately by potential and sense wires, where the sense wires are staggered by $11\,\mu$m to the left and the right to allow solving of the left and right ambiguity of passing particles. The chamber had a resolution of $55\,\mu$m in the r, ϕ-plane and $700\,\mu$m in the direction of the beam. The vertex chamber is essential for the extrapolation of tracks out of the jet chamber to the micro vertex detector.

4.1.3 The Jet Chamber

The cylindrical volume of the jet chamber has a length of 4 m, and outer and inner radii of 185 cm and 25 cm, respectively. The volume is subdivided into 24 sectors numbered anti-clockwise and separated by cathode planes. A sector is sketched in Figure 4.2. The planes are realised by potential wires strung between the endplates. The anode plane in the middle of each sector is built by potential wires and 159 sense wires. The sense wires are spaced equidistantly in the radial direction with a spacing of 1 cm and are staggered 100μm to the left and to the right of the plane.

In order to provide a homogeneous electric field, the wires of the cathode were set to a linearly increasing potential from 5kV at the innermost wire up to 25kV at the outermost wire. Separate power supplies provided intermediate wires with voltages of 10kV, 15kV and 20kV. A resistor chain subdivided these potentials and supplied the remaining wires with the correct voltage. In each sector, the electric field was terminated in the z and radial direction by copper strips mounted on the endplates and the cylindrical shell of the chamber. Each copper strip was connected with a cathode wire of the appropriate voltage.

A charged particle crossing the gas volume ionises gas atoms thereby losing energy. In the homogeneous electric and magnetic field, the released electrons start to drift on straight, parallel lines towards the anode plane. Close to the anode wires, the electric field rises sharply and the electrons are accelerated to the sense wires initiating an ionisation avalanche. The large number of released electrons lead to a sizable signal on the sense wires. The amplitude of the signal depends on the gas amplification and on the ionisation density caused by the initial

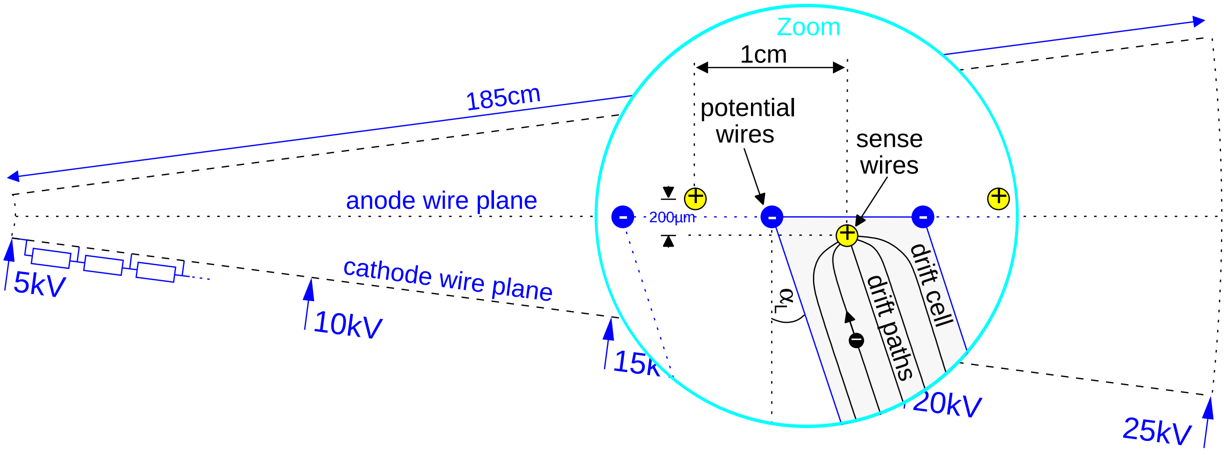

Figure 4.2: A sector of the central jet chamber. The sectors are bounded by wire planes. The anode plane contains 159 sense wires in addition to the potential wires. The zoomed view sketches the electron drift in the electromagnetic field.

charged particle. Thus, the amplitude is a measure of the specific energy loss per distance (dE/dx). The time difference between the arrival of the integrated signal, and the time of the interaction is used to determine the distance of the charged particle from the sense wire (*hit*). In this case the position could be measured in the drift direction, i.e. in the r, ϕ plane, with a resolution $\sigma_{r,\phi} = 150\,\mu$m. Since the signal was measured at both ends of the sense wire the relative fraction measured at one and at the other end could be used to determine the coordinate along the sense wire, i.e. the z coordinate. This technique allowed an accuracy of $\sigma_z \simeq 4\,$cm. More detail about the performance of the jet chamber is exposed in [61].

Finally, a helical path is fitted to all hits taking the energy loss into account. The parameters of the helix are the flight direction, impact parameter and transverse momentum. The following resolution was obtained for electron and muon pairs using the jet chamber and the z-chambers, which are discussed in the next section: the resolution of the transverse momentum was $\sigma_{p_t}/p_t = \sqrt{(0.02)^2 + (0.0015 p_t/\,\mathrm{GeV})^2}$, where the first term is caused by multiple scattering. The resolution of the impact parameter in the $r-\phi$ plane was $\sigma_{d_0} = 113\,\mu$m, the resolution of the polar angle[1] amounted to $\sigma_\theta = 2.5\,$mrad, and the z coordinate at the point of closest approach to the interaction point in the $r-\phi$ plane was measured with an accuracy of $\sigma_{z_0} = 6.2\,$cm. Additionally, the specific energy loss per path length, dE/dx, was measured. This quantity in conjunction with the measured momentum was used to identify particles [62].

4.1.4 The z-Chambers

Since the z coordinates of the hits are measured less precisely than the coordinates in the r, ϕ plane, the polar angle of the fitted tracks shows a much bigger error. In order to reduce this error further, drift chambers of 59 mm thickness were installed outside the jet chamber measuring accurately the z coordinate of tracks which leave the central jet chamber. The drift cells had a size of $50 \times 50\,\mathrm{cm}^2$ and one anode plane aligned in the radial direction in the middle of each cell. The anode plane is formed by 6 sense wires tightened in the tangential direction with a staggering of $250\,\mu$m in the direction of the beam axis and additional field shaping

---

[1] The error was reduced to 0.25 mrad if the tracks were constrained to the primary vertex.

wires. In this setup, the z-coordinate was measured with an accuracy of $300\,\mu$m, The position in the tangential direction was determined with an accuracy of 1.5 cm, by measuring the relative charge collected on each wire end.

4.2 The Calorimeters

4.2.1 The Presampler

The calorimeters were located outside the pressure vessel, the solenoid, and the time-of-flight counters. Since the material located in front of the calorimeters corresponded to approximately 2 radiation lengths usually the electromagnetic showers were initiated before reaching the calorimeters. In order to measure the shower size and to estimate the amount of energy deposited already, the presampler was installed outside the solenoid, between the time of flight counter and the electromagnetic calorimeter. The presampler consisted of streamer chambers of 3 cm thickness. A separate presampler was installed in front of the endcap calorimeters. Here drift chambers were used. The energy deposition was derived from the number of particles measured in the shower. The typical shower size was $4-6$ mm and $2-4$ mm in the endcap presampler.

4.2.2 The Electromagnetic Calorimeter

The electromagnetic calorimeter was built of lead glass blocks each with a dimension of $10 \times 10 \times 37\,\text{cm}^3$ (barrel part), and $9.4 \times 9.4 \times 33\,\text{cm}^3$ in the endcap. The depth corresponded to approximately 25 and 22 electromagnetic radiation lengths, respectively. The blocks of the barrel part pointed roughly towards the interaction point. In order to prevent particles from leaving the detector through the gaps between the individual blocks, they were not perfectly aligned but missed the nominal interaction point by $56-159$ mm in the direction of the beam axis and by 30 mm perpendicular to this. The blocks in the endcap region were aligned parallel to the beam axis. Therefore, the reconstruction of electromagnetic showers was more difficult here. Particles passing the lead class blocks produced Čerenkov radiation, which was collected by photomultipliers attached to the end of each block.

The achieved energy resolution was $\sigma_E/E \simeq 0.002 + 0.063/\sqrt{E/1\,\text{GeV}}$ and in the endcap $\sigma_E/E \simeq 0.05/\sqrt{E/1\,\text{GeV}}$ combining data from the electromagnetic calorimeter and the presampler. The spatial resolution of individual particles was better than 5 cm fitting a shower profile to signals from block clusters. However, two particles could only be resolved if the angle between them was larger than approximately 5°.

4.2.3 The Hadron Calorimeter

The return yoke of the magnetic field covering the whole detector was instrumented and served as a hadronic calorimeter. Additionally, poletip calorimeters were installed around the beam pipe in the forward and backward direction extending the coverage from $|\cos\theta| < 0.91$ to $|\cos\theta| < 0.99$. The modules of the return yoke were assembled by alternating layers of 100 mm thick iron slabs and streamer tubes. Signals were collected with cathode pads with a typical area of $500\,\text{cm}^2$ corresponding to the average shower size and strips on the opposite cathode aligned perpendicular to the anode wire. The total material of all detector parts including the hadron calorimeter corresponded to approximately 8 absorption lengths. At a few places support channels pass through the detector shells to deliver power, and signals in and out of the inner parts, here significantly less material shielded the interaction region. However, the total material corresponded to at least 4 interaction lengths. The energy resolution was $\sigma_E/E = 1.2/\sqrt{E/1\,\mathrm{GeV}}$.

4.3 The Muon Chambers

The muon chambers formed the final detector layers. The total material in front of the muon chambers corresponded to 7 interaction lengths for pions. This translates into a probability for pions not to interact before reaching these chambers of less than 0.001. In the barrel region, the muon chambers were composed of 4 layers of 1.5 cm thick drift chambers coated with 1 mm of lead. The achieved spatial resolution was 2 mm in the direction of the beam axis and 1.5 cm in the perpendicular direction. The muon chambers in forward and backward region consisted of 4 layers of pairs of cross mounted streamer tubes. They covered the region down to $|\cos\theta| < 0.985$. The spatial resolution was 1 mm.

4.4 The Forward Detectors

The hermeticity of the OPAL detector was improved by a detector zoo placed close to the beam pipe. An important task was to measure the luminosity using small angle Bhabha scattering. Additionally, they were used to estimate the energy of initial state photons in order to determine the effective centre-of-mass energy $\sqrt{\mathrm{s}'}$.

4.4.1 The Original Forward Detector

Before the silicon tungsten calorimeter was installed, the forward detector was the only instrument to measure the luminosity. It was composed of drift chambers, scintillators and a lead-scintillator sampling calorimeter with an angular coverage of $47\,\mathrm{mrad} < \theta < 120\,\mathrm{mrad}$. It was supplemented by a further lead-scintillator sampling calorimeter at 7.85 m distance from the interaction point covering the angular space $5\,\mathrm{mrad} < \theta < 10\,\mathrm{mrad}$.

4.4.2 The Silicon Tungsten Calorimeter

The silicon tungsten calorimeter was installed in 1993 in order to improve the accuracy of the luminosity measurement [63]. It offered similar functionality compared to the original forward detector. However, it covers a smaller angular region and features a higher granularity. Therefore, the forward detector was still needed to ensure hermeticity. It was composed of alternating layers of tungsten and double sided silicon detectors with perpendicular aligned strips on each side. It was designed for LEPI energies, therefore, only showers of electrons with an energy less than 45 GeV are fully contained inside the calorimeter. The accuracy of the luminosity measurement was improved to a total relative error of 0.15%.

4.4.3 The MIP Plug

The MIP plug was installed in 1997 to supplement the poletip calorimeter [57]. The instrumented region was extended from 200 mrad down to 43 mrad. The main purpose was to reject muons from the beam halo, and from atmospheric showers at small polar angles. This required a time resolution better than 5 ns. The detector was realised by 4 layers of 1 cm thick plastic scintillators. The light was collected by immersed, curled optical fibres. The efficiency was larger than 99%.

4.4.4 The Gamma Catcher

The gamma catcher filled the hole between the forward detector and the electromagnetic calorimeter. It was composed of several lead-scintillator modules corresponding to 7 radiation lengths. It was sensitive to electrons or photons with a momentum larger than 2 GeV, originally used to veto $\mathrm{e^+e^-} \to \mathrm{Z}^0\gamma$ backgrounds for the neutrino counting in $\mathrm{e^+e^-} \to \mathrm{Z}^0 \to \nu\bar{\nu}$.

Chapter 5

Correction of Field Distortions in the Central Jet Chamber

During the OPAL startup in April 1999 an electrical short appeared in the central jet chamber in the outermost region of the cathode between sectors 4 and 5 ($\Phi_0 = 60°$). The short was most likely located between two of the copper strips on the endplate. A repair was impossible and a reduction of the maximal field potential would not have guaranteed a stable operation of the chamber because the conductivity through the short was found to be variable with time. The only solution was setting the power supplies on both sides of the short to the same potential.

In this new setup of cathode 5, the voltage still increased linearly up to 20 kV, which was reached at a radius of $r = 145\,\mathrm{cm}$ (wire 119). The potential stayed constant over the remaining 40 cm. This solution allowed full voltage to be achieved, however, the homogeneity of the electric field was lost in the outermost region in the two adjacent sectors of this cathode. The electric field in the two configurations is shown in Figure 5.1. If these field inhomogeneities are not taken into account, the position of the reconstructed outer hits deviates from the real position by centimetres. Since the momentum resolution strongly depends on the inner- and outermost hit, the field distortions have a significant impact on the momentum resolution (see Figure 5.2).

The following section summarises briefly the reconstruction of single tracks in the OPAL jet chamber. In a first attempt, described in Section 5.2, a correction was determined from simulations of the electron drift within the new electric field. The correction did not fully recover the resolution. In a second step, described in Section 5.3, the correction was further improved using calibration data. This chapter concludes with an account of the final performance.

5.1 OPAL Track Reconstruction

A profound description and analysis of the electron drift in the OPAL jet chamber is given in [64]. The following paragraphs summarise the main aspects.

As described in Section 4.1.3, charged particles traversing sectors of the jet chamber ionise the gas and the released electrons start drifting in the direction of the anode plane. On their way they scatter with multiple gas atoms. In the homogeneous electric field E, these two effects lead to a constant drift velocity $v_\mathrm{D}(\tilde{\mathrm{E}})$ and direction. The drift velocity depends on the gas mixture and pressure, and the electric field strength. If the gas volume is contained in a magnetic field perpendicular to the direction of the electric field, i.e. perpendicular to the drift

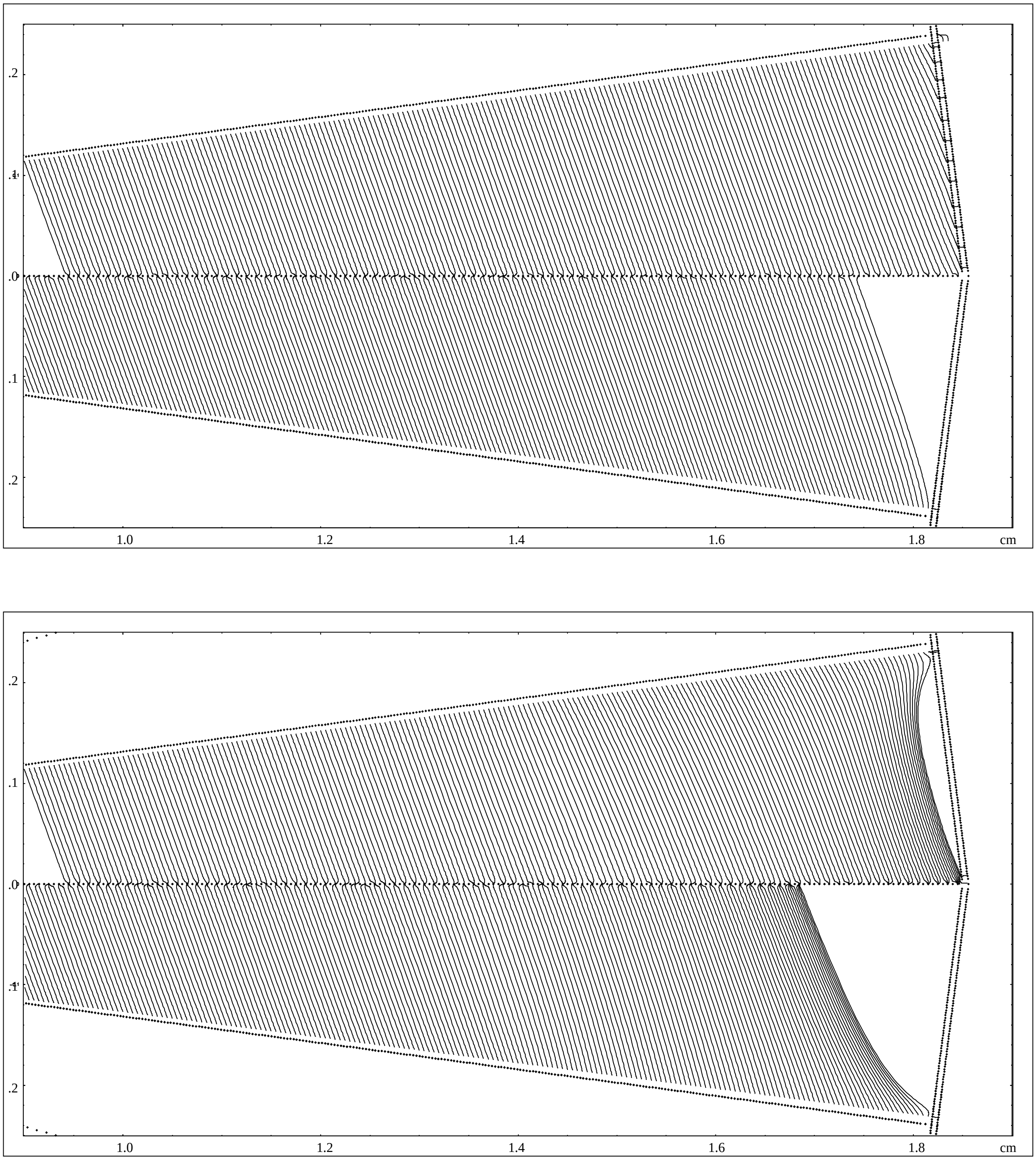

Figure 5.1: Simulated drift paths of electrons within sectors 4 and 5 of the OPAL jet chamber. Top: the voltage of the cathode increased linearly from 5kV up to 25kV. The resulting electric field was homogeneous and led to straight drift paths. Bottom: the voltage increased linearly up to a radius of 145cm. In the outer region, the voltage remained constant at 20kV. The electric field became more and more inhomogeneous with increasing radius. The formerly straight drift paths were bent. Drift paths are shown only if they connect the cathode and the anode.

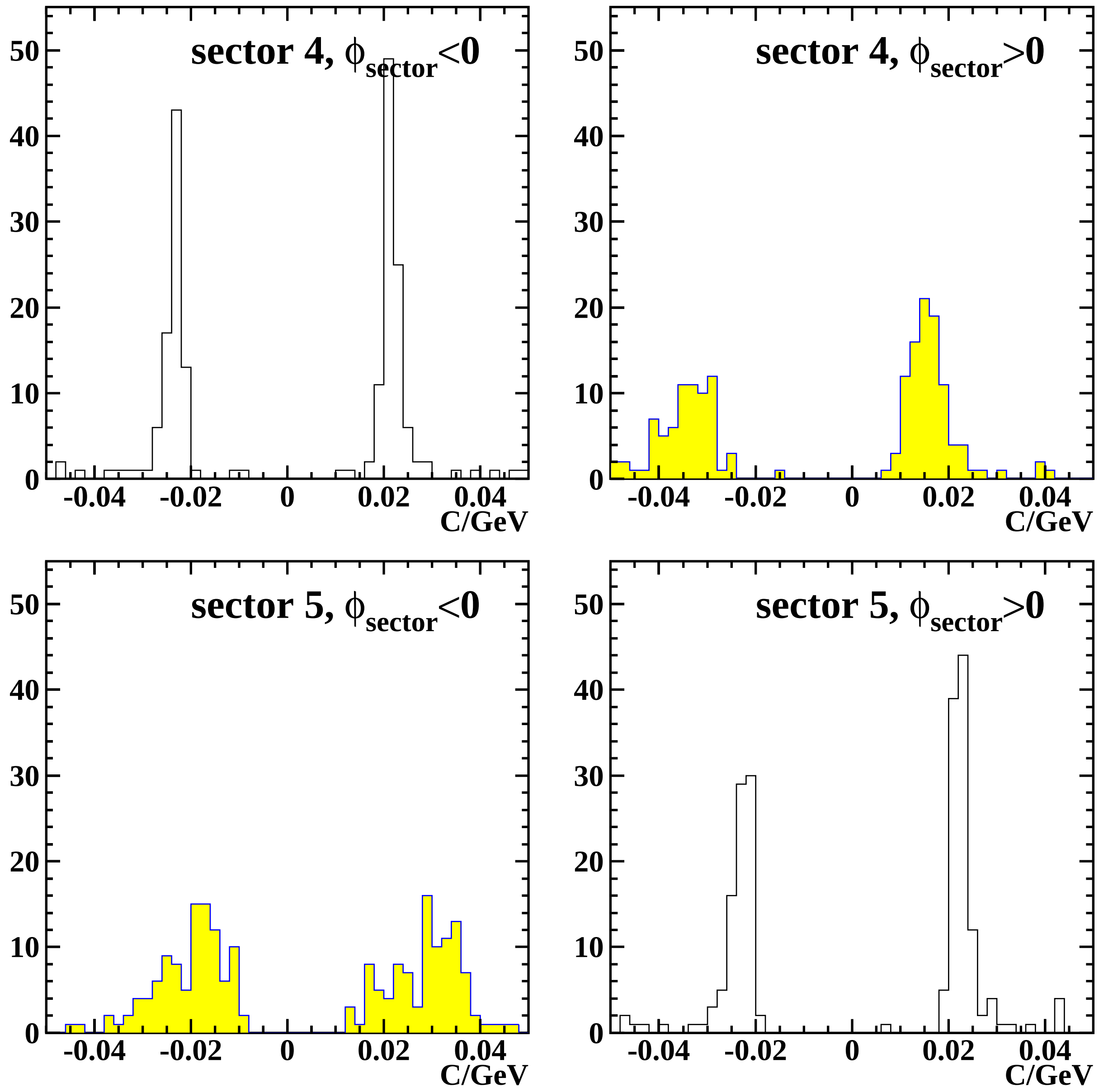

Figure 5.2: Distribution of charge over momentum, q/p, of muons and electrons from muon pair production and Bhabha scattering at $\sqrt{s} = m_{\mathrm{Z}}$. The upper(lower) row refers to particles which traversed sector 4(5) of the OPAL jet chamber. The angle Φ denotes the angle between the track and the anode plane. The impact of the field inhomogeneities on the momentum resolution is clearly evident in the parts of sectors 4 ($\Phi > 0$) and 5 ($\Phi < 0$) adjacent to the cathode plane which suffered the short. The distribution of q/p was expected to be Gaussian with the mean value at $\pm 2/m_{\mathrm{Z}}$.

direction, as in the case of the OPAL jet chamber, the electrons experience a Lorentz force. This force alone will lead to circular motion. But the interplay of forces, the Lorentz force, the electrostatic force and the interaction with the gas atoms, cause a constant drift velocity and direction. The presence of the magnetic fields tilts the drift path by the Lorentz angle $\alpha_\mathrm{L}(\vec{E}, \vec{B})$ with respect to the direction of the electric field. The Lorentz angle depended on the magnetic field $\vec{B}$, the electric field $\vec{E}$, the gas mixture and pressure. The drift velocity within the OPAL jet chamber turned out to be independent of the magnetic field. It was $v_\mathrm{D} \simeq 53\,\mu\mathrm{m/ns}$. The Lorentz angle was $\alpha_\mathrm{L} \simeq 20^\circ$.

In a distance $r \geq 5\,\mathrm{mm}$ from the wire planes, the electric field was approximately homogeneous. However, close to the wires, the electric field rose sharply with the inverse of the distance to the closest wire. The drift electrons were accelerated and started an ionisation avalanche, which was detected by the sense wires.

The drift time, i.e. the time difference between the arrival of the signal and the $\mathrm{e}^+\mathrm{e}^-$ collision, together with the drift velocity was used to measure the drift length, i.e. the distance of the track from the wire. In order to achieve the desired precision, the signal propagation time from the sense wire to the amplifier and digitiser had to be taken into account. Neglecting the inhomogeneities close to the wires, the absolute value of the drift velocity and the direction were constant, thus the drift length was a linear function of the drift time.

The gas mixture and pressure of the OPAL jet chamber were adjusted such that the increasing electric field close to the sense wire led to a decreasing drift velocity. Thus, neglecting the inhomogeneities close to the wires, the drift length would be overestimated. This was compensated by adding a small negative offset. If the track passed by the sense wire in a distance closer than $\sim 5\,\mathrm{mm}$ a non-linear correction as a function of the drift time was applied in order to determine the drift length accurately. In Figure 5.3a and b, drift paths are sketched, where the initial charged particle track crossed the drift cell at different angles β. In Figure 5.3a, the central drift paths was the fastest. However, at low crossing angles the fastest drift paths were non-central (see Figure 5.3b). Thus, a correction depending on the crossing angle β was necessary.

The drift length and the Lorentz angle permit to determine one point on the track, referred to as a *hit*. However, from one hit alone it was impossible to determine whether the track passed by on the left or right side of the anode plane. Therefore, both possibilities were considered at first. Then helical paths were fitted to the hits starting at the outermost one. Due to the staggering of adjacent sense wires one of the two hypotheses matches significantly better and the location of each hit can be chosen nearly unambiguously.

In order to achieve the desired resolution, the positions of the sense wires had to be known with high precision. Since the mount points of the sense wires deviated from their nominal values and the endplates were tilted slightly, the wire position changed with the z coordinate in ϕ and the radial direction. Under the influence of gravity, the sense wires sagged. Since they spanned the large distance of $4\,\mathrm{m}$ the effect is significant. The difference between the wire position at the mount points and at the middle of the jet chamber amounted to $200\,\mu\mathrm{m}$. Moreover, the staggering of the sense wires caused a mutual repulsive force in the direction perpendicular to the anode plane. In the middle of the chamber, the wire position was shifted by $70\,\mu\mathrm{m}$. These effects were corrected and the positions of the sense wires were functions of the z-coordinate.

Since several corrections depended on properties of the track which are initially unknown, the reconstruction passes through several iterations.

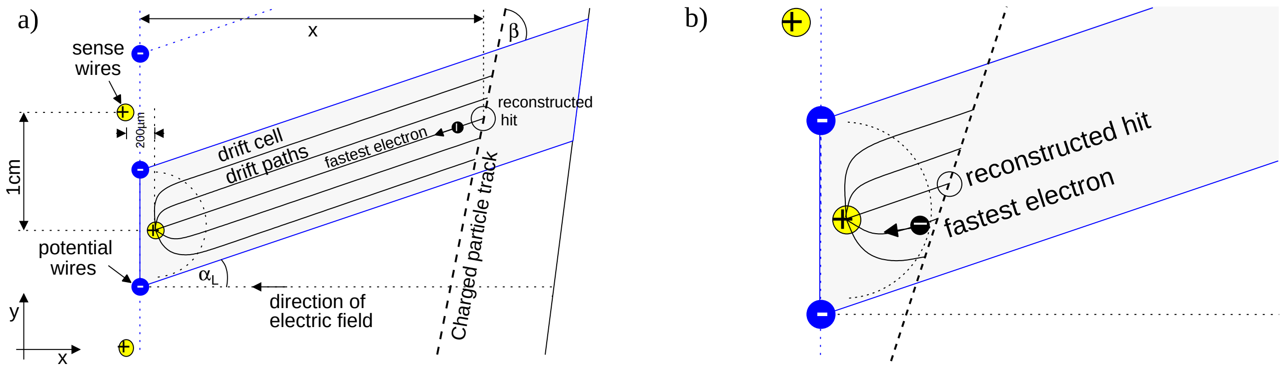

Figure 5.3: Electron drift within one drift cell. In Figure a) the drift paths of electrons are sketched which give rise to a signal on the sense wire of the marked drift cell. The central drift path is the fastest path. In Figure b) the track crosses the drift cell at a lower angle. In this case not the central, but the marked drift path is the fastest.

5.2 Corrections from Electric Field Calculations

In order to develop a correction for the new inhomogeneities of the electric field, the electron drift in the new and the original electric field was simulated [65] and the results were compared. The simulation was performed in two dimensions in the $r-\phi$ plane using the geometry of one sector of the OPAL jet chamber[1]. The starting points of the simulated drift electrons were defined by tracks crossing the drift cells at various angles β and distances x from the anode plane (see Figure 5.3a).

In addition to the geometry, the simulation needed, as inputs, the drift velocity and the Lorentz angle as a function of the electric and magnetic field. In a homogeneous electric and magnetic field, the drift velocity and the Lorentz angle are constant. This was valid for the original setup except in the region close to the sense or potential wires.

The drift velocity had been measured in 1989 as a function of the electric field using exactly the same gas composition as used inside the OPAL jet chamber, but without a magnetic field. It turned out that the drift velocity was nearly independent of the magnetic field B i.e. $v_D(E,B) \equiv v_D(E)$. The Lorentz angle was measured using a slightly different gas composition and only for a few different electric and magnetic fields E and B. Hence, the Lorentz angle as a function of the electric and magnetic field $\alpha_L(E,B)$ is less well known.

In the original electric field, the paths of drifting electrons were straight, parallel lines except the region close to the wires (distance smaller than 5 mm). In the distorted electric field the paths were bent in the outer regions (see Figure 5.1). In order to compare the two simulations, the effective drift velocity $v_{\text{eff.}}$ and Lorentz angle $\alpha_{\text{L eff.}}$ were computed:

$$v_{\text{eff.}} = \frac{|\vec{x}_{\text{hit}} - \vec{x}_{\text{wire}}| + s_{0\,\text{wire}}}{t_{\text{drift}}} \quad \text{and} \quad \tan\alpha_{\text{L eff.}} = \frac{x_{\text{hit}} - x_{\text{wire}}}{y_{\text{hit}} - y_{\text{wire}}}, \tag{5.1}$$

where $\vec{x}_{\text{wire}}$ denoted the position of the sense wire, $\vec{x}_{\text{hit}}$ the starting position of an electron and t_{drift} the corresponding drift time. For the comparison, only electrons starting at the centre of each drift cell were used. Since the drift velocity decreases in the region close to the sense wire,

---

[1] As the simulation was carried out in two dimensions, differences in the z-direction i.e. gravitational effects of the sense wires and the small relative twist of the endcaps were not taken into account.

$|\vec{x}_{\text{hit}} - \vec{x}_{\text{wire}}| < 5\,\text{mm}$, a small negative offset $s_{0\,\text{wire}}$ was added to the drift length such that $v_{\text{eff.}}$ became a constant quantity in the first setup, in which the electric field was homogeneous.

The quantities (5.1) were used only to investigate the influence of the new field inhomogeneities in the new setup. Since the new setup mainly influenced the drift properties close to the cathode no care was taken that the effective drift velocity and Lorentz angle reflected the real values at small drift lengths.

In all outer drift cells, starting at the 97th ($r > 122$cm), the effective drift velocity and Lorentz angle, $v_{\text{eff.}}$ and $\alpha_{\text{L}\,\text{eff.}}$, were determined from the two simulations for several drift lengths corresponding to drift times t_i. A second order polynomial $P_2(t;\,\text{wire})$ of the drift time was fitted to the ratios of $v_{\text{eff.}}(t_i, \text{wire})$ for each cell, or sense wire, separately[2]:

$$\sum_i \left| \frac{v'_{\text{eff.}}(t_i, \text{wire})}{v_{\text{eff.}}(t_i\ , \text{wire})} - P_2(t_i;\ \text{wire}) \right|^2 = \text{min.}\,,$$

where $v'_{\text{eff.}}(t_i, \text{wire})$ denotes the drift velocity resulting from the simulation of the new setup. The effective Lorentz angle $\alpha_{\text{L}\,\text{eff.}}(t_i, \text{wire})$ was influenced in a stronger way and a fifth order polynomial $P_5^{\alpha_\text{L}}(t_i;\ \text{wire})$ was needed to approximate the ratio.

The correction polynomials were determined for electrons that start at the drift cell centres. However, the signal is initiated by the drift electron which reaches the sense wire first and if the particle track crosses the drift cell at small angles (see Figure 5.3b), the fastest drift path does not start at the centre of a cell. Therefore, simulations were performed of tracks crossing the drift cells at various angles and the correction factors, as described above, were obtained, however, the drift time of the fastest electron was used this time. The correction factors did not show a significant difference compared to those obtained from the central drift electrons.

The correction was tested on a sample of electron and muon pairs selected from the calibration data in 1999. The samples were composed of lepton pairs each with a momentum of $m_{\text{Z}}/2$. In addition to the corrections mentioned in Section 5.1, the correction polynomials were used to compute correction factors for the drift velocities and Lorentz angles, depending on the measured and corrected drift time. Then, the corrected Lorentz angle and drift velocity were used in the full reconstruction.

In order to test the quality of the correction, the track fit was initially limited to use only hits from the first 97 wires of the 159 available wires. The field inhomogeneities in the corresponding drift cells were negligible. Then hits from more and more outer wires were considered. Each time a Gaussian was fitted to the distribution of charge over track momentum, q/p, (compare with Figure 5.2); the average width of the Gaussians obtained from negatively and positively charged particles is considered as the inverse momentum resolution ($\sigma_{p^{-1}} = \sigma_p/p^2$), which is shown in Figure 5.4 as a function of the last contributing wire. With the correction applied, the resolution is almost recovered in the sectors adjacent to the affected cathode 5, if only the first 118 wires are considered in the track fit. Without any corrections, the momentum resolution was about five times as bad (see Figure 5.2), or if the fit was limited to the first 105 wires it was twice as bad .

---

[2] As the two simulations do not give results for exactly the same drift times t_i, the results are interpolated in the homogeneous case.

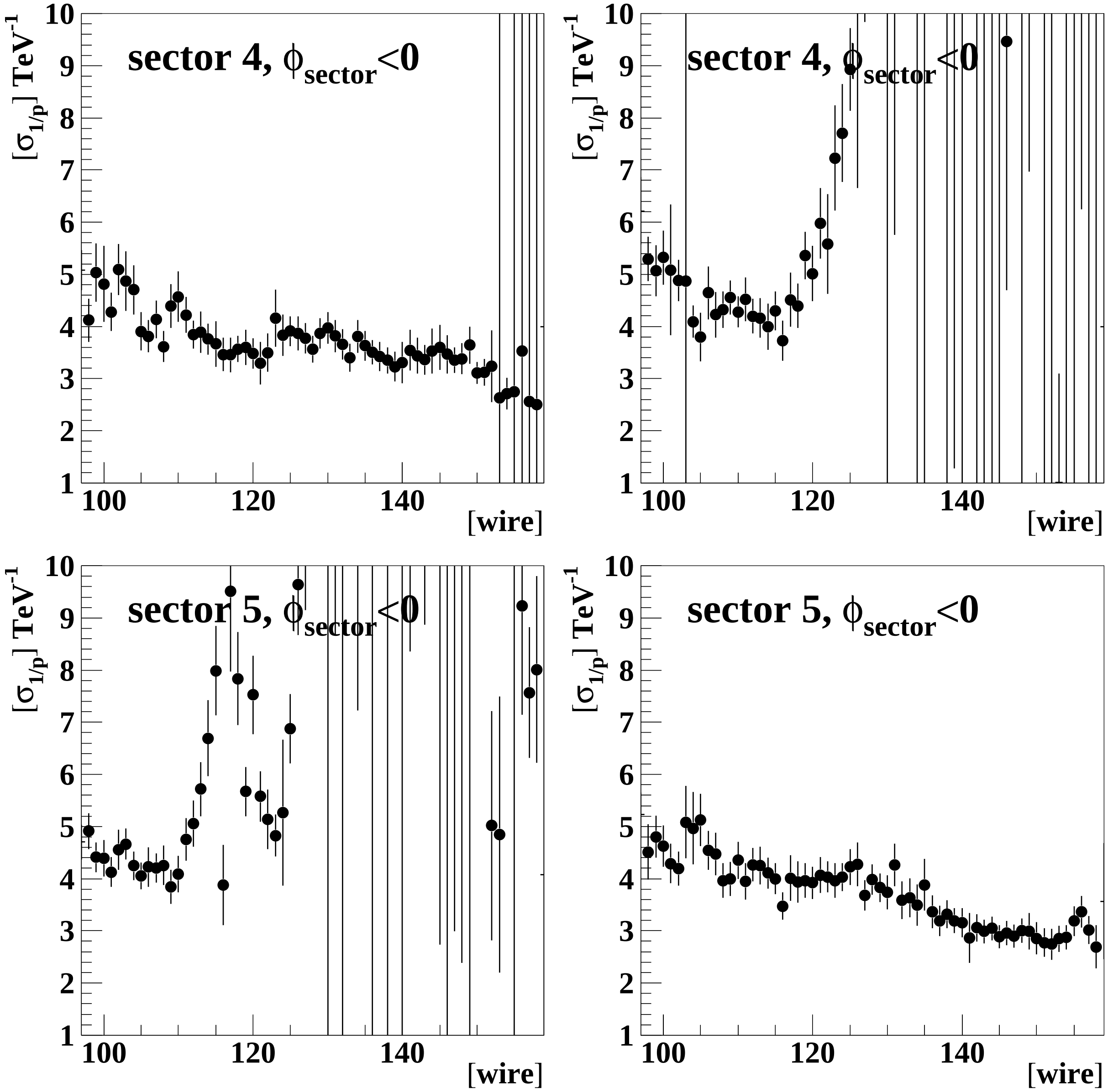

Figure 5.4: Resolution of $1/p$ of electron and muon pairs recorded at $\sqrt{s} \simeq m_{Z^0}$, as a function of the outermost wire which was considered in the track fit. The corrections obtained from the field calculations have been applied to the Lorentz angle and drift velocity. The figures at the upper left and lower right show the sides of the sectors 4 and 5 adjacent to cathode 4 and 6, respectively, which are unaffected by the modified potentials of cathode 5. The resolution improves in the affected sectors until hits are used beyond wire $\sim$ 120.

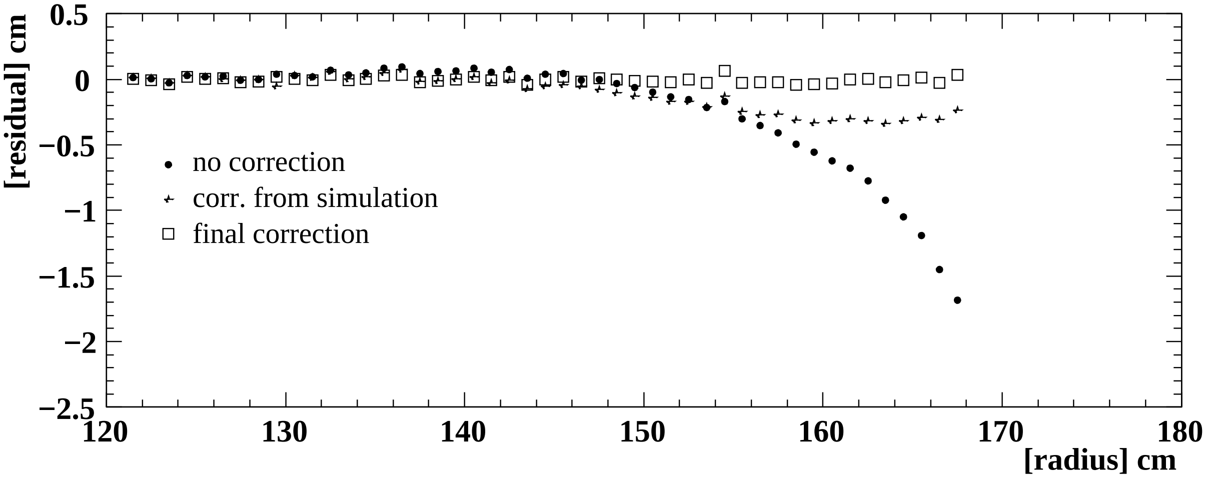

Figure 5.5: Deviation of the reconstructed hit position from one electron candidate track with a momentum of 45GeV. The track was fitted to the hits from the first 100 wires. The hits were reconstructed without applying any correction (solid circles), applying the correction obtained from the field calculations (stars) and applying the correction adjusted with the calibration data (squares).

5.3 Tuning the Correction Polynomials with Calibration Data

After the corrections extracted from the field calculations were applied, the hits reconstructed from wires 97 to 118 showed similar errors as the inner hits. However, the errors from outer hits (wire>118) remained in the order of several mm (see Figure 5.5). Possible reasons for the incomplete correction included wrong assumptions on the:

- drift velocity $v_D(E, B)$, and
- Lorentz angle $\alpha_L(E, B)$.

The drift velocity $v_D(E, B)$ used in the simulation was measured in exactly the same gas mixture used in the OPAL jet chamber, however, the assumed contamination with water was slightly different. In order to estimate the effect of this difference, the simulation was repeated using drift velocities measured in environments suffering less and more water contamination [65]. Corrections were extracted and applied to the hit reconstruction. The resulting differences were negligible.

The Lorentz angle $\alpha_L(E, B)$ was measured only for a few different electrostatic and magnetic field strengths and the gas mixture used for the measurements differed slightly from the gas in the OPAL jet chamber.

Since there was no reason to doubt the assumptions of the drift velocity, the drift length was considered to be correctly measured. The correction of the Lorentz angle was adjusted, using calibration data recorded in 1999 at $\sqrt{\mathrm{s}} = m_{\mathrm{Z}}$. From this data set, electron and muon pair events were selected, in which one track passed the sectors adjacent to cathode 5, and the correction of the previous section was applied to the reconstruction. The track fit was limited

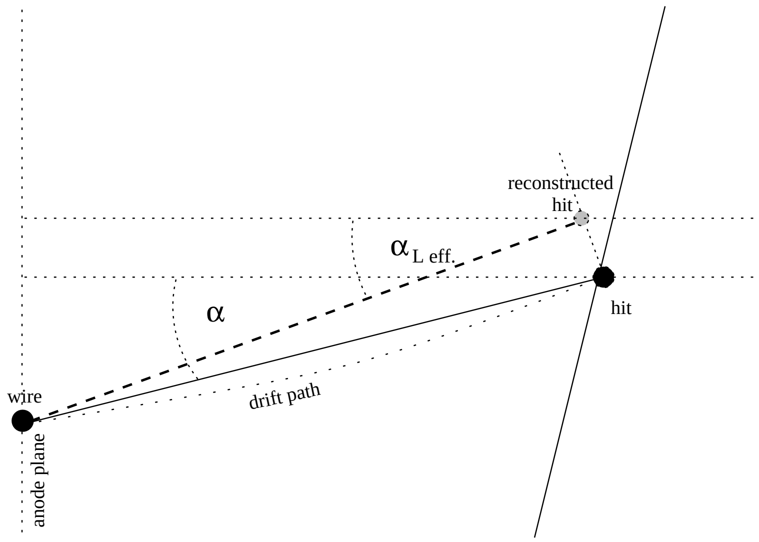

Figure 5.6: It is assumed that the effective drift length is reconstructed correctly but the effective Lorentz angle $\alpha_{\mathrm{L\ eff.}}(t_{\mathrm{drift}})$ used to reconstruct the hit is wrong. The hit is rotated until the hit meets the extrapolation of a track which was fitted to the hits from all wires up to wire 100. The ratio $\int \alpha/\alpha_{\mathrm{L\ eff.}}(t_{\mathrm{drift}})dt_{\mathrm{drift}}/\int dt_{\mathrm{drift}}$ is taken as a correction factor for $\alpha_{\mathrm{L\ eff.}}$.

to hits from the first 100 wires, since the momentum resolution was disturbed if further hits were used.

In order to improve the correction of the Lorentz angle, the reconstructed hits were rotated around the sense wire until the distance to the extrapolated track was minimised. This is sketched in Figure 5.6. The nominal Lorentz angle $\alpha_{\mathrm{L}}(t_{\mathrm{drift}},\ \mathrm{wire})$ and the final angle after the additional rotation $\tilde{\alpha}_{\mathrm{L\,eff.}}(t,\ \mathrm{wire}) := \alpha_{\mathrm{L}}(t,\ \mathrm{wire}) + \Delta\alpha_{\mathrm{min.}}(t,\ \mathrm{wire})$ were compared for all selected electron and muon pairs averaging over drift lengths in bins of 1 cm. The average angles obtained at some wires are shown in Figure 5.7. In the homogeneous electric field, the Lorentz angle was constant. This was the assumption of the totally uncorrected reconstruction. In the outer region, the electric field became more and more inhomogeneous and the assumption of a constant Lorentz angle became invalid, as suggested by the simulation. Therefore, the effective Lorentz angle, necessary to reconstruct the hit on top of the extrapolated track, varied with the drift length or drift time (see Figure 5.7a). After the correction polynomial $P_5^{\alpha_{\mathrm{L}}}(t_{\mathrm{drift}};\ \mathrm{wire})$ was applied to the Lorentz angle, the effective angle $\alpha_{\mathrm{L\ eff.}}$ depended on the drift time:

$$\alpha_{\mathrm{L\,eff.}}(t_{\mathrm{drift}}) \simeq \alpha_{\mathrm{L}} P_5^{\alpha_{\mathrm{L}}}(t_{\mathrm{drift}};\ \mathrm{wire}).$$

However, the Lorentz angle was underestimated beyond wire 118 and an additional rotation $\Delta\alpha_{\mathrm{min.}}$ was needed, in order to reconstruct the hit on top of the extrapolated track. It turned out that the ratio $(\alpha_{\mathrm{L\,eff.}} + \Delta\alpha_{\mathrm{min.}})/\alpha_{\mathrm{L\,eff.}}$ was nearly independent of the drift distance, i.e. drift time (see Figure 5.7b). Hence, an improvement was achieved by scaling the correction polynomial P_5^{α} by the average ratio:

$$\widetilde{P}_5^{\alpha}(t_{\mathrm{drift}};\ \mathrm{wire}) := \left(1 + \frac{1}{n}\sum_{i=1}^{n} \frac{\Delta\alpha_{\mathrm{min.}}(t_i,\ \mathrm{wire})}{\alpha_{\mathrm{L\,eff.}}(t_i,\ \mathrm{wire})}\right) \cdot P_5^{\alpha}(t_{\mathrm{drift}};\ \mathrm{wire}) = (1 + k(\mathrm{wire})) \cdot P_5^{\alpha}(t_{\mathrm{drift}};\ \mathrm{wire}). \tag{5.2}$$

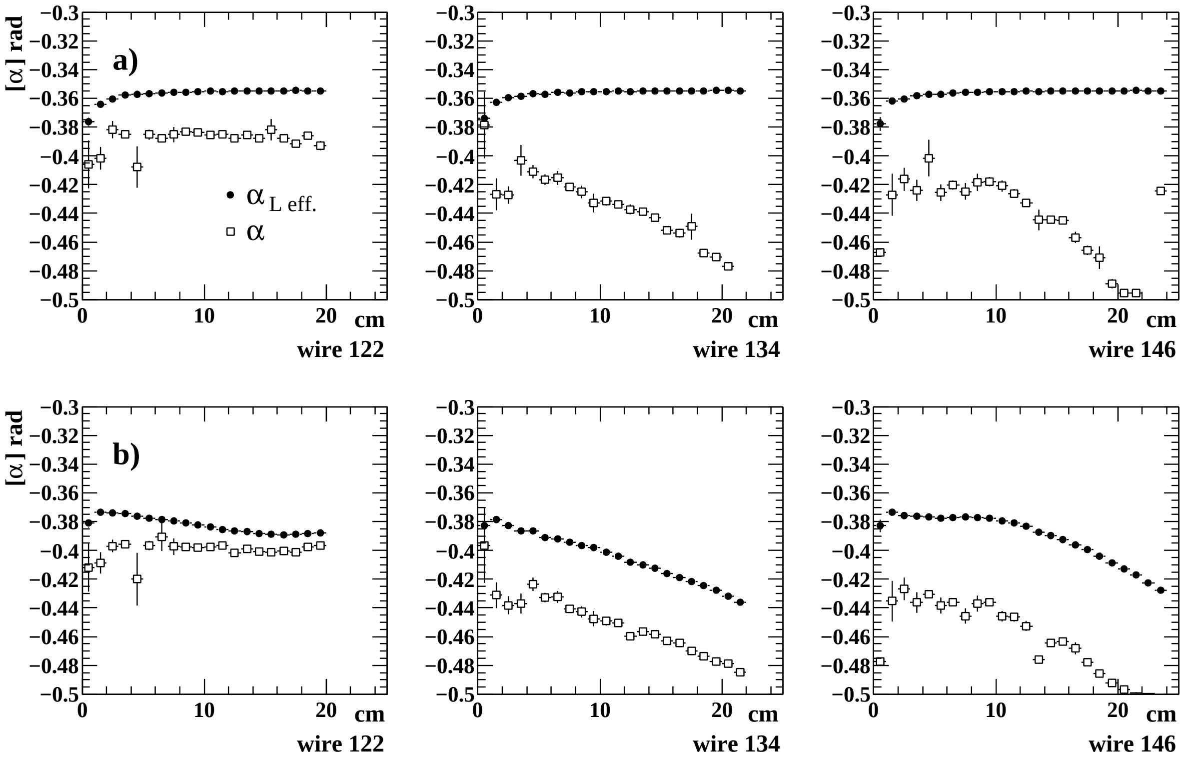

Figure 5.7: The angles $\alpha_{\mathrm{L\ eff.}}$ (filled circles) and α (open squares) as defined in Figure 5.6 are shown depending on the drift length in three drift cells at increasing radii. The angle $\alpha_{\mathrm{L\ eff.}}$ is calculated from the reconstructed hit position and the angle α denotes the necessary effective Lorentz angle in order to reconstruct the hit on top of extrapolated tracks which were fitted to the hits from the first 100 wires. The hits resulted from electrons or muons which passed the sectors adjacent to cathode 5 in electron or muon pair events ($\sqrt{\mathrm{s}} \simeq m_{\mathrm{Z}}$). In a), the drift velocity and Lorentz angle were uncorrected. In b), the corrections obtained from the field calculations were applied. In a), a constant Lorentz angle was assumed in order to reconstruct the hit position. Therefore, the calculated effective Lorentz angle was approximately constant. However, in order to reconstruct the hit on top of the extrapolated track, a much larger angle would be necessary depending on the drift length (open circles). In b), the corrected Lorentz angle depended on the drift length, however, depending on the drift cell (or wire number), a larger Lorentz angle was still needed in order to reconstruct the hit on top of the extrapolated track.

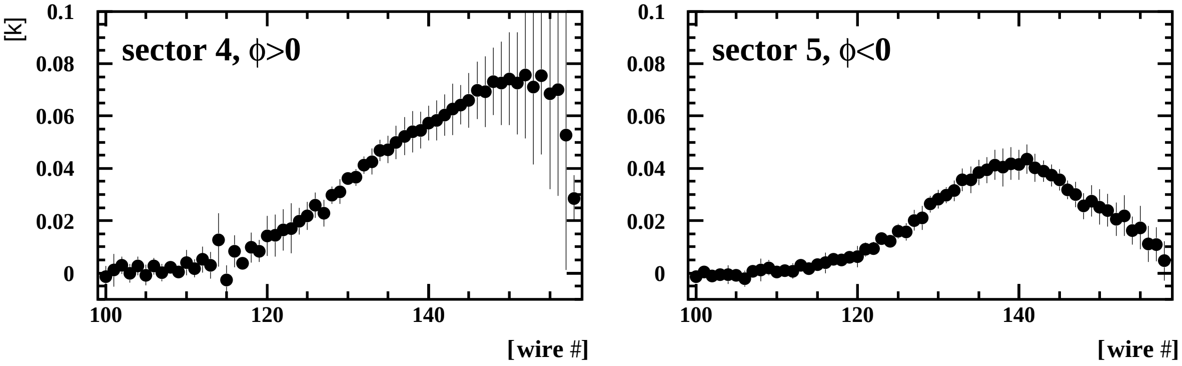

Figure 5.8: Relative difference between the effective Lorentz angle used in the reconstruction and the angle needed in order to reconstruct the hit on top of the corresponding extrapolated track (see Figure 5.6 and Equation 5.2). The track was fitted to hits from the first 100 wires. Shown are the average values determined from many electron or muon tracks ($p = m_{\mathrm{Z}}/2$) which passed the anode plane at various distances. The error bars indicate the standard deviation from the average value. The x-axis denotes the number of the corresponding wire.

where n denotes the number of considered drift time intervals and t_i the drift time at the central value of each interval. The averaging comprised only ratios at drift length $r > 5\,\mathrm{mm}$, because in the region close to the anode plane, the effective Lorentz angle (5.1) is a poorly defined quantity. Moreover, the hit position was less sensitive to the Lorentz angle in this region. The rescaling factors are shown in Figure 5.8. These factors were determined independently for tracks from electron and muon pairs and an agreement within statistical errors was found.

The reconstruction was repeated, using the new correction $\widetilde{P}_5^{\alpha}$ instead of P_5^{α}. In Figure 5.9, the evolution of the momentum resolution is shown, incrementally using hits from more and more wires in the trackfit. The momentum resolution in the parts of sectors 4 and 5 adjacent to cathode 5 was nearly as good as in the unaffected parts. The bump in sector 4 indicates that the correction did not work perfectly for 1 to 5 wires around wire 120. As the curvature of the fitted track depended strongly on the outermost hits, the momentum resolution became significantly worse if hits of these wires were the last hits used. The resolution did not improve if the troublesome wires around wire 120 were excluded from the track reconstruction.

5.4 Validity Check of the Correction

Additional tests were performed to assure that the correction was not tuned to yield only good momentum resolution in muon and electron pair events at $\sqrt{s} \simeq m_{\mathrm{Z}}$.

The deviation of hits from a fitted track helix in low multiplicity events was investigated with and without applying the correction, and the results were compared. The large deviations observed, if no correction was applied, vanished for hits up to wire 140. Significant deviations remained beyond wire 150.

In a further test, $\mathrm{K}^0_{\mathrm{S}}$ mesons were reconstructed using the method described in [66] which is based on [67]. Partly $\mathrm{K}^0_{\mathrm{S}}$ mesons decay inside the jet chamber and the decay products cross the drift cells at smaller or larger angles than particles which are produced close to the primary

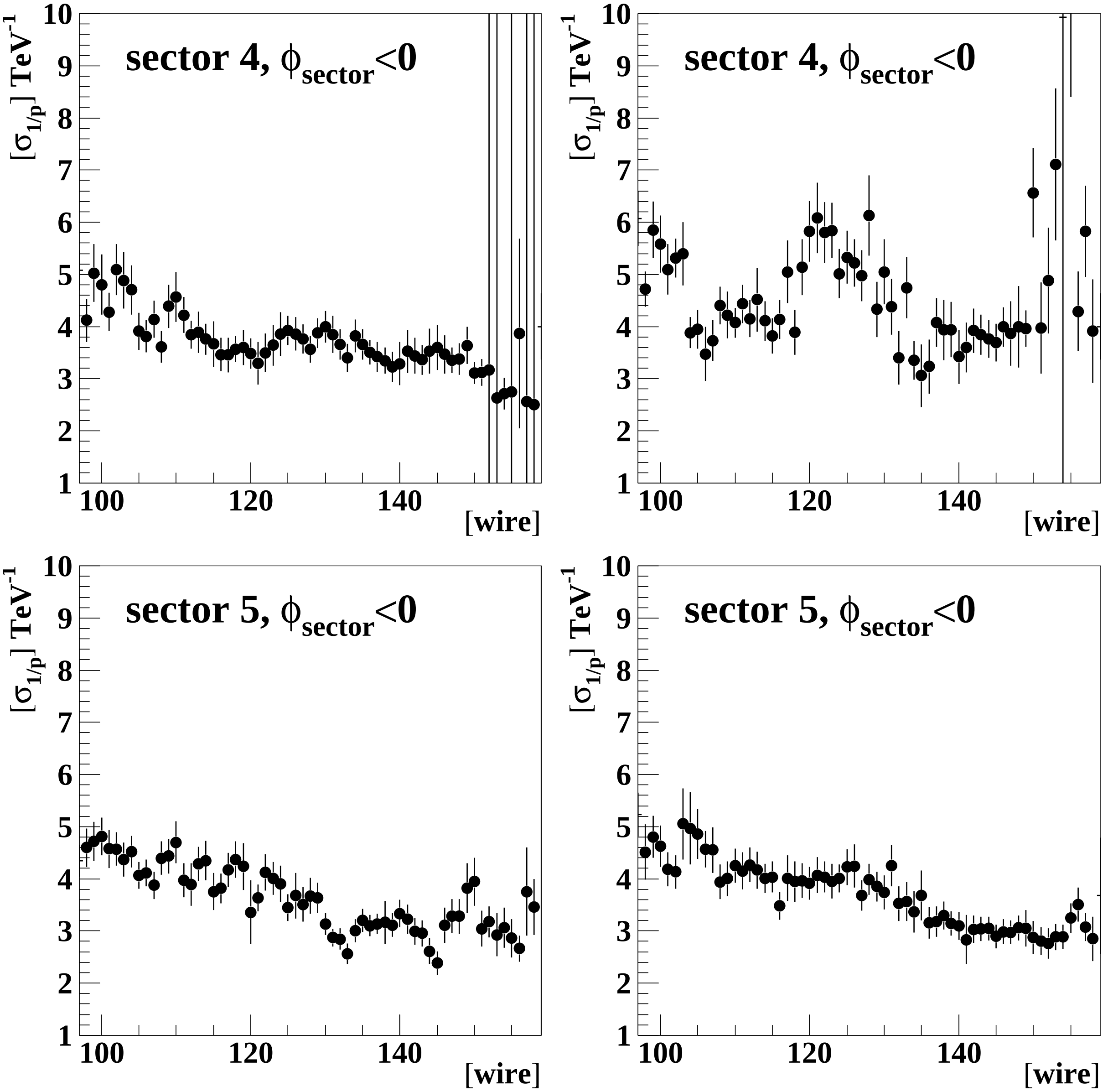

Figure 5.9: Resolution of $1/p$ of electron and muon pairs recorded at $\sqrt{s} \simeq m_{\mathrm{Z}^0}$, as a function of the outermost wire which is considered in the track fit. In contrast to Figure 5.4, the final correction was applied. The final correction was based on the field calculations, but the correction was further adjusted using calibration data, as described in Section 5.3. The resolution evolves similar in both sides of sector 5, indicating that the remaining deviations of the corrected hit positions are close to the expected resolution. In sector 4, the momentum resolution still worsens if the last considered hits are from wires 119 to ~ 121. However, the distortions are compensated if outer wires are used.

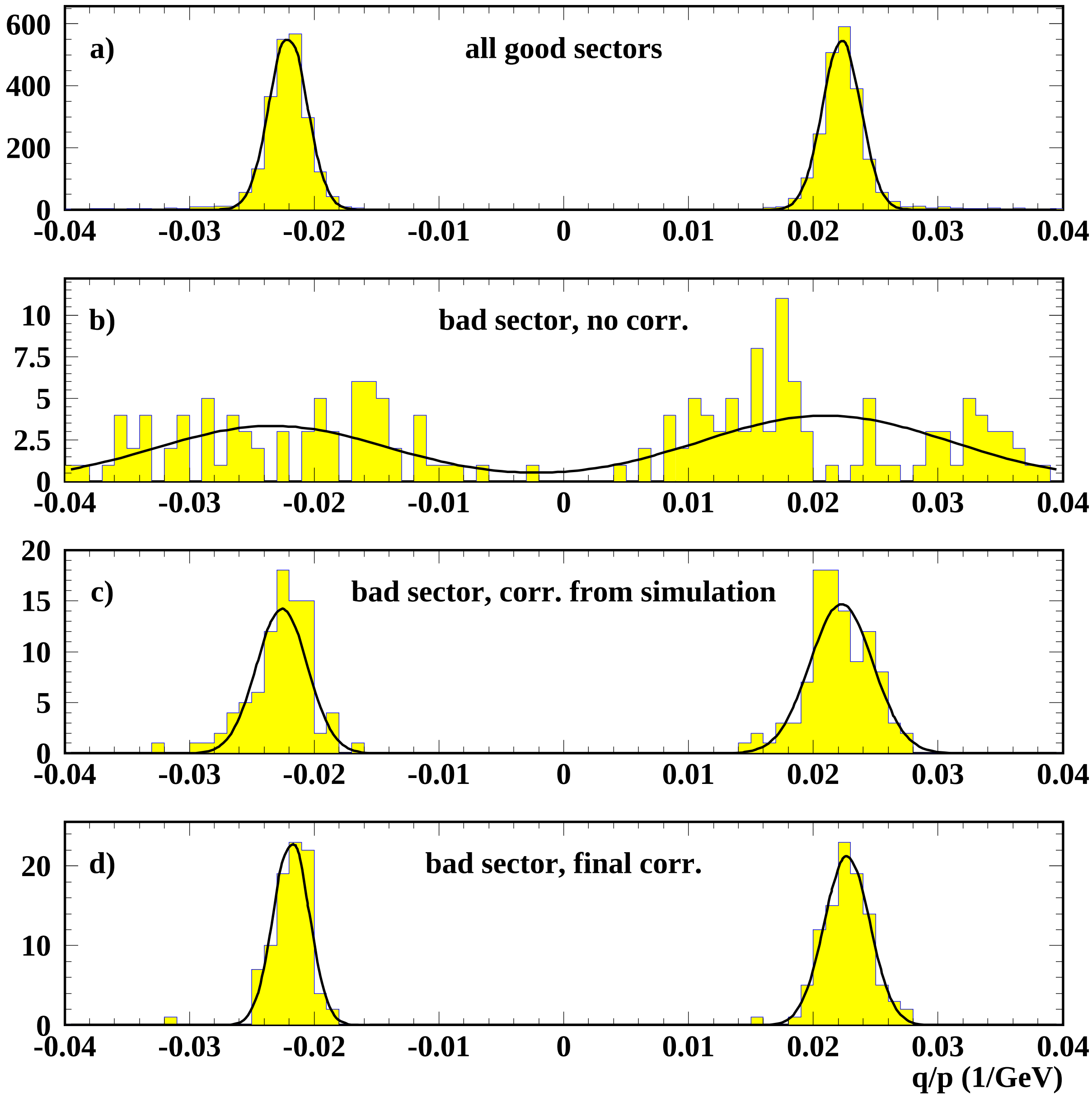

Figure 5.10: Momentum resolution of muon and electron pairs produced at $\sqrt{s} \simeq m_{Z^0}$. In a) the tracks passed unaffected sectors and in b), c) and d) the parts of sector 4 or 5 adjacent to cathode 5. Figure b) shows the momentum resolutions without any correction, in c) the correction which has been extracted from the field calculations was applied and in d) the full correction.

vertex. Since the crossing angle defines which drift path is the fastest, the correction might perform worse for these event topologies. The distribution of the reconstructed $\mathrm{K^0_S}$ mass is shown in Figure 5.11 before applying the correction. Only $\mathrm{K^0_S}$ mesons were considered whose decay products crossed sectors 4 or 5. The reconstructed mass is assigned to the sector which contained most of the outer hits. The signal was modelled by a Gaussian and the background by a polynomial. The combined function was fitted simultaneously. The statistical errors on the mass and the mass resolution were too large and the signal rate was too small to permit a clear statement about the quality of the reconstruction in the different sectors. Nevertheless, the mass resolution seemed to be worse in the sectors adjacent to cathode 5. After the correction had been applied the mass resolution, shown in Figure 5.12, did not improve significantly. However, the $\mathrm{K^0_S}$ mass resolution worsened during several attempts to improve the corrections even further.

Finally, the impact parameter resolution in the $r-\phi$ plane was investigated. For this purpose a subsample of the calibration data was used containing muon and electron pairs recorded at $\sqrt{\mathrm{s}} \simeq m_\mathrm{Z}$. Tracks are fitted to the hits resulting from electron and muon pairs and are extrapolated to determine the point of closest approach (p.c.a.) to the interaction point in the $r-\phi$ plane, i.e. the impact parameter d_0. Since both tracks ($i = 1, 2$) originated from the primary vertex, the distribution of:

$$\sigma_{d_0} := \frac{1}{\sqrt{2}}(d_0^1 + d_0^2) \tag{5.3}$$

is a measure of the impact parameter resolution σ_{d_0}. Events were considered in which one track passed cathode 5 (sectors 4 and 5) and cathode 10 (sectors 10 and 11), respectively. Figures 5.13 and 5.14 show the obtained distributions, before and after the corrections were applied. If both tracks traversed unaffected sectors, the resulting distributions were Gaussians around zero. However, without applying any corrections, the distributions were significantly shifted if one track passed cathode 5. The shift indicates, that the impact parameter resolution differed between the affected and the corresponding opposite sectors. After applying the correction, the shift was significantly reduced.

5.5 Summary

In order to take into account the field distortions in the sectors adjacent to cathode 5 Drift time dependent corrections to the drift velocity and Lorentz angle were extracted from field calculations, . The corrections partially recovered the reconstruction and the errors of the reconstructed hit positions were reduced from several millimetres (at $r = 143\,\mathrm{cm}$) to approximately $200\,\mu\mathrm{m}$ in $r-\phi$ for all hits with $r \leq 143\,\mathrm{cm}$ (wire 118). A further improvement was achieved, by adjusting the correction of the Lorentz angle using tracks of muon and electron pairs selected from the calibration data at $\sqrt{s} \simeq m_\mathrm{Z}$. Only in the region $r > 175\,\mathrm{cm}$ (beyond wire 150) errors larger than $200\,\mu\mathrm{m}$ remained. However, these hits had less impact on the track fit since generally larger errors are assigned to hits at large radii. Nevertheless, best momentum resolution in electron and muon pair events was achieved if hits from all wires were used. The improvement of the momentum resolution is summarised in Figure 5.10.

All performed tests indicated, that the correction improved the track quality almost to the same level as before the incident. Attempts to further improve the quality of the correction had

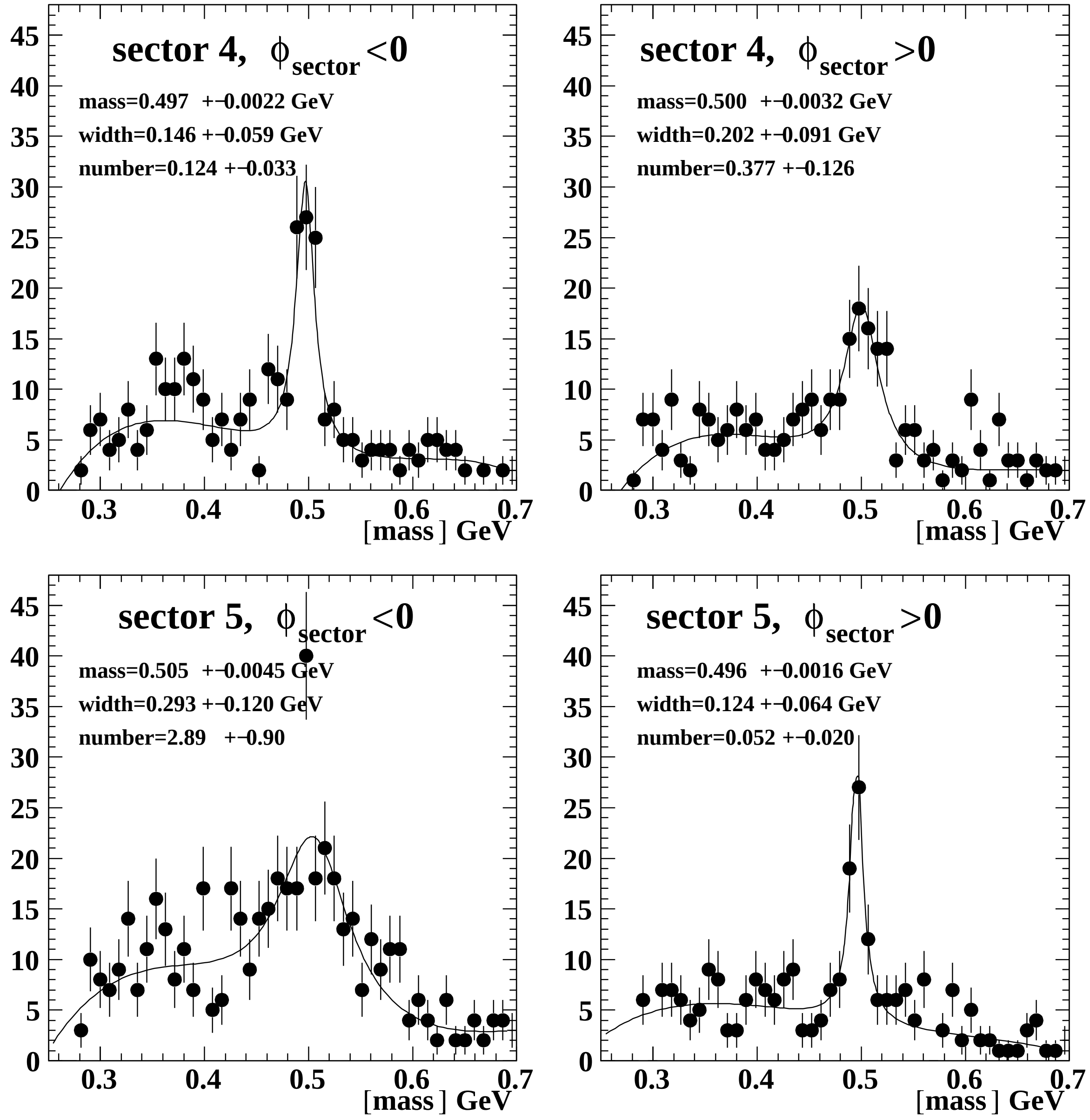

Figure 5.11: Mass distribution of K_S^0 meson candidates, where at least one secondary track is passing sector 4 and sector 5 in the outermost region ($r > 140$cm). Here, no correction was applied.The upper right and the lower left figure show the resulting distributions when at least one secondary is transversing sectors adjacent to cathode 5.

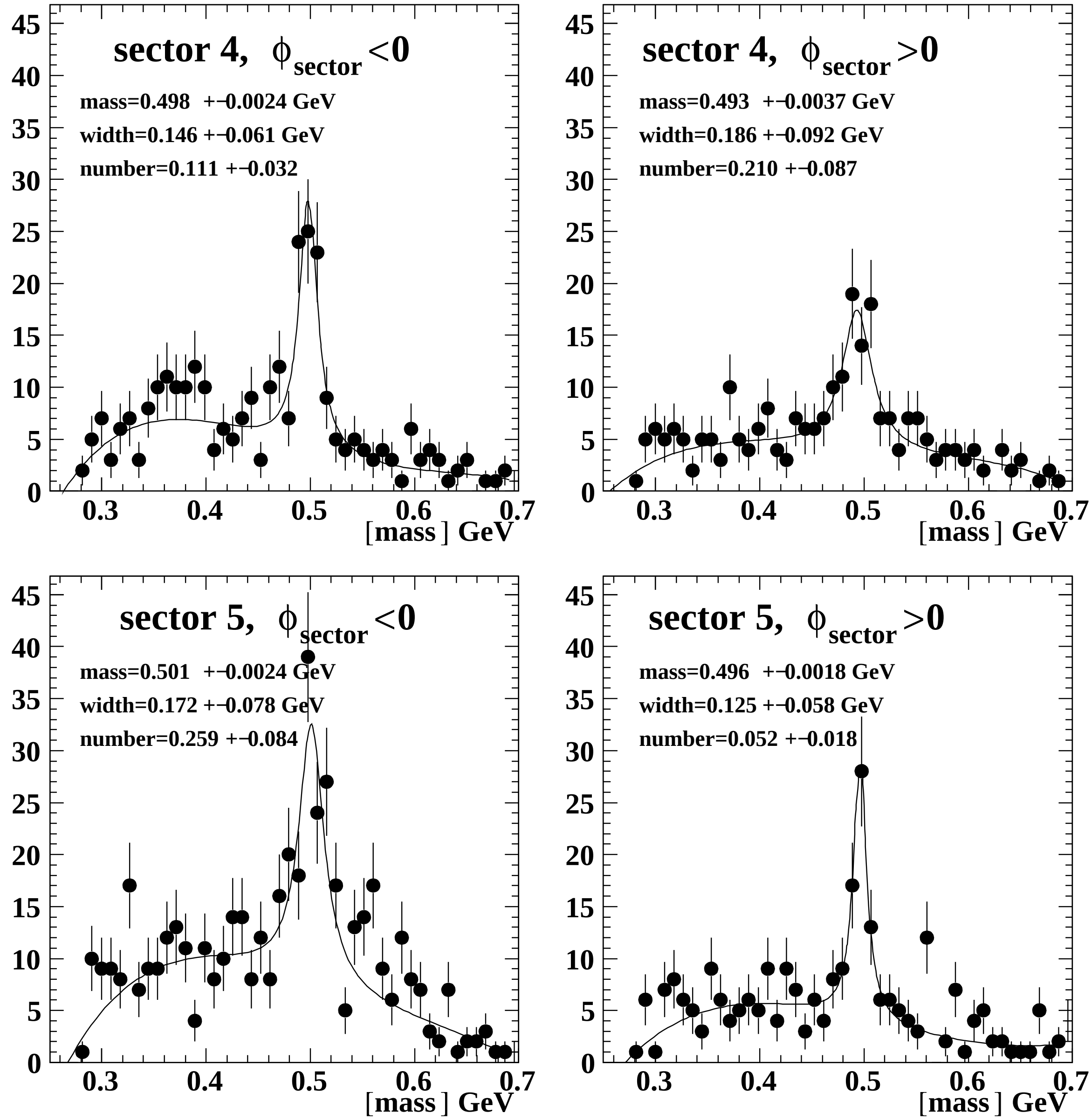

Figure 5.12: Mass distribution of K^0_S meson candidates, after the correction was enabled. The figures at the top (bottom) show the distribution when secondary particles were passing sector 4 (5). The upper right and the lower left figure show the resulting distributions when at least one secondary is traversing sectors adjacent to cathode 5.

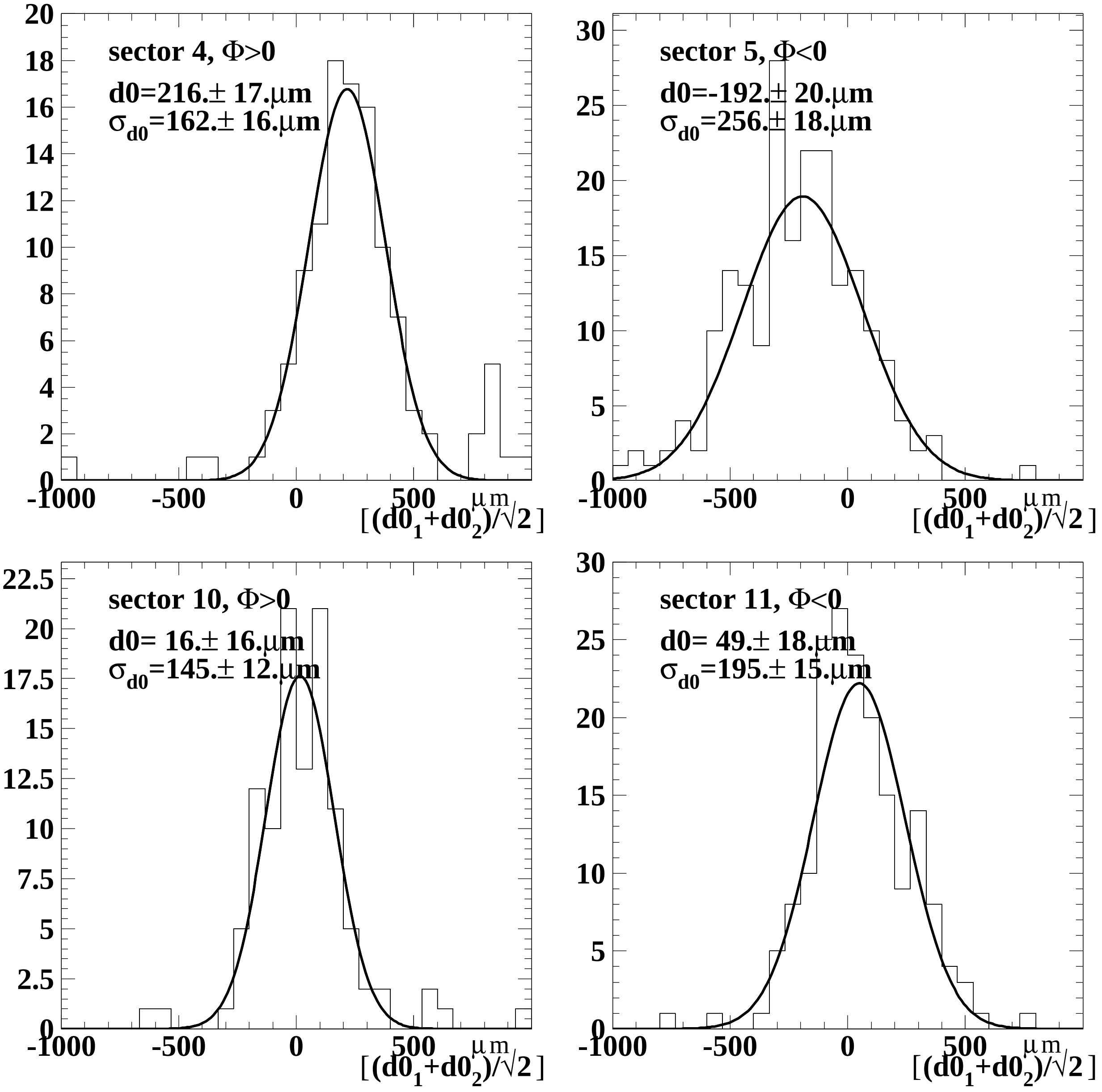

Figure 5.13: Impact parameter resolution in the $r-\phi$ plane before the correction was applied. In electron and muon pair events at $\sqrt{s} \simeq m_{\mathrm{Z}}$, the impact parameter d_0^i of both tracks was determined. If the impact parameter resolution was the same for both tracks, the sum should follow a Gaussian distribution with its mean at zero, which was the case if the electrons and muons traversed unaffected sectors (lower plots). The shift, seen in the upper plots, indicates that the resolution was significantly worse for tracks passing the adjacent sectors of cathode 5.

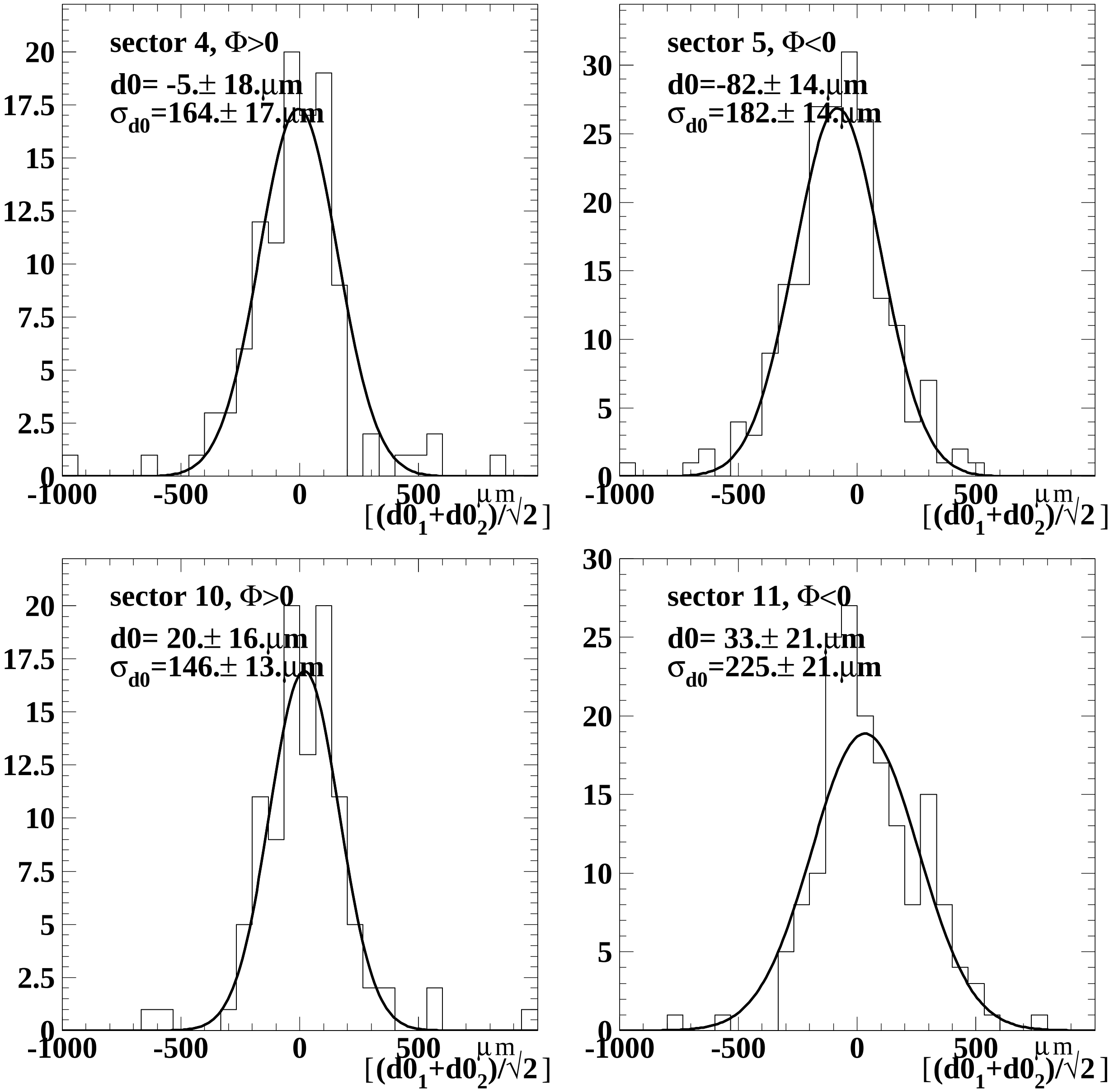

Figure 5.14: Impact parameter resolution in the $r - \phi$ plane after the correction was applied. The systematic shift of $(d0_1 + d0_2)/\sqrt{2}$ present in Figure 5.13 was reduced significantly and a resolution comparable to the resolution inside the unaffected sectors was found within the statistical errors.

been without success. The momentum resolution of electron and muon pairs could be improved by using higher order correction polynomials or by adjusting the individual coefficients of the correction polynomials, however, the K^0_S mass resolution was reduced at the same time.

The final corrections have been implemented into the OPAL reconstruction code and were used to reprocess 1999 data. From then on, hits from all wires were used in the track fit again. The data of 2000 was processed applying the same corrections.

Chapter 6

The OPAL Data Set and Event Simulations

The analysis presented in Chapter 7 uses multi-hadronic events taken in 1999 and 2000. The data set comprises different centre-of-mass energies in the range from 192 GeV to 209 GeV. The selection procedure is detailed in Section 7.1. Since the centre-of-mass energy directly influences the sensitivity of the analysis with respect to the Higgs boson mass, it is necessary to have a precise knowledge of the integrated luminosity as a function of the centre-of-mass energy. A brief description of the luminosity measurement follows in Section 6.1.

After the full selection, a huge amount of SM background remains. These remnants have to be known with a precision possibly better than the expected statistical error. The background level is determined by sophisticated simulations, of which an overview is given in Section 6.2.

6.1 Luminosity

The luminosity was measured using the silicon tungsten calorimeter (see Section 4.4). In rare cases this calorimeter was not functional and the forward calorimeters were used instead. Events with symmetric energy deposition in the forward and backward direction were selected. They were mainly due to Bhabha scattering. Since QED predicts accurately the cross-section of this process, the measured event rate could be used to determine the luminosity. At OPAL a relative accuracy of 10^{-3} was achieved. The method is detailed in [68].

The cross-sections of SM background processes and Higgs-strahlung as well as the distributions of the observables depend on the centre-of-mass energy. The centre-of-mass energy is derived from the bending radius of the electron and positron beams and the strength of the magnetic field in specific bending magnets [69]. The magnetic field strength is measured with NMR probes. In order to measure the bending radius, there are four beam position monitors at each of these magnets, which pick up an induction current. An accuracy of $< 3 \cdot 10^{-2}$ GeV is reached.

In 1999 the accelerator was operated at 4 different centre-of-mass energies 192, 196, 200 and 202 GeV. Generally, the centre-of-mass energy varied during one fill by up to 0.2 GeV, due to occasional cavity trips. In 2000 the operation mode was changed in order to reach highest possible centre-of-mass energies with reasonable luminosity [70]. First the beams were accelerated to 200 GeV. At this energy the margin of the RF power was large enough to handle occasional cavity trips. Having stable beams the experiments started data taking. After the

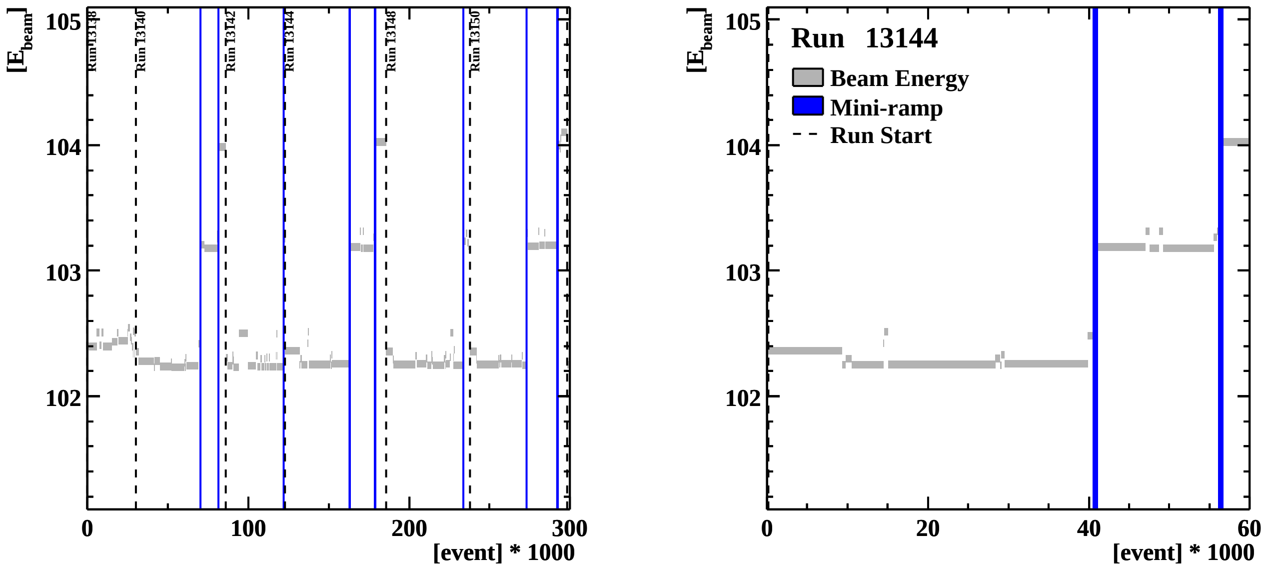

Figure 6.1: The beam energy during subsequent fills of year 2000. In year 2000, *miniramps* were introduced to reach highest possible centre-of-mass energies. After the currents decreased to a level permitting higher beam energies, the beam energy was ramped up in steps of several 100 MeV. Additional variation is caused by occasional cavity trips, which alter the beam energy by up to 200 MeV.

beam currents decreased to values permitting a further increase of centre-of-mass energy, the beams were ramped up in small steps of 0.2 GeV (*miniramps*), finally arriving at zero RF margin. In this operation mode the highest energy reached was 209 GeV. An example of the evolution of the beam energy during subsequent fills is shown in Figure 6.1.

In order to take these effects into account, Bhabha events are counted until the centre-of-mass energy changes by more than 30 MeV, which corresponds to the resolution of the energy measurement. Then the integrated luminosity $\mathcal{L}_i$ of this interval i is calculated: $\mathcal{L}_i = n_i/(\sigma(<E>_i) \times \epsilon)$, where n_i is the number of Bhabha events, ϵ is the acceptance of the silicon tungsten or forward calorimeters, and $\sigma(<E>_i)$ the cross-section at the average centre-of-mass energy $<E>_i$ in the time interval i. The luminosity versus the centre-of-mass energy collected during these two years is displayed in Figure 6.2. The data sets are limited to events in which the following detector components, where fully functional: the central jet chamber, the vertex chamber, the barrel and endcap electromagnetic calorimeters, the hadron calorimeter including the poletip calorimeter, the silicon tungsten calorimeter (or the forward detector) and the silicon micro vertex detector. The silicon micro vertex detector is not essential for this analysis, however, the same data set also is used for the four-jet analysis of the SM Higgs boson search [71], which relies on detection of secondary vertices. The additional data set, without a fully functional micro vertex detector, is negligible.

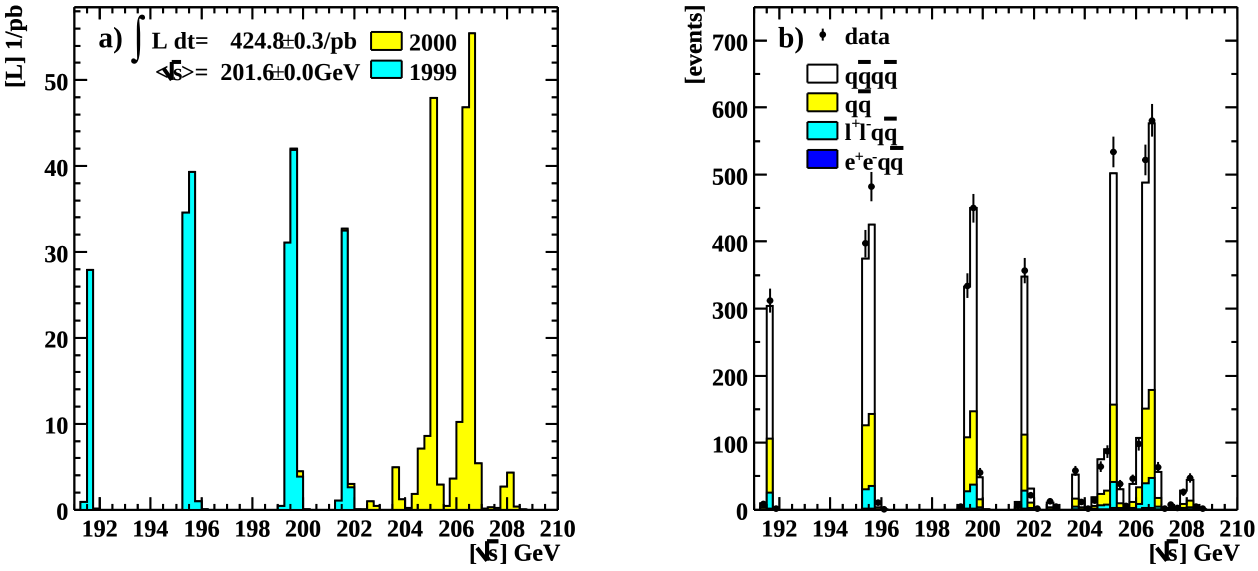

Figure 6.2: Luminosity per centre-of-mass energy in 1999 and 2000. Figure a) shows the luminosity collected in 1999 and 2000. In 1999 the nominal centre-of-mass energies were 192, 196, 200 and 202 GeV. In 2000 the energy was ramped up in steps of several hundred MeV during a fill to reach highest possible energies. In Figure b) the measured luminosity was used to calculate the expected amount of SM background after the first to fourth steps of the selection described in Section 7.1.1.

6.2 Event Simulation

At the achieved centre-of-mass energies $\sqrt{\mathrm{s}} \lesssim 209\,\mathrm{GeV}$, there are three main classes of SM final states which result in a four-jet topology: two fermion processes $\mathrm{e}^+\mathrm{e}^- \to (\mathrm{Z}^0/\gamma)^* \to \mathrm{q}\overline{\mathrm{q}}(g\ldots)$, four fermion processes $\mathrm{e}^+\mathrm{e}^- \to \mathrm{q}\overline{\mathrm{q}}\mathrm{q}\overline{\mathrm{q}}$, $\mathrm{q}\overline{\mathrm{q}}\ell^+\ell^-$ and two photon events $\mathrm{e}^+\mathrm{e}^- \to \gamma\gamma \to \mathrm{e}^+\mathrm{e}^-\mathrm{q}\overline{\mathrm{q}}(\mathrm{q}\overline{\mathrm{q}}, g\ldots)$. The cross-sections of important processes are shown in Figures 6.3a to c. Especially four fermion processes with four quark final states are a severe background for this analysis. The dominant contribution to these events are those in which W or Z boson pairs are produced. Z pair events represent a hardly reducible background, but this background is of minor importance due to the low rate compared to W pair production. Two photon processes and four fermion process with at least two final state leptons are rejected efficiently and can be neglected at the final selection stage.

The event simulation proceeds in several steps. First events with two or four final state particles are generated according to the prediction of matrix element calculations of finite order. The calculations include initial and final state radiation of photons. Two fermion processes are generated with KK2F [72] and four fermion processes with grc4f [73]. Signal events are generated with HZHA [24]. This perturbative approach is accurate for the description of leptonic final states but becomes invalid in the case of final state quarks. Therefore, phenomenological models are used to further propagate final state quarks and to produce additional quark pairs and triplets (fragmentation). Finally, mesons and baryons are formed (hadronisation). The alternative models, HERWIG [74] and JETSET/PYTHIA [75]. Both models were tuned to yield a proper agreement with the data taken at $\sqrt{\mathrm{s}} = m_{\mathrm{Z}}$ [76]. The decay of unstable hadrons is

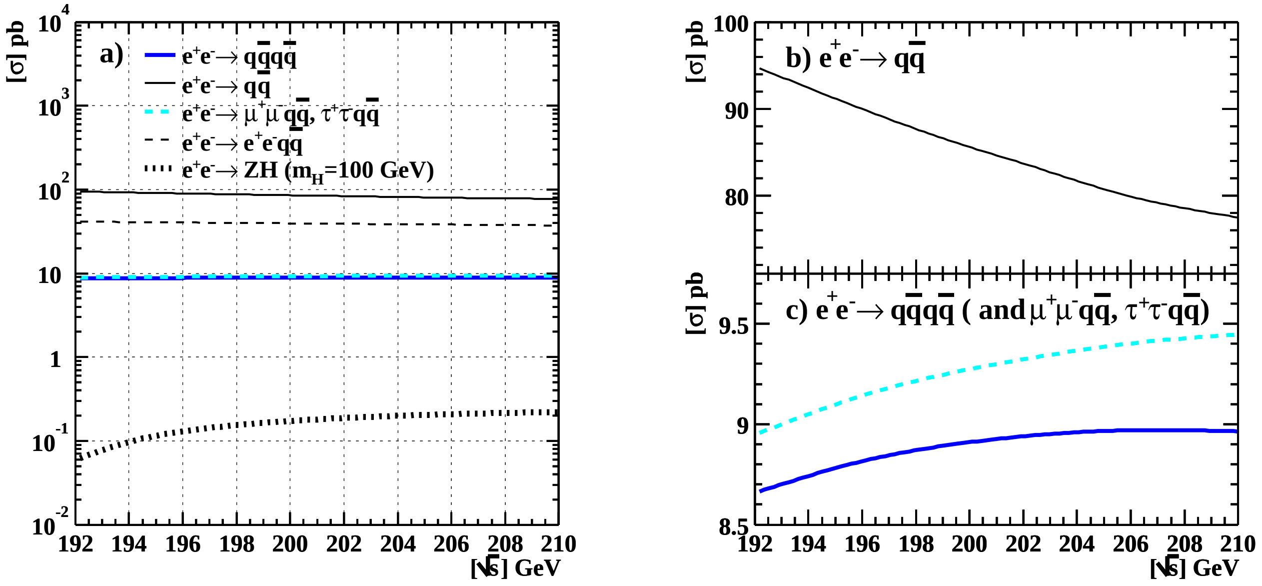

Figure 6.3: a) Cross-sections of dominant background processes in comparison to the cross-section of a SM Higgs boson with a mass $m_{\mathrm{H}} = 100\,\mathrm{GeV}$. The cross-section of signal events $\mathrm{e}^+\mathrm{e}^- \to \mathrm{Z}^0\mathrm{H}^0$ is 2 orders of magnitude smaller than four fermion processes, which yield similar topologies. Figures b) and c) show a small range around the cross-sections of two and four fermion background.

simulated with the help of decay tables which are based on measurements compiled in [28]. The decays are performed by PYTHIA. In the final step, all sufficiently stable particles are fed into a full detector simulation, of which a detailed description is given in [77]. The detector simulation is based on GEANT3 and accurately simulates the effect of active and inactive material on the particles and the response of active elements. The resolution of the simulation is calibrated using well known processes like Bhabha scattering or muon pairs, $\mathrm{e}^+\mathrm{e}^- \to Z^0/\gamma \to \mu^+\mu^-$.

Simulations of two and four fermion processes were performed at several centre-of-mass energies in the range from 192 GeV to 210 GeV. A detailed list of used samples can be found in Tables A.2 and A.4 in the appendix. In Figure 6.2b the expected event rates at the different centre-of-mass energies are compared to the data. These rates are obtained after the fourth step of the preselection as described in Section 7.1.1.

Chapter 7

Search for Hadronically Decaying Higgs Bosons

An analysis is presented searching for Higgs bosons in $\mathrm{e^+e^-}$ collision data. In these events, neutral Higgs bosons are dominantly produced in Higgs-strahlung, $\mathrm{e^+e^-} \rightarrow \mathrm{Z^0h^0}$. Other production processes like W-fusion are small at the centre-of-mass energies achieved at LEP and are not considered. The Higgs boson is assumed to decay into pairs of quarks or gluons, $\mathrm{h^0} \rightarrow \mathrm{q\overline{q}}$ or $\mathrm{h^0} \rightarrow gg$, which are the favoured decay modes in most models for accessible Higgs boson masses ($m_\mathrm{h} \ll 2m_\mathrm{W}$). However, no assumptions are made about the flavour of the decay products. In particular, identification of bottom-flavoured jets is not pursued. Dedicated analyses have been developed for each of the four possible Z decay modes: the four-jet channel, $\mathrm{Z^0} \rightarrow \mathrm{q\overline{q}}$, the missing energy channel, $\mathrm{Z^0} \rightarrow \nu\overline{\nu}$, the electron and muon channels, $\mathrm{Z^0} \rightarrow \mathrm{e^+e^-}$ or $\mathrm{Z^0} \rightarrow \mu^+\mu^-$, and the tau channel, $\mathrm{Z^0} \rightarrow \tau^+\tau^-$. The search strategies are similar to searches for the SM Higgs boson as described in [78], however, the “b-tag” is omitted. In the four-jet channel in particular, a huge amount of background due to W-pair production remains if the b-tag requirement is dropped. In order to regain sensitivity, the analysis is performed under explicit hypotheses for the Higgs boson mass. This permits full exploitation if the kinematic signature of Higgs-strahlung.

This chapter focusses on the four-jet channel. The selection is based on [4], but has been reoptimised for higher centre-of-mass energies. It is fully described in the subsequent section. In order to treat the broad distribution of centre-of-mass energies interpolation techniques became necessary to generate the needed reference distributions from the available set of simulated events. The interpolation techniques are detailed in Section 7.2. In Section 7.3 the four-jet channel is considered under specific assumptions about the Higgs boson decay. Finally, systematic errors are discussed in Section 7.4.

7.1 Event Selection

The selection consists of two parts. First, a preselection is performed to select four-jet events and reduce explicitly dominant background sources, which are four and two fermion processes. The second part is performed under mass hypotheses for the Higgs boson.

All selection cuts were optimised to maximise the ratio between the signal selection efficiency and the statistical error of the background rate as a figure of merit, assuming the systematic uncertainties are small compared to the statistical error. This figure of merit is best approximated by [79]:

$$\text{f.o.m.} := \frac{\epsilon}{\sqrt{\mathrm{B}+2}}, \tag{7.1}$$

where ϵ is the signal selection efficiency and B the number of selected background events.

7.1.1 Preselection

Events with four-jet topology are selected following [80]:

1. Events must have been classified as multi-hadronic event [81]. At least 7 clusters in the electromagnetic calorimeter and 5 tracks in the central tracking chamber are required. Clusters in the barrel region must contain more than one block with a measured energy deposition of $\mathrm{E}^i_{\mathrm{raw}} > 0.1\,\mathrm{GeV}$, respectively, end-cap clusters must contain at least two blocks with $\mathrm{E}^i_{\mathrm{raw}} > 0.2\,\mathrm{GeV}$. At least 14% of the total centre-of-mass energy must be deposited in such clusters.

   Tracks are considered if:

   - They are built by more than 20 hits and the first hit starts at a radius $r_{\mathrm{first}} < 60\,\mathrm{cm}$, close to the innermost wire of the jet chamber ($r_0 = 55\,\mathrm{cm}$).
   - The χ^2 of the track fit in the $r-\phi$ -plane, the plane perpendicular to the beam axis, and in the $s-z$ -plane, i.e. the plane spanned by the path length and the beam-axis, is smaller than 999.
   - The measured transverse momentum ($\mathrm{p}_{r\phi}$) is larger than 0.05 GeV.
   - The impact parameter does not exceed 2 cm in the $r-\phi$ -plane ($|d_0|$), and 50 cm in the $s-z$ -plane ($|z_0|$).
   - The track is well contained in the detector $|\cos\theta| < 0.995$.

   Beam-gas interaction is not restricted to the IP. Therefore, the energy is not evenly spread in the forward and backward direction. This background can be reduced by the requirement: $\sum_i \mathrm{E}^i_{\mathrm{raw}} \cdot \cos\theta^i / \sum_i \mathrm{E}^i_{\mathrm{raw}} < 0.75$.

2. A large fraction of multi-hadronic events are from the process $\mathrm{e}^+\mathrm{e}^- \rightarrow \gamma/\mathrm{Z} \rightarrow \mathrm{q}\bar{\mathrm{q}}$. They are often accompanied by photons from initial state radiation (ISR photons) reducing the effective centre-of-mass energy to $\sqrt{\mathrm{s}'} \simeq m_{\mathrm{Z}}$. They can be strongly suppressed by the requirement $\sqrt{\mathrm{s}'/\mathrm{s}} > 0.794$, where $\sqrt{\mathrm{s}'}$ denotes the centre-of-mass energy of the hadronic system after subtracting the energy of ISR photons. The energy of ISR photons is determined as described in [82]. First isolated photons are searched for explicitly in the detector. If no such photons are found a kinematic fit is performed with one or two hypothetical photons in the direction of the beam axis. In case this fit does not converge, the event is forced into two jets and $\sqrt{\mathrm{s}'}$ is calculated from the acoplanarity angle.

3. The reconstructed tracks and clusters in the electromagnetic and hadronic calorimeter are used to build *energy flow objects* [71]. Clusters can result from more than one charged or neutral particle. In order to reduce double counting of energy, the energy measured from tracks is subtracted from clusters to which the tracks are pointing. Clusters whose

remaining energy is larger than zero are considered to originate from a neutral particle. Most tracks originate from pions and most clusters from photons. Consequently, tracks are assigned the pion mass and clusters zero mass.

The energy flow objects are grouped into four jets with the Durham jet finding algorithm [83]. The transition point when the event is more three-jet than four-jet like is quantified by the jet resolution parameter y_{43}, which has to fulfil $y_{43} > 0.003$.

Often low energetic particles are assigned to wrong jets. This compromises the invariant mass resolution slightly. Therefore, jet finding is performed initially only for particles with $E > 1.2\,\text{GeV}$. After that particles are reassigned to the four jets using the Jade E0 scheme [84]. The most energetic particle of each of the previously constructed jets is used as a seed to build up the new jet. Then all particles ν are assigned to the jet i to whose leading particle it has the smallest distance $d_{i\nu}$. In the Jade scheme, this distance is defined by:

$$d_{i\nu} := (2\,E_{\text{part}\,\text{max}\,i}\,E_{\text{part}\,\nu}(1-\cos(P_{\text{part}\,\text{max}\,\text{i}},\,p_{\text{part}\,\nu})),$$

where $P_{\text{part}\,\text{max}\,\text{i}}$, $p_{\text{part}\,\nu}$, $E_{\text{part}\,\text{max}\,i}$ and $E_{\text{part}\,\nu}$ denote the momenta (three-momenta) and energies of the leading particle of the i-th jet and the ν-th particle, respectively. This procedure yields smaller misassignment rates than the Durham algorithm. An improvement of the mass resolution of up to 15% can be achieved [85]. For a complete discussion see [86].

4. At LEP2 energies, hadronic jets are composed of 9 charged particle tracks in average. In order to reject events with isolated leptons ($e^+e^- \rightarrow q\bar{q}\ell^+\ell^-$), all four jets must have at least two charged particle tracks.

Two photon background is completely negligible after the cut on $\sqrt{s'/s}$ and y_{43}. The number of mistagged $e^+e^- \rightarrow q\bar{q}\ell^+\ell^-$ events is small compared to the expected number of signal events. The dominant backgrounds are hadronic two and four fermion events. The major contribution to the four fermion background is due to W and Z pair production. These backgrounds are vetoed explicitly:

5. The QCD matrix element ME_{420} [87], permits a good separation of two fermion background. The matrix element ME_{420} comprises the QCD processes $e^+e^- \rightarrow q\bar{q}gg$ and $e^+e^- \rightarrow q\bar{q}q\bar{q}$. The jet momenta are used to approximate the momenta of the final state quarks. The quantity ME_{420} reflects the average of all possible combinations. Events are selected in case $-3 < \log_{10}\text{ME}_{420} < -1$ (compare with Figure 7.2a).

6. Similarly, four fermion background can be reduced by the requirement $-8.5 < \log_{10}\text{ME}_{4\text{f}} < -4.9$ (see Figures 7.2b and d). The four fermion matrix element $\text{ME}_{4\text{f}}$ describes the electroweak processes: $e^+e^- \rightarrow q\bar{q}q\bar{q}$. The matrix element is calculated after a kinematic fit imposing energy and momentum conservation. More detail about kinematic fits is given in Section 7.1.2 and in the Appendix A.1. Badly measured events are rejected requiring the probability of the kinematic fit, P(4C), to be larger than 10^{-6}. The fit improved jet momenta are used to approximate the momenta of the final state quarks. The average matrix element is calculated using EXCALIBUR [88], where all possible assignments of the jets to up- and down-type quarks are considered.

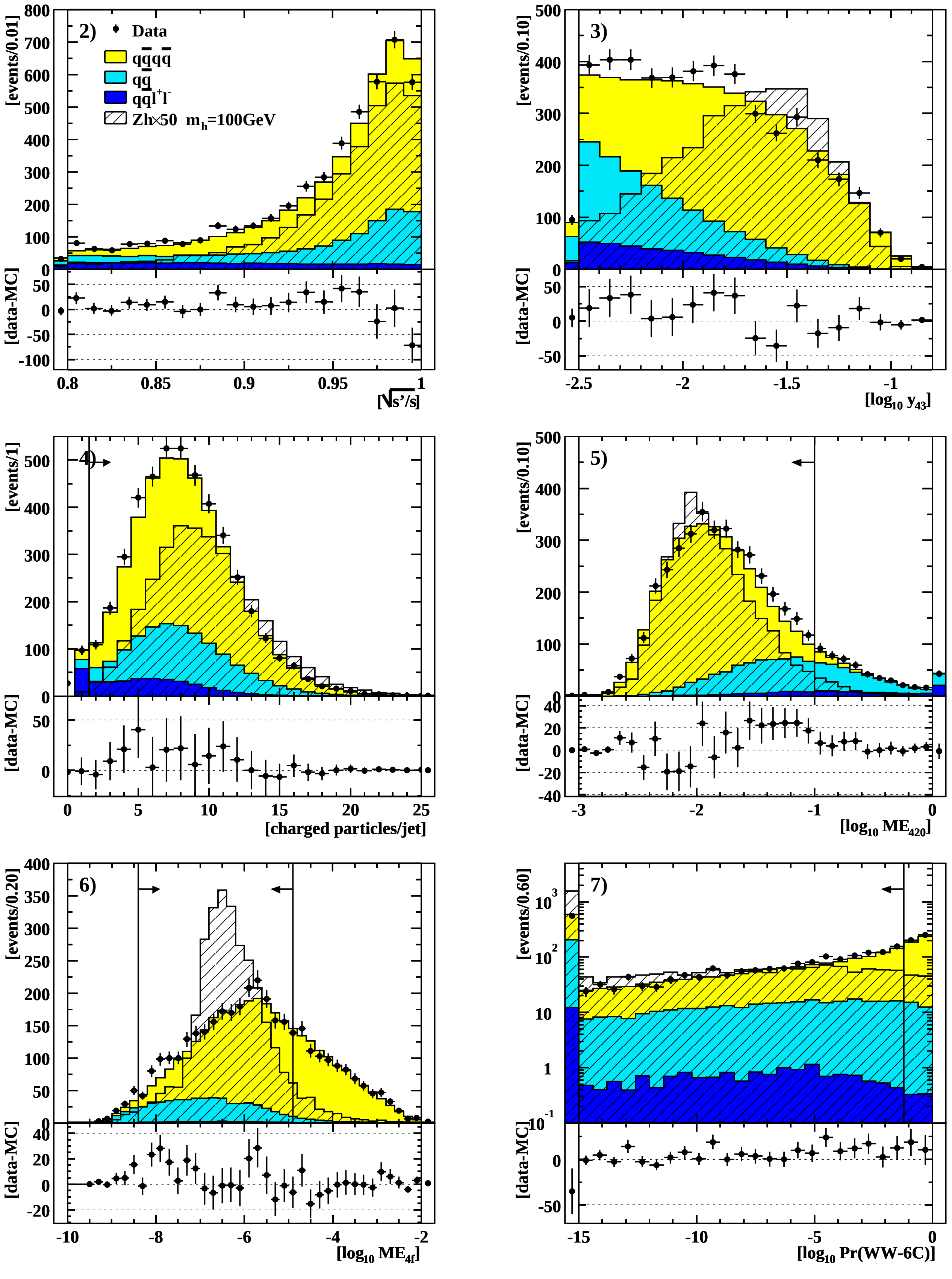

Figure 7.1: Variables used in the preselection. Shown are the number of selected events in 1999 and 2000 compared to simulation results of dominant background processes (MC): $e^+e^- \rightarrow q\bar{q}q\bar{q}$, $e^+e^- \rightarrow q\bar{q}$ and $e^+e^- \rightarrow q\bar{q}\ell^+\ell^-$. The overlaid distributions resulting from SM Higgs-strahlung are scaled by 50. The assumed mass of the Higgs boson was $m_{\mathrm{H}} = 100\,\mathrm{GeV}$. The events outside the region indicated by the vertical line and the arrow are rejected.

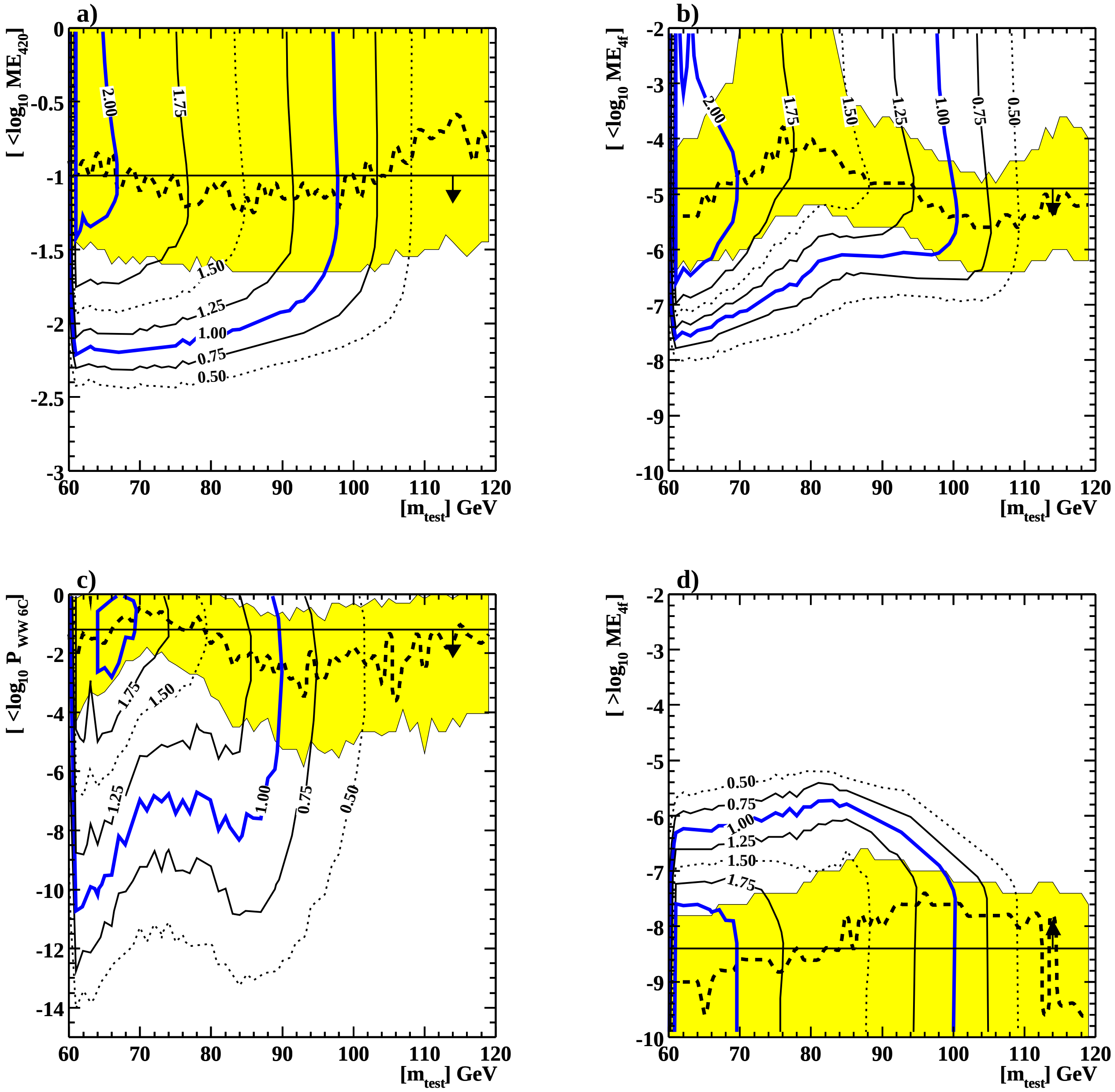

Figure 7.2: Lines of equal figure of merit depending on the test mass and the chosen upper (<) or lower (>) cut. In Figures a, b and c the upper cut was adjusted keeping the lower cut fixed at the same time. In Figure d the lower cut was adjusted. For each test mass and chosen cut, the figure of merit was calculated according to formula (7.1), where the sensitivity increases with the figure of merit. The cut position which maximises the figure of merit at each test mass is indicated by the dashed line. The shaded area indicates the area in which the figure of merit changes by less than ±5%. The horizontal line shows the position of the chosen cut.

	$\mathrm{q\bar{q}q\bar{q}}$	$\mathrm{q\bar{q}}$	MC total	data	ϵ_{ZH} ($m_{\mathrm{H}} = 100\,\mathrm{GeV}$)	
1.	1904.4	16332.3	20840.9	20848	1.00	LEP2 multi hadron
2.	1789.6	4662.3	7216.5	7254	1.00	$\sqrt{\mathrm{s'/s}} > 0.794$
3.	1561.5	581.0	2335.5	2431	0.95	$y_{43} \geq 0.003$
4.	1512.9	500.8	2093.7	2182	0.95	$N_{ctk} \geq 2$
5.	1481.2	311.2	1823.0	1908	0.90	$-3.0 < \ln(\mathrm{ME}_{420}) < -1.0$
	1450.2	299.5	1766.3	1865	0.89	$\mathrm{P(4C)} > 10^{-6}$
6.	950.0	260.0	1224.9	1315	0.81	$-8.5 < \ln(\mathrm{ME}_{4\mathrm{f}}) < -4.9$
7.	746.8	244.5	1005.7	1071	0.78	$\log_{10} P(\text{WW-6C-fit}) < -1.2$
	225.6	69.7	298.5	291	0.65	$P(\text{ZH-fit}) > 10^{-6}$
	134.2	42.7	178.7	176	0.52	Likelihood > 0.1

Table 7.1: Number of expected background events and events observed in the data of year 1999, passing successive cuts. The signal efficiency ϵ_{ZH} is given for a SM-Higgs boson with a mass of $m_{\mathrm{H}} = 100\,\mathrm{GeV}$. After cut 7., the selection is mass dependent (see Section r7.1.2). The listed values are for a mass hypothesis of $m_{\mathrm{test}} = 100\,\mathrm{GeV}$. In addition to hadronic four fermion background ($\mathrm{q\bar{q}q\bar{q}}$) and two fermion ($\mathrm{q\bar{q}}$) background, the total number of expected background events (MC total) also contains semi-leptonic events, $\mathrm{e^+e^-} \rightarrow \mathrm{q\bar{q}}\ell^-\ell^+$ including $\mathrm{e^+e^-} \rightarrow \mathrm{q\bar{q}e^-e^+}$.

7. W-pair background can be reduced further by rejecting events with large probabilities of a 6C-kinematic fit. The measured jet momenta are varied according to their measurement error with the additional constraints of momentum and energy conservation and the invariant masses of two jet pairs to be equal to the W-mass[1] $m_{\mathrm{W}} = 80.3\,\mathrm{GeV}$. The fit is performed for all possible jet pairings and the probability for each combination must satisfy: $\log_{10} \mathrm{P}_{\mathrm{WW}6C-\mathrm{fit}} < -1.2$ (compare with Figure 7.2c).

The numbers of selected events after consecutive cuts are shown in Tables 7.1 and 7.2 for the data set of year 1999 and 2000, respectively, in comparison to the simulation results. The corresponding distributions are displayed in Figures 7.1 2) to 7). The shown data sets fulfil the first to third selection criteria and the criteria on the preceding variables. The figure of merit as function of the cut values is shown in figure 7.2a to d for a few examples.

The simulations are performed at several centre-of-mass energies and are linearly interpolated according to the centre-of-mass energies of the data sets. Depending on the Higgs boson mass and decay modes, $60-80\%$ of the signal events pass the preselection. Assuming the luminosity and centre-of-mass energies of year 2000, this corresponds to 56.2 events of SM-Higgs-strahlung with Higgs boson mass of $m_H = 100\,\mathrm{GeV}$. This has to be compared to background prediction composed of 1470 four fermion and 477 two fermion events adding up to 1975 including background due to mistagged $\mathrm{e^+e^-} \rightarrow \mathrm{q\bar{q}}\ell^+\ell^-$ events. Of the recorded data, 2081 events remain, which is compatible with both the background only and background plus signal hypotheses, assuming the couplings of a SM Higgs boson.

---

[1] No significant changes were observed when using a more recent measurement of m_{W}.

	$\mathrm{q\bar{q}q\bar{q}}$	$\mathrm{q\bar{q}}$	MC total	data	ϵ_{ZH} ($m_{\mathrm{H}} = 100\,\mathrm{GeV}$)	
1.	1848.5	13816.1	17990.2	18242	1.00	LEP2 multi hadron
2.	1733.6	3981.7	6440.5	6441	1.00	$\sqrt{\mathrm{s'/s}} > 0.794$
3.	1493.8	497.5	2168.3	2227	0.95	$y_{43} \geq 0.003$
4.	1443.8	431.9	1944.7	2018	0.94	$N_{ctk} \geq 2$
5.	1419.1	292.0	1738.3	1787	0.92	$-3.0 < \ln(\mathrm{ME}_{420}) < -1.0$
	1384.2	281.7	1680.9	1729	0.90	$\mathrm{P(4C)} > 10^{-6}$
6.	916.8	244.2	1174.7	1220	0.85	$-8.5 < \ln(\mathrm{ME}_{4\mathrm{f}}) < -4.9$
7.	723.4	232.7	969.6	1010	0.82	$\log_{10} P(\text{WW-6C-fit}) < -1.2$
	249.1	86.1	338.9	368	0.66	$P(\text{ZH-fit}) > 10^{-6}$
	171.6	61.1	235.3	263	0.55	Likelihood > 0.1

Table 7.2: Number of expected background events and events observed in the data of year 2000, passing successive cuts. The signal efficiency ϵ_{ZH} is given for a SM-Higgs boson with a mass of $m_{\mathrm{H}} = 100\,\mathrm{GeV}$. After cut 7., the selection is mass dependent (see Section r7.1.2). The listed values are for a mass hypothesis of $m_{\mathrm{test}} = 100\,\mathrm{GeV}$. In addition to hadronic four fermion background ($\mathrm{q\bar{q}q\bar{q}}$) and two fermion ($\mathrm{q\bar{q}}$) background, the total number of expected background events (MC total) also contains semi-leptonic events, $\mathrm{e^+e^-} \rightarrow \mathrm{q\bar{q}}\ell^-\ell^+$ including $\mathrm{e^+e^-} \rightarrow \mathrm{q\bar{q}e^-e^+}$.

7.1.2 Selection with Mass Hypothesis

The background is reduced further by taking advantage of the kinematic signature of Higgs-strahlung. In order to fully exploit the kinematics, the analysis is performed under a *hypothesis* for the Higgs boson mass. This allows to make use of the invariant masses of both jet pairs, those from the Z and from the Higgs boson decays. Due to the different spins of the involved bosons, the angular distributions of the jets are different in Higgs-strahlung events and background processes. For example, in W pair production, jets are emitted more frequently in the direction of the electron or positron beam in contrast to the more isotropic distribution in Higgs-strahlung events.

Mass Constrained Kinematic Fit (ZH-Fit)

The jet momentum resolution is greatly improved by constrained kinematic fits. The technique is explained in the Appendix A.1. Detailed studies are documented in [89]. A short summary follows. When performing the kinematic fit, the jet momenta are adjusted within their measurement errors under the constraints:

- energy and momentum are conserved: $\sum_{\mathrm{jet}} E_{\mathrm{jet}} - \sqrt{\mathrm{s}} = 0$ and $\sum_{\mathrm{jet}} p_{i,\,\mathrm{jet}} = 0$, where E_{jet} and p_{jet}denote the measured jet energy and momentum.

- the invariant mass of the jet pair assigned to the Higgs boson candidate equals the hypothetical Higgs boson mass m_{test}: $(E_{\mathrm{jet1}} + E_{\mathrm{jet2}})^2 - \|p_{\mathrm{jet1}} + p_{\mathrm{jet2}}\|^2 - {m_{\mathrm{test}}}^2 = 0$.

Due to the large width of the Z boson, efficiency is lost, if a constraint is enforced on the dijet mass assigned to the Z boson. Nevertheless, the invariant mass should be close to the nominal value m_{Z}. Thus the deviation of the invariant mass from the nominal value is a measure of the fit quality complementing $\chi^2 := (p-\tilde{p})^T\sigma^{-1}(p-\tilde{p})$ + constraints. The complete measure of goodness of the fit (ZH-fit) becomes:

$$\hat{\chi}^2 := (p-\tilde{p})^T\sigma^{-1}(p-\tilde{p}) + \left((\tilde{E}_{\mathrm{jet3}}+\tilde{E}_{\mathrm{jet4}})^2 - \|\tilde{p}_{\mathrm{jet3}}+\tilde{p}_{\mathrm{jet4}}\|^2 - m_{\mathrm{Z}}^2\right)/\hat{\Gamma}_{\mathrm{Z}} + \text{constraints}, \quad (7.2)$$

where p denotes the combined vector of the measured jet momenta (three-momenta), $\tilde{p}$ the fitted quantities, σ the covariance matrix of the jet momenta and $\hat{\Gamma}_{\mathrm{Z}}$ the assumed width of the Z boson. The jet energies $\tilde{E}$ are calculated from the jet momenta $\tilde{p}_{\mathrm{jet}}$ and the invariant masses m_{jet} of each single jet. The masses m_{jet} are not modified by the fit. The additional term reflects a Z boson mass distributed according to a Gaussian of width $\hat{\Gamma}_{\mathrm{Z}}$ which is approximately correct. The Z resonance is better described by a Breit-Wigner distribution which has much wider tails. However, these wide tails allow invariant masses far away from m_{Z} without increasing significantly a measure of goodness defined according to (7.2). Additionally, this measure of goodness would not follow a χ^2-distribution. It turned out that the Gaussian approximation (7.2) leads to a more useful selection criterion (See [89] for a thorough analysis). Moreover, the best performance is obtained if the width of the Gaussian $\hat{\Gamma}_{\mathrm{Z}}$ is broadened such that the envelops of the Gaussian distribution G and the Breit-Wigner distribution B cross at Γ_{Z}: $G(\Gamma_{\mathrm{Z}}) = B(\Gamma_{\mathrm{Z}})$, where Γ_{Z} is the width the Z boson and of B.

If the kinematic limit is approached, $m_{\mathrm{h}} + m_{\mathrm{Z}} \simeq \sqrt{\mathrm{s}}$, the observed Z mass is pushed to lower values due to the limited phase space at higher Z boson masses. This effect is taken into account and the most probable value of the observed Z mass is used instead of the nominal value of the resonance.

If the fit has converged the criteria of convergence guarantee that the contributions of the constraints to (7.2) are negligible. Since the first two terms of (7.2) follow a χ^2-distribution, the probability to observe a value $\hat{\chi}^2$ or a larger value in Higgs-strahlung is given by:

$$\mathcal{P}(\hat{\chi}^2;\, N) := \frac{1}{\sqrt{2^N}\,\Gamma(N/2)}\int_{\hat{\chi}}^{\infty} dt\, e^{-t/2}\, t^{N/2-1}, \quad (7.3)$$

where $N = 16 - 5$ denotes the number of degrees of freedom.

A priori, the association of the jets to the Z and Higgs boson is not known. Therefore, the fit is performed for each of the 6 possible combinations and the combination which yields the largest probability (7.3) is chosen. Generally, the fit converges only for the two combinations in Higgs-strahlung events, which correctly pair the jets but do not necessarily correctly associate the pairs with the right bosons. The event fraction with correct and incorrectly assigned jets is depicted in Figure 7.3 as a function of the Higgs boson mass. For comparison, the results from a kinematic fit with 6 constraints are also shown (6C). The 6C fit constrains both invariant masses to their nominal value. The 6C fit has a slightly lower chance to correctly assign the jets than the ZH fit.

The figure of merit (7.1) is significantly enhanced by the requirement that at least one combination has a fit probability $\mathrm{P}_{\mathrm{ZH-fit}} > 10^{-6}$ (see Figure 7.5a). It is further improved by a likelihood selection described in the following.

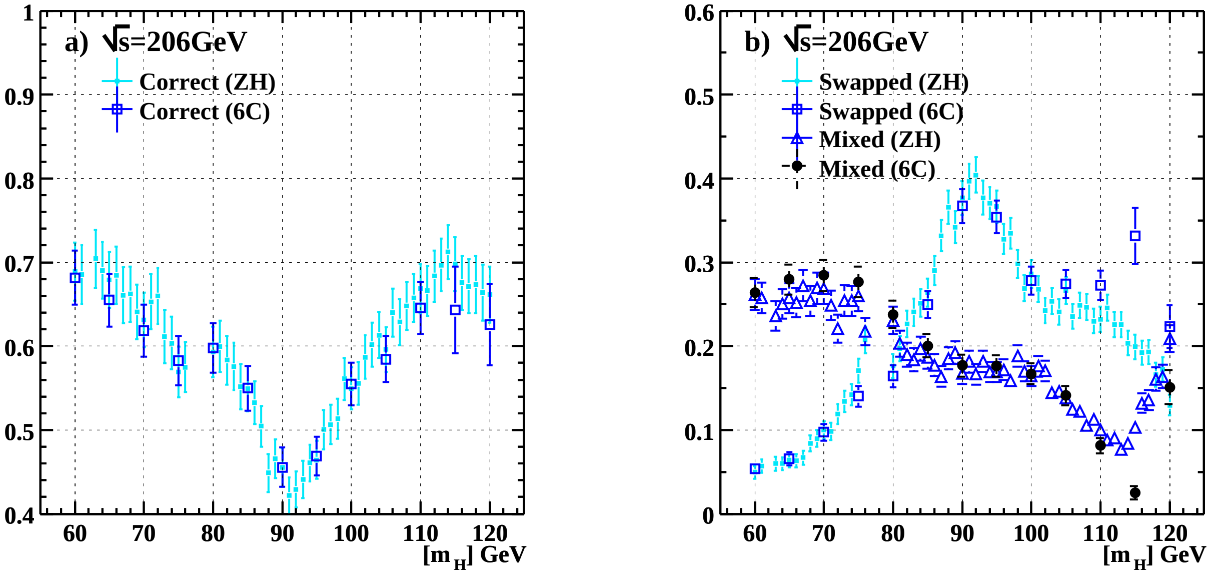

Figure 7.3: Correctness of the jet assignment to the Higgs and Z bosons. In Figure a), the event fraction is shown in which the jets are correctly assigned to the two bosons. The points labelled ZH refer to the fit described in Section 7.1.2 with the Higgs boson mass constraint and whose χ^2 is defined by (7.2). The points labelled 6C refer to the kinematic fit which constrained the Higgs and Z boson masses to their nominal values. The performance worsens by approximately 3% if the kinematic fit with 6 constraints is used. In Figure b), the fraction of wrong combinations is shown. The cases are distinguished in which the jets are correctly paired but assigned to the wrong bosons (swapped) and those in which the two jets resulting from the decay of one boson are assigned to different bosons (mixed).

Likelihood Selection

For every selected event, a likelihood for the signal hypothesis is calculated from observables x_i. The likelihood is defined in the following way:

$$\mathrm{LH}(x_i;\, m_{\mathrm{test}}) := \frac{\omega^{\mathrm{sig}}\Pi_i P_i^{\mathrm{sig}}(x_i;\, m_{\mathrm{test}})}{\omega^{\mathrm{sig}}\Pi_i P_i^{\mathrm{sig}}(x_i;\, m_{\mathrm{test}}) + \sum_j \omega^{\mathrm{bg}\cdot j}\Pi_i P_i^{\mathrm{bg}_j}(x_i;\, m_{\mathrm{test}})}. \tag{7.4}$$

Here, P_i^{sig} and P_i^{bg} denote the probability density functions (p.d.f.) of variable i for signal and background, respectively. The different contributions of the signal and background p.d.f.s to the likelihood are weighted by ω^{sig} and ω^{bg_j}. Four fermion and two fermion backgrounds are considered separately. Best separation of signal and background is achieved by choosing equal weights for signal and the total background: $\omega^{\mathrm{sig}} \equiv \sum_j \omega^{\mathrm{bg}_j}$ and by weighting the p.d.f.s of different background sources according to their effective cross-section: $\omega^{\mathrm{bg}_j} := \epsilon^{\mathrm{bg}_j}\sigma^{\mathrm{bg}_j}$, with the selection efficiency ϵ^{bg_j} and the cross-section σ^{bg_j} of background j.

The variables used in the likelihood are restricted to regions which maximise the figure of merit. The optimal criteria are weak and remove only the very tails of the distributions. No efficiency is lost and the figure-of-merit does not improve significantly. The main purpose is to assure that the input variables have reasonable values. The variables are:

1. $\log_{10} P_{\mathrm{ZH}}^{\max}$, the fit probability of the kinematic fit with Z and Higgs boson mass constraints,

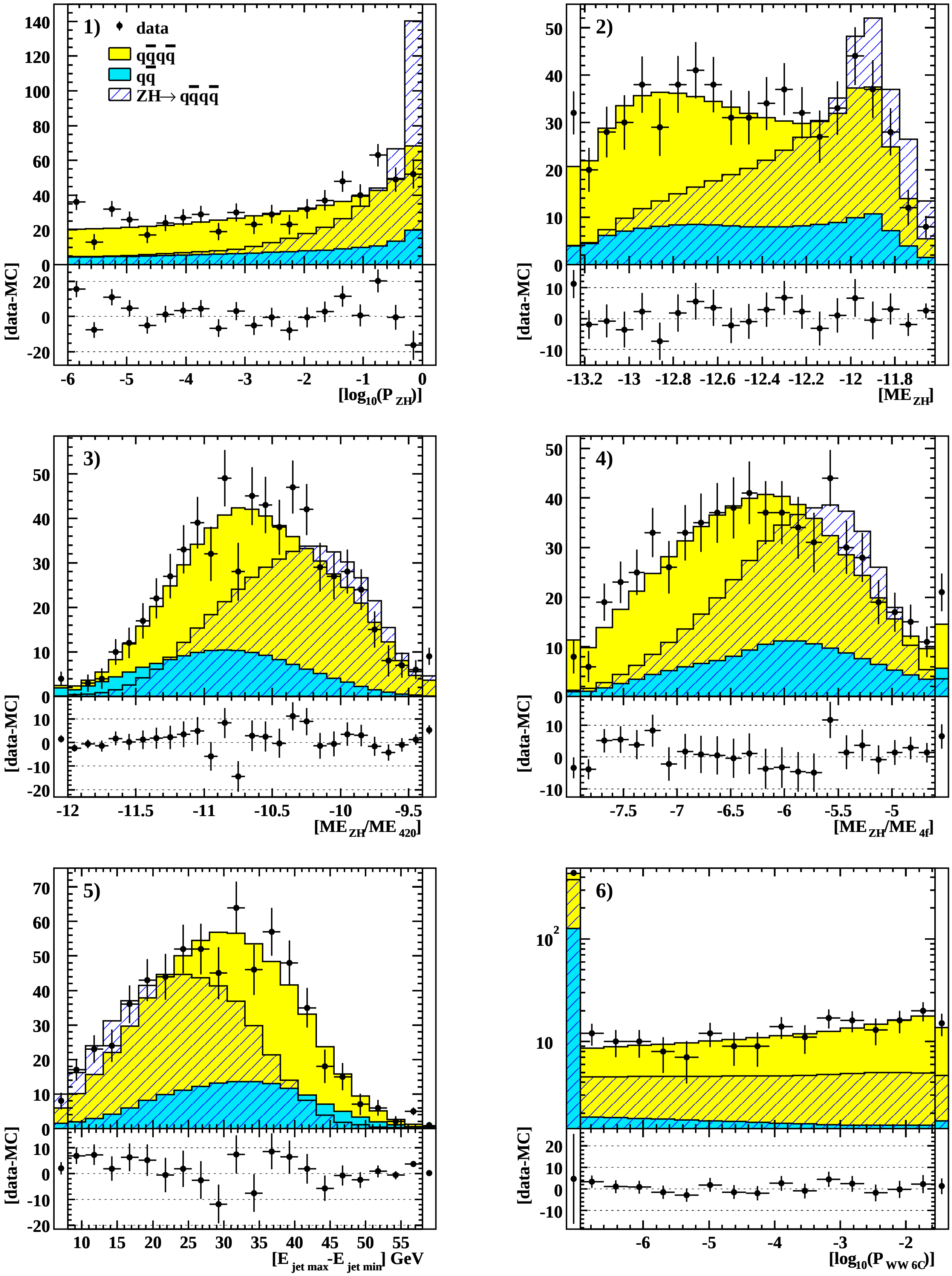

Figure 7.4: Input variables of the likelihood selection. Shown are the distributions of the input variables resulting from the whole considered data set of year 2000 and 1999 compared to the probability density scaled to the expected rate (MC). The signal distribution is scaled by a factor of 10. The probability density functions are obtained from simulation. Here the mass hypothesis is $m_{\text{test}} = 100\,\text{GeV}$.

as described at the beginning of this section. From the six possible jet pairings, the pairing which leads to the largest probability is used.

2. $\mathrm{ME_{ZH}}$, the event weight from the Higgs-strahlung matrix element [90]. The calculation is performed to first order plus initial state radiation $\mathcal{O}(\alpha)$. The parton momenta are approximated by the jet momenta resulting from the kinematic fit which achieved the highest fit probability. It is required: $-13.5 < \log_{10}\mathrm{ME_{ZH}} < -11.6$. The hypothetical Higgs boson mass is used in the calculation.

3. $\mathrm{ME_{ZH}}/\mathrm{ME_{QCD}}$, ratio of the Higgs-strahlung and QCD matrix elements (see preselection). This ratio has to fulfil $-13.0 < \log_{10}\mathrm{ME_{ZH}}/\mathrm{ME_{QCD}} < -8.54$.

4. $\mathrm{ME_{ZH}}/\mathrm{ME_{4f}}$, ratio of the Higgs-strahlung and four fermion matrix elements (see preselection). The value has to be within the range: $-8.5 < \log_{10}\mathrm{ME_{ZH}}/\mathrm{ME_{4f}} < -4.0$.

5. The energy difference between the most and least energetic jet. This variable is strongly mass dependent. Events must fulfil $5\,\mathrm{GeV} < \Delta\mathrm{E} < 60\,\mathrm{GeV}$.

6. $P_{\mathrm{WW6C-fit}}$, the probability of the W-pair kinematic 6C-fit. All three possible jet combinations are considered. The combination which yields the highest probability $P^{\mathrm{max}}_{\mathrm{WW6C-fit}}$ is used.

As an example, the distributions of the input variables are shown in Figure 7.4 for a mass hypothesis $m_{\mathrm{test}} = 100\,\mathrm{GeV}$. The data of 1999 and 2000 is compared to the distributions expected from dominant backgrounds and those expected from signal events. The signal distributions are scaled by a factor of 10 to improve the visibility. Simulations were performed at centre-of-mass energies from 192 to 200 GeV, and 202 GeV to 210 GeV in steps of 2 GeV and 4 GeV, respectively. Interpolation techniques are used to match the centre-of-mass energy composition of the data sets. The same interpolation techniques are used to generate 3D probability density functions which are used to calculate the likelihood. The 3D p.d.f.s are functions of the variable, the centre-of-mass energy and the test mass. Since the p.d.f.s are evaluated after the kinematic fit, and since the kinematic fit selects different events depending on the test mass, not only the signal but the background p.d.f.s also depend on the test mass. Thus, the 3D approximation is needed for both signal and background p.d.f.s. The interpolation technique is discussed in Section 7.2. The technique guarantees that the p.d.f.s depend smoothly on the variable, the centre-of-mass energy and the test mass. This proper behaviour propagates into the resulting likelihood distributions.

Due to the limited statistics, the p.d.f.s are based on, the probability densities are not well known in regions in which they are close to zero. In order to avoid systematic effects, the p.d.f.s are evaluated only in the regions shown in Figure 7.4. Outside these regions $[a, b]$ the integrated probability densities[2] are used: $\int_{-\infty}^{a} dx\,\mathcal{P}(x)$ and $\int_{b}^{\infty} dx\,\mathcal{P}(x)$. The integrated probability is visualised by the over- and underflow bin. The different normalisation factors used inside and outside these regions cancel in (7.4).

Examples of the resulting likelihood distribution for mass hypotheses from 70 to 110 GeV are given in Figure 7.6. Events with a likelihood larger than LH > 0.1 are selected. Only a

---

[2] Similar compared to the treatment of p.d.f.s a smooth surface (depending on $\sqrt{\mathrm{s}}$ and m_{test}) is fitted to the integrated probability densities.

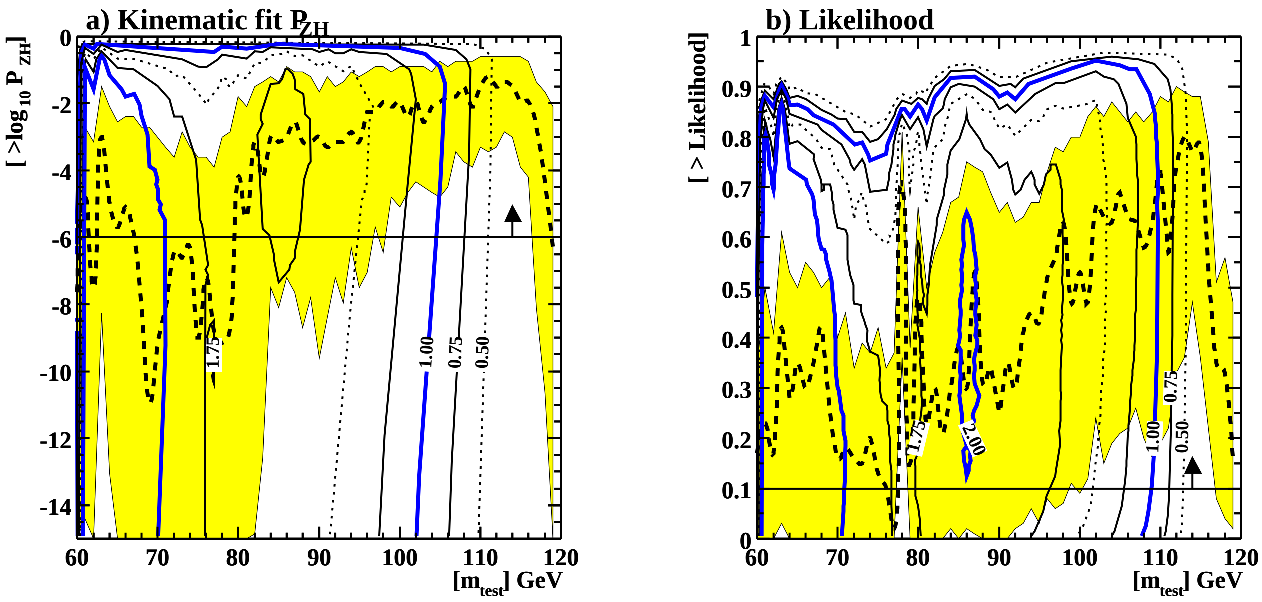

Figure 7.5: Lines of equal figure of merit depending on the test mass and the lower (>) cut on the fit probability of the kinematic fit P(ZH) (Figure a) and on the likelihood (Figures b). For each test mass and chosen cut, the figure of merit was calculated according to formula (7.1), where the sensitivity increases with the figure of merit. The cut position which maximises the figure of merit at each test mass is indicated by the dashed line. The shaded area indicates the area in which the figure of merit changes by less than ±5%. The horizontal line shows the position of the chosen cut.

weak cut is chosen, since the likelihood is used as a discriminating variable in the interpretation of the result in Section 8. The optimal cut with respect to Formular (7.1) strongly depends on the considered test mass and is stricter over the whole test mass range from 60 GeV to 120 GeV than the one chosen (see Figure 7.5b).

7.1.3 Selection Results

The selection efficiencies of background processes and Higgs-strahlung are shown in Figures 7.7 and 7.8, respectively. The efficiency to select four fermion background is maximal around $m_{\mathrm{H}} \simeq 77\,\mathrm{GeV}$. In this region the kinematic fit pushes the reconstructed mass of one W towards m_{Z} and the other to lower values resulting in a configuration similar, to Higgs-strahlung. Around test masses $m_{\mathrm{H}} \simeq 91\,\mathrm{GeV}$, Z pair production is nearly inseparable since only the angular distributions show differences. However, the contribution of Z-pair production to the total background is small and leads only to a small increase of the background. Above the kinematic limit, $m_{\mathrm{H}} = \sqrt{\mathrm{s}} - m_{\mathrm{Z}} \simeq 110\,\mathrm{GeV}$ (at $\sqrt{\mathrm{s}} = 206\,\mathrm{GeV}$), the Z boson is pushed to lower masses[3]. Partially, the kinematic fit takes this into account by using the observed maximal value instead of the nominal value of the Z boson mass in (7.2). However, the mass distribution is poorly approximated by the assumed Gaussian distribution. Hence, events close and beyond the

---

[3] Due to the broader width of the Z boson the Z boson moves further away from the mass shell than the Higgs boson in average.

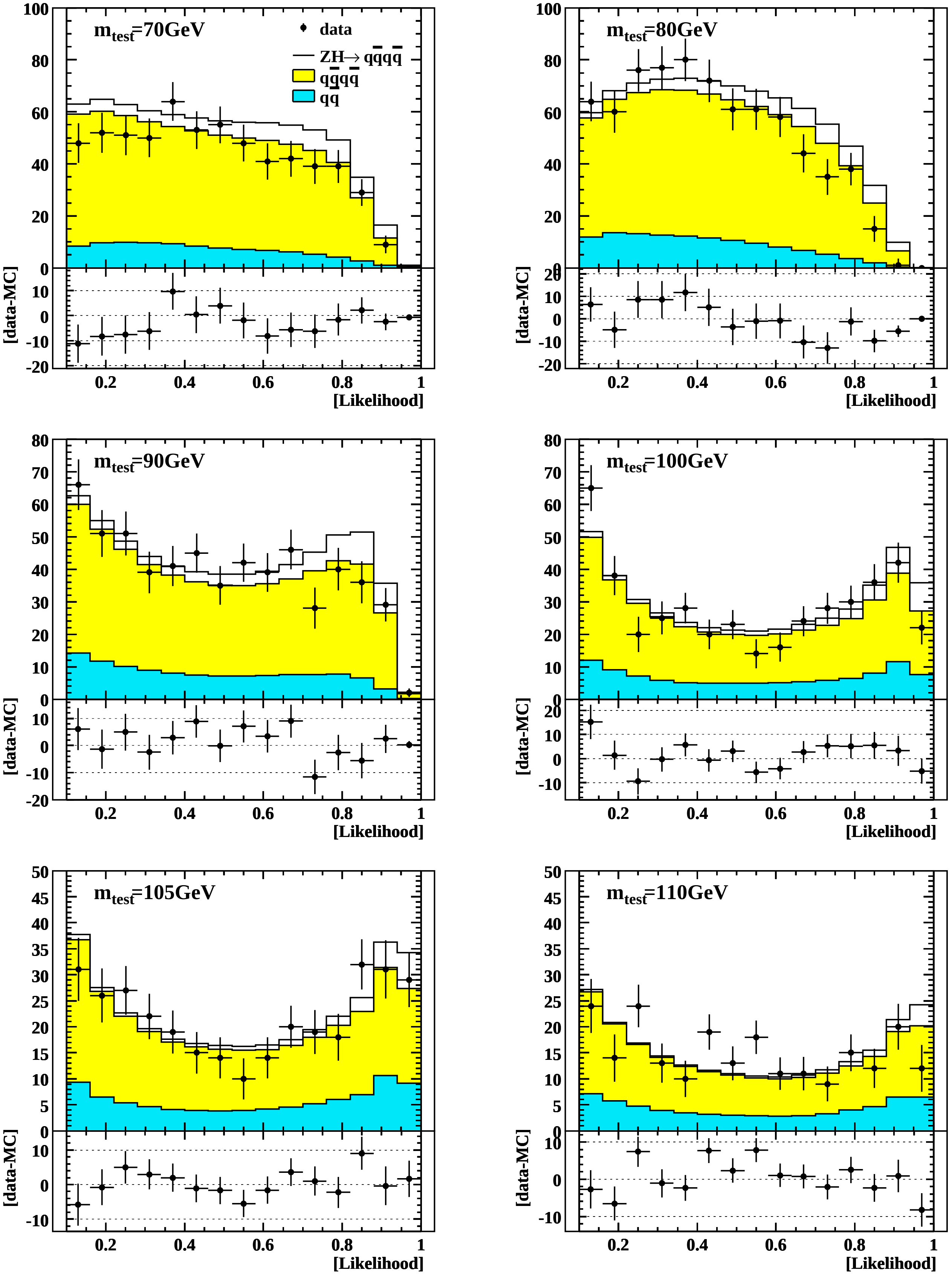

Figure 7.6: Likelihood distributions for different test masses. Shown is the data set of 2000 and 1999 compared to the histograms generated from 3D splines. The 3D splines are fitted to the distributions expected from signal, four and two fermion background (see Section 7.2). The signal expectation is placed on top of the total background.

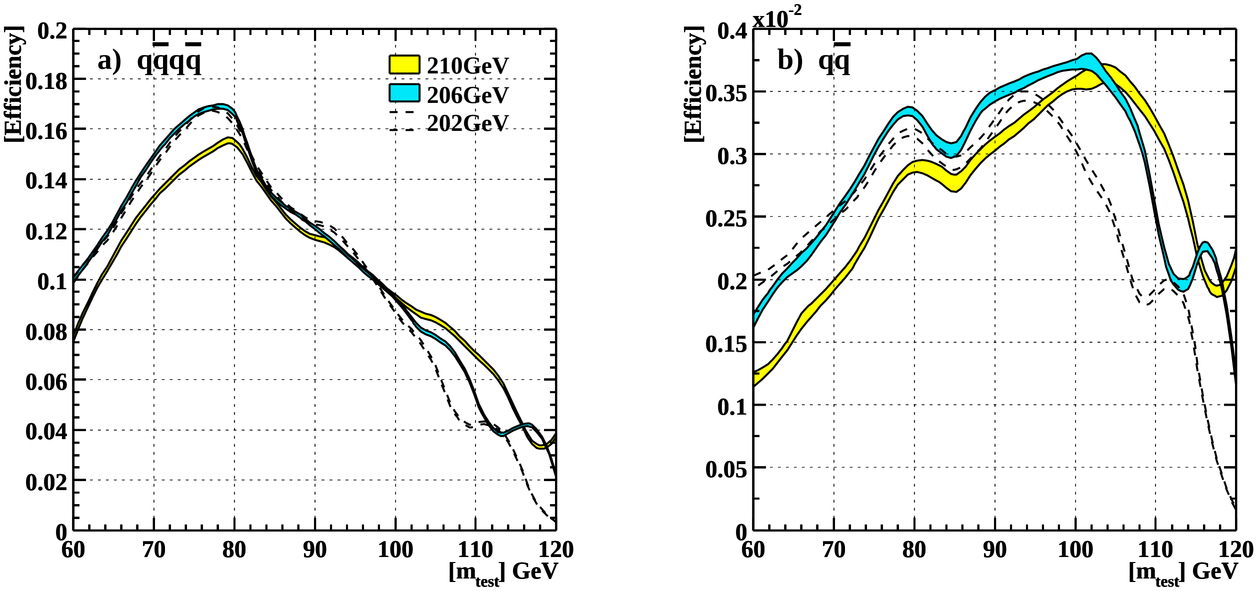

Figure 7.7: Background selection efficiencies. Shown are the efficiencies after full selection depending on the Higgs boson mass hypothesis at $\sqrt{\mathrm{s}} = 202, 206,$ and $210\,\mathrm{GeV}$. The efficiencies reflect that W-pair production is similar to Higgs-strahlung if the hypothetical Higgs has masses around 75 GeV. Beyond the kinematic limit $m_{\mathrm{H}} = \sqrt{\mathrm{s}} - m_{\mathrm{Z}} \simeq 110\,\mathrm{GeV}$, due to the virtuality of the Higgs or Z-boson, the kinematics of Higgs-strahlung do not match the constraints of the fit. Therefore, the background is less distinguishable from signal events.

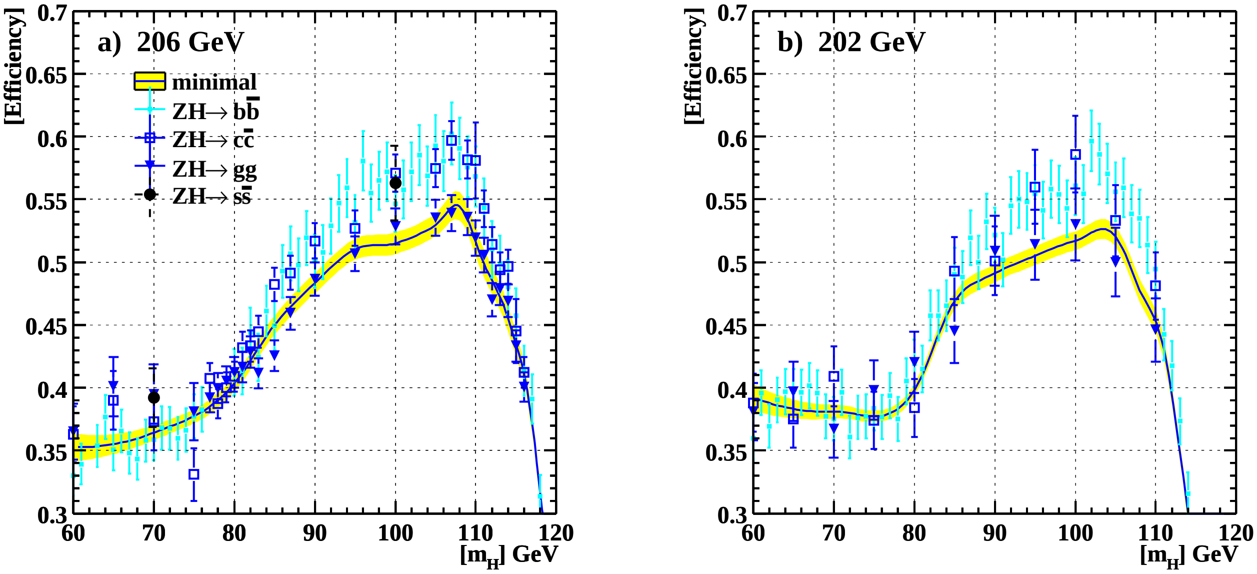

Figure 7.8: Selection efficiency of Higgs-strahlung events. The selection efficiencies of various hadronic decay modes are compared at $\sqrt{\mathrm{s}} = 202\,\mathrm{GeV}$ and $\sqrt{s} = 206\,\mathrm{GeV}$. The selection efficiency does not depend on the quark flavour. However, in events in which the Higgs boson decays into gluons (triangles), the efficiency is reduced by up to 8%. The bands are the projection of a 2D spline fitted to the minimal selection efficiency as a function of the Higgs boson mass and centre-of-mass energy. The width of the bands indicates the statistical error.

kinematic limit do no meet the event hypotheses very well and a smaller fit probability results. As a direct consequence, the final separation between signal and background becomes worse and the background is rejected less efficiently. Consequently, the background rises beyond $m_{\text{test}} = 110\,\text{GeV}$ (at $\sqrt{\text{s}} = 206\,\text{GeV}$).

Since larger weights are assigned to the probability densities of four fermion background in (7.4) the probability densities of two fermion background have little impact and change the likelihood only little in regions, where the probability is large to find four fermion background or signal. Therefore, the two fermion background rises with the four fermion background, which explains the increase below 80 GeV and above 110 GeV. The intermediate maximum is present since the two fermion rate also follows the signal efficiency.

The signal efficiency is strongly influenced by the 7th preselection criterion, the veto on the probability of the kinematic fit with W mass constraints. This requirement leads to the minimum around 77 GeV. The selection efficiency shows a small dependence on the Higgs decay products, although, no explicit use has been made of properties of specific decay modes. The minimal efficiency results from Higgs bosons decaying into gluons. In these events, jets contain more tracks and are broader. As a consequence, the reconstruction algorithm assigns tracks and clusters more frequently to wrong partons, i.e. primary gluons in this case, and the invariant mass resolution becomes worse compared to events in which the Higgs decays into quarks. The invariant mass resolution impacts the result of the kinematic fit and the Higgs-strahlung matrix element, finally leading to a reduced selection efficiency by up to 8%. However, the selection is relatively insensitive to the flavour of the Higgs decay products in $\text{h} \rightarrow \text{q}\bar{\text{q}}$. This has been tested for decays into bottom, charm and strange quarks (see Figure 7.8). Since jets from lighter quarks are more narrow and, generally, do not contain semi-leptonic quark decays their momentum is better reconstructed. Thus, it is not expected that the selection efficiency of Higgs bosons decaying into up and down type quarks is smaller than the selection efficiency of Higgs bosons decaying into heavy quarks. A dedicated simulation of Higgs decays into up and down quarks has not been performed. As an additional cross-check, simulated Z pair events, $\text{e}^+\text{e}^- \rightarrow \text{Z}^0\text{Z}^0$ with $\text{Z}^0 \rightarrow \text{u}\bar{\text{u}}, \text{d}\bar{\text{d}}, \ldots$ were analysed under a Higgs boson mass hypothesis $m_{\text{test}} = m_{\text{Z}}$. The resulting likelihood distributions are shown in Figure 7.9. The distributions are classified according to the flavour of the jet pair assigned to the Higgs boson candidate. Events are considered only if both jets from one Z boson are assigned to either to the Higgs or the Z boson candidate. The distributions are normalised relative to the original quark flavour content. Jets resulting from a Z boson decaying into bottom quarks were considered least frequently to originate from a Higgs candidate, while strange-flavoured jets were assigned most frequently to the Higgs candidate. However, the relative difference is smaller than 6.3%. The opposed jet pair was mostly charm or bottom flavoured, where the relative difference to the least represented type amounts to 3%. Since the topology of Z pair events is similar to Higgs-strahlung the results can be transferred. Thus, the minimal selection efficiency of $\text{h} \rightarrow \text{gg}$ and $\text{h} \rightarrow \text{b}\bar{\text{b}}$ also is minimal with respect to all hadronic Higgs decays.

The likelihood selection reduces the background significantly for test masses larger than 85 GeV and below 70 GeV, but the improvement w.r.t. to the preselection is only marginal in the mass region, $m_{\text{test}} = 70-80\,\text{GeV}$, where the topology of Higgs-strahlung is similar to W-pair production. Figure 7.10 shows the number of events passing the selection under various mass hypotheses, along with the predicted background and the expectation from Higgs-strahlung. The mass resolution of signal events with $\text{LH} > 0.1$ is roughly 10 GeV. Better mass resolution is obtained by increasing the cut on the likelihood (see Figure 7.11).

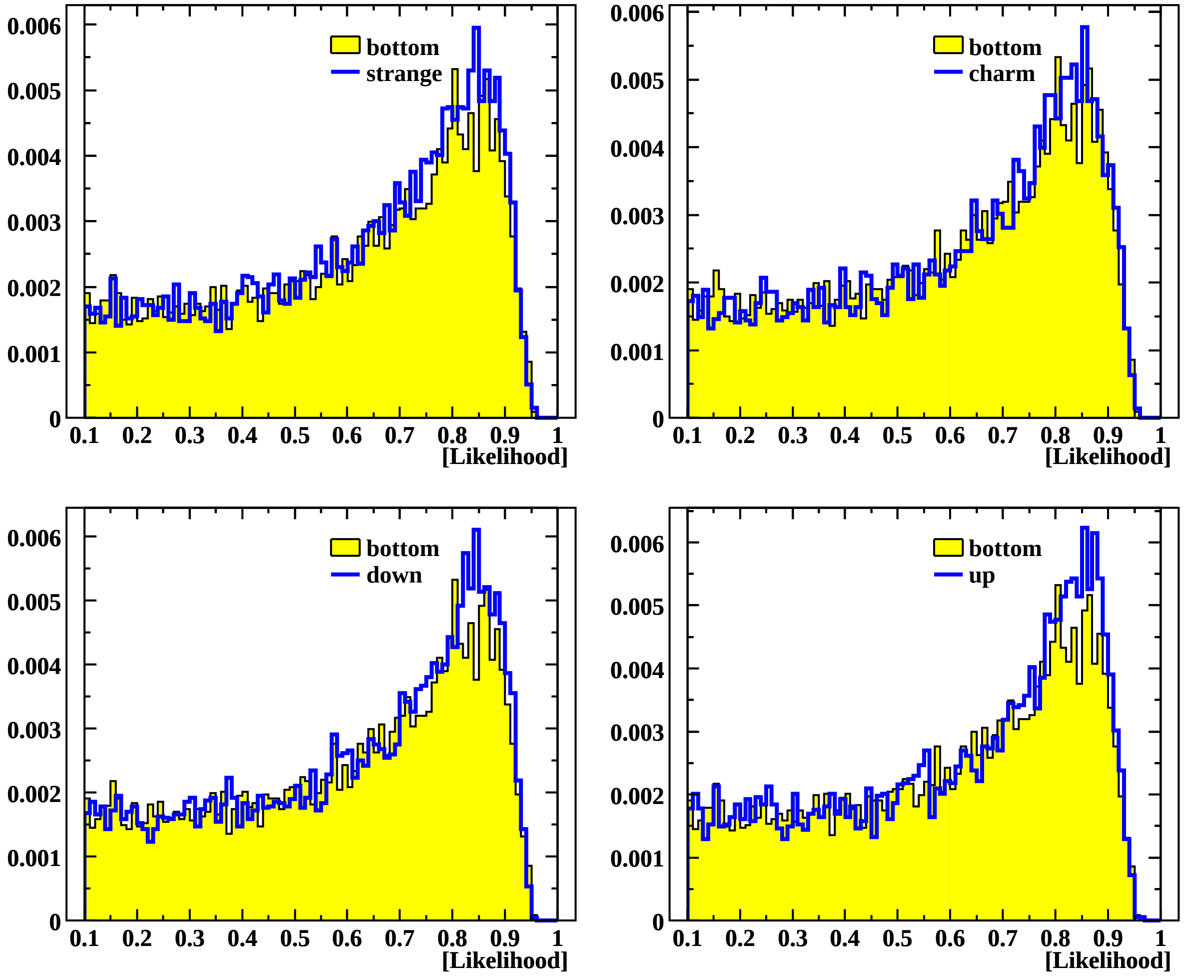

Figure 7.9: Likelihood distributions of simulated Z pair events $e^+e^- \rightarrow Z^0Z^0$ for a test mass $m_{\text{test}} = m_Z$. The events are classified according to the flavour of the primary quark pair forming the jets, which are assigned to the Higgs candidate. The Higgs candidate is defined according to Section 7.1.2. Events are considered only if the quark pair assigned to the Higgs candidate is composed of a quark and anti-quark of the same flavour. The distributions are normalised to the initial flavour content. The figures indicate that jets from light flavour quarks are selected and assigned with equal or higher probability to the Higgs candidate than heavy flavour jets. Moreover, their distributions are more strongly peaked towards LH = 1. Thus, events, in which the Higgs boson decays into light flavour quarks compared to decays into heavy flavour quarks, are even better discriminated from the background.

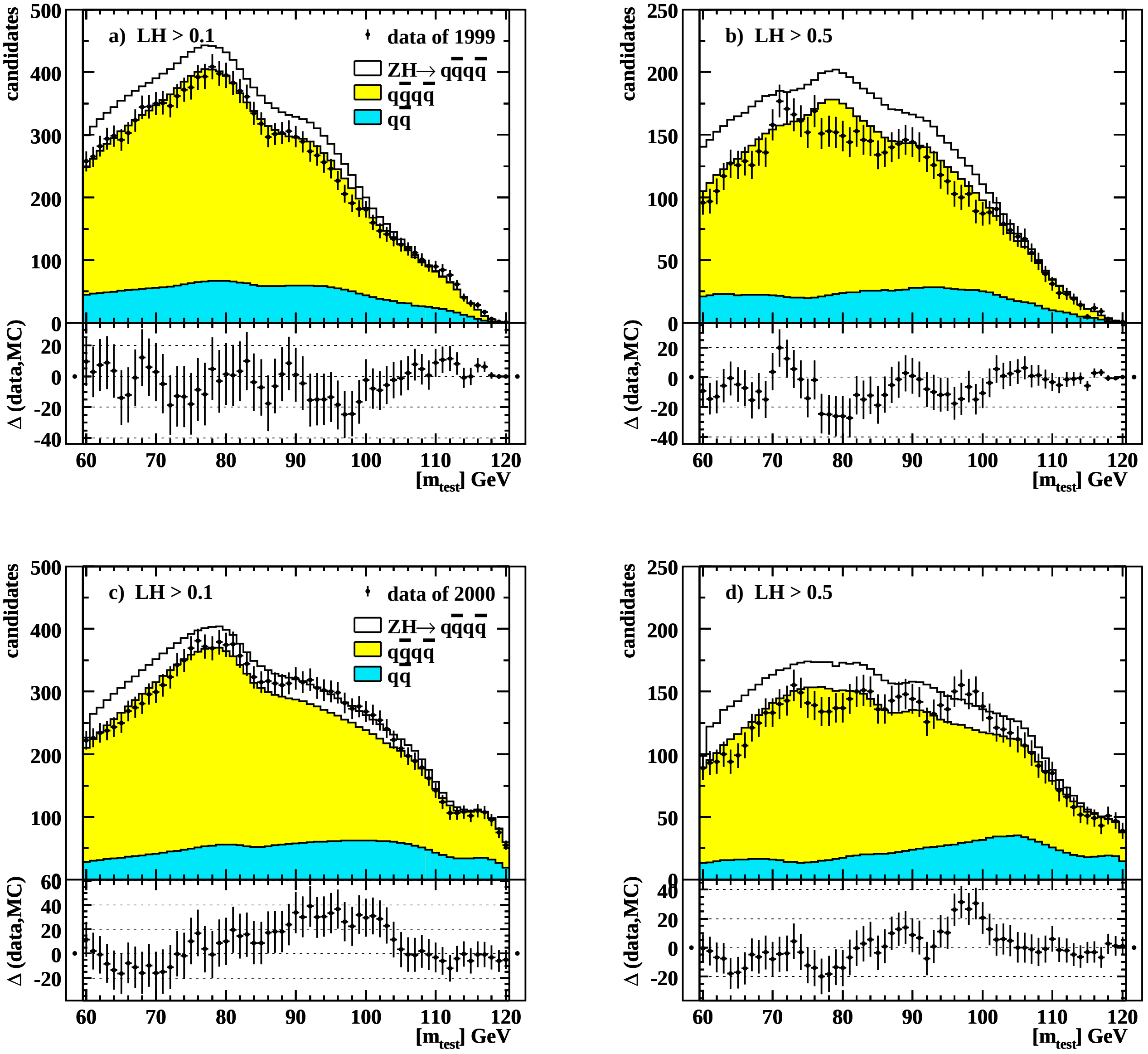

Figure 7.10: Number of candidates in 1999 and 2000 with Likelihood values LH > 0.1 and LH > 0.5 depending on the test mass m_{test}, in comparison to the predicted background and the expectation from Higgs-strahlung. Each bin contains all candidates passing the selection under one mass hypothesis. Since many events equally pass the selection under similar hypotheses, the number of candidates is highly correlated between adjacent bins.

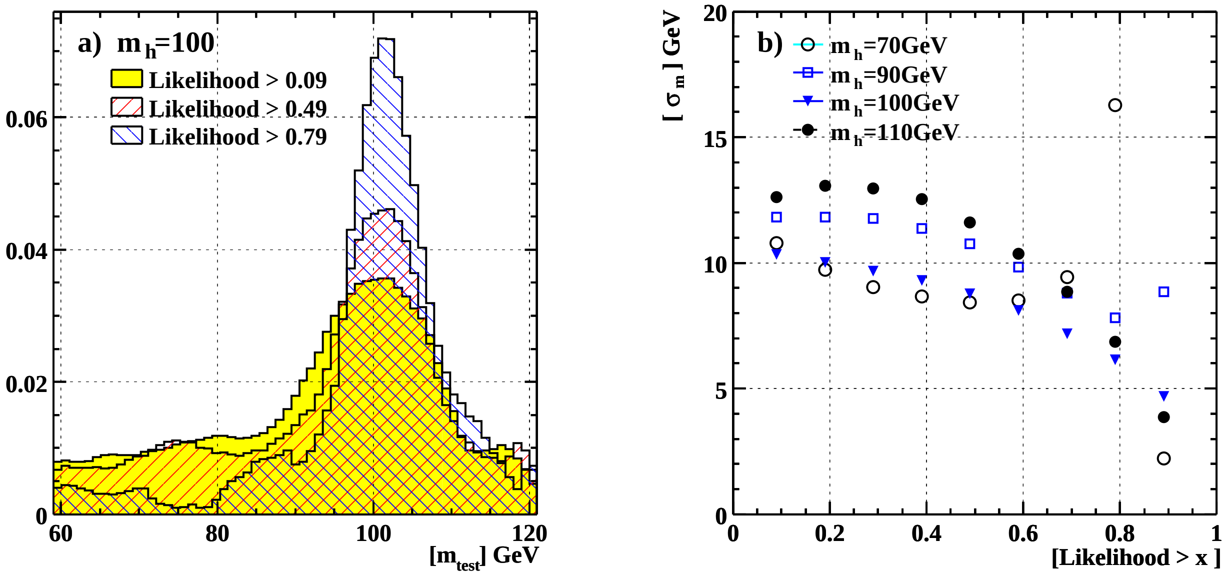

Figure 7.11: Signal events at a fixed Higgs boson mass are tested against various mass hypotheses. In Figure a), the signal efficiency is shown as a function of the test mass for different likelihood cuts. The mass of the Higgs boson is $m_{\mathrm{h}} = 100\,\mathrm{GeV}$. Figure b) shows the width of the peak in the selection efficiency as a function of the likelihood cut and for different Higgs boson masses.

No evidence for a Higgs boson was found. Generally, an excess of more than 5σ would be considered as an observation. Statistical fluctuation can explain the excess of 2σ observed in the data of 2000 around 98 GeV. Fluctuations extend over a broad range of test masses since almost the same events are selected if the mass hypothesis is varied by less than $\pm \sim 5\,\mathrm{GeV}$. This result is used to derive a limit on the Higgs-strahlung cross-section as described in Chapter 8.

7.2 Interpolation of Reference Distributions

The limit calculation as well as the likelihood selection rely on reference distributions for signal and background events. These distributions are extracted from simulations at centre-of-mass energies between 192 and 210 GeV in steps of 2 GeV (and 4 GeV at $\sqrt{s} < 200\,\mathrm{GeV}$). Signal simulation is available for masses from 60 to 120 GeV in steps of 1 or 5 GeV (a detailed list is given in Table A.2). The reference distributions are created from histograms of the considered variables after the test mass dependent kinematic fit. Therefore, background as well as signal reference distributions depend on m_{test}. As the number of simulated events is rather low, the histograms undergo significant statistical fluctuations. So, besides delivering distributions for arbitrary $\sqrt{s}$ and m_{test}, a further goal of the interpolation procedure is to reduce statistical fluctuations.

Two methods were tried: linear interpolation in conjunction with a smoothing procedure and a 3 dimensional surface fit to a set of histograms. These methods are presented in the following sections.

7.2.1 Linear Interpolation of Smoothed Functions

Smoothing Procedure

In a first step, smooth functions were created for several centre-of-mass energies and mass hypotheses using the KEYS method, described in [91] based on [92]. In order to obtain smooth distributions, the resolution of a measured value is reduced by a more or less arbitrary amount on an event-by-event basis. Instead of considering the values directly it is assumed that they are distributed according to a Gaussian distribution around the measured value. The width of the Gaussian is chosen with respect to its frequency, where high frequency means small width and low frequency means a broad distribution. These Gaussians are accumulated instead of the measured values. The actual width of the individual Gaussians is adjusted by a global factor in order to obtain sufficiently smooth distributions. If the distributions have physical boundaries, the Gaussians are reflected at the limits. Smooth distributions are produced by construction, however, the distributions are broadened and spikes are flattened. Thus, information may be lost and separation power may be reduced.

As this smoothing procedure is performed independently for different centre-of-mass energies and test masses, differences due to statistical fluctuations between distributions of adjacent centre-of-mass energies or test masses, can be amplified by the smoothing procedure.

Linear Interpolation

The smooth functions are then used to generate functions for arbitrary centre-of-mass energies or test masses by linear interpolation. If functions do not match the desired centre-of-mass energy and test mass, four functions have to be interpolated:

$$f(x;\sqrt{\mathrm{s}},m_{\mathrm{test}}) := \left[\nu(\lambda f_{\sqrt{\mathrm{s}_1}m_{11}}+(1-\lambda)f_{\sqrt{\mathrm{s}_1}m_{12}})+(1-\nu)(\lambda f_{\sqrt{\mathrm{s}_2}m_{21}}+(1-\lambda)f_{\sqrt{\mathrm{s}_2}m_{22}})\right](x).$$

The values λ and ν have to be chosen appropriate depending on the distance of $\sqrt{\mathrm{s}_1}$ and $\sqrt{\mathrm{s}_2}$ to $\sqrt{\mathrm{s}}$ and the distance of m_{ij} to m . A priori, it is not clear which choice of functions $f_{\sqrt{\mathrm{s}_i}m_{ij}}$yields the best approximation. There are basically two possibilities:

a.) The obvious choice is to use functions with adjacent centre-of-mass energy and test masses, where the same test masses are used at all centre-of-mass energies:

$$\mathrm{s}_1 < \mathrm{s} < \mathrm{s}_2, \quad m_{11} = m_{21}, \quad m_{12} = m_{22} \quad \text{and} \quad m_{11} < m < m_{12}.$$

b.) However, approaching the kinematic limit the functions depend more on the distance to the kinematic limit than on the test mass itself. A better choice would be to use functions of test masses which have the same distance to the kinematic limit:

$$\begin{aligned} \mathrm{s}_1 < \mathrm{s} < \mathrm{s}_2,\ & m_{11}+\sqrt{\mathrm{s}_1}-\sqrt{s} < m < m_{12}+\sqrt{\mathrm{s}_1}-\sqrt{s} \\ \text{and } & m_{21}+\sqrt{\mathrm{s}_2}-\sqrt{s} < m < m_{22}+\sqrt{\mathrm{s}_2}-\sqrt{s} \quad . \end{aligned}$$

The performance of the two interpolation schemes is illustrated in Figure 7.12. Linear interpolation using the first interpolation scheme yields satisfactory results at low test masses. However, the description is poor close to the kinematic limit. Here, the second interpolation yields a good approximation. But, at lower test masses the shape is more sensitive to the distance to m_{Z} and

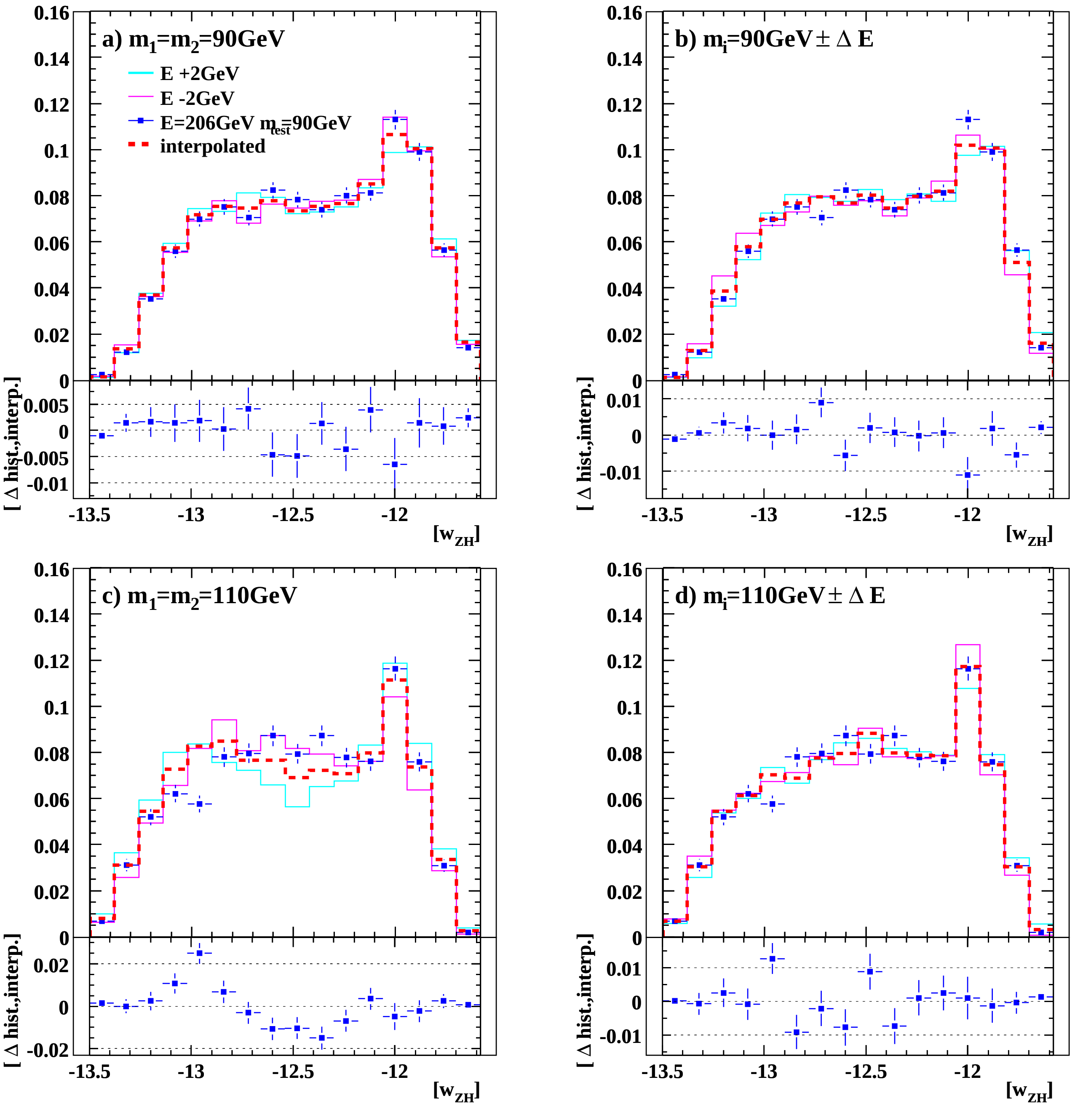

Figure 7.12: Linear interpolation of the Higgs-strahlung matrix element. The distribution of the Higgs-strahlung matrix element obtained from the simulation of four fermion background at $\sqrt{s} = 206\,\text{GeV}$ (squares with error bars) is approximated via linear interpolation using distributions obtained at $\sqrt{s} = 204\,\text{GeV}$ and $208\,\text{GeV}$ (thin and thick solid lines) . In Figures a) and b) the test mass is $m_{\text{test}} = 90\,\text{GeV}$ and in Figures c) and d) $m_{\text{test}} = 110\,\text{GeV}$. In a) and c), the distributions, which are interpolated, are obtained under the same mass hypothesis of $m_{\text{test}} = 90\,\text{GeV}$ and $m_{\text{test}} = 110\,\text{GeV}$, respectively. In b) and d), the distributions, which are interpolated, have been obtained under mass hypotheses which keep the distance to the kinematic limit constant, i.e $m_{\text{test}} = 90 \pm 2\,\text{GeV}$ and $m_{\text{test}} = 110 \pm 2\,\text{GeV}$. The distributions resulting from the linear interpolation are indicated by the dashed line. The results shown in Figures a) and d) agree within errors with the distributions to be approximated. In both cases the other interpolation scheme yields only a poor approximation as shown in Figures b) and c). Thus, different interpolation schemes are favourable for different mass regions.

the interpolation using the second scheme performs worse. The dependence of the sensitivity on the distance to m_{Z} and m_{W}, respectively, can be explained by the kinematic fits. If, for example, the test mass is larger than m_{Z}, the assignment of the kinematic fit with the Higgs and Z mass constraints will favour a different association of the jets to the bosons compared to a fit with a test mass lower than m_{Z}. This leads to a rather different behaviour above and below m_{Z}.

In order to achieve a good approximation for masses close to the kinematic limit and masses around m_{Z}, respectively, a complex combination of the two interpolation schemes would be necessary. Moreover, the resulting likelihood looses its intrinsic dependence on the centre-of-mass energy and test mass, because many independently smoothed functions contribute to the likelihood and errors due to the smoothing procedure, as well as interpolation errors, pile up. A further interpolation becomes even more difficult. Mainly due to the last reason, the linear interpolation scheme has been abandoned in favour of the method described in the following.

7.2.2 Multidimensional Spline Fit

A more complicated approach is cubic interpolation, performed simultaneously in all three dimensions (the variable, $\sqrt{\mathrm{s}}$ and m_{test}). In order to reduce statistical fluctuations, no direct interpolation is desirable, rather a smooth 3D surface is fitted to histograms of various centre-of-mass energies $\sqrt{\mathrm{s}}$ and different test masses m_{test}. Histograms are available for $\sqrt{\mathrm{s}}$ in steps of 2 GeV or 4 GeV and for m_{test} in steps of 1 GeV or 5 GeV. In the following it is assumed that all these histograms are compiled into one three dimensional histogram with a bin size of 2 GeV and 1 GeV in the direction of $\sqrt{\mathrm{s}}$ and m_{test}. A satisfactory approximation can be obtained as long as the following assumptions are fulfilled:

- The distributions are continuous and differentiable;
- The variation of the distributions with the centre-of-mass energy and test mass can be described by third order polynomials within a region of ~ 5 GeV;
- the distribution itself can be approximated across several bins by third order polynomials.

The simplest functions describing arbitrary histograms are piecewise defined polynomials which are joined together requiring continuity of the function itself and of its first and second order derivative at the joint planes, usually referred to as *splines*. Splines are completely defined by a given set of function values f_i at support points x_i. In order to prevent the spline to follow all statistical fluctuations, the spacing of the support points has to be chosen wider than the bin size of the histogram. Moreover, the histogrammed values h_i are not used directly, but the function values f_i, which define the spline, are adjusted until the resulting surface fits to the histogram. In order to optimise the spline, a χ^2 minimisation is performed using MINUIT [93][4].

---

[4] In the 1D case the χ^2 minimisation problem is linearisable and can be solved exactly. In two or higher dimensional space, a quadratic equation has to be solved. In order to shorten implementation time, the optimisation package MINUIT was used.

The χ^2 is defined by:

$$\begin{aligned}
\chi^2 \quad &:= \quad \sum_i \chi_i^2 \quad \text{with} \quad \chi_i^2 := \frac{1}{\sigma_{h_i}}(P(\hat{\mathbf{x}}_i;\, \{\mathbf{x}_j,\, f_j\}) - h_i)^2 \\
P \quad &\hat{=} \text{ spline with function values } f_j \text{ at support points } \mathbf{x}_j \\
h_i \quad &\hat{=} \text{ value of bin whose center is located at } \hat{\mathbf{x}}_i \\
\sigma_{h_i} \quad &\hat{=} \text{ statistical error of corresponding bin value .}
\end{aligned}$$

Here, an Akima spline [94] is chosen which is defined piecewise by third order Polynomials:

$$P(x_1, x_2, x_3) := P^3_{1,i_1,i_2,i_3}(x_1 - \tilde{x}_{1,i_1}) \cdot P^3_{2,i_1,i_2,i_3}(x_2 - \tilde{x}_{2,i_2}) \cdot P^3_{3,i_1,i_2,i_3}(x_3 - \tilde{x}_{3,i_3}),$$

where $P^3_{\nu,i_1,i_2,i_3}(x_\nu - \tilde{x}_{\nu,i_\nu})$ is a one dimensional third order polynomial. The first index denotes the axis and the second to forth the location of the cell in which the polynomial describes the histogram: $i_\nu\,:\,\tilde{x}_{\nu,i_\nu} < x_\nu < \tilde{x}_{\nu,i_\nu+1};\ \nu = 1, 2, 3$. The function values have to be given on a not necessarily uniform but rectangular grid. An Akima spline is defined such that one polynomial piece of the spline is determined exclusively by the support points at the corners of one mesh and their nearest neighbours. For example, in the one dimensional case P_j is defined by $(x_{j-1},\, f_{j-1}),\, \ldots (x_{j+2},\, f_{j+2})$. The polynomial P_j is set to the function values f_j and f_{j+1} at the corners of the mesh x_j and x_{j+1}. First and second order derivatives are defined by the central differential quotients[5]:

$$\frac{dP_j}{dx}(x_j) \equiv \frac{f(x_{j+1}) - f(x_{j-1})}{x_{j+1} - x_{j-1}} \quad \text{and} \quad \frac{d^2P_j}{dx^2}(x_j) \equiv \frac{\frac{f(x_{j+1})-f(x_j)}{x_{j+1}-x_j} - \frac{f(x_j)-f(x_{j-1})}{x_j-x_{j-1}}}{\frac{1}{2}\cdot[(x_{j+1}+x_j)-(x_j+x_{j-1})]}.$$

The optimisation can be performed for each piece separately, because adjusting the function values defining a certain piece j has only influence on the direct neighbours.

Before the optimisation is started, all function values f_j are initialised with the weighted sum over the histogrammed values close to the support point j. The distance of the bin centre x_ν to the support point x_j is used as a weight: $\omega = \exp(-(x_j - x_\nu)^2/2)$. The resulting surface achieves a first level of approximation which is optimised further piece by piece. The optimisation is started in one corner $j_0 = (0, 0, 0)$ and continues successively piece after piece, $\boldsymbol{j}_{\nu+1} = (j^1_\nu{+}1, j^2_\nu, j^3_\nu)$, row after row, $\boldsymbol{j}_{\nu+1} = (0, j^2_\nu{+}1, j^3_\nu)$, plane after plane, $\boldsymbol{j}_{\nu+1} = (0, 0, j^3_\nu{+}1)$. When optimising the polynomial P_j the function values $f_j, \ldots,\, f_{j+2}$ are adjusted (simplified to 1D-case), these values influence in addition to the polynomial P_j the preceding polynomials $P_{j-1},\ P_{j-2}$ and subsequent polynomials P_{j+1}, P_{j+2}, which have not yet been optimised. In order not to destroy preceding optimisations, the χ^2 is calculated not only from the sum of the weighted difference between the spline and all bin values h_i which are located in piece j, i.e. the domain of polynomial P_j, but additionally all bins h_i whose bin centre $\hat{x}_i$ is in the region $\hat{x}_i \in [x_{j-2},\, x_{j+2}]$, covering additionally the domain of the two precedential and the successive polynomials.

In a final step polynomials P_j with too large $\widetilde{\chi_j}^2 := \sum_i \chi_i^2(\hat{x}_i, h_i)$ with $\hat{x}_i \in [x_j, x_{j+1}]$ are optimised for a second time in descending order of $\widetilde{\chi_j}^2$. The final step is performed because in the first pass, when optimising a certain polynomial, subsequent polynomials are not yet optimised, however, they have impact on the corresponding χ^2. Thus, the result of the first

---

[5] Derivatives at the boundaries i.e. $j = 1$ or $j = N$ are treated specially.

optimisation pass might not be optimal. However, the improvement due to the second pass is small.

There are heuristic methods to chose the number and locations of the support points automatically but they are time consuming and the resulting grids are rarely optimal. Often the position of support points can be treated as free parameters in the χ^2 minimisation. However, if the surface to be approximated is locally cubic the positions of the support points are not unique and the fit would not converge. The ambiguity of the support point position is reduced if the positions are permitted to vary in one dimension only. But there is no guaranteed convergence.

Here, the support points are chosen manually, equidistant in $\sqrt{s}$ in steps of 4 GeV, and in m_{test} in 3 GeV. in the direction of the variable, a grid is chosen such that a spline fit to a one dimensional histogram yields good approximation i.e. χ^2/d.o.f. close to one, for several test masses and centre-of-mass energies. In order to provide stringent constraints on the surface, the distance of support points is chosen to be larger than the width of two bins[6].

The approximation of the p.d.f.s and the likelihood distribution works sufficiently well. Examples of the approximation of the p.d.f.s and the likelihood distribution are shown for background and signal in Figures 7.13 to 7.15. The original histograms of distributions at centre-of-mass energies 192, 196, 200, 202, . . . 210 and 207, and for different mass hypotheses are compared bin-by-bin to histograms generated from the 3D spline taking into account the statistical error of the original histograms. For each histogram a χ^2 is calculated:

$$\chi^2 := \sum_{\text{bins}} (h_i - h^{\text{gen}}(x_i))^2 / \sigma_{h_i}^2.$$

The resulting χ^2 distribution is shown on the left hand side of Figure 7.16 for background and signal distributions. The observed χ^2 distributions are slightly broader compared to the expectation. This indicates that there is a small systematic disagreement between the spline and the histograms. However, looking at individual histograms shows that large contributions to the χ^2 are mainly from hardly populated bins.

On the right hand side of Figure 7.16, the probability to obtain a certain χ^2 is displayed for three centre-of-mass energies. The probabilities are expected to be evenly spread between zero and one, if the differences between the spline and the histograms are purely statistical. This is roughly the case.

7.3 Extensions to The Event Selection

7.3.1 Optimisation for $\text{H} \rightarrow gg$

As pointed out at the end of Section 7.1.3 the efficiency to select events in which Higgs bosons decay into gluons is reduced by up to 8%. The selection of $\text{H} \rightarrow gg$ can be improved by making use of the increased multiplicity in hadronic jets resulting from gluons.

The selection is performed as described in Section 7.1. The assignment of the jets to the Higgs and the Z boson candidates which yields highest probability of the kinematic fit is chosen. The total multiplicity of both jets assigned to the Higgs boson candidate is determined and

---

[6] In some cases of quickly changing tangents, support points with a spacing of only one bin width had to be chosen to achieve a small enough χ^2.

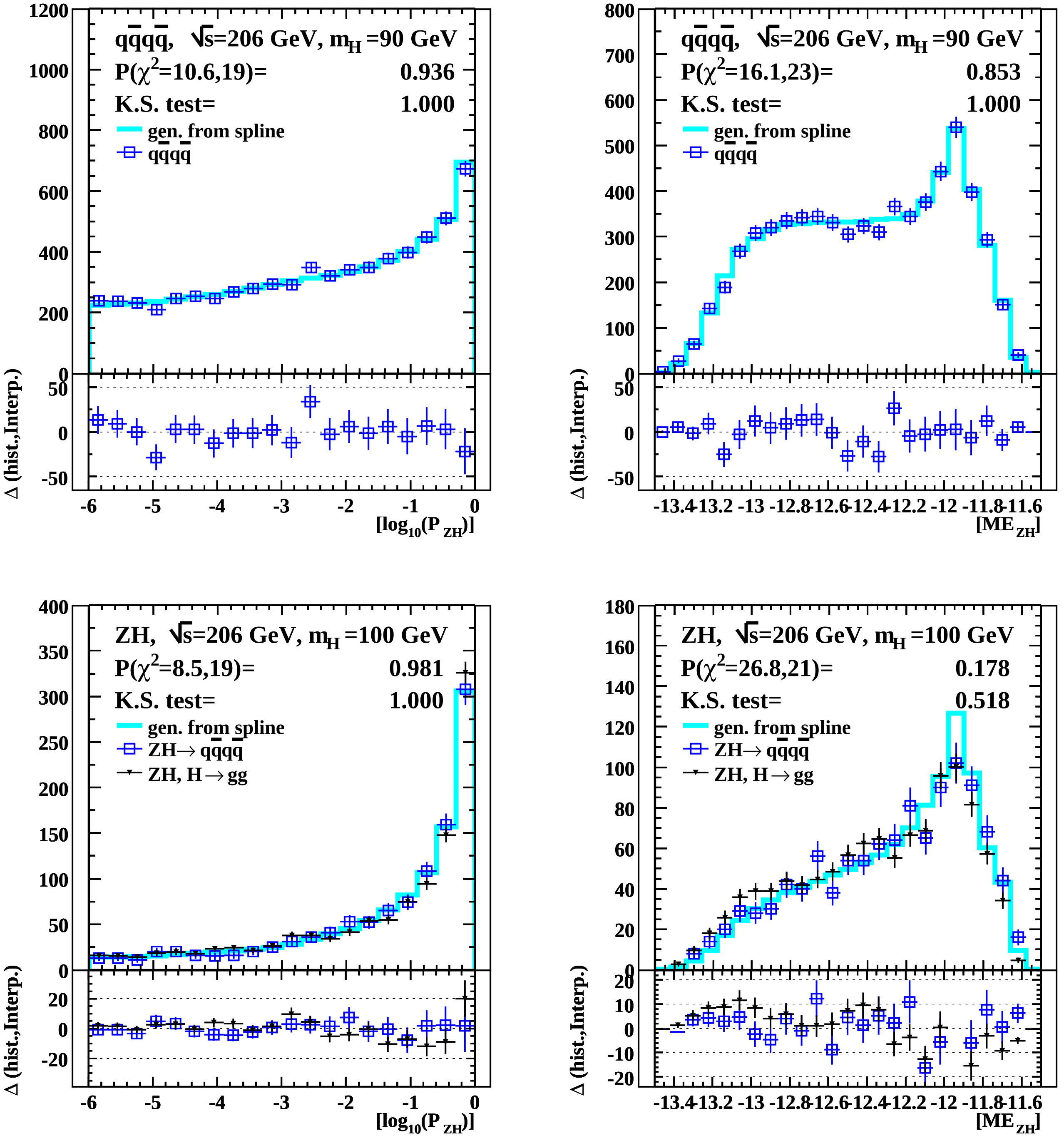

Figure 7.13: Comparison between the original histogram and a histogram generated from the 3D spline for a centre-of-mass energy of $\sqrt{s} = 206\,\mathrm{GeV}$ and a test mass of 100 GeV. Distributions of the probability of the ZH-fit P(ZH) and of the Higgs-strahlung matrix element $\mathrm{ME}_{\mathrm{ZH}}$ are shown for hadronic four-fermion background and Higgs-strahlung. The listed numbers indicate the χ^2 of a bin-by-bin comparison and the probability of a Kolmogorov Smirnov test (K.S. test).

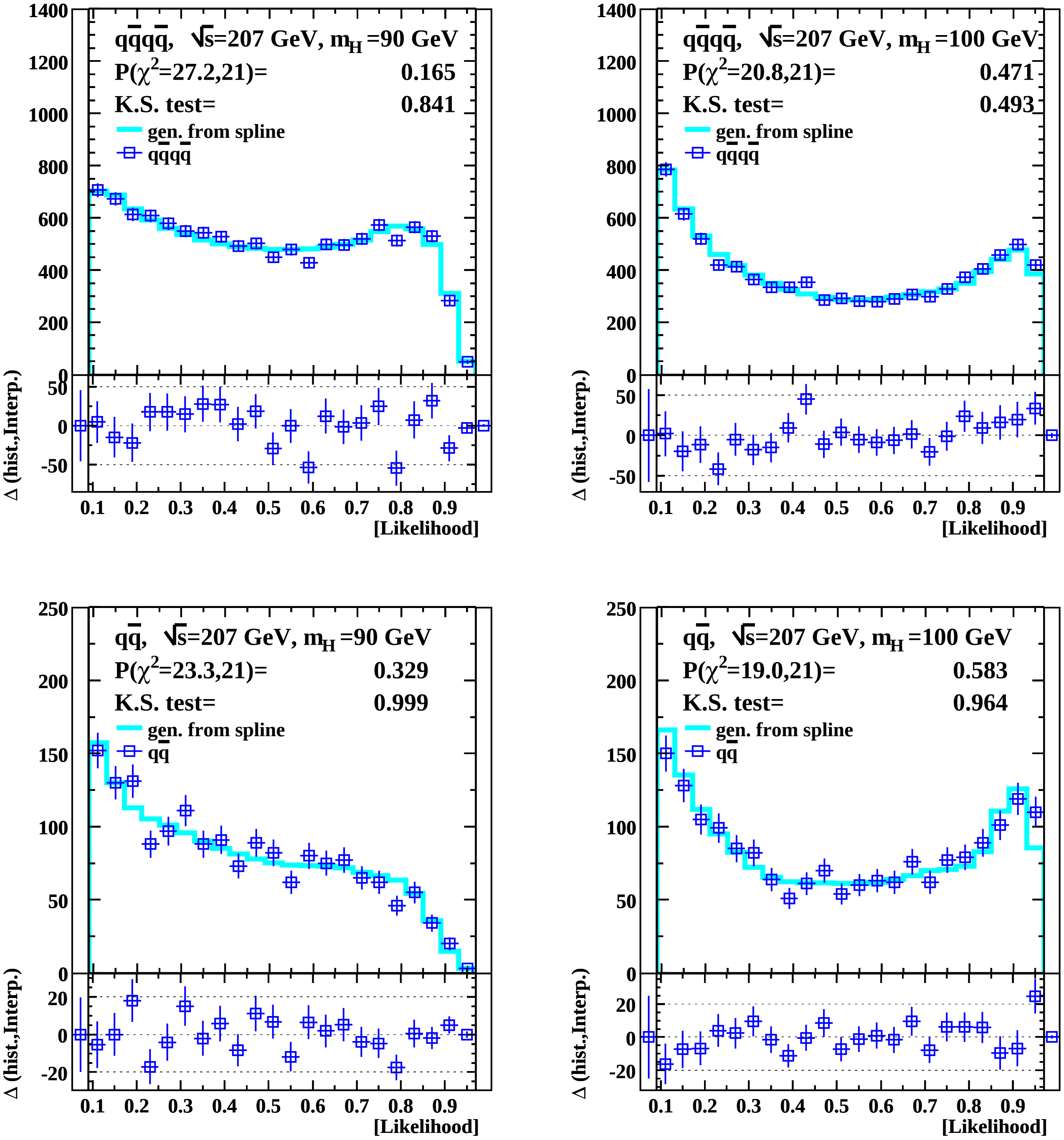

Figure 7.14: Comparison between the original histogram and a histogram generated from the 3D spline for a centre-of-mass energy of $\sqrt{s} = 207\,\text{GeV}$ and test masses of 90 and 100 GeV. The upper two figures show the likelihood distributions of hadronic four fermion background. The corresponding distributions of two fermion background are shown below. The histograms and the spline are statistically independent. The listed numbers indicate the χ^2 of a bin-by-bin comparison and the probability of a Kolmogorov Smirnov test (K.S. test).

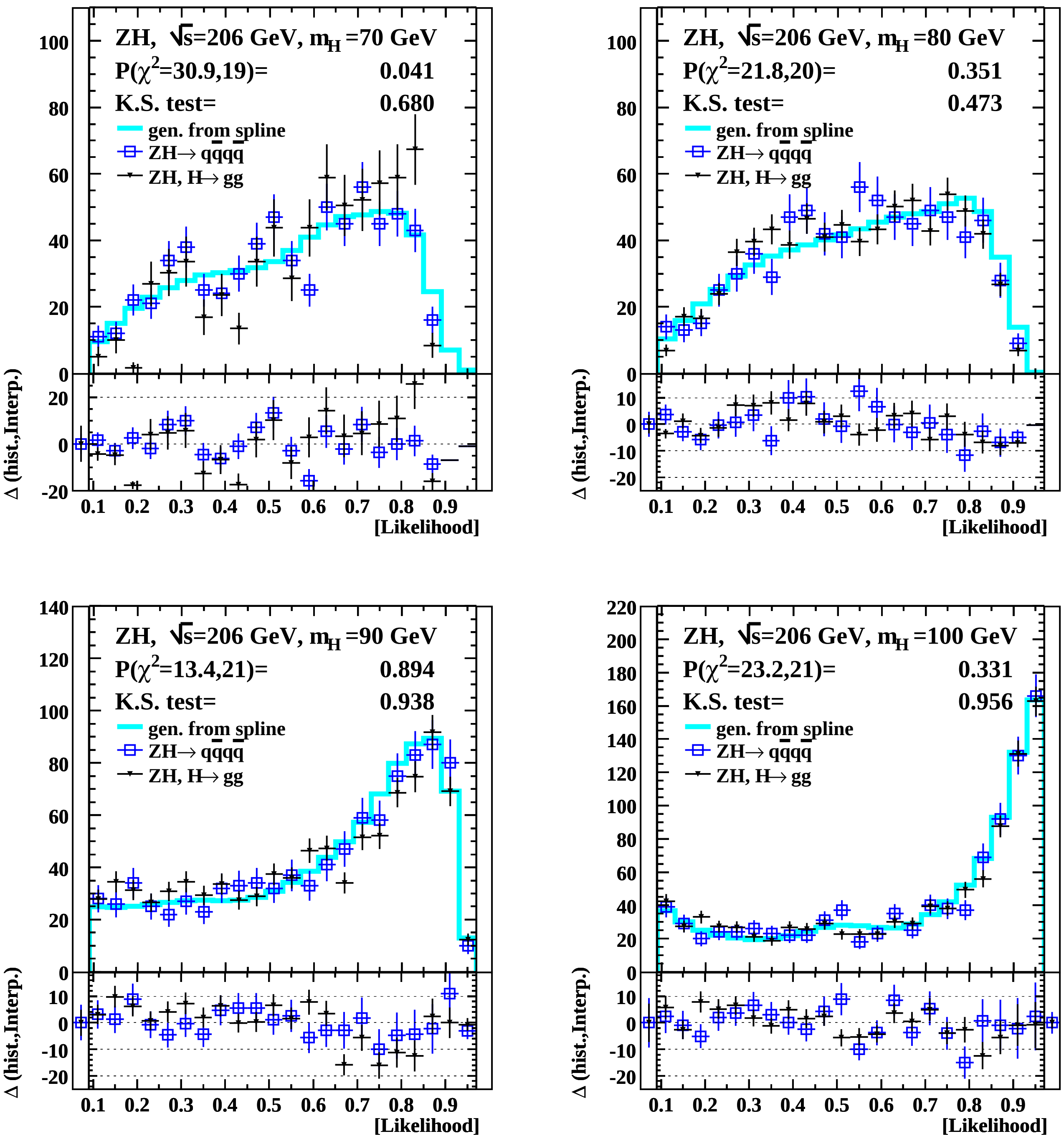

Figure 7.15: Likelihood distributions of signal events, ZH → q$\overline{\text{q}}$q$\overline{\text{q}}$ and ZH → q$\overline{\text{q}}gg$, compared to a histogram generated from a 3D spline. The spline was fitted to distributions obtained from ZH → q$\overline{\text{q}}$q$\overline{\text{q}}$ events. The listed numbers, the χ^2 and the probability of the K.S test, refer to the comparison between the generated histogram and the histogram obtained from ZH → q$\overline{\text{q}}$q$\overline{\text{q}}$ events.

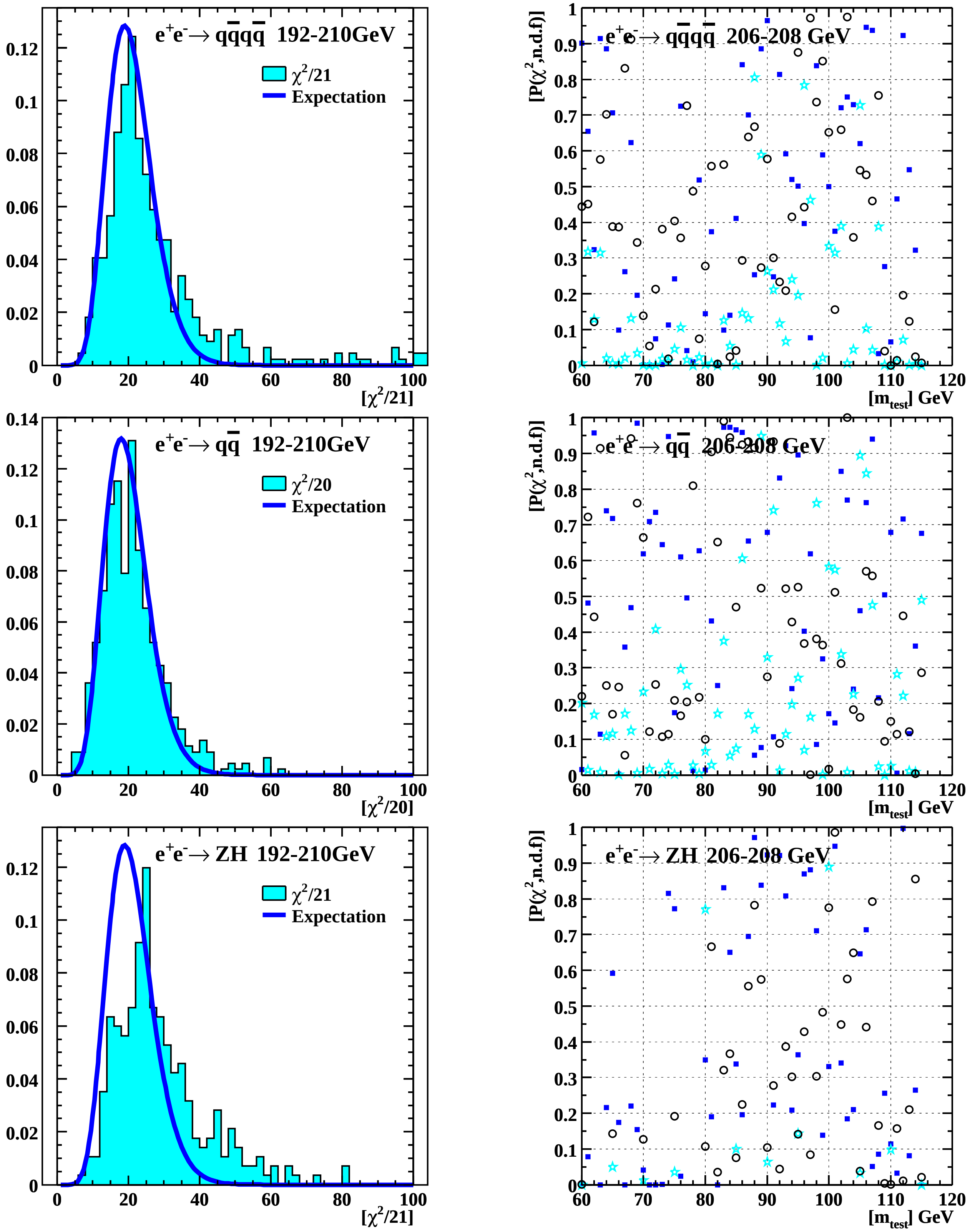

Figure 7.16: The figures on the left show the χ^2 distributions of bin-by-bin comparisons between the histograms obtained from the simulated events (four and two fermion background and Higgs-strahlung) and the histograms generated from the spline at all considered test masses (1 GeV steps) and centre-of-mass energies (2/4 GeV steps). Furthermore, the expected χ^2-distribution is depicted. The figures on the right show the corresponding χ^2-probabilities as a function of the test mass for some centre-of-mass energies. The probabilities are expected to be homogeneously distributed between 0 and 1.

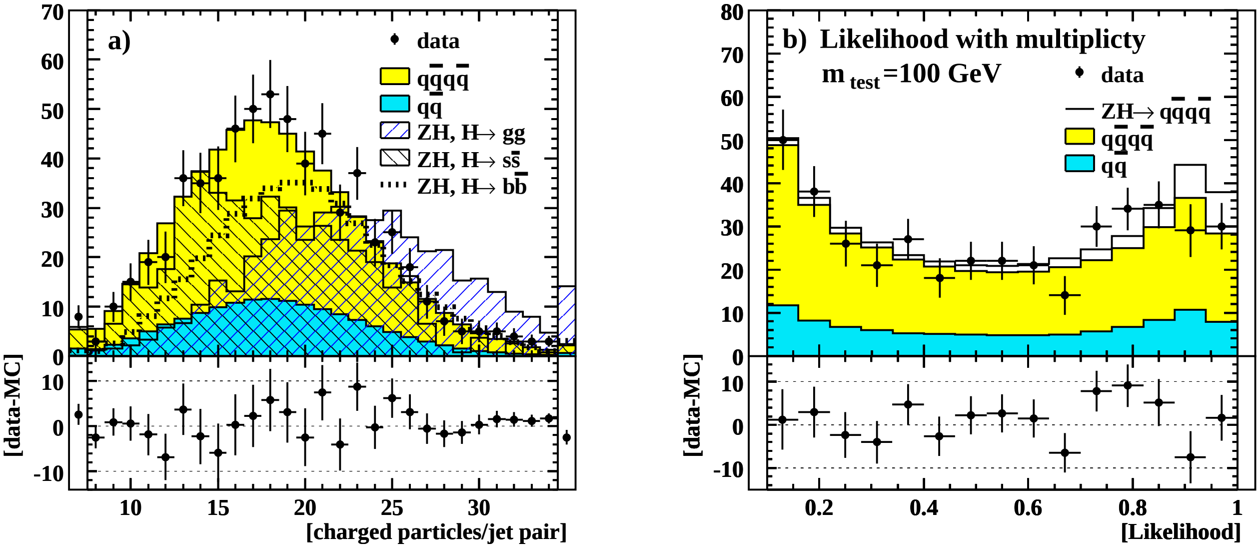

Figure 7.17: a) The total number of tracks within the two jets assigned to the Higgs boson candidate. The jets from $h^0 \rightarrow gg$ show an enhanced multiplicity compared to the background. However, the multiplicity in jets caused by light flavour quarks ($h^0 \rightarrow s\bar{s}$) is smaller than the average multiplicity in background events. In order to improve the selection efficiency of $h^0 \rightarrow gg$, this variable is used additionally to calculate a likelihood. Figure b) shows the likelihood distributions obtained from the data of the years 1999 and 2000 and the expectation under a mass hypothesis of $m_{\mathrm{test}} = 100\,\mathrm{GeV}$.

used as an additional variable in the likelihood. The multiplicity distribution of $\mathrm{H} \rightarrow gg$ is used as signal reference distribution to calculate the likelihood. The signal p.d.f.s of the other distributions are still those of $\mathrm{H} \rightarrow \mathrm{q\bar{q}}$. The reconstructed multiplicity and the resulting likelihood for a test and Higgs boson mass of 100 GeV is shown in Figure 7.17. The multiplicity allows a clear separation of $\mathrm{H} \rightarrow gg$ from the background. The multiplicity in SM Higgs boson decays also is larger compared to background events since the SM Higgs boson decays dominantly into $\mathrm{b\bar{b}}$. However, if the Higgs boson decays into light quarks, the multiplicity is only enhanced by the larger centre-of-mass energy of the Higgs boson rest frame in case $m_{\mathrm{h}} > m_{\mathrm{W}}, m_{\mathrm{Z}}$.

The efficiency, displayed in Figure 7.19, to select $\mathrm{H} \rightarrow gg$ is improved by up to 4%. The reduction of the efficiency to select $\mathrm{H} \rightarrow \mathrm{q\bar{q}}$ is negligible. The resulting signal efficiencies are much closer together. However, an explicit dependence on the final state has been introduced. The number of selected candidates, shown in Figure 7.18, changes insignificantly compared to the analysis of Section 7.1.3.

7.3.2 Sensitivity to H → AA

In Section 3.2, Two-Higgs-Doublet models were presented. In these models, a heavy and a lighter CP-even, H^0 and h^0, and a CP-odd Higgs boson, A^0, appear. Generally, the CP-odd Higgs boson A^0 is produced in pair production, $\mathrm{e^+e^-} \rightarrow \mathrm{Z}^0 \rightarrow \mathrm{h}^0\mathrm{A}^0$. However, if $\cos(\beta-\alpha) \simeq 0$ this process is strongly suppressed and the A^0 is dominantly produced in conjunction with the

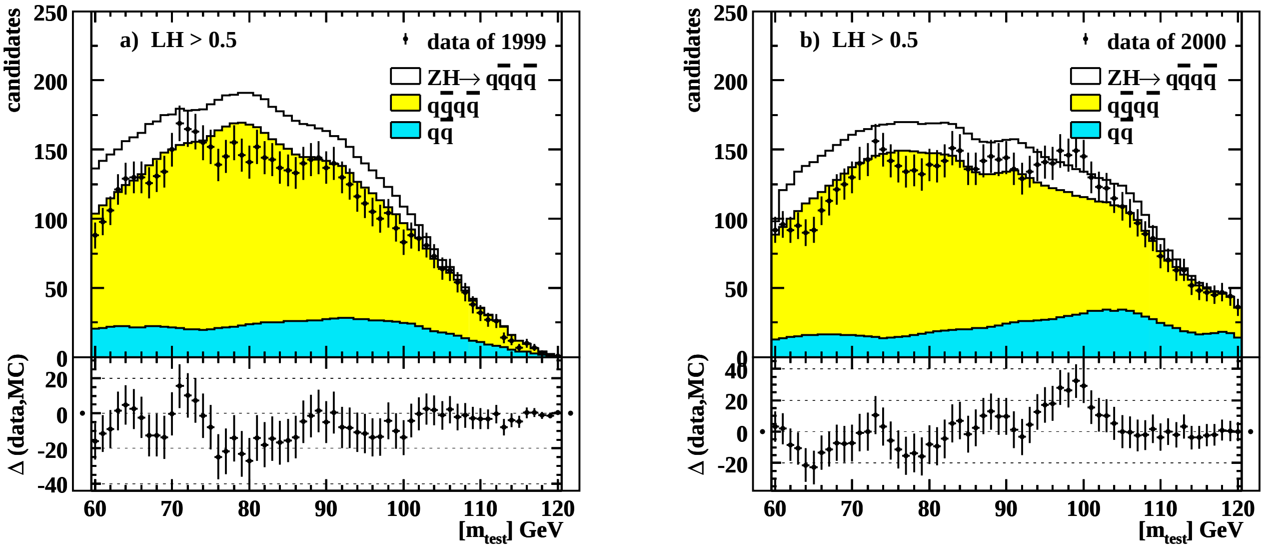

Figure 7.18: The number of selected candidates with likelihood values LH > 0.5 in the years 1999 and 2000. The charged particle track multiplicity of the Higgs candidate jets is used as an additional variable in the likelihood. Similar yields are observed compared to the selection of Section 7.1. The signal expectation represents Higgs decays into quark pairs. The selection efficiency of $h^0 \rightarrow gg$ is lower by $2 - 4\%$ (see Figure 7.19).

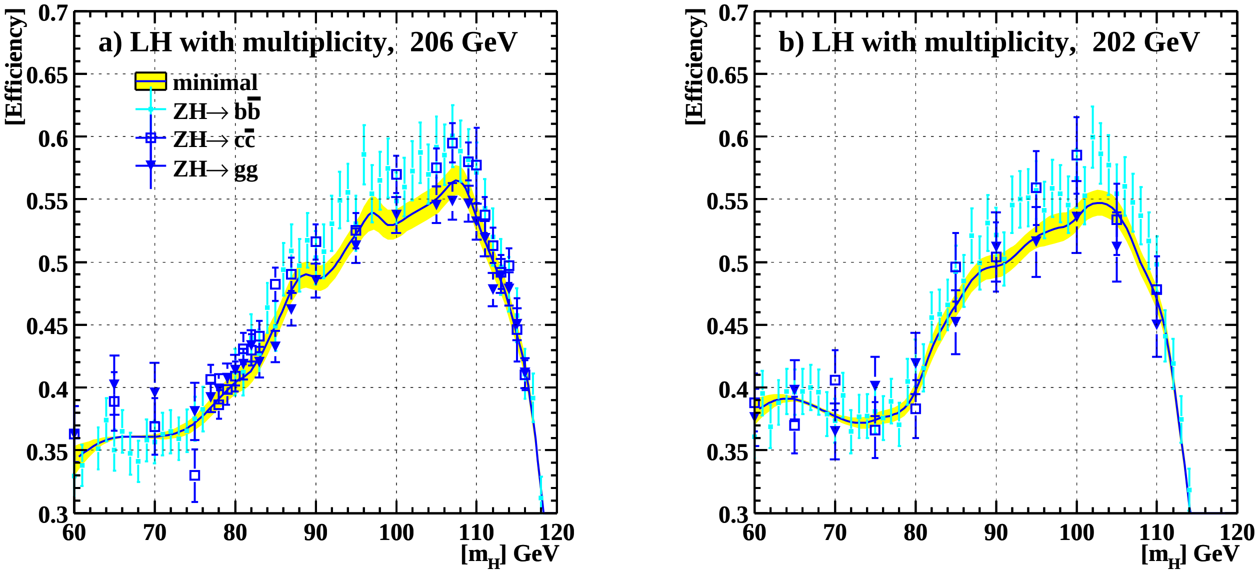

Figure 7.19: Selection efficiency of Higgs-strahlung after adding the multiplicity to the likelihood. Compared to Figure 7.8 the efficiency to select events in which Higgs bosons decay into gluons improves by up to 4%. The efficiency to select other hadronic Higgs decays does not change significantly.

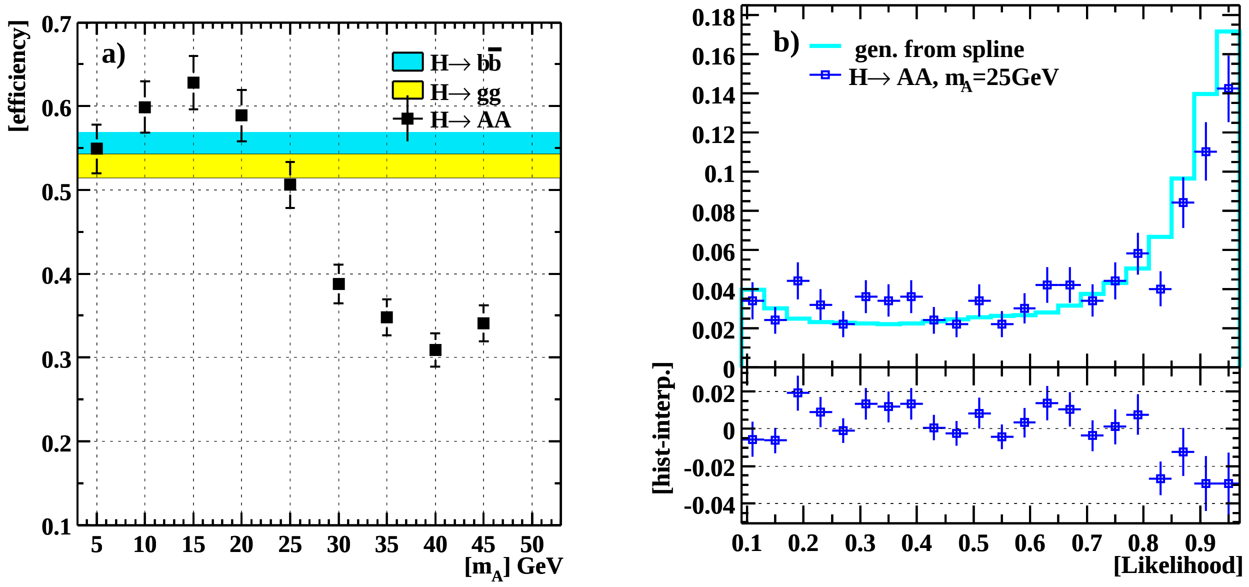

Figure 7.20: a) Selection efficiency of Higgs-strahlung in which the Higgs boson decays into a pair of CP-odd A bosons for a Higgs boson mass $m_{\mathrm{H}} = 100\,\mathrm{GeV}$ as a function of m_{A}. If the A is light enough the two hadronic jets caused by each A boson decay overlap and are reconstructed as only one jet. Thus, these events show a similar signature as hadronic Higgs boson decays. With increasing A boson mass, the boost decreases and the overlap of the jets becomes smaller. A 6-jet topology appears. The bands and the width indicate the selection efficiency and the statistical error of hadronic decays of Higgs bosons. b) Likelihood distribution obtained from Higgs-strahlung events in which the Higgs bosons decays into a pair of A bosons compared to a histogram generated from a 3D spline. The spline was fitted to histograms obtained from $\mathrm{e^+e^-} \to \mathrm{ZH} \to \mathrm{q\bar{q}q\bar{q}}$.

heavier state H^0. If H^0 is kinematically inaccessible a light A^0 might not be produced directly. However, if $m_{\mathrm{h}} > 2m_{\mathrm{A}}$, the decay mode $\mathrm{h}^0 \to \mathrm{A}^0\mathrm{A}^0$ becomes possible for certain choices of α and β, and may even dominate. Since, searches for the SM Higgs boson or flavour independent searches expect the lightest Higgs boson to decay into bottom quarks, tau leptons, light quarks or gluons, the lightest Higgs boson may escape detection.

The selection of Section 7.1 is applied unchanged to Higgs-strahlung, where the only considered decays of the Higgs boson are $\mathrm{h}^0 \to \mathrm{A}^0\mathrm{A}^0$. The Z and the A boson decay further into quark pairs. Thus, a 6-jet topology results. However, if the A boson is light enough the two jets resulting from each A boson decay overlap significantly and are reconstructed as one jet only.

The resulting selection efficiency and likelihood distribution for a Higgs boson with a mass $m_{\mathrm{h}} = 100\,\mathrm{GeV}$ is shown in Figure 7.20 . The selection achieves similar performance compared to $\mathrm{H} \to \mathrm{q\bar{q}}$ or $\mathrm{H} \to gg$ if $m_{\mathrm{A}} \lesssim 25\,\mathrm{GeV}$. The selection of $\mathrm{h}^0 \to \mathrm{A}^0\mathrm{A}^0$ is not expected to be less efficient for $m_{\mathrm{A}} \lesssim 25\,\mathrm{GeV}$ if the Higgs boson is heavier. However, if the Higgs boson is lighter the A bosons get smaller boosts, the two jets overlap less and the topology becomes more and more 6-jet-like.

The efficiency for this final state will be used in future joint interpretation of Higgs boson searches within the THDM.

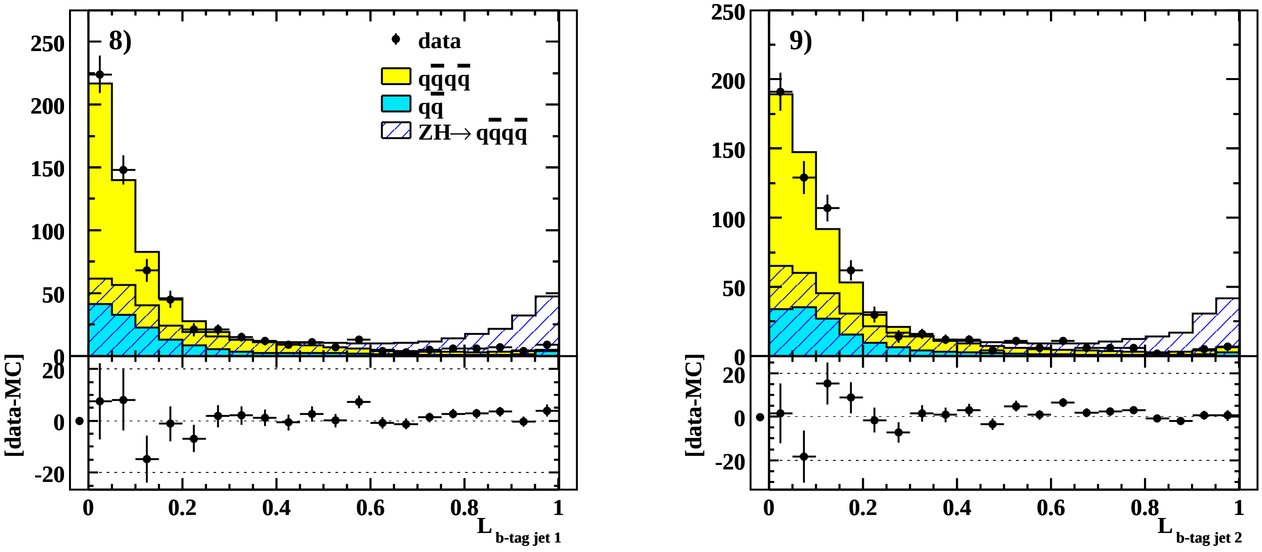

Figure 7.21: In the search for the SM Higgs boson, the background is reduced significantly by exploiting the properties of the dominant decay mode $\mathrm{H_{SM}} \to \mathrm{b\bar{b}}$. The b-likeliness of the two jets assigned to the Higgs boson candidate is estimated (b-tag). Figure 8 and 9 show the b-likelihood distribution of the more and less energetic jet under a mass hypothesis $m_{\mathrm{test}} = 100\,\mathrm{GeV}$. The signal distribution is scaled by a factor of 10.

7.3.3 Selection of SM-Higgs Bosons

If the search is limited to SM Higgs bosons, backgrounds are greatly reduced exploiting the properties of the dominant decay mode, $\mathrm{H_{SM}} \to \mathrm{b\bar{b}}$ ($m_{\mathrm{H_{SM}}} < 120\,\mathrm{GeV}$). The selection is performed as described in Section 7.1. In extension, the b-likeliness is calculated as described in [95] for both of the two jets which are assigned to the Higgs boson. The b-likeliness is determined from a variety of observables. Among them are: the displacement of secondary vertices if any, the vertex mass, and the transverse momentum of lepton candidates with respect to the jet axis, which is distinctive in semileptonic b decays.

The jets are ordered with respect to their energy and the b-likeliness assigned to each jet is used as an additional variable in the likelihood. The distributions of the b-likeliness of the more and less energetic jet is shown in Figures 7.21a and b. The data set recorded in 2000 does not show any enhanced b quark production.

The resulting likelihood is strongly peaked at one, unfortunately, for both signal and background. In order to get a flat background distribution at large likelihood values, the following transformation is applied:

$$\widetilde{\mathrm{LH}} := \frac{1}{1 + \exp\left\{1.3 \cdot \log_{10} \tan\left(\frac{\pi}{2}\mathrm{LH}\right)\right\}}.$$

The resulting background distribution becomes flat at large $\widetilde{\mathrm{LH}}$ while signal likelihood values still pile up at one (see Figures 7.22 a and b). The selection efficiency is shown for a weak cut $\widetilde{\mathrm{LH}} > 0.5$ in Figure 7.23a. In Figure 7.23b, the analysis is compared to the official SM Higgs boson search also using the 4-jet topology [71]. For the comparison a cut on the final

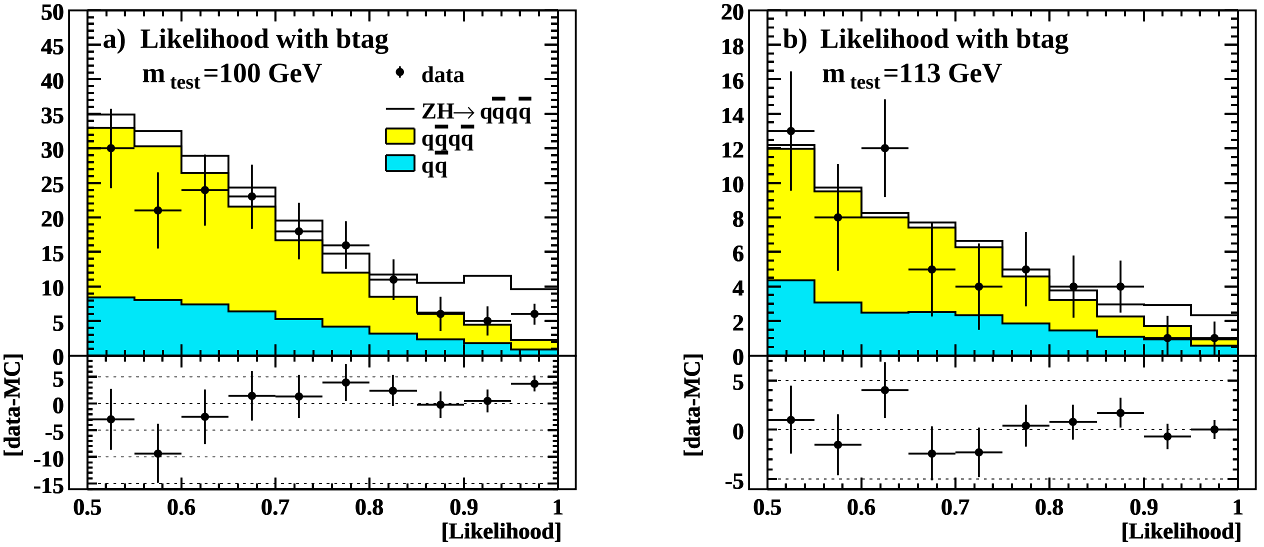

Figure 7.22: The b-tag dominates the likelihood, leading to a greatly enhanced separation of background and signal compared to the flavour independent analysis. The distribution represents the transformed likelihood. The mass hypothesis was $m_{\text{test}} = 100\,\text{GeV}$ and 113 GeV.

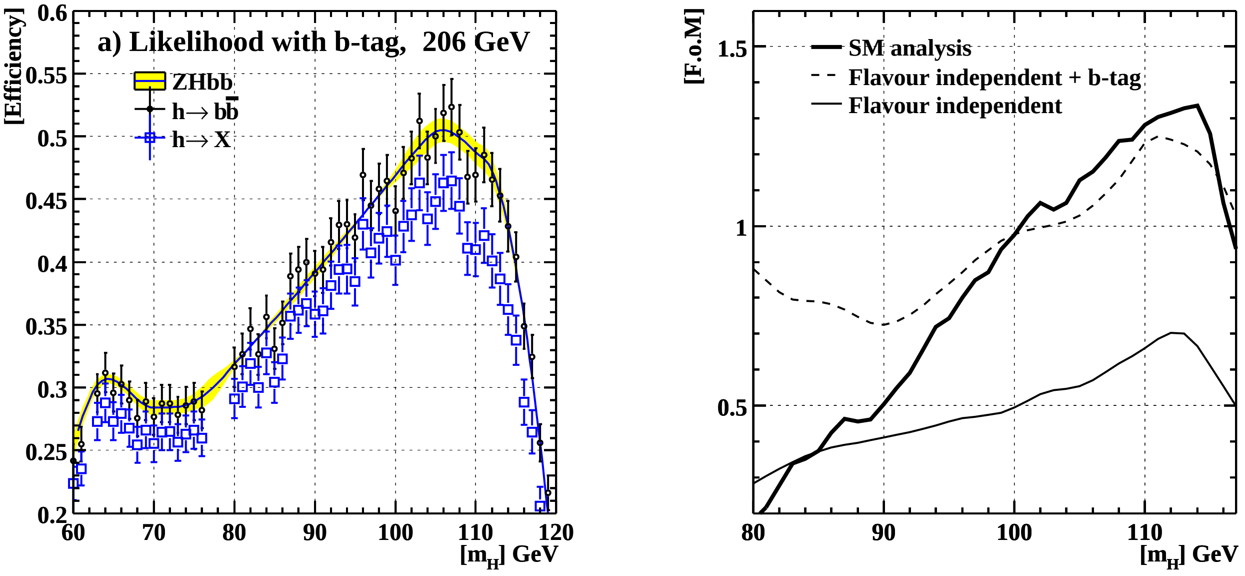

Figure 7.23: a) Selection efficiency of the b-tag enhanced analysis requiring $\widetilde{\mathrm{LH}} > 0.5$. The efficiency is shown for $\mathrm{h} \rightarrow \mathrm{b}\bar{\mathrm{b}}$ and for a Higgs boson assuming SM branching ratios ($\mathrm{h} \rightarrow \mathrm{X}$). b) Comparison with the official SM Higgs boson search also using the 4-jet topology. In the region below 100 GeV, better sensitivity is achieved analysing other than the 4-jet topology. Therefore, the official SM Higgs boson search was essentially designed for optimal performance close to the kinematic limit.

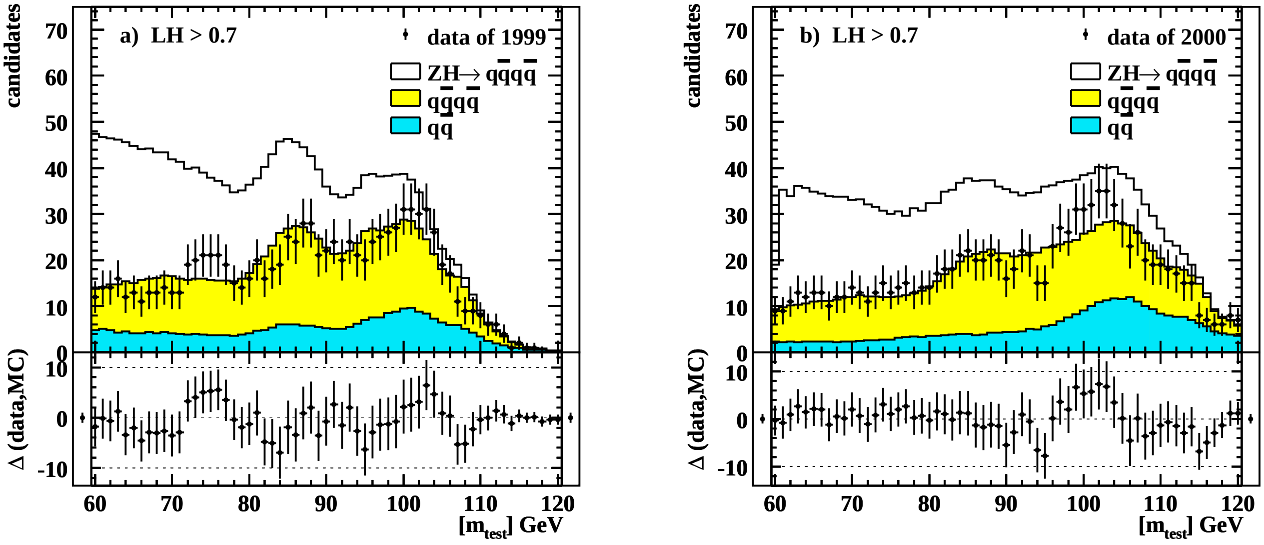

Figure 7.24: Number of candidates with likelihood values LH > 0.5 and LH > 0.7 after the likelihood was extended with the b-tag.

discriminating variable was chosen, such that optimal figure of merit is achieved close to the kinematic limit (see Formula (7.1)). At lower masses, the performance is improved relaxing the cut. The figure only shows an estimate of the sensitivity, since for the final interpretation, the events are weighted with their signal likeliness as will be described in Section 8.1. Due to the event weighting, the effective background is smaller.

Since, this analysis is less performant than the official search, it is not further pursued. Systematic errors have not been evaluated. They may turn out to be large since the applied transformation broadly spreads the very edge of the Likelihood distribution which may not be modelled correctly in this detail.

Nevertheless, the analysis does not reveal any deviation from the predicted SM background and yields results consistent with the official SM Higgs boson search. The number of selected candidates with likelihood values larger than 0.5 and 0.7 are shown for different mass hypotheses in Figures 7.24 a and b.

.

7.4 Systematic Errors

The signal selection efficiencies, background rates and the shape of the final discriminant are solely obtained from simulations. Since the analysis depends strongly on the reconstructed jet momenta, the modelling of the fragmentation process and the resulting resolution of the reconstructed jet momenta impact the selection efficiency.

A comparison of background simulation and data reveals differences in some of the used observables, which cannot be explained easily. Their treatment is described in Section 7.4.1. The influence of the jet momentum resolution and the fragmentation model are discussed in Section 7.4.2 and Section 7.4.3. The following additional potential error sources are considered:

- *Statistical error of simulation*: The limited number of simulated events limits the accuracy of the estimated background rate and the signal selection efficiency. The rate and the signal efficiency are approximated by a 2D spline describing the mass and centre-of-mass energy dependence. The spline is fitted to the resulting rates and efficiencies of various simulations. The fit error on the spline parameters is used as systematic error.

- *Track resolution:* while single track resolution especially the resolution of the impact parameter is an important issue in case bottom flavoured hadrons are reconstructed, the resolution plays only a minor role in this case as only properties calculated from reconstructed jet momenta are used in the selection. The mismodelling of the jet resolution has been investigated separately and covers the mismodelling of single track resolution.

- *Flavour composition*: the selection has only a small dependency on the flavour of the primary quarks responsible for a jet. Therefore, a change of the flavour composition within the uncertainties has only a negligible effect. However, the jet resolution of gluon jets is worse, as a result the selection efficiency of $\mathrm{H} \rightarrow gg$ is smaller than the one of $\mathrm{H} \rightarrow \mathrm{q\overline{q}}$. This has been taken into account by considering only the minimal selection efficiency.

- *Colour reconnection* [96]: the gluon exchange between quarks of different bosons is not taken into account by the four fermion event simulations. This effect is usually referred to as *colour reconnection.* Special simulations implementing phenomenological models have been used in order to estimate the effect on the W mass measurement [97]. An error smaller than 0.1 GeV has been assigned. The achieved resolution of the Higgs boson mass is of the order of 5 to 10 GeV depending on the cut on the likelihood distribution. Thus, the effect of colour reconnection is completely negligible.

The likelihood distribution is used as a final discriminant. The likelihood distribution does not depend directly on the shape of the input variables but rather on the ratio of signal over signal and background expectation. Since all the input variables have only limited separation power the ratio of signal over signal and background expectation changes slowly. It turned out that the shape of the likelihood is robust against the tested uncertainties.

7.4.1 MC Reweighting

Some of the observables used during preselection show differences between the simulation and data. The differences neither vanish after adding signal, nor is there an obvious connection to parameters of the simulation. Nonetheless, to estimate the effect of this mismodelling, weights are assigned to the simulated events in order to improve the agreement of simulation and data. The weights are normalised such that the sum over the weights of all four-jet events[7] equals the number of four-jet events prior to reweighting. The difference in the resulting selection efficiency of the unweighted and weighted samples is considered as systematic error.

The mismodelling of the preselection variables is not assumed to depend on the centre-of-mass energy. However, it may differ between the years 1999 and 2000, since the detector calibration changed and the parameter set of the simulation was tuned separately. Therefore,

---

[7] Events are denoted *four-jet events* if they pass steps 1. to 3. of the preselection (Section 7.1.1): LEP2 multi-hadron, $y_{43} > 0.03$, and $\sqrt{\mathrm{s'/s}} > 0.794$.

the procedure described in the following was performed independently for the data set of 1999 and 2000. The whole data set of each year was combined to gather enough statistics for a comparison. In order to match the centre-of-mass energies of the data set samples of simulated events are combined such that average energy and luminosity in each interval $[E_i, E_{i+1}]$ agrees:

$$\lambda_i E_i N_i + (1-\lambda_i) E_{i+1} N_i = \left(\sum_j E_j \mathcal{L}_j \right) / \sum \mathcal{L}_j;\ \forall E_i \leq E_j < E_{i+1},$$

where E_i and N_i denote the centre-of-mass energy and the number of simulated events in each sample, E_j and $\mathcal{L}_j$ the centre-of-mass energy and corresponding luminosity of a data sub sample, and λ_i a weight applied to all simulated events of the whole sample i.

The distribution of one preselection variable[8] is determined from data and the background simulation, and a spline is fitted to ratio of the normalised distributions. The spline is constructed such that a $\chi^2/\text{d.o.f.} \simeq 1$ is obtained. The value of the spline is used to weight each simulated event, unless the considered preselection variable yields values outside of the domain of the spline. In the latter case, the ratio of the integrated distributions is used as an event weight. The integral is built over the region below and above the domain, respectively. The weighted events of the background and signal simulation are reanalysed and the resulting difference of the background rate and signal selection efficiency is used as systematic error. The procedure is repeated for each preselection variable. The distributions before and after reweighting are shown in Figures 7.25 and 7.26. Since the preselection variables enter the likelihood directly or indirectly and their significance varies with respect to the test mass, the systematic errors, shown in Figure 7.28, also depend on the test mass. The relative errors of two and four fermion background are in the ranges $0.04\ldots0.09$ and $0.03\ldots0.10$. The error on the signal selection efficiency varies within the range $0.01\ldots0.03$.

7.4.2 Jet momentum resolution

The main selection criteria are based on the measured jet momenta. The momentum resolution was compared between data and simulation, and the observed difference was considered as source of systematic errors.. The resolution was investigated following [98]. The method is described in the following paragraphs. The observed difference in the resolution is used to modify the measured jet momenta in each simulated event, the analysis of signal and background is repeated and the resulting difference of the signal selection efficiency and background rate is used as systematic error.

The jet resolution is investigated using calibration data of 1999 and 2000, respectively, and the corresponding simulations. The calibration data samples are taken at the $\sqrt{\mathrm{s}} = m_\mathrm{Z}$. From these events, a sample with two hadronic jets is selected, requiring the event to be tagged as LEP2 multi-hadron event and that 2 jets are constructed with a jet resolution parameter $y_{32} < 0.02$. Further, the energy has to be disposed evenly in the forward and backward part of the detector, i.e. the z-component of the reconstructed total momentum has to fulfil $|p_z| < 20\,\text{GeV}$. Events with ISR photons (see Section 7.1.1) are rejected by the requirement $\sqrt{\mathrm{s}'/s} > .8$.

The selected events should contain two back to back jets resulting from the two quarks of the Z decay. Thus, the sum of the polar angles of the two jets, $\theta_1 + \theta_2$, is expected to be 180°, the two azimuthal angles, ϕ_i, are expected to add up to a full circle $\phi_1 + \phi_2 \text{ modulo } 2\pi = 0$ and

---

[8] Item 2., and 4. to 7. of Section 7.1.1

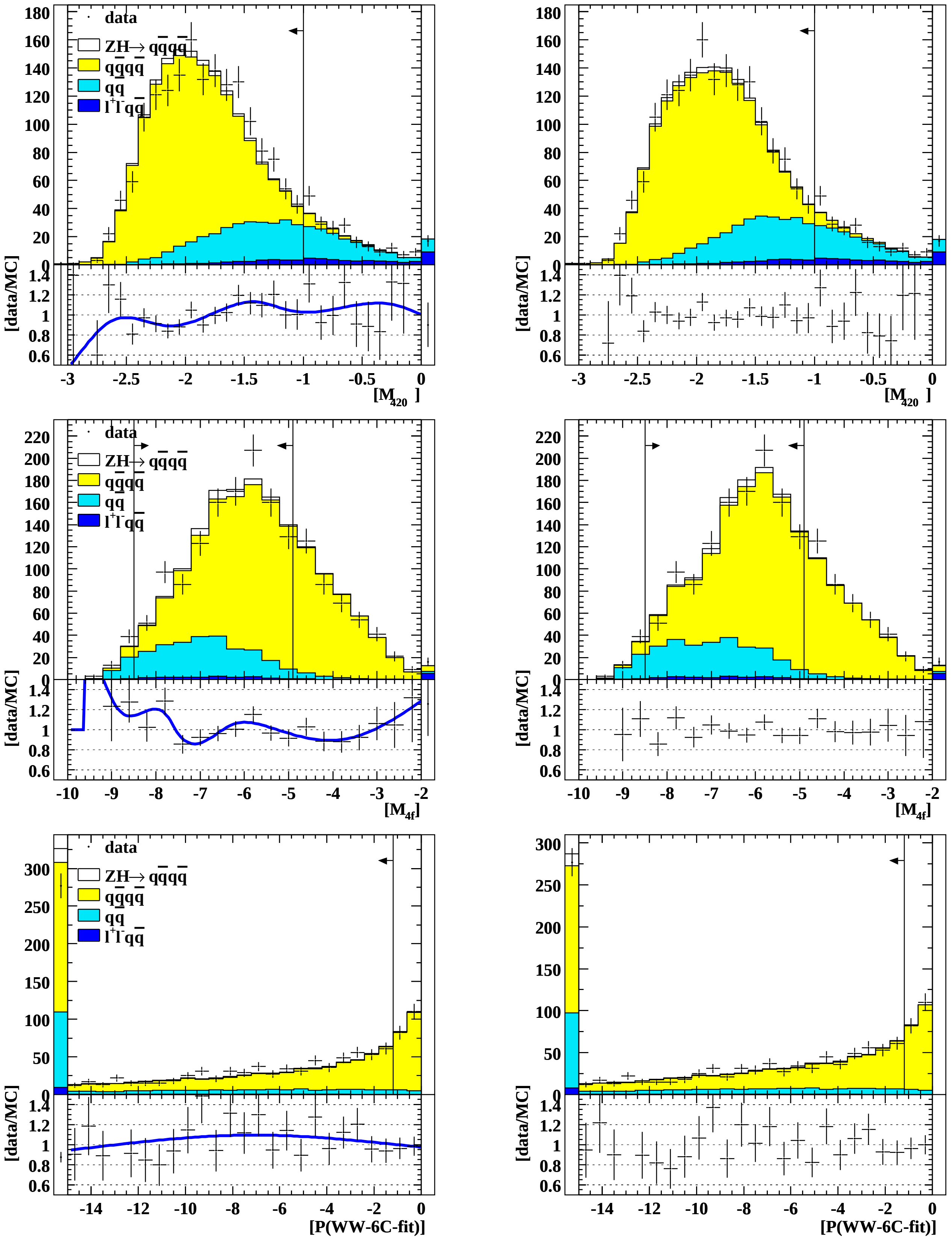

Figure 7.25: Preselection variables before(left) and after(right) reweighting as described in Section 7.4.1. Each figure shows the distribution found in data of 2000 and the expectation from simulation. Below the ratio of the normalised distributions is shown and a spline fitted to this ratio.

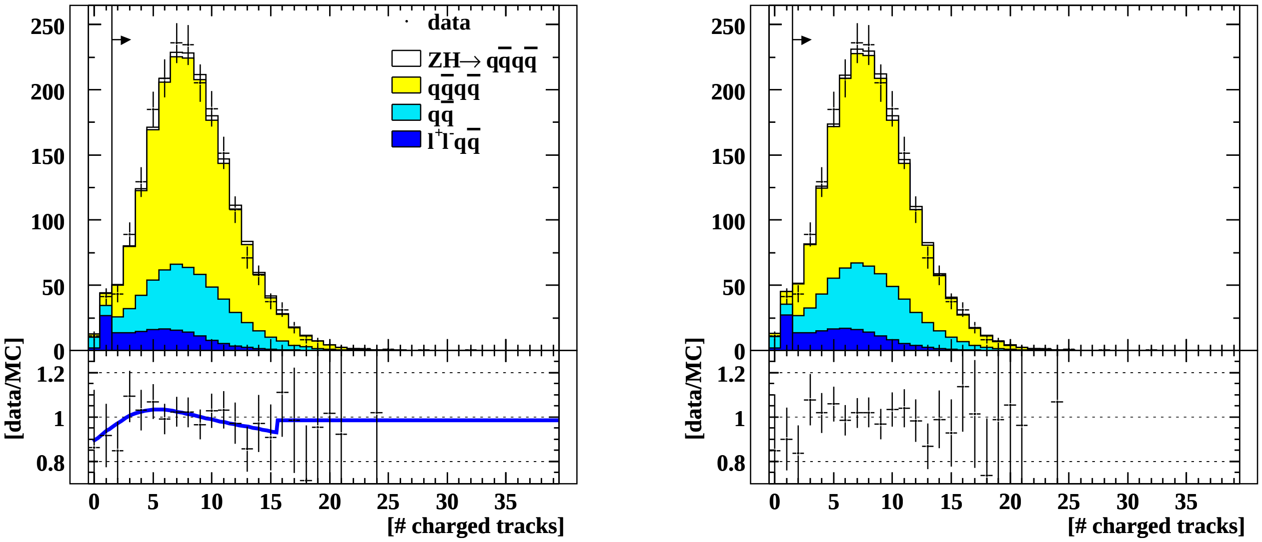

Figure 7.26: Total number of tracks seen in the jet chamber before(left) and after reweighting(right). The simulation suggests a slightly broader distribution.

the total reconstructed energy of the two jets, $E_1 + E_2$, should be equal to the centre-of-mass energy $\sqrt{\mathrm{s}}$. Distributions of these relations are generated from simulated events and data. The ratios in bins of $\cos\theta$ are then used to extract correction factors as a function of $\cos\theta$ on the jet momentum resolution, σ_θ, σ_ϕ, on the resolution of the reconstructed energy σ_{E}, and on the mean value of the reconstructed energy $< E >$. The correction factors, depicted in 7.27, show a dependence on θ. Therefore, individual correction factors are obtained for ten equidistant regions in $\cos\theta$ and a spline is fitted such that a χ^2 per degree of freedom of the order of 1 results. The resolution is generally better in the simulation.

With the help of the correction splines the reconstructed jet properties, ϕ, θ and $\log p$, are modify in each simulated event separately. In order to correct the overestimated resolution, the jet properties are modified by Gaussian distributed random values. The width of the Gaussians are chosen to be $\sqrt{\sigma_i c_i(\theta)}$, where σ_i is the measured error of θ, ϕ or $\log p$ and $c_i(\theta)$ the corresponding correction spline. The resulting distributions equal the original distribution folded with a Gaussian of the width $c_i(\theta)$. Additionally, a global scaling factor is applied to $\log p$ to correct the jet energy, which is overestimated. The procedure has been verified using the calibration data. The data is compared to simulated events with and without the smearing applied. The resulting ratio is depicted in Figure 7.27.

The selection, described in 7.1, is repeated for the modified events. This involves recalculation of the matrix elements and redoing the kinematic fits. The resulting difference of the selection efficiency, shown in Figure 7.29, is taken as systematic error. The contribution is relatively small compared to the statistical error on the background and signal expectation. The relative errors of the background rate and of the signal selection efficiency are in the ranges $0.00 \ldots 0.02$ and $0.00 \ldots 0.02$, respectively.

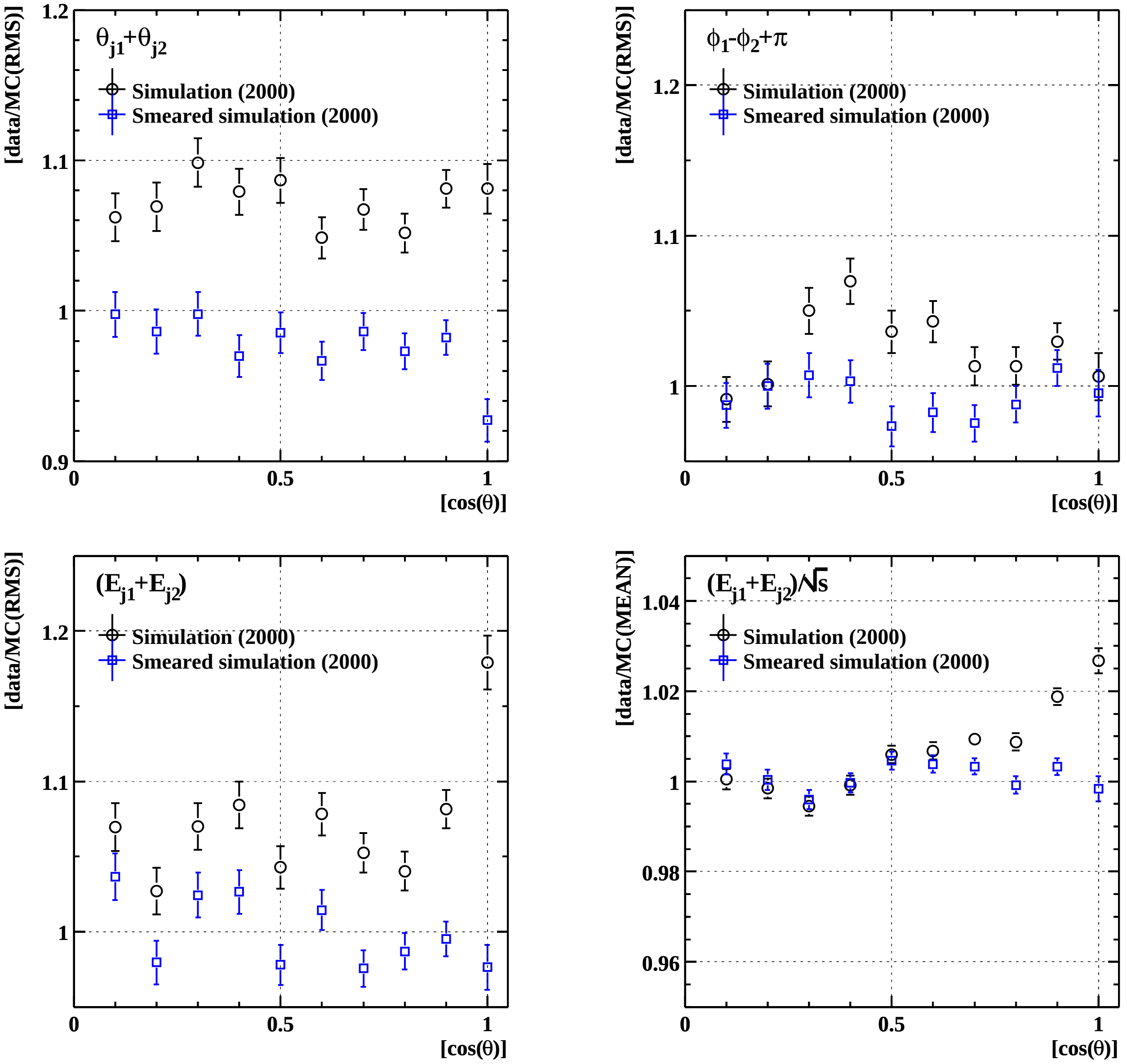

Figure 7.27: Jet momentum resolution of data versus simulation. The data was taken in the calibration runs at the beginning of 2000 at $\sqrt{\mathrm{s}} = m_{\mathrm{Z}}$. Shown is the ratio between the RMS values of $\theta_1 + \theta_2$, $\phi_1 - \phi_2 + \pi$ and $\mathrm{E}_1 + \mathrm{E}_2$, and the ratio of the mean values of $(\mathrm{E}_1 + \mathrm{E}_2)/\sqrt{\mathrm{s}}$.

Source	Total background	Signal
Modelling of variables	0.04 ... 0.09	0.01 ... 0.03
$\mathrm{ME}_{\mathrm{QCD}}$	0.00 ... 0.02	0.00 ... 0.02
$\mathrm{ME}_{\mathrm{4f}}$	0.02 ... 0.07	0.01 ... 0.02
P(WW 6C-fit)	0.02 ... 0.06	0.00 ... 0.02
y_{34}	0.00 ... 0.01	0.00 ... 0.01
Multiplicity	0.00 ... 0.01	0.00 ... 0.00
Jet momentum resolution	0.00 ... 0.02	0.00 ... 0.02
Fragmentation	0.02 ... 0.08	
4 Fermion Cross-sections	0.02	
Total error	0.05 ... 0.12	0.01 ... 0.03
Limited statistic of simulation	0.00 ... 0.02	0.01 ... 0.05

Table 7.3: Relative systematic errors on background rate and signal selection efficiency. The systematic errors vary within the indicated range depending on the test mass and centre-of-mass energy.

7.4.3 Fragmentation

The fragmentation process cannot be calculated completely in perturbation theory. However, phenomenological models exist which can be tuned to match the observations (see Section 6.2). The considered models are string and cluster fragmentation. The first model is implemented in JETSET, which is part of the event generator PYTHIA. The second model is implement in HERWIG. The latter model does not describe the data as good as a properly tuned version of JETSET, which has more parameters to be adapted. The two simulations of the fragmentation process were compared at a centre-of-mass energy of 206 GeV. In both cases the same partons were fragmented and hadronised. The difference in the selection efficiency was taken as systematic error. The error varies significantly with the test mass as depicted in Figure 7.30. The relative errors on the four and two fermion event rates are in the ranges 0.01 . . . 0.07 and 0.09 . . . 0.16. These are the major contributions to the systematic error.

7.4.4 Summary on Systematic Errors

The systematic errors are summarised in Table 7.3. The individual errors are considered to be uncorrelated, but each source, except the statistical component, is considered to be correlated over the two years and with respect to the various centre-of-mass energies.

The total systematic error on the background rate and signal efficiencies varies with the test mass but only slightly with the centre-of-mass energy. The relative errors are in the ranges 0.05 . . . 0.12 and 0.01 . . . 0.03 for background and signal events, respectively. The dominant contributions are due to uncertainties of the modelling of the fragmentation process (0.02 . . . 0.08) and due to the modelling of the variables (0.04 . . . 0.09). The modelling of the jet resolution has only little impact.

Due to the large background rate, the systematic error on the background has significant impact on the final result. This is discussed further in Section 8.1.2. The error on the signal selection efficiency is of minor importance.

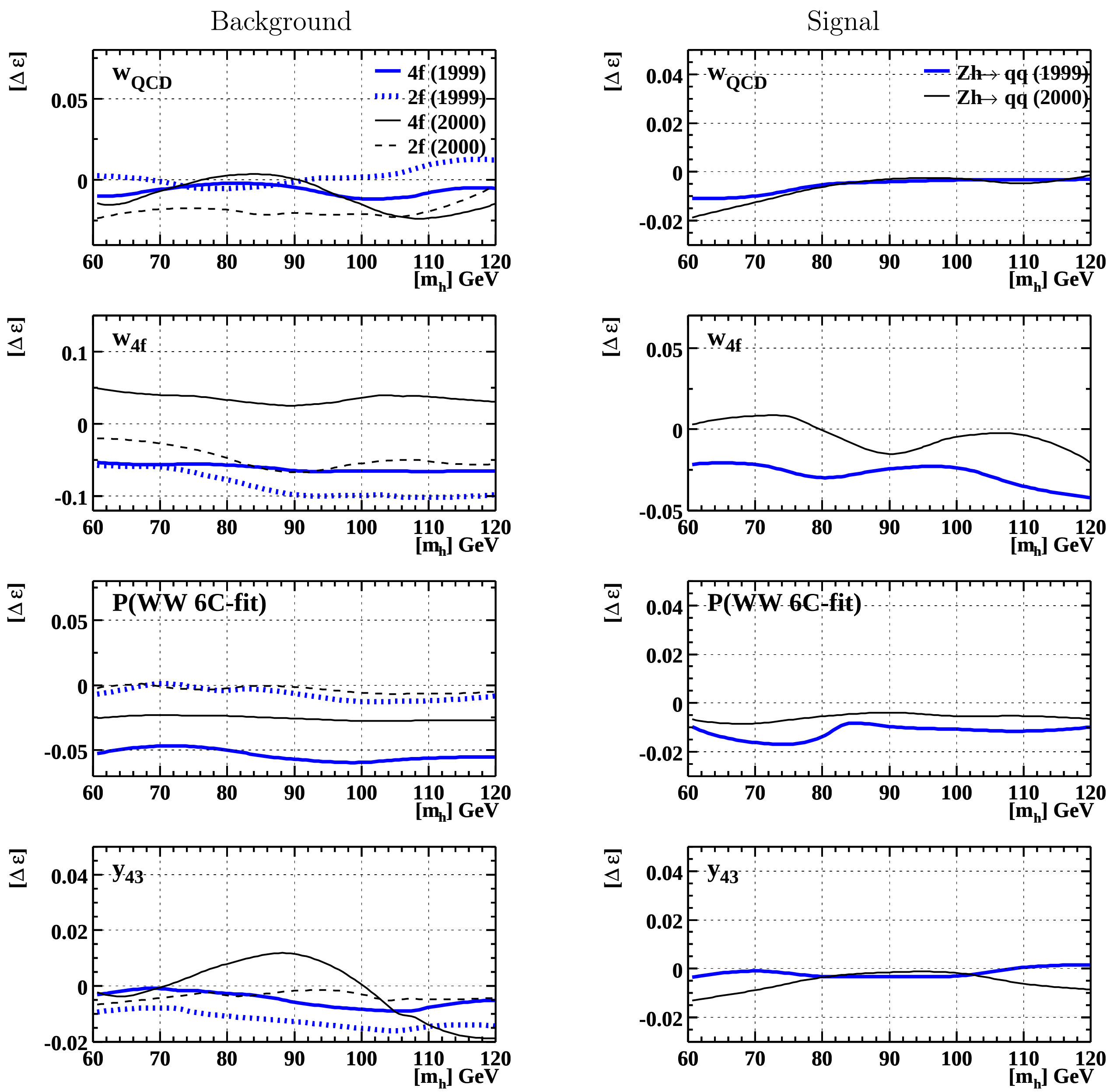

Figure 7.28: Relative difference of selection efficiencies after reweighting as described in Section 7.4.1. The simulated events have been reweighted according to the relative difference between simulation and data of the preselection variables. The reweighting has been performed independently for the data of year 1999 and 2000. The relative differences obtained from 1999 and 2000 data are shown at $\sqrt{s} = 200\,\text{GeV}$ and $\sqrt{s} = 206\,\text{GeV}$, respectively. The impact of the reweighting depends only slightly on the centre-of-mass energy.

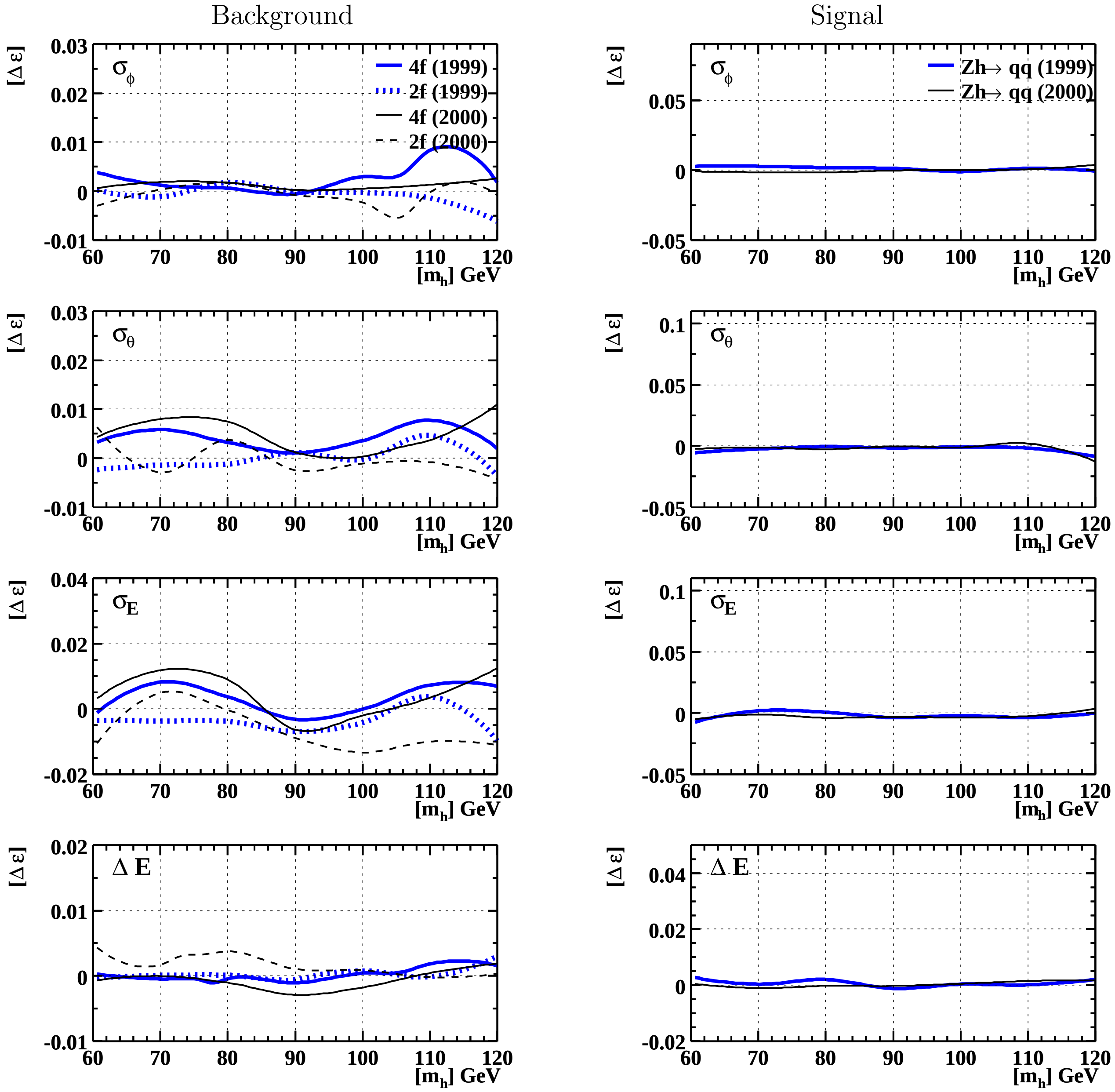

Figure 7.29: Relative difference of selection efficiencies after modifying the resolution of jet momenta as described in Section 7.4.2. This procedure has been performed independently for the data of year 1999 and 2000. The relative differences obtained from 1999 and 2000 data are shown at $\sqrt{s} = 200\,\text{GeV}$ and $\sqrt{s} = 206\,\text{GeV}$, respectively. The systematic errors depend only slightly on the centre-of-mass energy.

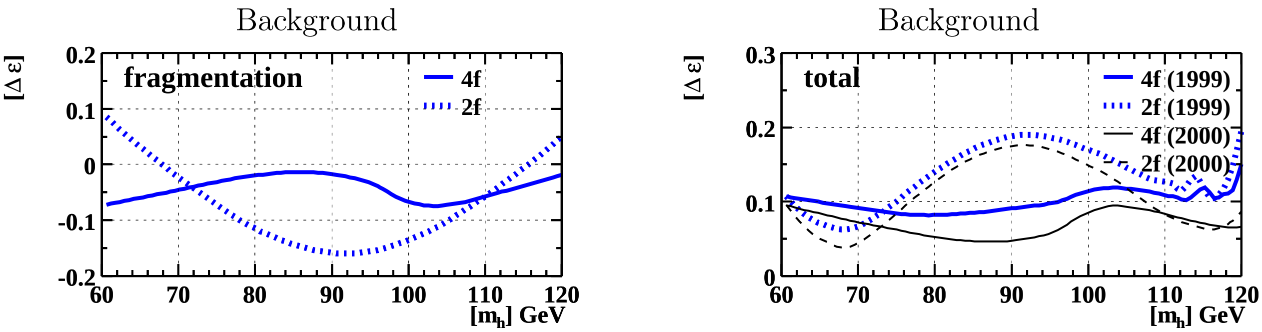

Figure 7.30: Relative difference of selection efficiency of background events if HERWIG is used instead of JETSET to simulate the fragmentation process(left). This is the dominant contribution to the total systematic error (right). The error was evaluated at $\sqrt{s} = 206\,\mathrm{GeV}$. The same error is assigned to the analysis of 1999 and 2000 data.

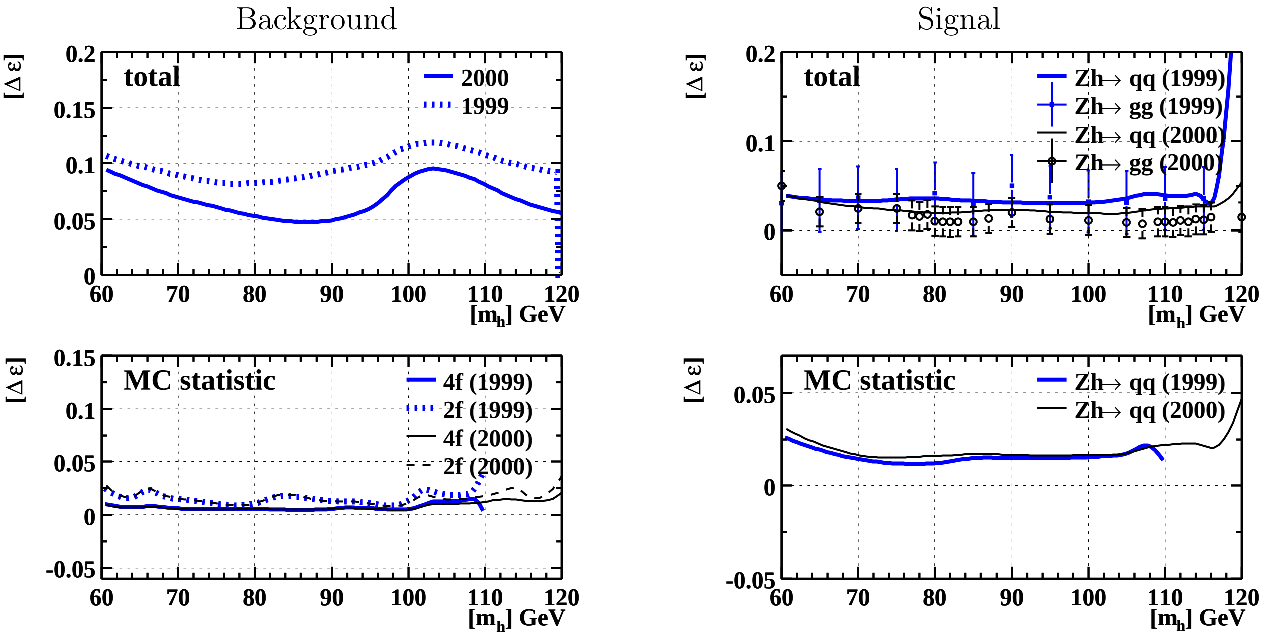

Figure 7.31: Statistical error of selection efficiencies and combined systematic error. The systematic error sources are assumed to be uncorrelated, and the errors are added quadratically. The systematic errors of four and two fermion background are combined according to the composition of the total background. The errors are shown for a centre-of-mass energy of 206 GeV and 200 GeV for the analysis of 2000 and 1999 data.

Chapter 8

Interpretation

No evidence has been found for the existence of Higgs bosons, neither in the four-jet channel, nor in other flavour independent search channels performed by the ALEPH, DELPHI, L3 and OPAL collaborations. Therefore, the observed candidates, together with the background expectation, are used to calculate limits on the production rate of scalar bosons in Higgs-strahlung. The method used to derive the limit is described in the following section. Initially, the method is applied to the four-jet channel only. The sensitivity is significantly increased by combining all flavour independent searches performed within the OPAL collaboration. The additional channels are summarised in Section 8.2 and the combined limit is discussed. The preliminary LEP combined limit is shown in Section 8.3. In Sections 8.4 to 8.6, the combined limit is interpreted within general THDMs, the large-μ scenario of the MSSM, and the Randall-Sundrum model.

8.1 Upper Limit on the Higgs-Strahlung Cross-Section

The upper limit on the production rate of Higgs bosons is calculated following the method described in [99]. A summary is given in the subsequent section. The method is tested with toy experiments simulating results of the four-jet channel, which correspond to the years 1999 and 2000, and the method is applied to the candidates found in these two years. The rate limit is quoted in terms of a scale factor $k95$:

$$k95 := \frac{\sigma_{95}(\mathrm{e^+e^-} \to \mathrm{Z^0h^0} \to \mathrm{Xq\bar{q}})}{\sigma_{\mathrm{SM}}(\mathrm{e^+e^-} \to \mathrm{Z^0h^0})} \tag{8.1}$$

which relates the maximally permitted cross-section at 95% confidence level, σ_{95}, to the hypothetical cross-section, σ_{SM}, of a SM Higgs boson. In this case, the scale factor is the product of the branching ratio $\mathrm{Br}(\mathrm{h^0} \to 2\,\mathrm{jets})$ and the coupling to the Z boson squared. In order to combine data from various $\sqrt{\mathrm{s}}$, it is assumed that the $\sqrt{\mathrm{s}}$-dependence of a possible signal cross-section is the same as that for a SM Higgs boson of the same mass.

8.1.1 Calculation of Exclusion Limits

An upper limit on the production cross-section is calculated by comparing the number of selected events n with the predictions, obtained from simulations. If the selection is not completely background free, a more stringent limit can be obtained by weighting the events according to their signal likeliness and comparing the measured sum of weights, $\omega_{\text{obs}} := \sum_i \omega_i \leq n$, with the prediction ω_{exp}. There are two widely used weighting schemes. There is the likelihood ratio estimator [28]:

$$\omega_i := \ln\left(1 + \frac{s(x_i)}{b(x_i)}\right), \tag{8.2}$$

where x_i denotes the value of a discriminating variable of the i-th candidate, $s(x_i)$ and $b(x_i)$ the signal and background density. This weighting scheme is disadvantageous in regions where the background expectation vanishes, since the weights diverge there, and are highly sensitive to systematic errors. A similar weighting scheme is:

$$\omega_i := \frac{s(x_i)}{s(x_i) + 2 \cdot b(x_i)} \tag{8.3}$$

This weighting scheme is not the optimal choice for small rates, but it is less sensitive to vanishing background. In order to calculate a limit with a certain confidence level, the probability $\mathcal{P}(N_{\text{prod}}, \omega)$ to observe a certain weight sum ω for a total production rate N_{prod} is needed. This probability is calculated separately for every Higgs boson mass hypothesis to be tested. The probability is given by the sum over the individual probabilities of all possible observable rates n giving rise to ω. The probability is given by the Poisson probability to measure n events if the average production rate is N_{prod} times the probability $\mathcal{P}_n(\omega)$ that n events sum up to a weight ω. Altogether this yields:

$$\mathcal{P}(N_{\text{prod}}, \omega) = \sum_{n \geq \omega}^{\infty} \frac{N_{\text{prod}}^n}{n!} \mathrm{e}^{-N_{\text{prod}}} \cdot \mathcal{P}_n(\omega). \tag{8.4}$$

Obviously, $\mathcal{P}_n(\omega) \equiv 0$ in case $\omega > n$ or $\omega < 0$. If the probability $\mathcal{P}_1(\omega)$ is known, the probability $\mathcal{P}_2(\omega)$, i.e. the probability to observe a certain weight sum ω from two selected events, is given by the combined probability of all possible combinations of weights ω_1 and ω_2 adding up to ω. This can be derived from $\mathcal{P}_1$ by folding: $\mathcal{P}_2(\omega) = \int \mathcal{P}_1(\omega - \widetilde{\omega}) \cdot \mathcal{P}_1(\widetilde{\omega}) d\widetilde{\omega}$. The integrand vanishes outside the boundaries $\max(0, \omega - 1) \leq \widetilde{\omega} \leq \min(\omega, 1)$ because $\mathcal{P}_n \equiv 0$ outside the domain $[0, n]$. Successive folding leads to the recursive formula:

$$\mathcal{P}_n(\omega) = \int_{\max(0, \omega-(n-1))}^{\min(1,\omega)} \mathcal{P}_{n-1}(\omega - \widetilde{\omega}) \cdot \mathcal{P}_1(\widetilde{\omega}) d\widetilde{\omega} \tag{8.5}$$

If the candidate sample is not absolutely background free, the weight sum of the background has to be taken into account. In the same way, the probability $\mathcal{P}^{\text{bg}}(\nu)$ to observe a certain weight sum ν for an average number of background events N_{bg} is given by (8.4) and the probability $\mathcal{P}_n^{\text{bg}}(\nu)$ that n background events have a weight ν is defined by (8.5). The combined probability $\widetilde{\mathcal{P}}(N_{\text{prod}}, \omega_{\text{obs}})$ to observe a certain weight sum ω_{obs} for a given signal hypothesis N_{prod} and background expectation N_{bg} is the sum over all possible combinations of signal and background rates with $\omega_{\text{obs}} \equiv \omega_{\text{sig}} + \nu$. This probability is obtained by folding the signal and background probabilities:

$$\widetilde{\mathcal{P}}(N_{\text{prod}}, \omega_{\text{obs}}) := \int_0^{\omega_{\text{obs}}} \mathcal{P}(\omega_{\text{obs}} - \nu) \cdot \mathcal{P}^{\text{bg}}(\nu) d\nu \tag{8.6}$$

Using this probability $\widetilde{\mathcal{P}}(N_{\mathrm{prod}}, \omega_{\mathrm{obs}})$, a limit N_{CL} on the average production rate N_{prod} can be calculated with a certain confidence level CL. The limit N_{CL} is placed such that for $\widetilde{N}_{\mathrm{prod}}$ larger than the upper limit N_{CL}, the probability to measure this weight sum ω_{obs} or a smaller value is less than $1-\mathrm{CL}$. The limit can be obtained by solving the following equation for N_{CL}:

$$1-\mathrm{CL} \overset{!}{=} \int_0^{\omega_{\mathrm{obs}}} \widetilde{\mathcal{P}}(N_{\mathrm{CL}}, \omega) d\omega \tag{8.7}$$

Usually N_{95}, the limit on the production rate with 95% confidence level, is quoted. In order to quantify the significance of the observed N_{95}, the rate limit, which is expected from background only, is computed.

The expected rate limit, N_{95}^{exp}, is calculated from the weight sum ω^{exp}, where ω^{exp} is defined as the median of the distribution (8.6) under the "background only" hypothesis, i.e. $N_{\mathrm{prod}} = 0$:

$$\int_0^{w^{\mathrm{exp}}} \widetilde{\mathcal{P}}(N_{\mathrm{prod}}, \omega) d\omega \overset{!}{=} \mathcal{P}, \tag{8.8}$$

where $\mathcal{P} = \frac{1}{2}$. The region $w^{\mathrm{exp}} \pm \sigma_\omega$, which contains weights resulting from 68% of the experiments, is obtained by solving (8.8) with $\mathcal{P} = \frac{1}{2} \pm 34\%$. Finally, Equation (8.7) is solved for N_{95}^{exp} replacing ω_{obs} with ω^{exp} and $\omega^{\mathrm{exp}} \pm \omega_\sigma$. The expected rate limit is a good measure of the sensitivity of a search and allows the comparison between different channels and experiments.

This method allows to combine different analysis easily if the analysed data samples do not overlap. This is achieved by calculating the combined weight sum ω of all the analyses: $\omega = \sum_i \sum_{j_i} \omega_{j_i}$, where ω_{j_i} denotes the weight of the j-th candidate of analysis i. In order to perform the computation, the probabilities $\mathcal{P}^{\mathrm{bg}_i}(\nu)$ and $\mathcal{P}_1^i(\omega)$ are needed for each analysis.

8.1.2 Treatment of Systematic Errors

Due to systematic errors, the average background rate and signal efficiency are not known exactly. Therefore, the calculated limit might be too optimistic if systematic errors are not taken into account. Here, the systematic errors are treated according to [100]. The implementation can be found in [101].

Errors are treated either as fully correlated or fully uncorrelated among different channels and between signal and background. Correlated errors are considered to result from a single error source.

In order to estimate the impact of the systematic errors, toy experiments are performed. In each toy experiment j a normal distributed random number ξ_j^l is chosen for each independent error source l. The random number is used to modify the signal[1] and background expectation $\langle s_i \rangle$ and $\langle b_i \rangle$ of all channels i to which the error l applies. The magnitude of the relative errors $\sigma_{s_i}^l$ and $\sigma_{b_i}^l$ of the signal and background rate and the relative sign defines the amount by which the expectation is increased or decreased. The resulting expected rates are $\langle s_{ij} \rangle$ and $\langle b_{ij} \rangle$:

$$\langle s_{ij} \rangle := \sum_l \sigma_{s_i}^l \xi_j^l \langle s_i \rangle \;\text{ and }\; \langle b_{ij} \rangle := \sum_l \sigma_{b_i}^l \xi_j^l \langle b_i \rangle \,.$$

---

[1] The signal expectation is defined up to a factor k_0, which is the product of the couplings of the lightest Higgs boson to quarks and the Z boson squared.

In [101], the whole calculation, which is described in the previous section, is repeated for each toy experiment, using the modified signal and background expectations. However, the numerical difference is not significant if the weight sum ω is fixed, and only the probabilities $\mathcal{P}^{\mathrm{bg_i}}(\nu)$ and $\mathcal{P}_1^i(\omega)$ are modified in each toy experiment.

If the systematic errors are of similar magnitude compared to the statistical errors, the weights chosen according to (8.2) or (8.3) are not optimal. The additional uncertainty of the signal and background rate due to systematic errors reduces the sensitivity of a search. Thus, a search method with small systematic errors can turn out to be more sensitive than a search method which yields larger weights but also has larger systematic errors.

Since in this case (see the following section) systematic errors have a significant impact on the resulting limit a weighting scheme was used that takes systematic errors into consideration [101]:

$$\omega_{ij} := \frac{k_0 s_i(x_j)\left(1 - \sum_l \sigma^l_{s_i}\right) - b_i(x_j)\sum_l \sigma^l_{b_i}}{k_0 s_i(x_j) + b_i(x_j)}. \tag{8.9}$$

The index j denotes a bin of the discrete signal or background density function of the discriminating variable of channel i, $s_i(x_j)$ or $b_i(x_j)$. The relative systematic errors on the signal or background expectation are given by $\sigma^l_{s_i}$ and $\sigma^l_{b_i}$, where different error sources are distinguished by the index l. The parameter k_0 denotes a scaling factor, applied to the signal rates of each channel. As a consequence of this weighting scheme, channels are switched off if the expected signal rate $k_0 s_i(x_j)\left(1 - \sum_l \sigma^l_{s_i}\right)$ is smaller than the error on the background rate. The optimal weights for a cross-section limit are obtained if the scaling factor k_0 is close to the actual limit $k_0 \simeq N_{95}/\sum_{ij} s_i(x_j)$. However, in this analysis k_0 was chosen to be 1, thus the signal rates are those expected from a SM Higgs boson.

8.1.3 Upper Limit on Higgs-Strahlung Using 4-Jet Events

The candidates passing the selection of Section 7 are now used to calculate a limit on the Higgs boson production rate. Selected events are weighted according to the value of the likelihood x_i(7.4):

$$s(x_i) \equiv \mathrm{LH}^{\mathrm{sig}}(x_i) \qquad \text{and} \qquad b(x_i) \equiv \sum_j \widetilde{\sigma}_j \mathrm{LH}^{\mathrm{bg}_j}(x_i)$$

$\mathrm{LH}^{\mathrm{sig}}$ and $\mathrm{LH}^{\mathrm{bg}}$ denote the signal and, respectively, background likelihood distribution and x_i the actual likelihood value of the i-th event. The likelihood values of the different background sources are weighted with their effective cross-sections, i.e. cross-section σ_j times selection efficiency ϵ_j, $\widetilde{\sigma}_j := \sigma_j \epsilon_j$. For the actual calculation $\mathcal{P}_1(\omega)$ and $\mathcal{P}_1^{\mathrm{bg}}(\omega)$ are needed. These probabilities can be calculated from the signal and background likelihood distributions. Since the selection depends on the Higgs boson mass hypothesis, likelihood distributions are needed for all masses to be tested. Additionally, the likelihood distributions are needed for centre-of-mass energies in the range from $192 - 209\,\mathrm{GeV}$ at which data was recorded. The distributions are created as described in Section 7.2. The candidate events are grouped in separate channels according to their centre-of-mass energy. Each group extends over a range of $2\,\mathrm{GeV}$. The total systematic error of the signal and background expectation given in Section 7.4 is conservatively assumed to be anti-correlated between signal and background[2] and fully correlated between

---

[2] The impact of the systematic error on the signal selection efficiency is small.

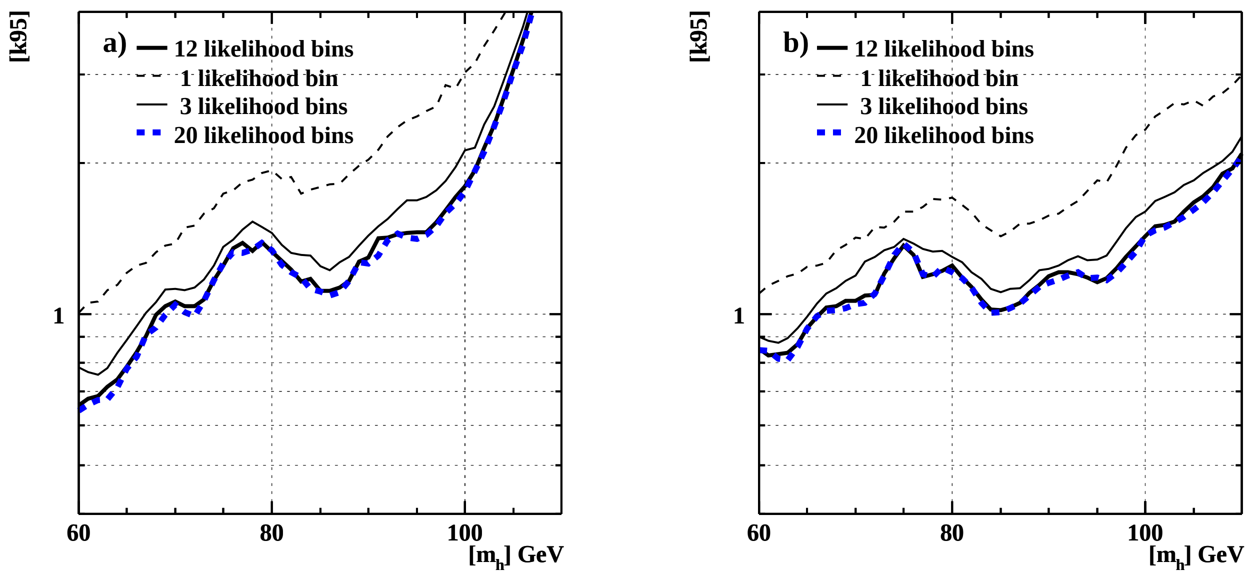

Figure 8.1: Expected exclusion limit on k using four-jet events of 1999 data (a) and 2000 data (b). The signal and background likelihood distributions used to weight the events are approximated by a varying number of bins. The case with only 1 bin corresponds to a counting experiment. The expected limit improves up to 12 bins.

the different channels, i.e. between the different centre-of-mass energy groups. The systematic errors due to the statistical uncertainty of the simulations are treated fully uncorrelated between signal and background and the different channels.

The limit calculator uses discrete reference distributions in order to determine the event weights ω_i and the probabilities $\mathcal{P}(\sum \omega_i)$, thus the number of different weights is finite. If the discrete reference distribution comprises only one bin all candidates get the same weight, and the method is equivalent to a counting method. The sensitivity of the analysis increases with the number of bins, until the signal and background expectation does not change significantly over the range of one bin.

The number of bins is varied between 1 and 20, and the resulting expected limits are compared. The results are shown in Figure 8.1a and b assuming the rates expected from the data of the years 1999 and 2000. A significant improvement is achieved if the likelihood is used to weight the candidates compared to a counting experiment (comparison 1 bin with 3 bins). Maximal performance is achieved using 12 bins. A finer subdivisioning yields only a negligible improvement.

Due to the large remaining background after the full selection and the sizable systematic errors on the background rate, the sensitivity is improved significantly by using the weights (8.9) instead of (8.3), as shown in Figure 8.2.

The validity of the exclusion limits, obtained by the described method, has been verified with toy experiments. Candidates were simulated for test masses in the range from 60 GeV to 120 GeV according to the luminosity and centre-of-mass energies of the years 1999 and 2000. One set of candidates comprised only background events, and the other background and signal events. The observed excluded rate at each mass was chosen as signal rate in the

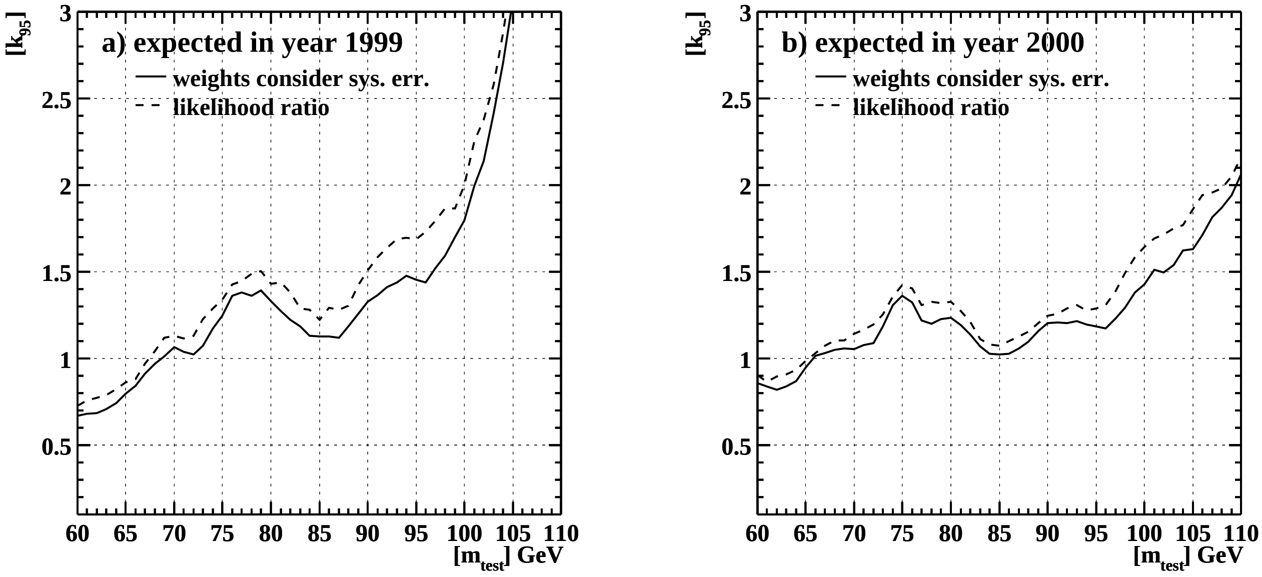

Figure 8.2: Expected limits on k using different weighting schemes. Figure a) and b) show the expected limit when applied to the results of the 1999 and 2000 data analysis. The expected limit, if no signal is present, improves significantly if the systematic errors are taken into account by the weighting scheme.

latter set of toy experiments. The expected number of signal and background events of each channel was varied according to the systematic errors. Normal distributed random numbers ξ_{il} were chosen for each independent error source l in each experiment i, and the expected number of events in each channel j was scaled by $\xi_{il}\sigma_j^l$, where σ_j^l denotes the systematic error of channel j, caused by the l-th error source. Signal and background errors were treated anti-correlated. In each experiment, the number of toy background and toy signal candidates was chosen according to a Poisson distributed random number, where the mean value was set to the modified expectation. For each candidate, a random likelihood value was chosen according to the shapes of the unbinned background and signal likelihood distributions. In each toy experiment, the rate limit was calculated.

Figures 8.3a-d illustrate the results of the approximately 500-1000 experiments, which were performed at each mass point. The distribution, shown in Figure 8.3a results from “background only” experiments. The median of the distribution should correspond to the expected limit, indicated by the vertical line. The results of similar experiments at different test masses are summarised in Figure 8.3c. The graphs show the integrals from 0 to $k95_{\text{exp}}$, $k95_{\text{exp}} \pm \sigma$ and $\pm 2\sigma$ and the statistical error, depending on the test mass. The horizontal lines indicate the average over the test mass range. The toy experiments show that $k95_{\text{exp}}$ is underestimated by $< 2\%$. Thus, the determined sensitivity is overestimated. Moreover, the error bands are too tight. This behaviour is expected since the 1σ and 2σ regions are calculated without taking systematic errors into account. At large masses, the statistical error dominates the systematic error and the agreement between the calculated and experimentally determined regions improves.

The distribution in Figure 8.3b is obtained from signal and background events. The signal fraction, indicated by the vertical line, corresponds to a scale factor $k = 1.4$ i.e. 1.4 times the expectation from a SM Higgs boson. This fraction is in agreement with the observed excluded rate. The integral from 0 to k is less than 5% which complies with the definition of $k95$. The graph in Figure 8.3d depicts the integrals and the statistical error, depending on the test mass. The horizontal line indicates the average. The average is far below 5%, thus the calculated $k95$ is conservative.

The discussed method is applied to the events of the four-jet channel selected in 1999 and 2000. The result is presented in Figures 8.4a and b. There is a general deficit in 1999 data and the observed limit is below the expectation, but mostly within the 2σ region. The limit obtained from 2000 data closely follows the expectation and is well contained in the 2σ region.

8.2 OPAL Combined Limit

Not only the four-jet channel, but also the other three topologies have been exploited at OPAL in the hunt for the Higgs boson. The three topologies are: the missing energy channel $\mathrm{Z^0h} \rightarrow \nu\bar{\nu}\mathrm{q\bar{q}}$, the electron and muon channel $\mathrm{e^+e^-} \rightarrow \mathrm{Z^0h} \rightarrow \mathrm{e^+e^-q\bar{q}}, \rightarrow \mu^+\mu^-\mathrm{q\bar{q}}$, and the tau channel $\mathrm{e^+e^-} \rightarrow \mathrm{Z^0h} \rightarrow \tau^+\tau^-\mathrm{q\bar{q}}$. In order to achieve flavour independence, all channels exclusively rely on the signature of the Z decay, and require only that the Higgs bosons decays into two separated jets. The analyses are based on searches for the SM Higgs boson described in [78]. However no identification of b quarks is performed. The modifications with respect to [78] are discussed in [4]. The missing energy channel has been optimised for higher energies [102]. A short overview is given in the three subsequent sections. In order to cover the region $m_h < 60\,\mathrm{GeV}$, the results are combined with an analysis using OPAL data recorded at 91 GeV [103]. The section concludes with the discussion of the combined limit.

8.2.1 The Missing Energy Channel

Signal events in the missing energy channel are characterised by two hadronic jets and a missing mass consistent with the Z boson mass. The dominant background processes are four-fermion processes, for example semileptonic decays of W pairs, $\mathrm{e^+e^-} \rightarrow \mathrm{q\bar{q}}\ell^\pm\nu$ and the irreducible process $\mathrm{e^+e^-} \rightarrow \mathrm{Z^0Z^0} \rightarrow \nu\bar{\nu}\mathrm{q\bar{q}}$. Further important contributions are events in which particles leave the detector close to the beam axis and escape detection. Among those are hadronic decays of Z bosons accompanied by initial state photons, $\mathrm{e^+e^-} \rightarrow \mathrm{q\bar{q}}(\gamma)$, and untagged two photon events, $\mathrm{e^+e^-} \rightarrow \mathrm{e^+e^-q\bar{q}}$. The latter two classes of background events can be reduced significantly requiring that the missing momentum points to sensitive parts of the detector and only little amount of energy was deposited in the forward detectors. Semileptonic decays of W pairs can be identified and rejected efficiently searching for energetic, isolated leptons. In order to reconstruct the mass of the hypothetical Higgs boson, a constrained kinematic fit is performed imposing energy and momentum conservation, and requiring the invariant mass of the two jets to equal the mass of the Z boson. The fitted mass of the Higgs candidate is used as final discriminant in the limit calculation.

The selection efficiencies for Higgs boson decays into $\mathrm{b\bar{b}}$, $\mathrm{c\bar{c}}$ and gluons have been investigated and their minimum is taken for the limit calculation. Depending on the Higgs boson mass, this is either the selection efficiency of $\mathrm{h^0} \rightarrow \mathrm{b\bar{b}}$ or $\mathrm{h^0} \rightarrow gg$. The minimum selection efficiency is in the range from 25% to $58\% \pm 2.1\%$(syst.). In total 123 events pass the selection in the two years 1999 and 2000, while 133.1 ± 11.5(stat.) $\pm$ 20.0(syst.) events are expected from SM background processes. The evaluation of the systematic errors is described in [78].

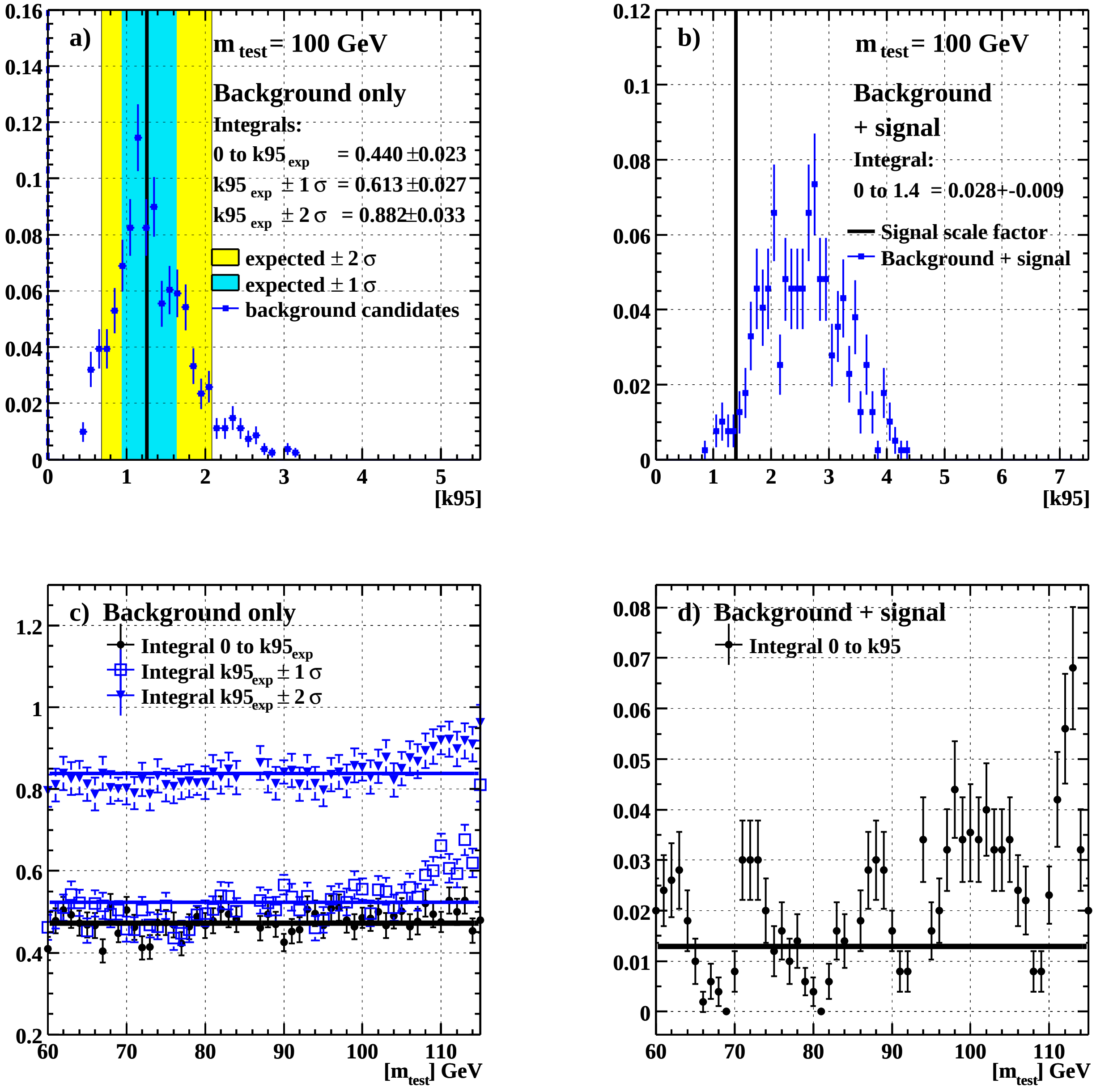

Figure 8.3: Rate limits resulting from toy experiments. In Figure a), the experiments comprise background candidates only. The vertical line and the shaded region indicate the calculated expected limit and the $\pm1\sigma$ and $\pm2\sigma$ regions. The expected limit should comply with the median of the distribution. The calculated $\pm1\sigma$ and $\pm2\sigma$ do not take systematic errors into account. Therefore they are too narrow. In Figure b), signal candidates were added according to a scale factor $k = 1.4$. The integral from 0 to $k95$ (vertical line) should yield 5% or less. Figures c) and d) depict the integrals depending on the test mass. The horizontal lines indicate the average values.

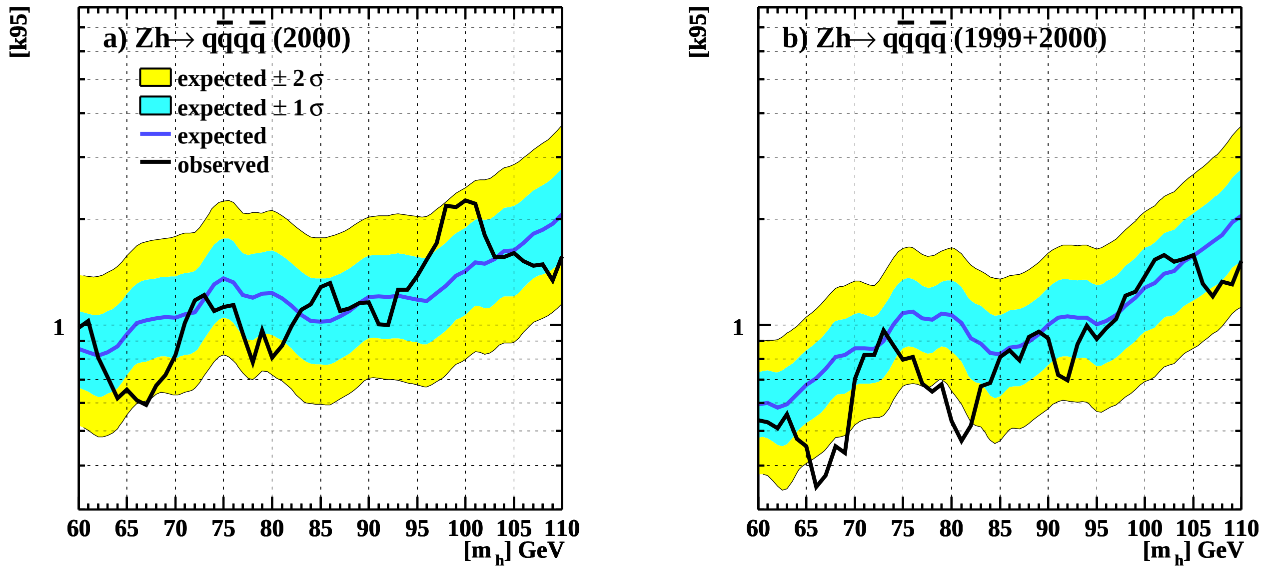

Figure 8.4: Limit on the Higgs-strahlung cross-section in the four-jet channel. Figures a) and b) show the observed and expected limit $k95$ on the scale factor of the Higgs-strahlung cross-section using the data set of year 2000 and additionally the data of year 1999. The shaded area indicates the $\pm 1\sigma$ and $\pm 2\sigma$ region. Assuming the coupling of the Higgs to the Z boson to equal to the SM coupling and a branching ratio $\mathrm{BR}(\mathrm{h}^0 \to \mathrm{q}\bar{\mathrm{q}}) = 100\%$, Higgs-strahlung is excluded up to $m_{\mathrm{h}} = 94\,\mathrm{GeV}$.

The dominant contribution results from the uncertainty in the modelling of the likelihood input variables. Further important uncertainties arise from the lepton isolation criteria used to suppress semileptonic W pair events, $\mathrm{e}^+\mathrm{e}^- \to \mathrm{q}\bar{\mathrm{q}}\ell\nu$.

8.2.2 The Electron and Muon Channel

The signature of the electron and muon channels are two energetic, oppositely charged leptons and two hadronic jets. The dominant backgrounds are $\mathrm{e}^+\mathrm{e}^- \to (\mathrm{Z}^0/\gamma)^*$ accompanied by initial state radiation (ISR) and general four-fermion processes such as W or Z pair production. Electrons and muons are identified as described in [104] making use of the shower profile in the electromagnetic calorimeter, the specific energy loss in the central jet chamber and signals in the muon chambers. Backgrounds, except Z pair production, can be identified efficiently by restricting the invariant mass of the lepton pair. The first background class can be suppressed further by requiring the event to be four-jet like, where leptons are considered as low multiplicity jets, and by requesting the lepton candidates to have large transverse momenta with respect to the nearest jet, since high energetic leptons are mainly due to semileptonic charm or bottom decays in these events. The recoil mass of the lepton pair is used as discriminating variable in order to calculate the limit.

The minimum selection efficiency amounts to 45% to 59% ± 1.7%(syst.) in the electron channel and 32% to 64%±1.6%(syst.) in the muon channel. The efficiencies for $\mathrm{h}^0 \to \mathrm{c}\bar{\mathrm{c}}$ or $\mathrm{h}^0 \to \mathrm{b}\bar{\mathrm{b}}$ are the lowest. The selection retains 23 events in the electron channel and 16 in the muon

years	$[\int dt\mathcal{L}]$ pb^{-1}	$[\sqrt{\mathrm{s}}]$ GeV	Reference
91-95	170	91	[103]
1998	170	189	[4]
1999	216	$192-202$	[102]
2000	207	$199-209$	[102]

Table 8.1: OPAL data used for the combined limit.

channel in both years together. The total background expectation is 16.6 ± 4.1(stat.)± 5.1(syst.) and 15.0 ± 3.9(stat.) ± 2.9(syst.) events, respectively. The systematic errors quoted above are evaluated for signal and background with the method described in [78]. The main contribution to the systematic error is due to the uncertainty about the fragmentation process determined from a comparison of HERWIG and JETSET. A further large uncertainty results from different predictions in four-fermion events given by grc4f, KORALW and EXCALIBUR.

8.2.3 The Tau Channel

The signal events of the tau channel are composed of two hadronic jets from the Higgs decay and from each tau decay one or three charged particle tracks plus possible calorimeter clusters resulting from neutral particles. In contrast to the SM Higgs boson search, Higgs bosons decaying into tau leptons are not considered. Important background sources are $\mathrm{e^+e^-} \rightarrow \mathrm{Z^0Z^{0(*)}} \rightarrow \mathrm{q\overline{q}}\ell^+\ell^-$, $\mathrm{e^+e^-} \rightarrow \mathrm{W^+W^-} \rightarrow \mathrm{q\overline{q}}\ell^\pm\nu$ and $\mathrm{e^+e^-} \rightarrow \mathrm{q\overline{q}}(\gamma)$. Two tau candidates are searched for assuming several possible topologies of the tau decay. A probability is assigned to each tau candidate and the combined probability is used as discriminating variable. The tau candidates and the remainder are grouped into four jets. Only four-jet like events are considered further. Since the energy of the tau candidates is not very well measurable, a constrained kinematic fit is performed which uses only the direction of the tau candidates and leaves the energy as a free parameter. Energy and momentum conservation are required and the invariant mass of the two tau candidates must equal the Z boson mass. The invariant mass of the two hadronic jets calculated after the kinematic fit is used as final discriminant to calculate the limit. The minimum efficiency is approximately $20\% \pm 3.1\%$(syst.). In 1999 and 2000 three events pass the selection compared to the background expectation of 8.8 ± 3.0(stat.) ± 1.5(syst.) events. The systematic errors quoted above are determined as described in [78]. The major contribution to the systematic error results from the uncertainties on the misidentification rate of tau leptons.

8.2.4 The Combined Limit

The combined limit is calculated using in addition to the analysis of 1999 and 2000 data also analyses of 1998 data at $\sqrt{\mathrm{s}} = 189\,\mathrm{GeV}$ described in [4] and analyses of data collected during the years $1991-1995$ at $\sqrt{\mathrm{s}} = 91\,\mathrm{GeV}$ [103]. In the mass region below 60 GeV, the limit is driven by the analyses at $\sqrt{s} = 91\,\mathrm{GeV}$. The data sets are summarised in Table 8.1. The methods used to derive the limit have improved since [4]. However the resulting limits are compatible. Figure 8.5a shows the expected limit resulting on k from the old and the advanced approximative method using all channels except the four-jet channel for 1999 and 2000 data.

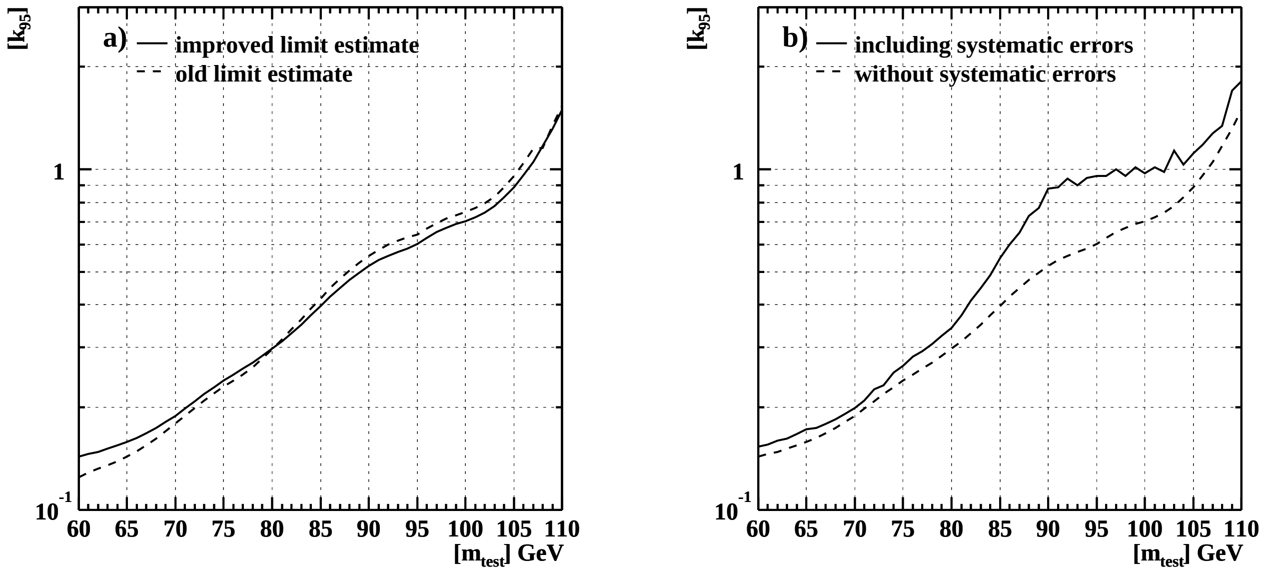

Figure 8.5: Combined expected limit on k. For 1999 data the previous four-jet analysis is used and no four-jet channel is used for 2000 data. Figure a) reveals the difference between the old and evolved limit calculator if systematic errors are not taken into account. Figure b) shows the impact of systematic errors on the limit using the new limit calculator.

Advances have also been made in the treatment of systematic errors. In [4] the impact of systematic errors was considered to be small which turned out to be too optimistic after a proper treatment of systematic errors was implemented [101] according to [100]. The impact of systematic errors is depicted in Figure 8.5b.

In Figure 8.6a, the performance of the combined analysis including the previous [4] and the new four-jet channel are compared. The four-jet analysis of 2000 data is not included. Previously, the fit improved invariant mass of the Higgs candidate was used as final discriminating variable of the four-jet analysis. At high Higgs boson masses ($m_h \gtrsim 95\,\text{GeV}$) the limit improves significantly by using the likelihood as discriminating variable instead. At smaller masses, an improvement is still achieved, however, it is mainly due to the reduced the systematic error.

The final sensitivity of all channels is shown in Figure 8.6b. The high centre-of-mass energies in 2000 and the high statistics of the four-jet channel yield a considerable improvement at masses above m_{W}.

The OPAL combined observed limit is depicted in Figure 8.7 together with the expectation under the background only hypothesis. The Higgs boson mass was varied in steps of 250 MeV. The shaded bands indicated the regions in which the limit is expected with a probability of 68% and 95%, respectively. Not all channels extend over the whole mass range. As a consequence, discontinuities are produced when channels are switched on or off. The small jitter of the expected limit is caused by numerical instabilities of the approximative method. The observed limit closely follows the expectation and is well contained in the 2σ region. Here, the jitter is expected. Due to the test mass dependence of the four jet channel, candidate events, which are newly selected or drop out when a certain test mass is passed, may cause a discontinuity. As discussed in Section 8.1.3, the $\pm 1\sigma$ and $\pm 2\sigma$ region do not take systematic errors into account. Thus, they may be optimistic.

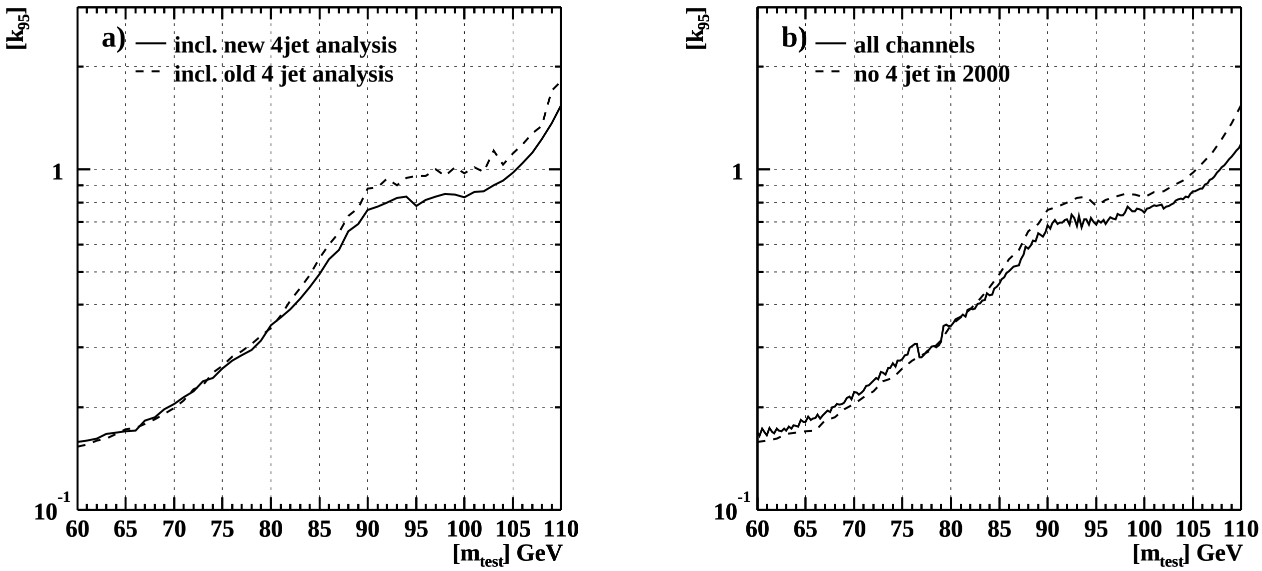

Figure 8.6: Expected limit on k using the new four-jet channel. The two curves in Figure a) show the limit including all channels but the four-jet channel in 2000, using the new and the old four-jet channel to handle 1999 data. In Figure b) the four-jet channel of 2000 data was considered additionally.

Assuming a SM-like coupling to the Z boson and a hadronic branching ratio of 100%, Higgs bosons are excluded for $m_{\mathrm{h}} < 105\,\mathrm{GeV}$ at the 95% confidence level. Assuming the SM branching ratios, they are excluded for $m_{\mathrm{h}} < 101\,\mathrm{GeV}$ at the 95% confidence level.

8.3 LEP Combined Limit

Similar flavour independent Higgs boson searches have been performed within the other LEP collaborations: ALEPH, DELPHI and L3 [3]. At time of writing only the ALEPH collaboration has published its final result. Thus, the limit presented in Figure 8.8 is preliminary and may change [105]. The contribution of the DELPHI collaboration does not yet include systematic errors and covers only the region $m_{\mathrm{h}} \leq 112\,\mathrm{GeV}$. The Higgs boson mass was varied in steps of

Channel	Data	Background	SM Higgs-strahlung ($m_{\mathrm{h}} = 100\,\mathrm{GeV}$)	Efficiency
Four-jet	477	468.1	41.0	0.50
Electron/Muon	37	27.4	4.9	0.61
Tau	4	9.0	0.9	0.23
Missing energy	100	113.8	10.9	0.46
Total	618	618	57.8	0.49

Table 8.2: Number of candidates in the data of 1998 to 2000 and expected candidates from the background and SM Higgs-strahlung for a mass hypothesis $m_{\mathrm{h}} = 100\,\mathrm{GeV}$. The number of signal events are computed assuming $\mathrm{Br}(\mathrm{h}^0 \rightarrow \mathrm{q\overline{q}}) = 100\%$. The quoted efficiency represents the average efficiency over the years.

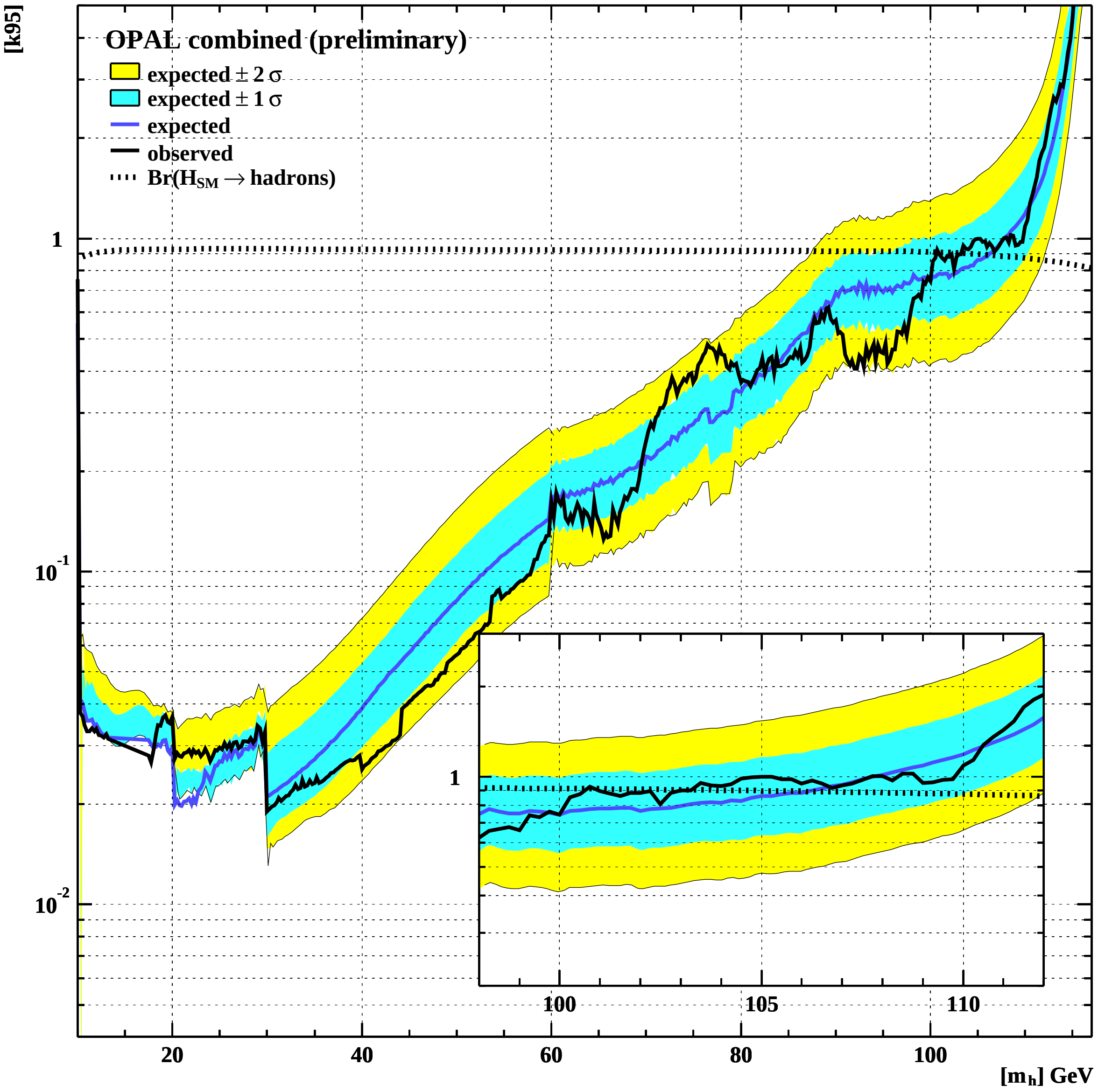

Figure 8.7: Observed and expected limits on k resulting from the analysis of LEPI and LEPII data. The LEPI analysis contributes in the region below $m_{\mathrm{H}} < 60\,\mathrm{GeV}$, where most LEPII analyses contribute only in the region above. The shaded area visualises the area in which the limit is expected in 68% and 95% of the experiments if no signal exists. Higgs bosons are excluded up to masses of 105 GeV at the 95% confidence level assuming a SM-like coupling to the Z boson but a branching ratio $\mathrm{Br}(\mathrm{h}^0 \rightarrow \mathrm{hadrons}) = 100\%$. Assuming SM branching ratios, Higgs bosons are still excluded up to a mass of 101 GeV at the 95% confidence level.

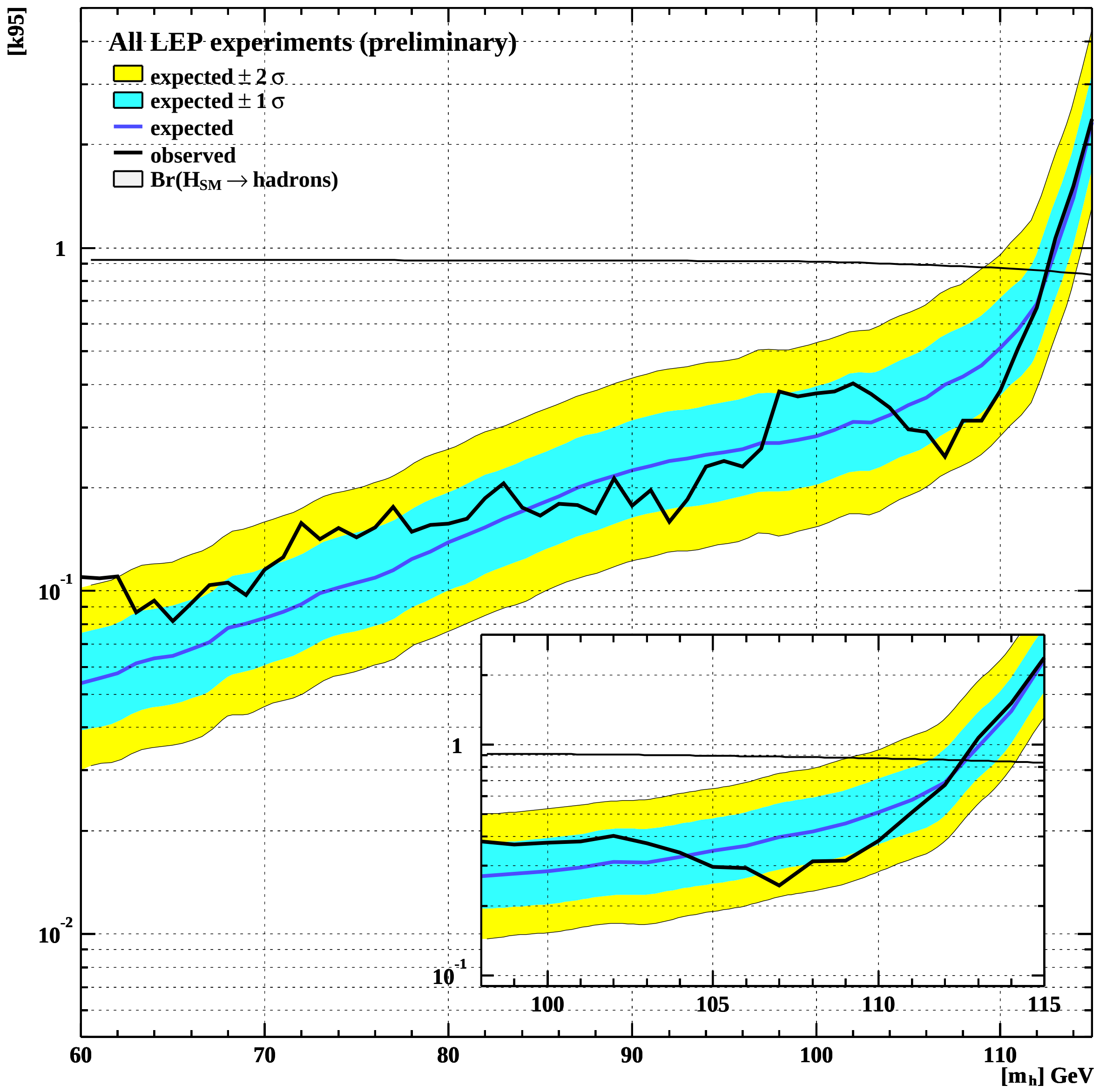

Figure 8.8: Preliminary combined limit of all LEP experiments. Shown is the flavour independent limit on the cross-section scaling factor, $\sigma/\sigma_{\mathrm{SM}}$, relative to the cross-section expected from a SM Higgs boson. Assuming a branching ratio Br(h → hadrons) = 100% a Higgs bosons with SM like coupling to the Z can be excluded with masses $m_{\mathrm{h}} < 113\,\mathrm{GeV}$ at the 95% confidence level.

1 GeV. The LEP combined search yields a sensitivity twice as good as OPAL alone, and equal or better than the SM search of a single LEP experiment. The observed limit is contained in the 2σ region around the expectation. Higgs bosons with SM like couplings to the Z boson are excluded for masses $m_{\mathrm{h}} < 113\,\mathrm{GeV}$ assuming a hadronic branching ratio $\mathrm{Br}(\mathrm{h} \rightarrow \mathrm{hadrons}) = 100\%$. Higgs bosons are still excluded for masses $m_{\mathrm{h}} \lesssim 112.5\,\mathrm{GeV}$ assuming SM branching ratios.

8.4 Interpretation within Two-Higgs-Doublet Models

The computed limit on the cross-section of Higgs-strahlung can be interpreted within the Two-Higgs-Doublet model as a limit on $\sin^2(\beta-\alpha)$, since the coupling to the Z is proportional to this factor (see Section 3.2). In order to calculate the limit, the minimal hadronic branching ratio $\mathrm{h}^0 \rightarrow$ hadrons has to be known for the parameter space of interest since the analyses are sensitive to hadronic Higgs decays only. The minimal hadronic branching ratio was determined in [4] performing the following parameter scan:

- $\alpha(\in [0, \frac{\pi}{2}])$ was chosen from 0, $\frac{\pi}{12}$, $\frac{\pi}{6}$, $\frac{\pi}{4}$ and $\frac{\pi}{2}$.
- $\tan\beta(\in [0, \infty))$ was varied from 0.4 to 57 (corresponding to $22° < \beta < 89°$), where β was incremented in steps of 1°. At larger or smaller values of $\tan\beta$ higher order corrections become important and the calculations become unreliable.
- m_{h^0} was varied from $30 - 110\,\mathrm{GeV}$ in steps of 1 or 2 GeV

The scan was restricted to regions in which the decay into two CP-odd Higgs bosons is kinematically suppressed ($2m_{\mathrm{A}^0} > m_{\mathrm{h}^0}$) since generally the analyses are insensitive to $\mathrm{h}^0 \rightarrow \mathrm{A}^0\mathrm{A}^0$ except regions with $m_{\mathrm{A}^0} \lesssim 25\,\mathrm{GeV}$, where a sensitivity comparable to $\mathrm{h}^0 \rightarrow \mathrm{q}\overline{\mathrm{q}}$ or $\mathrm{h}^0 \rightarrow gg$ is achieved as discussed in Section 7.3.2. For each m_{h^0}, the branching ratios were calculated using [24] at all the benchmark points, and the minimal hadronic branching ratio was determined. Since the decay modes into heavy vector bosons are kinematically suppressed for the considered Higgs boson masses the dominant non-hadronic decay modes are decays into τ leptons, and, by orders of magnitude smaller, decays into photon pairs via top quark loops. The coupling to τ leptons and the effective coupling to photons is influenced by α and β in a similar way to the couplings of down-type fermions and up-type fermions according to (3.7) to first order. Thus, the hadronic branching ratio will be minimal if the coupling to down-type fermions is maximal and consequently the minimal branching ratios are similar to the SM branching ratios. The resulting limit on $\sin^2(\beta-\alpha)$ is shown in Figure 8.9.

More restrictive exclusion regions in the parameter space of the Two-Higgs-Doublet model could be obtained if the upper limit on the cross-section of $\mathrm{e}^+\mathrm{e}^- \rightarrow \mathrm{Z}^* \rightarrow \mathrm{hA}$ was determined additionally. With this measurement, an upper limit on $\cos^2(\beta-\alpha)$ could be calculated, and all masses could be excluded at which $\max\cos^2(\beta-\alpha) + \max\sin^2(\beta-\alpha) < 1$. However, a flavour independent measurement is very difficult since the only observables, which distinguish these events from the huge background, are resonances in the invariant mass distributions and the angular distribution of jets. Nevertheless, an analysis has been developed [106] and will be exploited in a future publication.

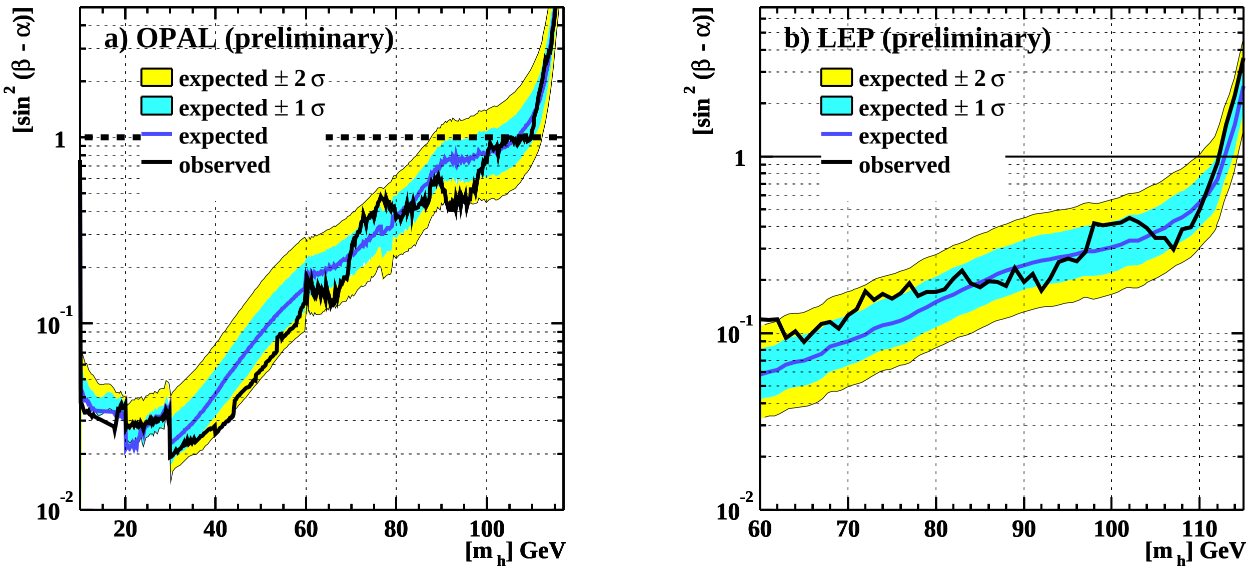

Figure 8.9: OPAL and LEP combined limit on $\sin^2(\beta-\alpha)$ within general Two-Higgs-Doublet models. The limit is valid only if the decay $h^0 \to A^0A^0$ is kinematically suppressed. However, should also be valid if the A bosons is light ($m_A \lesssim 25\,\mathrm{GeV}$). Figure a) and b) show the preliminary combined limit of OPAL and all four LEP experiments. The LEP combined result does not yet take systematic errors into account.

8.5 The Large-μ Scenario in the MSSM

The searches for the SM Higgs boson have been interpreted in several benchmark scenarios of the MSSM [107]. Since the MSSM features two Higgs doublets the coupling of the lightest CP-even Higgs boson h^0 to bottom quarks can be strongly suppressed, as discussed in Section 3.2. This is the case in the large-μ benchmark scenario in a small region of the m_A and $\tan\beta$ plane (see figure 3.2). In this scenario, the mass of lightest Higgs boson is below 108 GeV for all m_A and $\tan\beta$, thus it is well in the mass reach of the SM Higgs boson searches. Figure 8.10b shows the exclusion regions resulting from the OPAL SM Higgs boson search, the OPAL flavour independent search and the LEP combined flavour independent search. The OPAL SM Higgs boson search excludes a vast array of the m_A and $\tan\beta$ plane. In the region of light CP-odd A^0 bosons, the coupling of the lightest Higgs boson to the Z vanishes. In this area pair production, $e^+e^- \to h^0A^0$, dominates. The area is excluded by dedicated searches [107].

In the region of large $\tan\beta$ and $m_A \simeq 150 \pm 20\,\mathrm{GeV}$, the branching ratio $\mathrm{Br}(h^0 \to b\bar{b})$ is strongly suppressed and SM searches lose their sensitivity. Flavour independent Higgs searches retain some of their sensitivity since the hadronic branching ratio is still above 45% for $\tan\beta < 50$. As indicated by Figure 8.10a, the OPAL flavour independent Higgs boson search has only half the needed sensitivity to explore this area, and is able to exclude only the area below $\tan\beta < 10$, which also is covered by the SM Higgs boson search. However, the combined sensitivity of the four LEP experiments is sufficient to exclude this scenario up to the upper bound of the parameter scan, $\tan\beta = 50$.

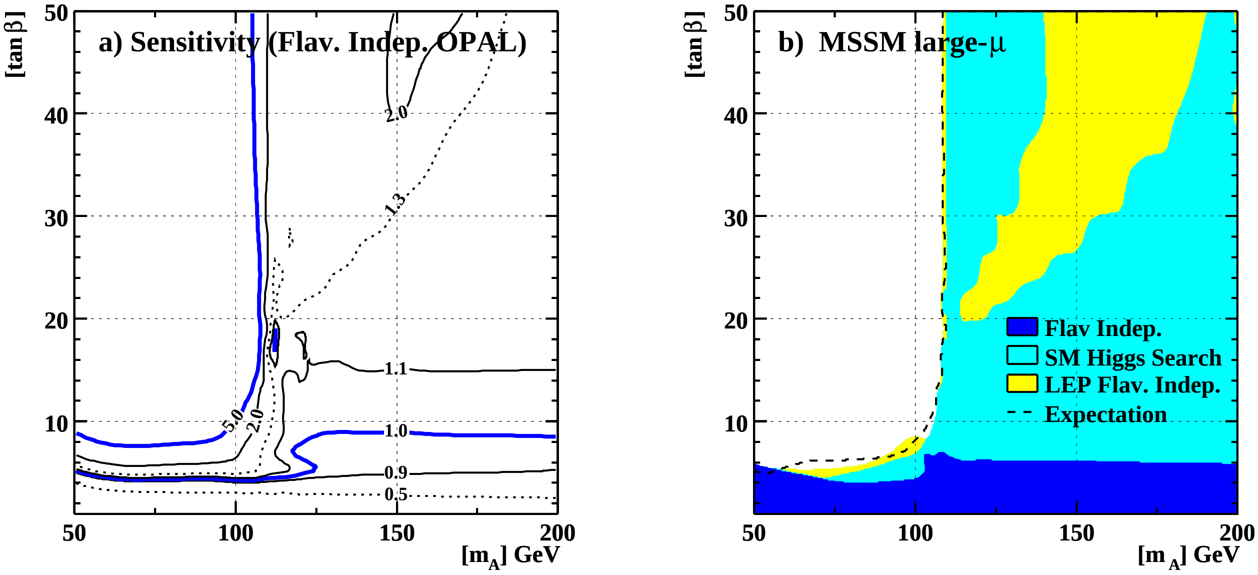

Figure 8.10: Exclusion region in the large-μ scenario of the MSSM. Figure a) shows the expected exclusion region from the OPAL flavour independent Higgs search. The contour lines indicate the expected lower limit on a coupling scale factor. Figure b) shows the observed and expected exclusion region resulting from the flavour independent search, the SM Higgs boson search and the LEP combined flavour independent search. In the region $m_\mathrm{A} < 107\,\mathrm{GeV}$, Higgs-strahlung is suppressed. In this region pair production, $\mathrm{e^+e^-} \rightarrow \mathrm{h^0A^0}$, dominates.

8.6 Constraints on RS-type Models

The derived cross-section limit is further used to restrict the parameter space of the Randall-Sundrum model (Section 3.4). Since the predicted radions can mix with the Higgs bosons, the properties of the physical Higgs-like state differ from the SM Higgs bosons in parts of the parameter space. Therefore, the current limits on the Higgs boson mass are not valid within the whole Randall-Sundrum parameter space and are reconsidered.

The cross-section limit of Section 8.2.4 is used to exclude all points in the allowed parameter space which predict a cross-section of the Higgs-like or radion-like state larger than the excluded one. Since the Higgs-like state has usually a large branching ratio into $\mathrm{b\bar{b}}$ and the SM Higgs boson search is roughly three times more sensitive to these decays than the flavour independent Higgs boson search, the exclusion region is extended by using additionally the cross-section limit obtained from the SM Higgs boson search [71, 1].

The observed and expected exclusion region is shown in several slices of the parameter space for different scales Λ_W in Figures 8.11 to 8.13. Figures 8.11a-f depict the exclusion region depending on the radion mass m_r and the mixing parameter ξ for increasing scales $\Lambda_\mathrm{W} = 246\,\mathrm{GeV}$, $500\,\mathrm{GeV}$, and $1\,\mathrm{TeV}$, and for two different Higgs boson masses, $m_\mathrm{h} = 110\,\mathrm{GeV}$ and $200\,\mathrm{GeV}$. The contribution from the SM Higgs search is not shown. The Higgs boson masses were chosen such that in the no-mixing case, $\xi = 0$, the flavour independent search is not sensitive to the Higgs boson in any of the two cases. However, the lower mass is close to the mass reach of the search, while the upper mass is chosen far beyond the scope. Since the coupling of the radion is suppressed by $v^2/6\Lambda_\mathrm{W}^2$ compared to the coupling of a SM Higgs boson, the sensitivity to the radion, and therefore the mass reach, is significantly lower. At maximally allowed mixing the fundamental masses of the radion and the Higgs boson, $\widetilde{m}_\mathrm{r}$ and $\widetilde{m}_\mathrm{h}$, are very close and the cross-sections of both states are resonantly enhanced (see equations (3.12), (3.14) and (3.15)). The cross-section of the radion-like state is only enhanced for positive mixing. The cross-section of the Higgs-like state is generally enhanced for negative mixing and for positive mixing only if the difference between the physical masses of the two states is large.

In Figures 8.12a-f the exclusion resulting from both, the SM Higgs boson search and the flavour independent search, are shown depending on m_r and m_h for moderate positive and negative mixing ξ. Since the allowed range of the mixing parameter increases with Λ_W, the absolute value of the mixing parameter is increased simultaneously with Λ_W, such that the effect caused by the mixing remains at the same order of magnitude. If the radion is not too heavy and the scale Λ_W is low, the flavour independent search is sensitive to the radion-like state and excludes regions independent of the Higgs boson mass m_h. The figures indicate further that the current mass limit resulting from the search for the SM Higgs boson looses its validity in case of maximal mixing. In the latter case, the sensitivity is generally reduced since the branching ratio of the Higgs-like state into bottom quarks decreases substantially. The effect is more clearly seen in Figures 8.13a-f showing m_h versus ξ planes.

In order to determine the mass limit on the Higgs boson mass m_h independent of the location in the parameter space of the Randall-Sundrum model, the following scan is performed:

- m_h is varied from 10 GeV to 120 GeV in steps of 1 GeV,
- m_r is varied from 10 GeV to 120 GeV in steps of 1 GeV and from 120 GeV to 1 TeV in steps of 50 GeV, and
- ξ is varied in steps of $(\xi_\mathrm{max} - \xi_\mathrm{min})/20$, where ξ_{min} and ξ_max denote the maximally allowed range (condition (3.13)).

Around each scan point, the lowest mass limit is searched by using nested intervals. The search is stopped if the intervals in m_r and m_h are smaller than 100 MeV and $\Delta\xi < 10^{-5}$. The allowed Higgs boson masses m_h are limited by condition (3.18). In case $m_\mathrm{h} < m_\mathrm{r}$, the cross-section times branching ratio decreases substantially close to the maximally allowed Higgs boson mass. In these regions, the lowest mass limits on m_h are obtained (see Figures 8.12 and 8.13, and Figures 8.14a and b). The lowest limit on m_h as a function of Λ_W is shown in Figures 8.14c and d. In comparison to the SM, the Higgs boson mass limits are significantly lower in the Randall-Sundrum model. At $\Lambda_\mathrm{W} = 246$ GeV, only a limit of $m_\mathrm{h} = 57$ GeV and $m_\mathrm{h} = 60$ GeV is obtained using the OPAL and LEP combined results, respectively. At $\Lambda_\mathrm{W} = 11$ TeV, the limit is still significantly below the one obtained within the SM; the OPAL and LEP combined limits are $m_\mathrm{h} = 89$ GeV and 97 GeV, respectively. The expected limit of the LEP combined result is significantly higher (110 GeV). The large difference is due to a 2σ excess in the LEP combined result of the SM Higgs boson search in the region from 90 GeV to 105 GeV. At high scales, the worst mass limits are obtained at large negative mixing $\xi < -10$ and for heavy radions $\widetilde{m}_\mathrm{r} \simeq 1$ TeV. Such large values for ξ and m_r are not expected, but they are not forbidden from a mathematical point of view.

At low values of Λ_W ($\lesssim 300$ GeV), a vast area can be excluded. However, uncovered spots remain. Since the Higgs boson and the radion are expected to be light, such a low scale Λ_W becomes unlikely. In [108] further limits on the parameter space are discussed. The results are

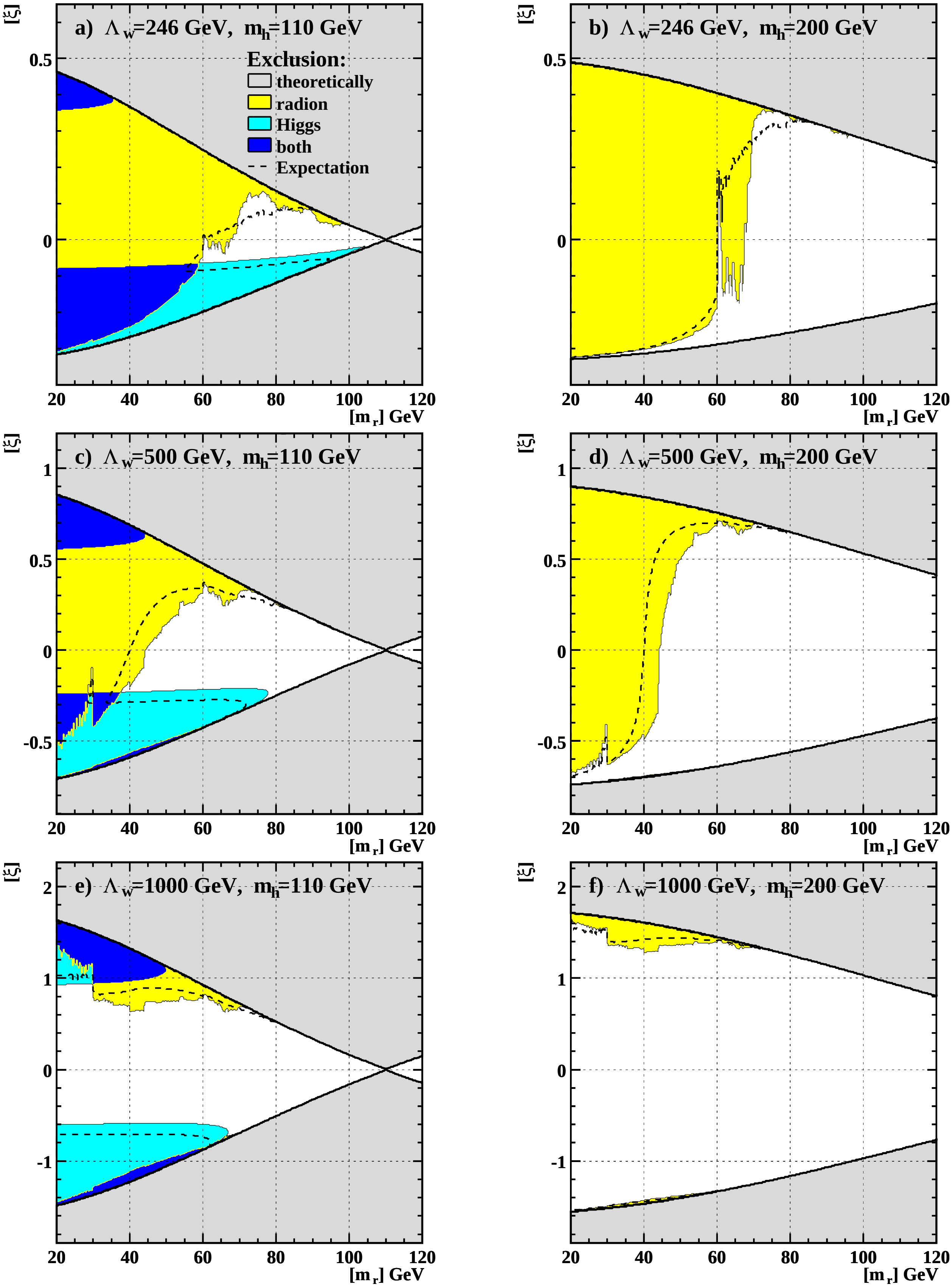

Figure 8.11: Observed and expected exclusion regions in the parameter space of the Randall-Sundrum model for a specific choice of the weak scale Λ_W = 246 GeV, 500 GeV and 1000 GeV (from top to bottom), and two Higgs boson masses m_h = 110 GeV (left) and 200 GeV (right). Only the flavour independent search was used to obtain the exclusion regions.

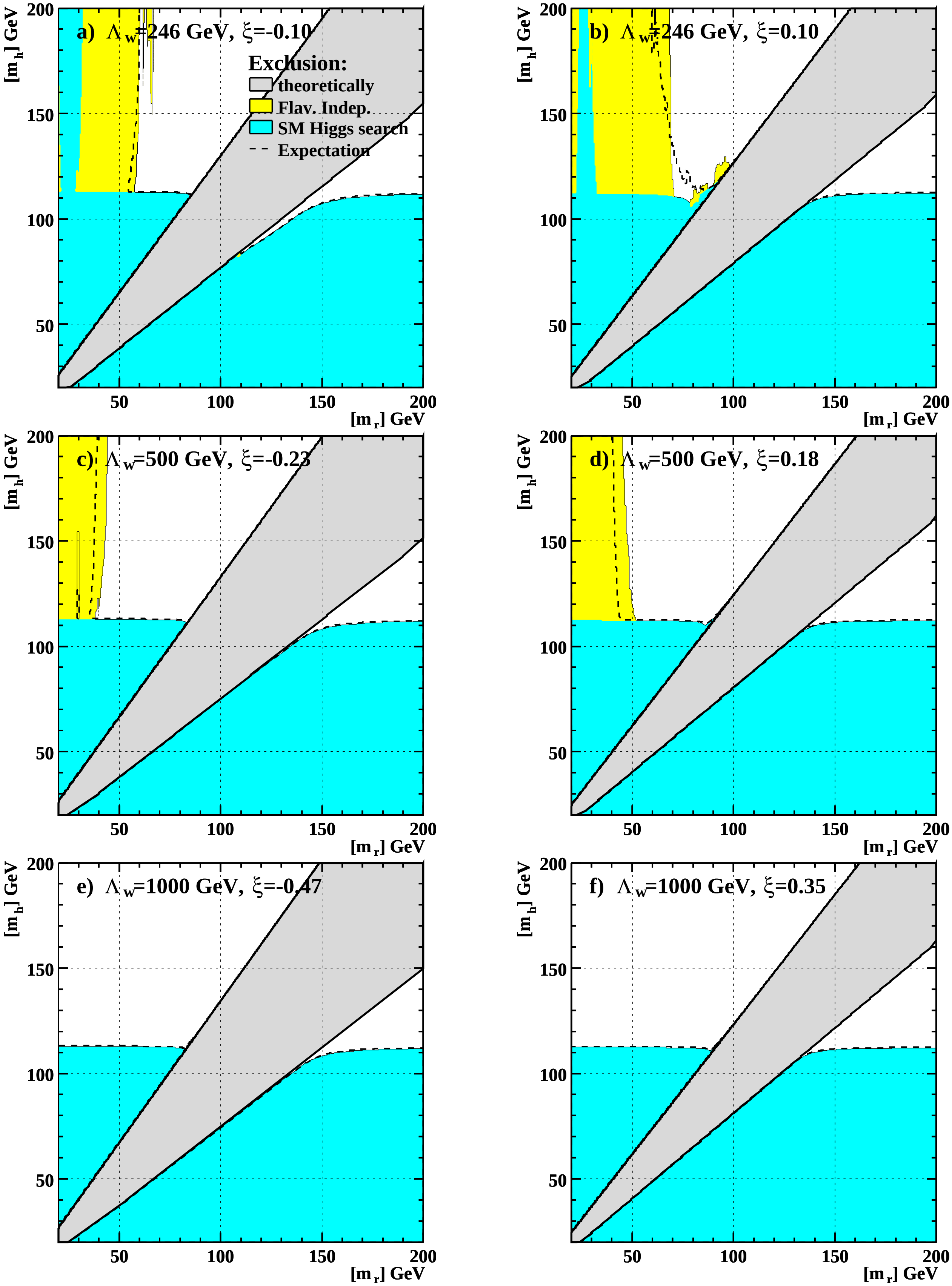

Figure 8.12: Observed and expected exclusion in the parameter space of the Randall Sundrum model in m_r and m_h plane for a specific choice of the weak scale $\Lambda_\mathrm{W} = 246\,\mathrm{GeV}$, $500\,\mathrm{GeV}$ and $1000\,\mathrm{GeV}$ (from top to bottom), and negative and positive mixing parameter ξ.

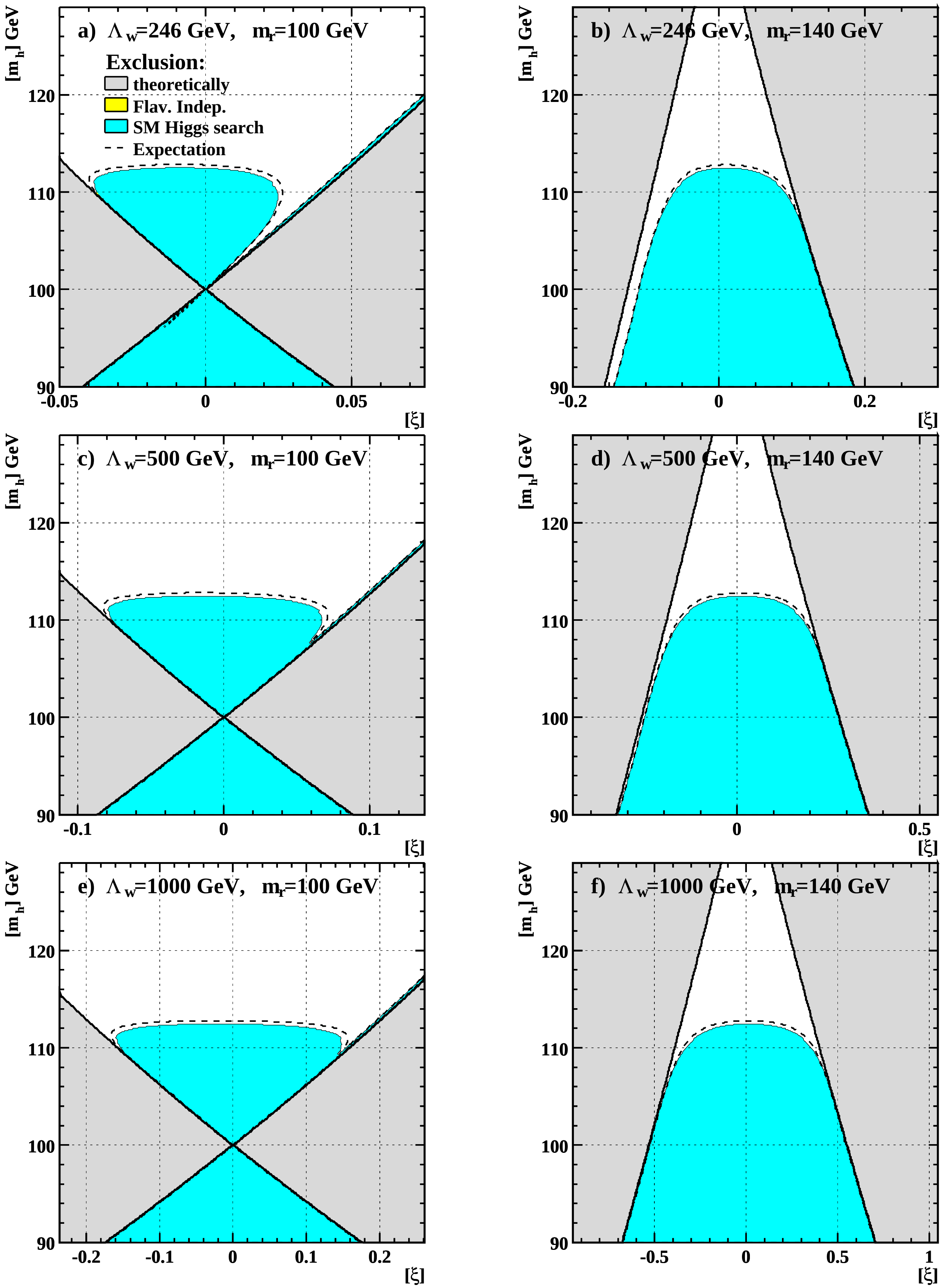

Figure 8.13: Observed and expected exclusion regions in the parameter space of the Randall-Sundrum model for a specific choice of the weak scale $\Lambda_{\rm W} = 246\,\text{GeV}$, 500 GeV and 1000 GeV (from top to bottom), and two radion masses $m_{\rm r} = 110\,\text{GeV}$ (left) and 200 GeV (right).

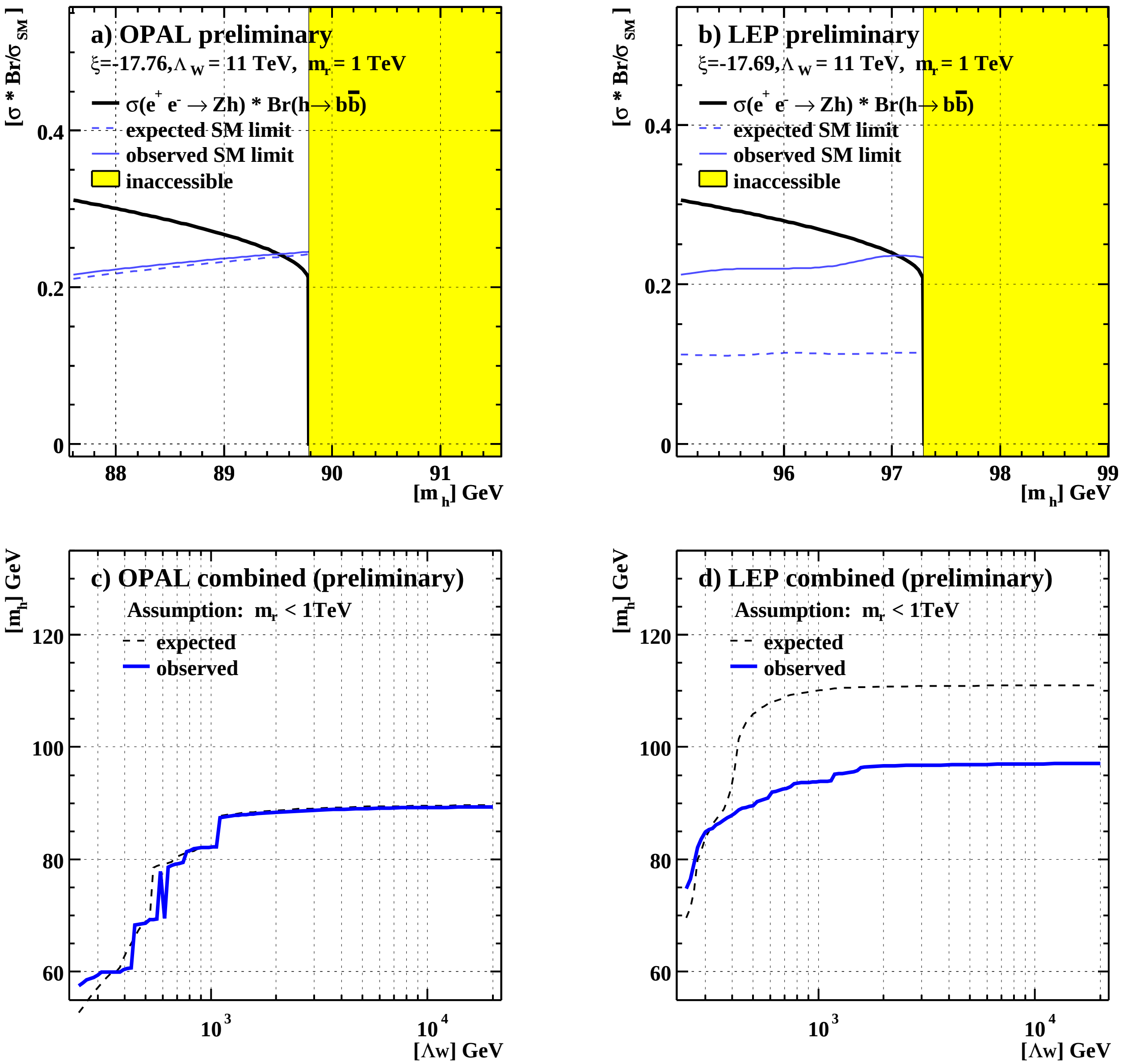

Figure 8.14: Upper limits on the SM Higgs boson mass in the Randall-Sundrum model. Figures a) and b) show the cross-section times branching ratio of the Higgs-like state at the indicated point in the Randall-Sundrum parameter space as a function of the Higgs boson mass m_h. The shown cross-section limits are obtain from the OPAL and LEP combined searches, respectively. Model points are excluded if the cross-section is above the limit. In both cases a tiny region is not excluded, just before the inaccessible region starts. A lower limit on the Higgs boson mass m_h of 89.5 GeV and 97 GeV is obtained, respectively. Figures c) and d) show the Higgs boson mass limit as a function of the scale Λ_W using the OPAL and LEP combined results. The lowest mass limits are obtained at large radion masses $m_\mathrm{r} > m_\mathrm{h}$ and maximally allowed negative mixing. The large difference of the observed and expected limit in Figure d) is due to a 2σ access in the LEP combined SM Higgs boson search.

summarised in the following. Massive spin two excitations, usually referred to as *Kaluza-Klein towers*, are excluded up to masses of 170 GeV by direct searches conducted at LEP, and searches performed at the TEVATRON exclude masses above 200 GeV up to 600 GeV. In the RS model, the masses of the massive spin two excitations are set by the weak scale Λ_{W}. In order to push the masses above 600 GeV, a scale $\Lambda_{\mathrm{W}} > 1$ TeV is required. A further indication that the scale has to be large is obtained from the electroweak precision observables [20]. In order to keep the impact on the precision observables small enough and to establish compatibility with the experimental observations, Λ_{W} has to exceed 4 TeV. Since there also is a weak bound on the scale from above $\Lambda_{\mathrm{W}} < 10$ TeV [109], a realisation of the Randall Sundrum model in its simplest realisation seems to be unlikely. However, there is still a small window for low values of Λ_{W} since there may be hidden contributions to the precision observables and a small mass window for the lightest spin two excitation is still allowed.

Chapter 9

Summary

The Higgs mechanism is the most attractive mechanism to break the electroweak gauge symmetry. In its minimal realisation, one additional massive Higgs boson is predicted, whose mass is a free parameter. The bounds obtained indirectly from precision measurements and by theoretical considerations suggest a relatively light Higgs boson, close to the mass reach of the LEP experiments. Direct searches for the SM Higgs boson at LEP exclude Higgs bosons up to 114.4 GeV.

However, a broad range of extensions is possible. In extended models, more than one Higgs boson or further massive scalars can appear. This is already the case in Two-Higgs-Doublet models in which two CP-even Higgs bosons appear, or in the Randall-Sundrum model in which the Radion appears as a second CP-even scalar particle. The additional particles can have rather different properties compared to the SM Higgs boson. Most notably, the coupling to bottom quarks may be suppressed. In these scenarios, searches for the SM Higgs boson are not sensitive. But often, the Higgs boson still decays into quarks or gluons. Thus, a search for hadronically decaying Higgs bosons remains sensitive, if it does not dependent on the quark flavour.

A flavour independent Higgs boson search has been performed using four-jet events recorded with the OPAL detector in years 1999 and 2000 at centre-of-mass energies from 192 to 209 GeV. The analysis is performed under an explicit Higgs boson mass hypothesis, allowing to fully exploit the kinematic signature of the production process. The analysis requires reference distributions which depend on the centre-of-mass energy and the mass hypothesis. In order to generate sufficiently smooth distributions over the broad range of centre-of-mass energies in 2000 and the Higgs boson mass range from 60 to 120 GeV, interpolation techniques became necessary. For this purpose a 3D spline fit has been developed.

The analysis relies on a precise measurement of the particle momenta. Due to a short at one cathode of the central jet chamber, the originally homogeneous drift field was distorted in the outerparts close to the cathode, causing sizable measurement errors of the momenta of nearby passing particles. A correction to the reconstruction was implemented successfully, lifting the momentum resolution nearly up to the previous level.

Higgs bosons, or scalars, have not been observed, neither within four-jet events, nor within other topologies which are considered by the OPAL and the other three LEP collaborations. The number of observed events together with the background expectation was used to calculate a limit on a scaling factor k of the Higgs-strahlung cross-section. Assuming the SM coupling to the Z boson and a branching ratio of Higgs bosons into quark pairs or gluons of 100%, Higgs bosons are excluded up to a mass of 105 GeV and 113 GeV by the OPAL and LEP combined searches, respectively.

The limit on k was used to derive a limit on $\sin^2(\beta-\alpha)$, within general Two-Higgs-Doublet models. In order to place mass limits independent of β and α, a flavour independent search for the pair production process $e^+e^- \to h^0A^0$ is necessary. A measurement is very difficult, but it is being worked on.

In the large-μ scenario of the MSSM, a small region is not excluded by SM Higgs boson searches since the branching ratio of the lightest Higgs boson into bottom quarks is strongly suppressed. The LEP combined flavour independent search is able to exclude the remaining area. The sensitivity of OPAL alone is not sufficient. A similar, not yet excluded benchmark scenario with regard to future experiments is proposed in [110].

In the Randall-Sundrum model, the radion, a further scalar particle, appears which can mix with the Higgs boson. Since the radion decays dominantly into gluons, the decay modes of the mass eigenstates may differ from those of the SM Higgs boson. The sensitivity to the Higgs like state is significantly reduced for large negative mixing and large radion masses. The limits on the Higgs boson mass obtained by the LEP combined Higgs boson search are as low as 60 GeV assuming a mass scale at the SM brane $\Lambda_W = 246$ GeV. At large scales $\Lambda_W > 11$ TeV the impact of the mixing is small and the limit is expected to be better than 110 GeV. But due to a 2σ excess in the LEP combined SM Higgs boson search, only a limit of 97 GeV is observed. A limit on the radion mass independent of the mixing and the Higgs boson mass is impossible because the sensitivity to the radion is strongly reduced at large negative mixing.

The hunt for the Higgs boson will be continued at the TEVATRON and later on at the LHC. Most likely, the TEVATRON will not gather enough statistic to observe the Higgs boson before the start of the LHC. Nevertheless, the experiments at the TEVATRON and the LHC are only sensitive to clear signatures provided by $H^0 \to \gamma\gamma$ and $H^0 \to W^+W^-$. Furthermore, the LHC experiments are capable to detect decays $H^0 \to b\bar{b}$ and $H^0 \to \tau\tau$ if the Higgs boson is produced in association with a top quark pair. More exotic scenarios are likely to escape detection. Moreover, measurements of $h^0 \to gg$, or decays into light flavours and the further exploration of the Randall-Sundrum parameter space will not become possible without a next generation collider providing a cleaner environment like the proposed e^+e^--colliders JLC, NLC or TESLA.

Appendix A

A.1 Kinematic Fitting

Although, all jet parameters are measured in the four-jet channel, they may have large errors due to tracks or clusters assigned to wrong jets, and unmeasured particles, like neutrinos or particles escaping through the beam pipe. Generally, the direction of the jets is measured precisely, however the measured energies and momenta show large measurement errors. The jet momentum resolution is improved by constrained kinematic fits. Useful constraints are energy and momentum conservation, and in event classes like Higgs-strahlung or W pair production, the invariant masses of the two jet pairs assigned to the W, Z or Higgs boson candidates.

During the fitting procedure all jet parameters are varied according to their errors. The constraints are enforced with the help of Lagrange multipliers. The technique is illustrated and necessary theorems are proven in §8 of [111] (also see [112] to gain some basic wisdom). The jet momenta are parametrised by $\log p$, θ and ϕ because in this parametrisation the errors are approximately Gaussian, uncorrelated, and because the variation of the parameters will never lead to unphysical momenta.

The goodness of the fit is measured by the deviation of the fitted jet momenta $\tilde{y}$ from the original measurement $y := (\log p_{\mathrm{jet1}}, \theta_{\mathrm{jet1}}, \phi_{\mathrm{jet1}}, \ldots \log p_{\mathrm{jet4}}, \ldots)$ weighted by their errors σ_{ij}. This can be written in matrix notation:

$$\chi^2 := (y - \tilde{y})^{\mathrm{T}} \sigma^{-1} (y - \tilde{y}) \tag{A.1}$$

The parameters $\tilde{y}$ are chosen such that the constraints $k = 1 \ldots n_c$ given in the form:

$$f_k(\tilde{y}) \equiv 0 \tag{A.2}$$

are fulfilled and χ^2 becomes minimal along the manifold defined by (A.2). In order to include the constraints into (A.1), theorem 4 in §8 of [111] is used:

> **Theorem:** *Let* $f,\, g \in \mathrm{C}^1$ $f,\, g : U \to \mathbb{R}$, U *open* $\mathbb{R}^m$ *and* $a \in \mathbb{R}^m$ *with* $\exists i : \partial f(a)/\partial x_i \neq 0$ *a local minimum of* g *under the constraint* $f \equiv 0$ *then* $\exists \lambda : \partial g(a)/\partial x_i = \lambda \partial f(a)/\partial x_i \forall i = 1 \ldots 3$.

The new measure of goodness reads[1]:

$$\tilde{\chi}^2 := (y - \tilde{y})^{\mathrm{T}} \sigma^{-1} (y - \tilde{y}) + \left| 2\lambda^k f_k(y) \right|, \tag{A.3}$$

---

[1] Summation over indices appearing twice is meant implicitly.

where the Lagrange multipliers λ^k are considered to be additional independent variables. The necessary condition for a local minimum of $\tilde{\chi}^2$ becomes:

$$0=\frac{\partial\tilde{\chi}^2(\tilde{y})}{\partial y_i}=-2\sigma^{-1}(y-\tilde{y})+2\lambda^k\left.\frac{\partial f_k}{\partial y_i}\right|_{\tilde{y}} \text{ and } 0=\frac{\partial\tilde{\chi}^2(\tilde{y})}{\partial\lambda_k}=2f_k(\tilde{y}),\ \forall i=1\dots3,\ k=1\dots n_c. \tag{A.4}$$

In general this set of equations cannot be solved analytically for $\tilde{y}$ and λ_k. A solution is searched with Newton's method. A reasonable starting value $\tilde{y}^0$ is chosen and improved in each iteration:

$$\tilde{y}^{(n+1)}:=\tilde{y}^{(n)}+\Delta\tilde{y}. \tag{A.5}$$

Generally, this approximate solution does not fulfil (A.2). The second equation of (A.4) is approximated to first order by the Taylor series in the neighbourhood of $\tilde{y}^{(n)}$:

$$f_k(\tilde{y}^{(n+1)})=f_k(\tilde{y}^{(n)})+\left.\frac{\partial f_k}{\partial y_i}\right|_{\tilde{y}^{(n)}}\Delta\tilde{y}+\mathcal{O}(\Delta\tilde{y}^2). \tag{A.6}$$

Inserting (A.5) and (A.6) into (A.4) yields a system of linear equations for $\Delta\tilde{y}$ and λ. The equations can be written in matrix notation with $\lambda:=(\lambda_0,\dots\lambda_{n_c})$, $F:=(f_1,\dots f_{n_c})$ and $DF^{(n)}_{ki}:=\partial f_k/\partial y_i|_{\tilde{y}^{(n)}}$:

$$\begin{array}{ccccccc} \mathbb{1} & \Delta\tilde{y} & + & \sigma DF^{(n)}\lambda^{(n)} & = & y-\tilde{y}^{(n)} \\ DF^{(n)} & \Delta\tilde{y} & + & 0 & = & -F^{(n)}. \end{array} \tag{A.7}$$

The second set of equations (A.7) can be used to eliminate $\Delta\tilde{y}$ and solve for $\lambda^{(n)}$:

$$\lambda^{(n)}=(DF^{(n)}\sigma DF^{(n)})^{-1}\left(DF^{(n)}\left(y-\tilde{y}^{(n)}\right)+F\right). \tag{A.8}$$

With $\lambda^{(n)}$ the new solution $\tilde{y}^{(n+1)}$ can be calculated from the first set of equations (A.7)

$$\tilde{y}^{(n+1)}=y-\sigma DF^{(n)}\lambda^{(n)}. \tag{A.9}$$

Convergence of the sequence $\tilde{y}^{(n)}$ is guaranteed by theorem 1 in §17 of [112] if $\left\|\tilde{y}^{(n+1)}-\tilde{x}^{(n+1)}\right\|\le C\left\|\tilde{y}^{(n)}-\tilde{x}^{(n)}\right\|$, $C<1$, $n\in\mathbb{N}$ and $\forall\tilde{y},\tilde{x}\in U\subset\mathbb{R}^m$. Generally, the sequence $\tilde{y}^{(n)}$ converges quickly. The iteration is stopped if the constraints are not fulfilled much better than in the previous step, the fitted momenta did not change significantly and the contribution of the constraints to the measure of goodness $\tilde{\chi}^2$ is small:

$$\begin{aligned} 2\left|\sum_k\left|\lambda_k f_k^{(n+1)}(\tilde{y}^{(n+1)})\right|-\sum_k\left|\lambda_k f_k^{(n)}(\tilde{y}^{(n)})\right|\right| &< 10^{-3} \\ \text{and}\quad \left|\left(\chi^2\right)^{(n)}-\left(\chi^2\right)^{(n+1)}\right| &< 10^{-4}\cdot\left(\chi^2\right)^{(n)} \\ \text{and}\quad 2\sum_k\left|\lambda_k f_k^{(n+1)}(\tilde{y}^{(n+1)})\right| &< 10^{-3}\left(\chi^2\right)^{(n+1)}. \end{aligned} \tag{A.10}$$

The fit is considered as bad and the iteration is stopped, if the new momenta do not fulfil (A.2) satisfactorily: $\sum_k\left|\lambda_k f_k^{(n+1)}(\tilde{y}^{(n+1)})\right|>10^{-3}\cdot(\chi^2)^{(n+1)}$, and they have drifted even further away: $\sum_k\left|\lambda_k f_k^{(n+1)}(\tilde{y}^{(n+1)})\right|>1.05\cdot\sum_k\left|\lambda_k f_k^{(n)}(\tilde{y}^{(n)})\right|$.

If the fit has converged as defined by (A.10) the contribution of the constraints to the measure of goodness is negligible and $\tilde{\chi}^2\cong\chi^2(\tilde{y})$ follows a χ^2-distribution. Thus, the probability $\mathcal{P}(\tilde{\chi}^2,\text{n.d.f})$ can be used as a probability for the correctness of the hypothesis (A.2).

A.2 Simulated Event Samples

Generator	Run	Event type	$[\sqrt{s}]$ GeV	Events	Comment
KK2F	5195	$\mathrm{q\bar{q}}$	192	250k	
OPAL99	5196		196	250k	
	5119		200	300k	
	5199		202	250k	
OPAL2000	5761		204	150k	
	5193		206	250k	
	5186		207	500k	
	5191		208	500k	
	12166		210	250k	
	5177		206	250k	events of 5193+HERWIG
grc4f	8751	$\mathrm{q\bar{q}q\bar{q}}$	192	43286	
OPAL99	9097		196	44082	
	9314		200	44545	
	9712		202	44722	
OPAL2000	10345		204	44780	
	10071		206	44870	
	10782		207	89696	
	10347		208	44831	
	10349		210	44824	
	10962		206	44870	events of 10071+HERWIG
grc4f	8750	$\mathrm{q\bar{q}}\ell^+\ell^-$	192	44735	
OPAL99	9096		196	45700	
	9313		200	46385	
	9711		202	46595	
OPAL2000	10070		206	47015	
	10346		208	47132	
grc4f	9277	$\mathrm{q\bar{q}e^+e^-}$	192	207129	
OPAL99	9280		196	202483	
	9318		200	197391	
	9713		202	195239	
OPAL2000	10075		206	191143	

Table A.2: Simulated events of background processes used to generate reference distributions and to determine the expected background rates. The final states resulting from the generators KK2F and grc4f are fragmented and hadronised using JETSET (or HERWIG). Then, all simulated hadrons, leptons and photons are passed through the OPAL detector simulation.

Generator	Run	Event type	$[\sqrt{s}]$ GeV	Events	Comment
HZHA v2.07	9825	$ZH \rightarrow \mathrm{q\bar{q}q\bar{q}}$	192	2000	$m_{\mathrm{H}} = 60,\, 61,\, \ldots 79\,\mathrm{GeV}$
OPAL99	8985		192	2000	$m_{\mathrm{H}} = 80,\, 81,\, \ldots 110\,\mathrm{GeV}$
	9826		196	2000	$m_{\mathrm{H}} = 60,\, 61,\, \ldots 79\,\mathrm{GeV}$
	9091		196	2000	$m_{\mathrm{H}} = 80,\, 81,\, \ldots 110\,\mathrm{GeV}$
	9307		200	2000	$m_{\mathrm{H}} = 80,\, 81,\, \ldots 110\,\mathrm{GeV}$
HZHA v3.03	9827	$ZH \rightarrow \mathrm{q\bar{q}q\bar{q}}$	200	2000	$m_{\mathrm{H}} = 60,\, 61,\, \ldots 79\,\mathrm{GeV}$
OPAL99	9616		202	2000	$m_{\mathrm{H}} = 80,\, 81,\, \ldots 120\,\mathrm{GeV}$
	9828		202	2000	$m_{\mathrm{H}} = 60,\, 61,\, \ldots 79\,\mathrm{GeV}$
HZHA v2.07	10054	$ZH \rightarrow \mathrm{q\bar{q}q\bar{q}}$	192	2000	$m_{\mathrm{H}} = 111,\, \ldots 120\,\mathrm{GeV}$
OPAL99	10059		196	2000	$m_{\mathrm{H}} = 111,\, \ldots 120\,\mathrm{GeV}$
HZHA v3.03	10225	$ZH \rightarrow \mathrm{q\bar{q}q\bar{q}}$	204	2000	$m_{\mathrm{H}} = 80,\, 81,\, \ldots 120\,\mathrm{GeV}$
OPAL2000	10109		206	2000	$m_{\mathrm{H}} = 80,\, 81,\, \ldots 120\,\mathrm{GeV}$
	10326		206	2000	$m_{\mathrm{H}} = 60,\, 61,\, \ldots 79\,\mathrm{GeV}$
	10789		207	1000	$m_{\mathrm{H}} = 60,\, 85,\, \ldots 120\,\mathrm{GeV}$
	10354		208	1000	$m_{\mathrm{H}} = 80,\, 81,\, \ldots 120\,\mathrm{GeV}$
	10363		210	1000	$m_{\mathrm{H}} = 60,\, 61,\, \ldots 120\,\mathrm{GeV}$
HZHA v3.03	9990	$\mathrm{ZH} \rightarrow \mathrm{q\bar{q}}gg$	196	1000	$m_{\mathrm{H}} = 60,\, 70,\, \ldots 120\,\mathrm{GeV}$
OPAL99	10028	$\mathrm{ZH} \rightarrow \mathrm{q\bar{q}}gg$	200	1000	$m_{\mathrm{H}} = 60,\, 85,\, \ldots 120\,\mathrm{GeV}$
	10033	$\mathrm{ZH} \rightarrow \mathrm{q\bar{q}c\bar{c}}$	200	1000	$m_{\mathrm{H}} = 60,\, 85,\, \ldots 120\,\mathrm{GeV}$
	10038	$\mathrm{ZH} \rightarrow \mathrm{q\bar{q}}gg$	202	1000	$m_{\mathrm{H}} = 60,\, 85,\, \ldots 120\,\mathrm{GeV}$
	10043	$\mathrm{ZH} \rightarrow \mathrm{q\bar{q}c\bar{c}}$	202	1000	$m_{\mathrm{H}} = 60,\, 85,\, \ldots 120\,\mathrm{GeV}$
HZHA v3.03	10327	$\mathrm{ZH} \rightarrow \mathrm{q\bar{q}}gg$	206	1000	$m_{\mathrm{H}} = 60,\, 85,\, \ldots 120\,\mathrm{GeV}$
OPAL2000	10697	$\mathrm{ZH} \rightarrow \mathrm{q\bar{q}}gg$	206	4000	$m_{\mathrm{H}} = 80,\, 85,\, \ldots 120\,\mathrm{GeV}$
	10699	$\mathrm{ZH} \rightarrow \mathrm{q\bar{q}}gg$	206	4000	$m_{\mathrm{H}} = 80 \pm 3,\, 110 \pm 3\,\mathrm{GeV}$
	10332	$\mathrm{ZH} \rightarrow \mathrm{q\bar{q}c\bar{c}}$	206	4000	$m_{\mathrm{H}} = 60,\, 85,\, \ldots 120\,\mathrm{GeV}$
	10698	$\mathrm{ZH} \rightarrow \mathrm{q\bar{q}c\bar{c}}$	206	4000	$m_{\mathrm{H}} = 80,\, 85,\, \ldots 120\,\mathrm{GeV}$
	10700	$\mathrm{ZH} \rightarrow \mathrm{q\bar{q}c\bar{c}}$	206	4000	$m_{\mathrm{H}} = 80 \pm 3,\, 110 \pm 3\,\mathrm{GeV}$
HZHA v3.03	12354	$\mathrm{ZH} \rightarrow \mathrm{q\bar{q}s\bar{s}}$	206	1000	$m_{\mathrm{H}} = 70,\, 100\,\mathrm{GeV}$
OPAL2000	12326	$\mathrm{ZH} \rightarrow \mathrm{q\bar{q}AA}$	206	1000	$m_{\mathrm{H}} = 100\,\mathrm{GeV},\, m_{\mathrm{A}} = 5 \ldots 50\,\mathrm{GeV}$

Table A.4: Simulated events of signal processes used to generate reference distributions and to determine the selection efficiencies. The final states resulting from the generator HZHA are fragmented and hadronised using JETSET. All simulated hadrons, leptons and photons are passed through the OPAL detector simulation.

Bibliography

[1] ALEPH, DELPHI, L3, OPAL Collaborations, “Search for the Standard Model Higgs Boson at LEP,” Preliminary Results of the LEP Higgs Working Group, to be submittded to Physics Lettes B.

A. Read, Private communication, 2003.

[2] OPAL Collaboration, G. Abbiendi *et al.*, “Decay-mode Independent Searches for New Scalar Bosons with the OPAL Detector at LEP,” `hep-ex/0206022`.

[3] LEP Higgs Working Group, “Flavor independent search for Hadronically Decaying Neutral Higgs Bosons at LEP,” `hep-ex/0107034`.

ALEPH Collaboration, A. Heister *et al.*, “A Flavor Independent Higgs Boson Search in e^+e^- Collisions at $\sqrt{s}$ up to 209 GeV,” *Phys. Lett.* **B544**, (2002) 25–34, `hep-ex/0205055`.

DELPHI Collaboration, “Generalised Search for Hadronic Decays of Higgs Bosons with the Delphi Detector at LEP2,” Contribution to the EPS conference, DELPHI 2001-070 CONF 498, July, 2001.

L3 Collaboration, “Flavour Independent Search for Hadronically Decaying Higgs Bosons in the Higgs-Strahlung Process at $\sqrt{s}$ up to 209 GeV,” Contribution to the EPS conference, L3 Note 2693, July, 2001.

[4] OPAL Collaboration, G. Abbiendi *et al.*, “Two Higgs Doublet Model and Model Independent Interpretation of Neutral Higgs Boson Searches,” *Eur. Phys. J.* **C18**, (2001) 425–445, `hep-ex/0007040`.

[5] I. J. R. Aitchison and A. J. G. Hey, *Gauge Theories in Particle Physics*. Hilger, 1989.

C. Quigg, *Gauge Theories of the Strong, Weak and Electromagnetic Interactions*. Benjamine-Cummings Publishing Company, second ed., 1983.

[6] F. Englert and R. Brout, “Broken Symmetry and the Mass of Gauge Vector Mesons,” *Phys. Rev. Lett.* **13**, (1964) 321–322.

P. W. Higgs, “Broken Symmetries, Massless Particles and Gauge Fields,” *Phys. Lett.* **12**, (1964) 132–133.

[7] G. S. Guralnik, C. R. Hagen, and T. W. B. Kibble, “Global Conservation Laws and Massless Particles,” *Phys. Rev. Lett.* **13**, (1964) 585–587.

T. W. B. Kibble, “Symmetry Breaking in Non-Abelian Gauge Theories,” *Phys. Rev.* **155**, (1967) 1554–1561.

[8] C. Quigg, *Gauge Theories of the Strong, Weak and Electromagnetic Interactions*, ch. 6.3. Benjamine-Cummings Publishing Company, second ed., 1983.

[9] C. Itzykson and J.-B. Zuber, *Quantum Field Theory*, ch. 12. McGraw-Hill, international ed., 1985.

[10] J. Goldstone, A. Salam, and S. Weinberg, "Broken Symmetries," *Phys. Rev.* **127**, (1962) 965–970.

S. Willenbrock, "Pair Production of Longitudinal W and Z Bosons and the Goldstone Boson Equivalence Theorem,". Invited talk presented at the 1987 DPF Meeting, Salt Lake City, Utah, Jan 14-17, 1987.

[11] P. Schmüser, *Feynman-Graphen und Eichtheorien für Experimentalphysiker*, ch. 11.5. Springer, second ed., 1995.

[12] T. Hambye and K. Riesselmann, "Matching Conditions and Higgs Mass Upper Bounds Revisited," *Phys. Rev.* **D55**, (1997) 7255–7262, `hep-ph/9610272`.

[13] J. A. Casas, J. R. Espinosa, and M. Quiros, "Standard Model Stability Bounds for New Physics within LHC Reach," *Phys. Lett.* **B382**, (1996) 374–382, `hep-ph/9603227`.

[14] B. W. Lee, C. Quigg, and H. B. Thacker, "The Strength of Weak Interactions at Very High-Energies and the Higgs Boson Mass," *Phys. Rev. Lett.* **38**, (1977) 883.

[15] J. F. Gunion, H. E. Haber, G. L. Kane, and S. Dawson, *The Higgs Hunter's Guide*, ch. 2.6. Addison-Wesley, Juli, 1989.

[16] C. Itzykson and J.-B. Zuber, *Quantum Field Theory*, ch. 12.4. McGraw-Hill, international ed., 1985.

[17] C. Itzykson and J.-B. Zuber, *Quantum Field Theory*, ch. 13. McGraw-Hill, international ed., 1985.

[18] B. Schrempp and M. Wimmer, "Top Quark and Higgs Boson Masses: Interplay Between Infrared and Ultraviolet Physics," *Prog. Part. Nucl. Phys.* **37**, (1996) 1–90, `hep-ph/9606386`.

[19] L. D. Landau, A. A. Abrikosov, and I. M. Halatnikov *Doklady Akad. Nauk SSS* **95**, (1954) 1177.

[20] The LEP Electroweak Working Group and the SLD Heavy Flavour Working Group, "A Combination of Preliminary Electroweak Measurements and Constraints on the Standard Model," `hep-ex/0212036`.

[21] NuTeV Collaboration, G. P. Zeller *et al.*, "A Precise Determination of Electroweak Parameters in Neutrino Nucleon Scattering," *Phys. Rev. Lett.* **88**, (2002) 091802, `hep-ex/0110059`.

[22] E. Gross, G. Wolf, and B. A. Kniehl, "Production and Decay of the Standard Model Higgs Boson LEP-200," *Z. Phys.* **C63**, (1994) 417–426, `hep-ph/9404220`.

[23] W. Kilian, M. Kramer, and P. M. Zerwas, "Higgs-strahlung and WW Fusion in e^+e^- Collisions," *Phys. Lett.* **B373**, (1996) 135–140, `hep-ph/9512355`.

[24] HZHA generator: P. Janot, G. Ganis, *Physics at LEP2*, CERN 96-01 (1996) Vol. 2, 309.

[25] A. Djouadi, M. Spira, and P. M. Zerwas, "Production of Higgs bosons in Proton Colliders: QCD Corrections," *Phys. Lett.* **B264**, (1991) 440–446.

[26] M. Spira, "QCD Effects in Higgs Physics," *Fortsch. Phys.* **46**, (1998) 203–284, `hep-ph/9705337`.

[27] G. L. Kane, *Perspectives on Searching for Higgs Physics.* World Scientific, Singapore, June, 1999. Lectures at the XXI GIFT International Seminar on Theoretical Physics and the XVIII International Meeting on Fundamental Physics.

D. A. Ross and M. J. G. Veltman, "Neutral Currents in Neutrino Experiments," *Nucl. Phys.* **B95**, (1975) 135.

[28] Particle Data Group , K. Hagiwara *et al.*, "Review of Particle Physics," *Phys. Rev.* **D66**, (2002) 010001.

[29] B. Lee in *Proceedings of the XVI Internation Conference on High Energy Physics*, J. D. Jackson, A. Roberts, and R. Donaldson, eds., vol. 4. Batavia, 1972.

[30] H.-S. Tsao in *Proceedings of the 1980 Guangzhou on Theoretical Patricle Physics*, H. Ning and T. Hung-yuan, eds., p. 1240. Science Press, Beijing, 1980.

[31] S. L. Glashow, J. Iliopoulos, and L. Maiani, "Weak Interactions with Lepton - Hadron Symmetry," *Phys. Rev.* **D2**, (1970) 1285–1292.

[32] S. L. Glashow and S. Weinberg, "Natural Conservation Laws for Neutral Currents," *Phys. Rev.* **D15**, (1977) 1958.

[33] J. F. Gunion, H. E. Haber, and J. Wudka, "Sum Rules for Higgs Bosons," *Phys. Rev.* **D43**, (1991) 904–912.

[34] J. F. Gunion, H. E. Haber, G. L. Kane, and S. Dawson, *The Higgs Hunter's Guide*, ch. 4. Addison-Wesley, Juli, 1989.

H. E. Haber, G. L. Kane, and T. Sterling, "The Fermion Mass Scale and Possible Effects of Higgs Bosons on Experimental Observables," *Nucl. Phys.* **B161**, (1979) 493.

[35] M. Carena, J. R. Ellis, A. Pilaftsis, and C. E. M. Wagner, "CP-violating MSSM Higgs bosons in the light of LEP 2," *Phys. Lett.* **B495**, (2000) 155–163, `hep-ph/0009212`.

OPAL Collaboration, G. Abbiendi *et al.*, "Interpretation of the Search for Neutral Higgs Bosons from $\sqrt{s} = 91\,\mathrm{GeV}$ to $\sqrt{s} = 209\,\mathrm{GeV}$ in a CP Violating MSSM Scenario," OPAL Physics Note PN505, July, 2002.

[36] S. P. Martin, "A Supersymmetry Primer," `hep-ph/9709356`.

[37] D. I. Kazakov, "Beyond the Standard Model (in Search of Supersymmetry)," `hep-ph/0012288`.

[38] S. R. Coleman and J. Mandula, "All Possible Symmetries of the S Matrix," *Phys. Rev.* **159**, (1967) 1251–1256.

[39] P. Schmüser, *Feynman-Graphen und Eichtheorien für Experimentalphysiker.* Springer, second ed., 1995.

[40] D. J. Gross and R. Jackiw, "Effect of Anomalies on Quasirenormalizable Theories," *Phys. Rev.* **D6**, (1972) 477–493.

[41] G. Degrassi, S. Heinemeyer, W. Hollik, P. Slavich, and G. Weiglein, "Towards High-Precision Predictions for the MSSM Higgs Sector," `hep-ph/0212020`.

[42] M. Carena, S. Heinemeyer, C. E. M. Wagner, and G. Weiglein, "Suggestions for Improved Benchmark Scenarios for Higgs- Boson Searches at LEP2," `hep-ph/9912223`.

[43] I. Antoniadis, N. Arkani-Hamed, S. Dimopoulos, and G. R. Dvali, "New Dimensions at a Millimeter to a Fermi and Superstrings at a TeV," *Phys. Lett.* **B436**, (1998) 257–263, `hep-ph/9804398`.

[44] I. Antoniadis and K. Benakli, "Limits on the Size of Extra Dimensions and the String Scale," `hep-ph/0108174`.

[45] N. Arkani-Hamed, S. Dimopoulos, and G. R. Dvali, "Phenomenology, Astrophysics and Cosmology of Theories with Sub-millimeter Dimensions and TeV Scale Quantum Gravity," *Phys. Rev.* **D59**, (1999) 086004, `hep-ph/9807344`.

[46] L. Randall and R. Sundrum, "A Large Mass Hierarchy from a Small Extra Dimension," *Phys. Rev. Lett.* **83**, (1999) 3370–3373, `hep-ph/9905221`.

L. Randall and R. Sundrum, "An Alternative to Compactification," *Phys. Rev. Lett.* **83**, (1999) 4690–4693, `hep-th/9906064`.

[47] A. Lukas, B. A. Ovrut, K. S. Stelle, and D. Waldram, "The Universe as a Domain Wall," *Phys. Rev.* **D59**, (1999) 086001, `hep-th/9803235`.

[48] G. F. Giudice, R. Rattazzi, and J. D. Wells, "Quantum Gravity and Extra Dimensions at High-Energy Colliders," *Nucl. Phys.* **B544**, (1999) 3–38, `hep-ph/9811291`.

[49] C. Csaki, M. L. Graesser, and G. D. Kribs, "Radion Dynamics and Electroweak Physics," *Phys. Rev.* **D63**, (2001) 065002, `hep-th/0008151`.

[50] C. Csaki, M. Graesser, L. Randall, and J. Terning, "Cosmology of Brane Models with Radion Stabilization," *Phys. Rev.* **D62**, (2000) 045015, `hep-ph/9911406`.

[51] J. C. Collins, A. Duncan, and S. D. Joglekar, "Trace and Dilatation Anomalies in Gauge Theories," *Phys. Rev.* **D16**, (1977) 438–449.

[52] X. Calmet and H. Fritzsch, "The Higgs Boson Might not Couple to b Quarks," *Phys. Lett.* **B496**, (2000) 190–194, `hep-ph/0008252`.

[53] E. L. Berger, C.-W. Chiang, J. Jiang, T. M. P. Tait, and C. E. M. Wagner, "Higgs Boson Decay into Hadronic Jets," *Phys. Rev.* **D66**, (2002) 095001, `hep-ph/0205342`.

[54] OPAL Collaboration, G. Abbiendi *et al.*, “Search for Associated Production of Massive States Decaying into two Photons in e^+e^- Annihilations at $\sqrt{s} = 88\,\mathrm{GeV} - 209\,\mathrm{GeV}$,” *Phys. Lett.* **B544**, (2002) 44–56, `hep-ex/0207027`.

LEP Collaboration, A. Rosca, “Fermiophobic Higgs Bosons at LEP,” `hep-ex/0212038`.

A. G. Akeroyd and M. A. Diaz, “Searching for a Light Fermiophobic Higgs Boson at the Tevatron,” `hep-ph/0301203`.

[55] OPAL Collaboration, K. Ahmet *et al.*, “The OPAL detector at LEP,” *Nucl. Instrum. Meth.* **A305**, (1991) 275–319.

[56] OPAL Collaboration, S. Anderson *et al.*, “The Extended OPAL Silicon Strip Microvertex Detector,” *Nucl. Instrum. Meth.* **A403**, (1998) 326–350.

[57] G. Aguillion *et al.*, “Thin Scintillating Tiles with High Light Yield for the OPAL Endcaps,” *Nucl. Instrum. Meth.* **A417**, (1998) 266–277.

[58] J. W. P.R. Hobson, “Using the Electromagnetic Clusters from the Gamma Catcher,” OPAL Technical Note TN254, September, 1994.

[59] OPAL Collaboration, P. P. Allport *et al.*, “The OPAL Silicon Microvertex Detector,” *Nucl. Instrum. Meth.* **A324**, (1993) 34–52.

[60] OPAL Collaboration, P. P. Allport *et al.*, “The OPAL Silicon Strip Microvertex Detector with Two Coordinate Readout,” *Nucl. Instrum. Meth.* **A346**, (1994) 476–495.

[61] O. Biebel *et al.*, “Performance of the OPAL Jet Chamber,” *Nucl. Instrum. Meth.* **A323**, (1992) 169–177.

[62] M. Hauschild *et al.*, “Particle Identification with the OPAL Jet Chamber,” *Nucl. Instrum. Meth.* **A314**, (1992) 74–85.

[63] OPAL Collaboration, B. E. Anderson *et al.*, “The OPAL Silicon-Tungsten Calorimeter Front End Electronics,” *IEEE Trans. Nucl. Sci.* **41**, (1994) 845–852.

[64] M. Hauschild, “Kalibration der zentralen Jetkammer des OPAL-Detektors mit UV-Laserstrahlen,” Ph.D. dissertation, BONN-IR-88-57, November, 1988.

[65] A. Weltin, “Elektrostatische Berechnungen an Jet-Driftkammern,” Ph.D. dissertation, 1987.

M. Hauschild, Private communication, 1999.

[66] OPAL Collaboration, R. Akers *et al.*, “The Production of Neutral Kaons in Z^0 Decays and their Bose-Einstein Correlations,” *Z. Phys.* **C67**, (1995) 389–402.

[67] OPAL Collaboration, G. Alexander *et al.*, “A Study of K^0_s Production in Z^0 Decays,” *Phys. Lett.* **B264**, (1991) 467–475.

[68] OPAL Collaboration, K. Ackerstaff *et al.*, “Production of Fermion-Pair Events in e^+e^- Collisions at 161 GeV Centre-of-Mass Energy,” *Phys. Lett.* **B391**, (1997) 221–234.

[69] LEP Energy Working Group , A. Blondel *et al.*, "Evaluation of the LEP Centre-of-mass Energy above the W Pair Production Threshold," *Eur. Phys. J.* **C11**, (1999) 573–585, `hep-ex/9901002`.

[70] R. W. Assmann, "LEP Operation and Performance with Electron Positron Collisions at 209 GeV," Prepared for 11th Workshop on LEP Performance, Chamonix, France, 15-19 Jan 2001.

[71] OPAL Collaboration, G. Abbiendi *et al.*, "Search for the Standard Model Higgs Boson with the OPAL Detector at LEP," `hep-ex/0209078`.

[72] B. F. L. Ward, S. Jadach, and Z. Was, "Precision Calculation for $e^+e^- \rightarrow$ 2f: The KK MC project," `hep-ph/0211132`.

[73] J. Fujimoto *et al.*, "grc4f v1.1: A Four-fermion Event Generator for $\mathrm{e^+e^-}$ Collisions," *Comput. Phys. Commun.* **100**, (1997) 128–156, `hep-ph/9605312`.

[74] G. Marchesini *et al.*, "HERWIG: A Monte Carlo Event Generator for Simulating Hadron Emission Reactions with Interfering Gluons. Version 5.1 - April 1991," *Comput. Phys. Commun.* **67**, (1992) 465–508.

[75] T. Sjöstrand, "High-Energy Physics Event Generator with PYTHIA and JETSET," *Comput. Phys. Commun.* **82**, (1994) 74–90.

[76] OPAL Collaboration, G. Alexander *et al.*, "A Comparison of b and (u d s) Quark Jets to Gluon Jets," *Z. Phys.* **C69**, (1996) 543–560.

[77] OPAL Collaboration, J. Allison *et al.*, "The Detector Simulation Program for the OPAL Experiment at LEP," *Nucl. Instrum. Meth.* **A317**, (1992) 47–74.

[78] OPAL Collaboration, G. Abbiendi *et al.*, "Search for Higgs Bosons in $\mathrm{e^+e^-}$ Collisions at 183 GeV," *Eur. Phys. J.* **C7**, (1999) 407–435, `hep-ex/9811025`.

[79] B. List, "A Simple Figure of Merit for Searches," OPAL Technical Note TN619, August, 1999.

[80] OPAL Collaboration, K. Ackerstaff *et al.*, "Searches for Higgs Bosons in $\mathrm{e^+e^-}$ Collisions at the Highest LEP Energies," OPAL Physics Note PN450, July, 2000.

[81] OPAL Collaboration, K. Ackerstaff *et al.*, "Tests of the Standard Model and Constraints on New Physics from Measurements of Fermion Pair Production at 130 GeV to 172 GeV at LEP," *Eur. Phys. J.* **C2**, (1998) 441–472, `hep-ex/9708024`.

[82] OPAL Collaboration, K. Ackerstaff *et al.*, "Photonic Events with Large Missing Energy in $\mathrm{e^+e^-}$ Collisions at $\sqrt{\mathrm{s}} = 161$ GeV," *Phys. Lett.* **B391**, (1997) 210–220.

[83] N. Brown and W. J. Stirling, "Jet Cross-Sections at Leading Double Logarithm in $\mathrm{e^+e^-}$ Annihilation," *Phys. Lett.* **B252**, (1990) 657–662.

S. Bethke, Z. Kunszt, D. E. Soper, and W. J. Stirling, "New Jet Cluster Algorithms: Next-to-leading Order QCD and Hadronization Corrections," *Nucl. Phys.* **B370**, (1992) 310–334.

S. Catani, Y. L. Dokshitzer, M. Olsson, G. Turnock, and B. R. Webber, “New Clustering Algorithm for Multi-jet Cross-sections in e^+e^-,” *Phys. Lett.* **B269**, (1991) 432–438.

N. Brown and W. J. Stirling, “Finding Jets and Summing Soft Gluons: A New Algorithm,” *Z. Phys.* **C53**, (1992) 629–636.

[84] JADE Collaboration, W. Bartel *et al.*, “Experimental Studies on Multi-jet Production in e^+e^- Annihilation at PETRA Energies,” *Z. Phys.* **C33**, (1986) 23.

OPAL Collaboration, M. Z. Akrawy *et al.*, “A Study of the Recombination Scheme Dependence of Jet Production Rates and of $\alpha_s(M_{Z^0})$ in Hadronic Z^0 Decays,” *Z. Phys.* **C49**, (1991) 375–384.

JADE Collaboration, S. Bethke *et al.*, “Experimental Investigation of the Energy Dependence of the Strong Coupling Strength,” *Phys. Lett.* **B213**, (1988) 235.

[85] M. Schumacher, *Suche nach Neutralen Higgs Bosonen mit dem Opal-Detektor bei LEP2.* 1999. Ph.D. dissertation, BN-IR-99.

[86] S. Yamashita, “Attempt to Develop New Jet-Particle Association Methods for Four-Jet Topology with OPAL Detector,” OPAL Technical Note TN579, November, 1998.

[87] S. Catani and M. H. Seymour, “The Dipole Formalism for the Calculation of QCD Jet Cross Sections at Next-to-Leading Order,” *Phys. Lett.* **B378**, (1996) 287–301, `hep-ph/9602277`.

[88] F. A. Berends, R. Pittau, and R. Kleiss, “Excalibur: A Monte Carlo Program to Evaluate all Four Fermion Processes at LEP-200 and Beyond,” *Comput. Phys. Commun.* **85**, (1995) 437–452, `hep-ph/9409326`.

[89] J. Böhme, “Alternative Kinematic Fits for Higgs Boson Search in the 4-Jet-Channel,” OPAL Technical Note TN593, January, 1999.

[90] F. A. Berends and R. Kleiss, “Initial State Radiation at LEP Energies and the Corrections to Higgs Boson Production,” *Nucl. Phys.* **B260**, (1985) 32.

J. Böhme and B. List, “Implementation of the Higgsstrahlung Matrix Element,” OPAL Technical Note TN607, April, 1999.

[91] K. S. Cranmer, “Kernel Estimation for Parametrisation of Discriminant Variable Distributions,” ALEPH 99-144, December, 1999.

[92] I. Abramson, “On Bandwidth Variation in Kernel Estimates: A Square Root Law,” *Ann. Statist.* **10**, (1992) 1217–1223.

J. Allison, “Multiquadric Radial Basis Functions for Representing Multidimensional High-Energy Physics Data,” *Comput. Phys. Commun.* **77**, (1993) 377–395.

[93] M. G. F. James, “MINUIT, Function Minimization and Error Analysis,” March, 1992.

[94] H. Akima, “A New Method of Interpolation and Smooth Curve Fitting Based on Local Procedures,” *J.ACM* **17**, (1970), no. 4, 589–602.

[95] I. N. S. Yamashita, "A New B-Tagging Tool for LEP2," OPAL Technical Note TN576, November, 1998.

I. N. S. Yamashita, "LB160: Upgraded B-Tagging for LEP2," OPAL Technical Note TN578, November, 1998.

[96] T. Sjostrand and V. A. Khoze, "Does the W mass Reconstruction Survive QCD Effects?," *Phys. Rev. Lett.* **72**, (1994) 28–31, `hep-ph/9310276`.

[97] OPAL Collaboration, G. Abbiendi *et al.*, "Measurement of the Mass and Width of the W Boson in e^+e^- Collisions at 189 GeV," *Phys. Lett.* **B507**, (2001) 29–46, `hep-ex/0009018`.

[98] C. D.R.Ward, "WWFIX - fixups for the W mass Analysis," OPAL Technical Note TN715, April, 2002.

[99] P. Bock, "Determination of Exclusion Limits for Particle Production Using Different Decay Channels with Different Energies, Mass Resolutions and Backgrounds," Heidelberg University Preprint HD-PY-96/05, to be submitted to Nucl. Instr. Meth., 1996.

[100] R. D. Cousins and V. L. Highland, "Incorporating Systematic Uncertainties into an Upper Limit," *Nucl. Instrum. Meth.* **A320**, (1992) 331–335.

[101] P. Bock, Private communication, implementation located at `/afs/cern.ch/user/b/bock/public/exclusion/confl20.f`, 2002.

[102] OPAL Collaboration, K. Ackerstaff *et al.*, "Flavour Independent Search for a Hadronically Decaying Higgs Boson in e^+e^- Collisions," OPAL Physics Note PN507, July, 2002.

[103] OPAL Collaboration, G. Alexander *et al.*, "Search for Neutral Higgs Bosons in Z^0 Decays Using the OPAL Detector at LEP," *Z. Phys.* **C73**, (1997) 189–199.

[104] OPAL Collaboration, K. Ackerstaff *et al.*, "Search for the Standard Model Higgs Boson in e^+e^- Collisions at $\sqrt{s} = 161$ GeV to 172 GeV," *Eur. Phys. J.* **C1**, (1998) 425–438, `hep-ex/9709003`.

OPAL Collaboration, G. Alexander *et al.*, "Measurement of the Z^0 Line Shape Parameters and the Electroweak Couplings of Charged Leptons," *Z. Phys.* **C52**, (1991) 175–208.

[105] A. Raspereza, Private communication, 2003.

[106] T. Junk, "Search for $e^+e^- \rightarrow hA$ in the Hadronic Channel Without Flavor Tagging in the 1999 and 2000 Data," OPAL Technical Note TN726, 2002.

[107] LEP Higgs Working Group, "Searches for the Neutral Higgs Bosons of the MSSM: Preliminary Combined Results Using LEP Data Collected at Energies up to 209 GeV," `hep-ex/0107030`.

[108] H. Davoudiasl, J. L. Hewett, and T. G. Rizzo, “Experimental Probes of Localized Gravity: On and off the Wall,” *Phys. Rev.* **D63**, (2001) 075004, `hep-ph/0006041`.

[109] H. Davoudiasl, J. L. Hewett, and T. G. Rizzo, “Phenomenology of the Randall-Sundrum Gauge Hierarchy Model,” *Phys. Rev. Lett.* **84**, (2000) 2080, `hep-ph/9909255`.

[110] M. Carena, S. Heinemeyer, C. E. M. Wagner, and G. Weiglein, “Suggestions for benchmark scenarios for MSSM Higgs boson searches at hadron colliders,” *Eur. Phys. J.* **C26**, (2003) 601–607, `hep-ph/0202167`.

[111] O. Forster, *Analysis 2.* Vieweg, 1984.

[112] A. Noitator, *Speudospektrale Vektoranalysis II.* No. ISBN 3-141-592653-5. Pi-soft, 1993.

Acknowledgements

I would like to thank my professor Rolf-Dieter Heuer that I got the opportunity to participate in the OPAL experiment and to work on this thesis. It was a pleasure to work with all the people of our group in Hamburg, who are: Markus Ball, Philip Bechtle, Ties Behnke, Jenny Böhme, Karsten Büsser, Mathieu Doucet, Filip Franco-Sollova, Nabil Ghodbane, Nils Gollub, Marius Groll, Markus Hamann, Kristian Harder, Jakob Hauschildt, Carsten Hensel, Petra Hüntemeyer, Andreas Imhof, Alexander Kaoukher, Klaus Desch, Tatsiana Klimkovich, Thomas Krämer, Thorsten Kuhl, Thorsten Lux, Ramona Matthes, Wolfgang Menges, Niels Meyer, Vasiliy Morgunov, Alexei Raspereza, Markus Schumacher, Felix Sefkow and Peter Wienemann, and with all the OPALists. Furthermore, I would like to thank for the possibility to participate in many collaboration meetings and to stay at CERN for an extended period. Even if modern technologies allow to communicate with people from all over the world, it is still much easier and more productive to discuss with people directly. This thesis was mostly sponsored by the BMBF. I just can express my gratitude that this project was selected for sponsoring. I hope that the BMBF will continue to support fundamental research to this large extend.

This thesis would not have been possible without the help of numerous people. I would like to thank Jenny Böhme and Klaus Desch, who guided and advised me while I was working on the main topic of this thesis, and who struggled with early versions of the text. Furthermore, the thesis was heavily influenced by all the suggestions and inputs I got from the OPAL Higgs working group. I would like to express my gratitude in particular to Amit Klier, Andy Hocker, Arnulf Quadt, Fredrik Åkesson, Gabriella Pásztor, Isamu Nakamura, Koichi Nagai, Pamela Ferrari, Peter Bock, Peter Igo-Kemenes, Richard Teuscher, Satoru Yamashita and Tom Junk. Moreover, I am indebted to Michael Hauschild for preparing and guiding the work Chapter 5 is about.

It needs many people to keep an experiment like OPAL running. The OPAL collaboration did a tremendous job in assuring data quality, and providing, organising, maintaining and documenting tools, saying nothing of the planning, construction and testing of the components of the OPAL detector and software which happened far before my time. Last but not least the OPAL collaboration created a wonderful working atmosphere, which lasted far beyond.

In addition to all members of this group and all OPALists, who I annoyed with an infinite amount of questions, several theoreticians helped patiently to reduce my ignorance. A big shout goes to Graham Kribs, James Wells, Laura Covi, Sven Heinemeyer and Thomas G. Rizzo.

The work on this thesis was not always just fun, fruitful or progressive. I am especially thankful about the support I got in such days from the group members and my friends, in particular Felix, Iñigo, Justus, Maik, Mar, Maria(s), Michael, Pablo and Robin. And last but not least I would like to thank my parents and my sister for the great support I got without giving much in return. I would like to apologise for neglecting most people in the last years. I hope that I can put this right in the future.

Götz Gaycken, Hamburg, March, 2003